Establishment and characterization of advanced hepatic cell culture models for the early assessment and mechanistic understanding of drug-induced liver injury

Dissertation

der Mathematisch-Naturwissenschaftlichen Fakultät

der Eberhard Karls Universität Tübingen

zur Erlangung des Grades eines

Doktors der Naturwissenschaften

(Dr. rer. nat.)

vorgelegt von

Jessica Katharina Dieckhoff

aus Pforzheim

Tübingen

2022

Gedruckt mit Genehmigung der Mathematisch-Naturwissenschaftlichen Fakultät der Eberhard Karls Universität Tübingen.

Tag der mündlichen Qualifikation:	23.06.2022
Dekan:	Prof. Dr. Thilo Stehle
1. Berichterstatter:	Prof. Dr. Robert Lukowski
2. Berichterstatter:	Prof. Dr. Peter Ruth

Dla mojej rodziny.

Declaration

This dissertation is the result of my own work and includes nothing, which is the outcome of work done in collaboration except where specifically indicated in the text. It has not been previously submitted, in part or whole, to any university of institution for any degree, diploma, or other qualification.

Signature: 

Date: 30.06.2022

Eidesstattliche Erklärung

Diese Dissertation ist das Ergebnis meiner eigenen Arbeit und enthält nichts, was das Ergebnis einer Zusammenarbeit ist, es sei denn, es wird im Text ausdrücklich darauf hingewiesen. Sie wurde zuvor weder ganz noch teilweise bei einer Universität oder Einrichtung zur Erlangung eines Abschlusses, Diploms oder einer anderen Qualifikation eingereicht.

Unterschrift: 

Datum: 30.06.2022

Table of contents

Abstract

Drug discovery and development is a very time-consuming and costly process that requires many *in vitro* and *in vivo* studies. Despite numerous studies, over 90 % of drug candidates fail in preclinical or clinical trials due to insufficient safety and efficacy [1]. *Drug-induced liver toxicity* (DILI) is one of the most common cause for the high failure rate and the withdrawal of already approved drugs. So far, the high loss of new drug candidates due to unpredictable hepatotoxicity is a major problem for the pharmaceutical industry. The reason that the DILI potential of a new drug cannot be determined as early as possible is attributed to the combination of the primitive human test models in toxicological studies, the incomplete knowledge of the DILI mechanism, and the lack of sensitive, reliable biomarkers. Primary human hepatocytes cultured flat on an optimized plastic surface are currently the gold standard for toxicology testing, even though this model lacks important organotypic physiology and thus impaired long-term functionality. Recently, advanced cell culture models have come into focus that promise long-term toxicological testing due to the extended functionality of hepatocytes by mimicking physiological conditions *in vitro*.

The aim of this thesis was to establish advanced hepatic cell culture models and evaluate new, more reliable sensitive biomarkers for DILI. The characterization of the advanced models confirmed the extended *in vitro* stability and performance of primary liver cells. This was seen by reconstructed polarization, and measurable metabolic activity for extended periods. Moreover, the present results showed that culture configuration has an impact on pathway activity which should be considered when addressing a scientific issue. Functional liver organoids have been differentiated from iPSCs that exhibit liver cell-specific properties. In addition, the data confirms their suitability for long-term toxicological studies.

Primary liver cells retain long-term stable *in vitro*. This allows the study of potential biomarkers to predict DILI events. Therefore, primary liver cell models were treated long-term with a series of compounds most and least likely to cause DILI. Subsequently, secreted and genetically expressed markers were examined. The study demonstrated the suitability of some proteins and genes as potential biomarkers, but also highlighted the need of the integration of multiple liver cell types, including an immune system, to reliable develop and detect DILI *in vitro*.

In conclusion, advanced liver models are a promising tool to evaluate potential DILI biomarkers, study liver biology, and metabolic and toxicologic profiles in a more physiological related environment. They can be integrated into early screening tools used in industry and academia, lead to a better understanding of drug action, and allow bridging the gap between simple 2D and complex *in vivo* models in the drug development process.

Zusammenfassung

Die Arzneimittelentwicklung ist ein sehr zeit- und kostenaufwändiger Prozess, der viele *in-vitro*- und *in-vivo*-Studien erfordert. Trotz zahlreicher Studien scheitern über 90 % der Arzneimittelkandidaten in der präklinischen oder klinischen Phase aufgrund unzureichender Sicherheit und Wirksamkeit [1]. Die *arzneimittel-induzierte Lebertoxizität* (DILI) ist eine der häufigsten Ursachen für die hohe Misserfolgsquote und die Rücknahme bereits zugelassener Arzneimittel. Bislang ist der hohe Verlust neuer Arzneimittelkandidaten aufgrund unvorhersehbarer Hepatotoxizität ein großes Problem für die Pharmaindustrie. Die Kombination aus den primitiven humanen Testmodellen in toxikologischen Studien, dem lückenhaften Verständnis des DILI-Mechanismus und dem Mangel an empfindlichen, zuverlässigen Biomarkern erschweren die frühe Bestimmung des DILI-Potentials eines neuen Medikaments. Der Goldstandard für hepatotoxische Experimente sind primäre humane Hepatozyten, die flach auf einer optimierten Kunststoffoberfläche kultiviert werden. Durch die Isolation aus dem Zellverband und die organuntypische Kultivierung verlieren sie sehr schnell ihre physiologischen Eigenschaften und Funktionalität. Deshalb rücken seit einigen Jahren erweiterte Zellkultursysteme immer mehr in den Fokus. Durch die Nachahmung der physiologischen Bedingungen *in vitro*, kann die Funktionalität der primären Leberzellen länger erhalten werden was toxikologische Langzeit-Versuche ermöglicht.

Ziel dieser Arbeit war die Etablierung von erweiterten Leberzellkulturmodellen und die Untersuchung neuer, potenzieller Biomarker für die *in vitro*-Identifizierung der DILI. Die Charakterisierung der Modelle bestätigte die verlängerte *in-vitro*-Stabilität der primären Leberzellen. Dies zeigte sich in der rekonstruierten Polarisierung und der messbaren Stoffwechselaktivität über längere Zeiträume. Darüber hinaus zeigten die Ergebnisse, dass die Kulturkonfiguration einen Einfluss auf die Aktivität der Stoffwechselwege hat. Dies sollte bei der Wahl eines geeigneten Zellkulturmodells berücksichtigt werden. Aus induzierten pluripotenten Stammzellen wurden funktionelle Leberorganoide differenziert, die Leberzell-spezifische Eigenschaften aufwiesen. Darüber hinaus bestätigen die erhobenen Daten ihre Eignung für toxikologische Langzeitstudien.

Primäre Leberzellen bleiben zwei Wochen in erweiterten Kulturmodellen stabil. Dies ermöglicht die Untersuchung potenzieller Biomarker zur Vorhersage der DILI. Dafür wurden primäre Leberzellmodelle langfristig mit einer Reihe von Substanzen behandelt, die bekanntermaßen DILI hervorrufen oder als sicher eingestuft wurden. Anschließend wurden sekretierte und genetisch exprimierte Biomarker untersucht. Die Studie zeigte die Eignung einiger Proteine und Gene als potenzielle Biomarker. Jedoch machten die Daten auch deutlich, dass für ein Entwicklung und Erkennung von DILI *in vitro*, die Integration mehrerer Leberzelltypen, einschließlich eines Immunsystems, erforderlich ist.

Die vorliegende Studie zeigte, dass erweiterte Leberzellmodelle in einer physiologischen nahen Umgebung ein vielversprechendes Instrument zur Untersuchung der Leberbiologie, potenzieller DILI-Biomarker und des metabolischen und toxikologischen Profils sind. Sie können in frühe Screening-Experimente integriert werden, die in der Industrie und im akademischen Bereich eingesetzt werden. Zudem könnten sie zu einem besseren Verständnis der Arzneimittelwirkung beitragen und die Lücke zwischen einfachen 2D- und komplexen *in-vivo*-Modellen schließen.

Abbreviations

°C	Degree Celsius
%	Percent
µg	Microgram
µL	Microliter
αGST	Alpha Glutathione S-Transferase
ABC	ATP-binding cassette
AMIO	Amiodarone
APAP	Acetaminophen/Paracetamol
ADME	Adsorption, distribution, metabolism, and excretion
AHR	Aryl-hydrocarbon receptor
AFP	Alpha-fetoprotein
ALP	Alkaline phosphatase
ALT	Alanine aminotransferase
AST	Aspartate aminotransferase
ATP	Adenosine triphosphate
bHGF	Basic Human Growth Factor
BOS	Bosentan
BSEP	Bile salt export pump
CAR	Constitutive androstane receptor
ccK18	Caspase-cleaved keratin 18
CDH5	Cadherin-5
CDK	Compound distribution kit
CMFDA	5-chloromethylfluorescein diacetate
CO_2	Carbon dioxide
CRM	Chemically reactive metabolites
CYP450	Cytochrome P450-dependent monooxygenase
DAB	Dabigatran
DAMP	Damage-Associated Molecular Patterns
DEX	Dexamethasone
DIC	Diclofenac
DILI	Drug-induced liver injury
DMEs	Drug metabolizing enzymes
DMSO	Dimethyl sulfoxide
EC_{50}	Half maximal effective concentration
ECVAM	European Centre for the Validation of Alternative Methods
EDTA	Ethylenediaminetetraacetic acid
ENT	Entacapone
EURL-ECVAM	European Union Reference Laboratory for alternatives to animal testing
ER	Endoplasmic reticulum
FABP1	Liver fatty acid-binding protein (Gene name)
FASLG	Fas Ligand (Gene name)
FasL	Fas Ligand (Protein name)
FBS	Fetal bovine serum
FDA	Food and Drug Administration
FGF	Fibroblast growth factor
FIA	Fialuridine
GFR	Growth factor reduced
GLDH	Glutamate dehydrogenase (Protein name)
GLUD1	Glutamate dehydrogenase (Gene name)
GSH	Glutathione
GST	Glutathione S-transferases (Protein name)
GSTA1	Alpha Glutathione S-transferase (Gene name)
HGF	Hepatocyte growth factor

HMGB1	High-Mobility-Group-Protein B1
iPSC	Induced pluripotent stem cell
ITGB3	Integrin Subunit Beta 3
IQR	Interquartile range
K18	Keratin 18
KCs	Kupffer cells
LDH	Lactate dehydrogenase
LECT2	Leukocyte cell-derived chemotaxin 2
L-FABP	Liver fatty acid-binding protein (Protein name)
Limma	Linear model for microarray
LLOD	Lower limit of detection
LSECs	Liver sinusoidal endothelial cells
LVX	Levofloxacin
MDR	Multidrug resistance protein
MET	Metformin
mg	Milligram
min	Minutes
miRNA	Micro ribonucleic acid
mL	Milliliters
MRP	Multidrug resistance-associated protein
mtDNA	Mitochondrial DNA
NAD^+	Oxidized nicotinamide adenine dinucleotide
NADH	Reduced Nicotinamide adenine dinucleotide (H for hydrogen)
NAPQI	N-Acetyl-p-benzochinonimin
NAT	N-acetyltransferase
NTCP	Na^+-taurocholate co-transporting polypeptides
OATP	Organic anion transporter
OCT	Organic cation transporter
OME	Omeprazole
OOC	Organ on a chip
OPN	Osteopontin
OSM	Oncostatin M
PB	Phenobarbital
PBS	Phosphate-buffered saline
PCA	Principal Component Analysis
PHH	Primary human hepatocytes
PIO	Pioglitazone
PPAR	Peroxisome proliferator-activated receptor
PXR	Pregnane-X-receptor
RIF	Rifampicin
RT	Room temperature
SC	Stellate cell
SDH	Succinate dehydrogenase
SDHA	Succinate dehydrogenase subunit A
SPP1	Osteopontin gene
SULT	Sulfotransferase
TBL	Total bilirubin
TCA	Tricarboxylic acid cycle
TOL	Tolcapone
TRO	Troglitazone
TVX	Trovafloxacin
UGT	UDP-glucuronosyltransferase
ULA	Ultra-low attachment
ULN	Upper limit of normal
XIM	Ximelagatran
xg	Times gravity

List of figures

List of tables

List of equations

1 Introduction

1.1 Toxicology

Toxicology is an interdisciplinary and data-rich field. It investigates the mechanisms underlying adverse effects of exposures to xenobiotics, particular related to human health [2]. In the pharmaceutical industry the main goal is the definition of a safe starting dose in human clinical trials.

Traditionally, toxicology is defined as "*the science of poison*", derived from the Greek words *toxicon* and *logos* meaning *poison* and *science* [3]. According to the Society of Toxicology, toxicology is defined as "the study of adverse effects of chemicals, physical, or biological agents to people, animal, and the environment" [2]. Paracelsus (1493–1541) was the first who described that the dose makes the poison which today can be defined as the dose-response relationship [4]. In 1862, Gerad Arink described that "*Poisoning results not only from substances taken into the stomach, but also still oftener by deadly influences operating in the lungs, or received into the system by means of the skin*" [5]. Therefore, not only the oral intake plays a role in a xenobiotic's toxicity potential. Whether a xenobiotic that is likely to be harmless remains harmless, depends on the metabolism [2]. Additional, different factors can increase the risk of an adverse effect, such as age, gender, disease state, genetic predisposition and/or interaction with other compounds [6].

Today, there are several specializations in toxicology, due to the broad spectrum of information (e.g., genetics, proteomic, and/or endocrinology), specialist fields (e.g., biology, math, and physics), and risk factors that can drive toxicity. Examples include, clinical, forensic, food, animal, reproduction, environmental, mechanistic, and regulatory toxicology [7]. The task of toxicological research is to determine a dose of a substance which is safe after exposure. For pharmaceuticals, dose finding and pivotal studies, mainly conducted in animal studies, are coupled with complex ethics applications and legislation to finally derive a specific risk assessment. [8]

Animal studies are helpful to understand the pathogenesis and mechanism of the particular toxicity. A retrospective investigation described the ability to predict 71 *percent* (%) of human relevant toxicities using rodents and non-rodents [9]. In *in vivo* studies, the reaction of a whole living organism to a potential drug can be investigated. Furthermore, there is a wide variety of "humanized" rodent models that reliably represent a broad spectrum of critical manifestations of the investigated disease [10][11]. The preferred species for biomedical research are rodents, such as mice and rats, due to their anatomical, physiological and genetical similarities to humans coupled with their small size and lower maintenance costs [11].

However, animals are often not informative enough to predict the response in humans. They differ from humans in several important respects, such as the expression of *drug metabolizing enzymes* (DMEs) and transporters or different anatomical features, like the absence of the gallbladder in rats [12].

On that account, nine out of ten compounds fail in clinical studies because of the lack of predictive pre-clinical models (efficacy, *pharmacokinetic* (PK), and safety) [13]. Many scientists, such as Shanks et al., have described the need for new non-animal testing methods, as animal data is difficult to transfer to the human species [14]. A promising alternative to animal models are advanced cell-based human *three-dimensional* (3D) cell culture models, such as spheroids, organoids, or *organ on a chip* (OOC) systems. The use of 3D cultures in preclinical phases may saves costs, allows a more precise prediction of toxicities and accelerates research projects, such as the development of a new drug [15].

The development and integration of novel animal-free test models is also attributed to William Russel and Rex Burch. In 1959, they published "*The principles of human experimental toxicology*". This book describes the 3R concept which stands for 'Reduction' (avoid animal experiments), 'Refinement' (minimize the number of animals) and 'Replacement' (minimize pain and stress of animals in experiments).[16] Even today, the 3Rs are widely accepted and attempts are made to adhere to the principles. Therefore, new alternative methods are continuously developed and actively supported by, e.g., the European Union. In 2011, the *European Union Reference Laboratory for alternatives to animal testing* (EURL-ECVAM) was established (previously called the *European Centre for the Validation of Alternative Methods* (ECVAM) in 1991) to promote the development and validation of animal-free experiments [17].

1.2 Toxicology in drug discovery and development

Drug discovery and development describes the process by which a new active pharmaceutical ingredient must go through before it can be approved. This process is very expensive and lasts many years. In 2020, Wouters et al. evaluated data of the development of 63 therapeutic agents and analyzed an average duration of around 12 years and a mean estimated cost of $1.3 billion until marketing [18][19]. In this time, the process is divided in the following four steps (Figure 1):

1) Target selection and validation to find first hits
2) Lead identification and optimization
3) Preclinical and clinical development studies
4) Final approval of the new drug [20]

Drug discovery is a multifaceted process. To enter the discovery phase, a broad knowledge about the molecular mechanisms of the disease in needed. This built the basis to identify a

biological target, such as a gene or protein. This target needs to be tested to verify if it is “druggable”. Further, compounds are tested regarding their ability to interact with this target. Therefore, large compound libraries are screened. The list generated from the screening composed > 10,000 compounds and is called ‘Hit discovery’. [21] Subsequently, *in silico*-based techniques help to reduce the hits to the most promising ones. Computer based methodologies play an increasing role in discovery. These methods compare the physicochemical properties by a chemical structure and sort out unfavorable ones. Additional, computational approaches are promising to reduce the use of animal models (Section 1.4.5). [22]

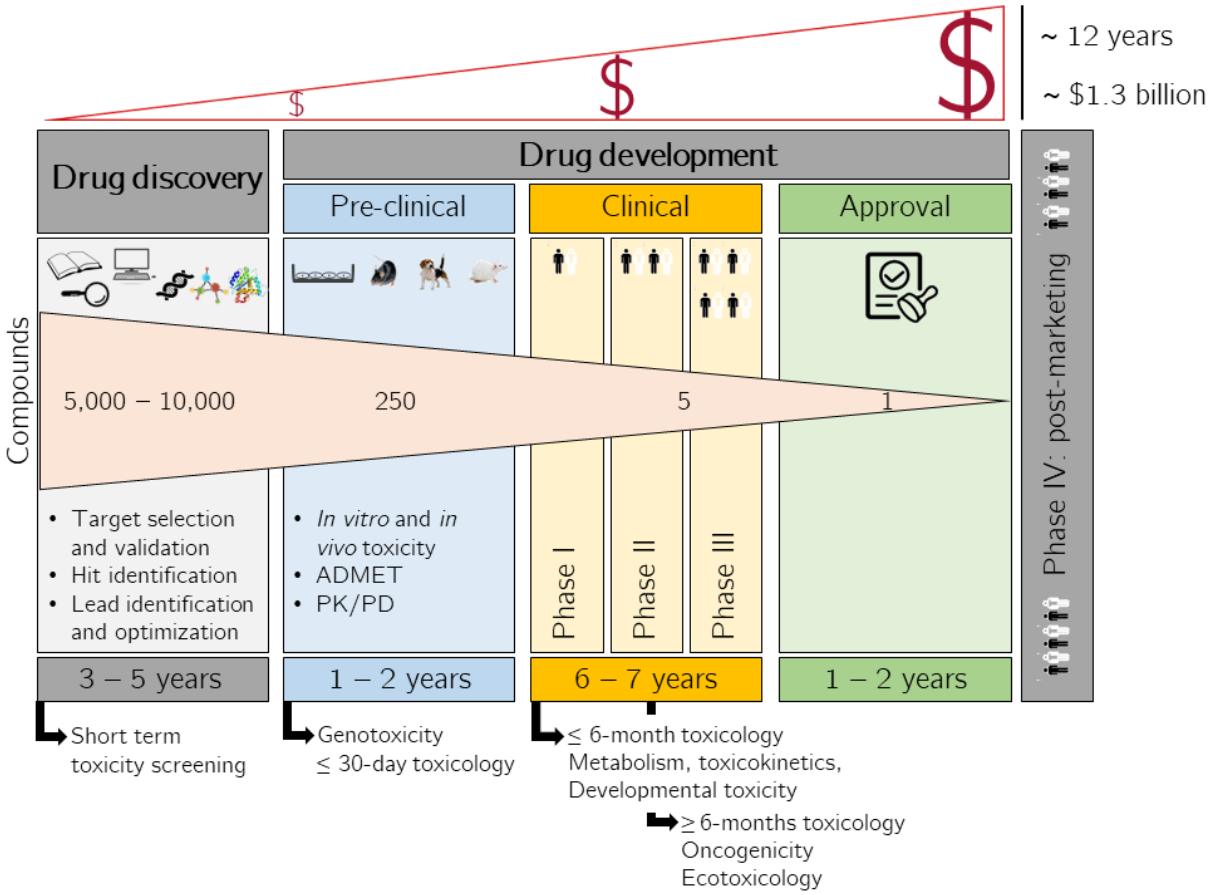

Figure 1: Phases of the drug discovery and development process.
[23]–[27]

Subsequently, compounds are ranked according to their potency to interact with the target at the achievable plasma concentrations. They are active in several assays with acceptable specificity, affinity, and selectivity for the target. These candidates are tested in a set of *in vitro* and *in vivo* experiments to analyze their *absorption, distribution, metabolism, and excretion* (ADME). In this nondefinite lead optimization studies, first short-term toxicology profiles are generated (Figure 1, grey) [23]. The evaluation of the studies leads to a short list of compounds entering the pre-clinical phases (Figure 1). [21] In the pre-clinical phase, compounds are tested for, e.g., efficacy, toxicology/safety pharmacology, metabolism and pharmacokinetics [28]. In phase I, the remaining drug candidate(s) is administrated usually to healthy volunteers (20 –

80) to test safety and exposure. However, agents being developed to prolong life in serious, life-threatening diseases (for example, cancer therapy), are tested in diseased patients. Often expected adverse effects of this class of therapeutics are severe but can be accepted for diseased patients but not for healthy volunteers. The aim of the Phase I trials is to address the tolerability, adverse effects, and pharmacokinetics of the potential new drug. [21]

In phase II, the compound is tested in a small group of patients (100 – 500). The aim is to confirm the therapeutic efficacy of a new drug candidate in proof-of-concept studies. Approximately 33 % of drug candidates fail in this phase. In phase III, the drug is tested in a larger group of patients (300 – 3,000) regarding its safety, dose-response relationship, and risk-benefit profile.

Finally, the successful completion of all phases leads in the best case to the approval of the new drug. It then can enter the market, where it also enters phase IV. Phase IV is called post-marketing or pharmacovigilance phase. In this phase adverse effect of a low incidence or a specific subpopulation are monitored.[21] In the past 50 years, liver toxicity was the leading cause of drug withdrawal during clinical phases and after market approval [29].

1.3 The human liver

The human liver is the most complex organ [30]. It is located in the upper right part of the abdomen and is responsible for several functions related to the maintenance of homeostasis within the body [31]. As an endocrine and exocrine gland, it covers many essential body function, described in Table 1 [32][33]. With these functions, it support almost every other organ in the body [34].

Due to its fundamental role in the body, an imbalance in the livers' function can result in a pathological condition. For example genetic and/or environmental influences can lead to hepatitis, fibrosis, cancer, cirrhosis, autoimmune or metabolic disorders.[31][35][36] However, the liver has an immense capability to resist changes and even recover after damage. A healthy organ has a remarkable reserve capacity, which allows a significant damage to occur without any symptoms [30][37]. Nevertheless, in the last decades, the number of liver diseases and mortality have constantly increased and become one of the leading cause of death and illness worldwide [38][39].

Table 1: Functions of the liver.
[40]

Function	Details
Detoxification	Drugs/alcohol, fatty acids, steroid hormones, ammonia, environmental toxins
Production of cholesterol	Precursor the sex hormones, vitamin D
Storage of micronutrients	Minerals, copper, zinc, magnesium, iron, vitamins (A, D, E, K, B12)
Endogenous metabolism	Conversion of T4 → T3, detoxification of fat
Exogenous metabolism	Secretion of bile acids and cholesterol, endocytosis of HDL
Immune system	Contains viruses and pathogens, maintenance of the hepatic and portal vein immune system
Protein synthesis	Blood clotting (prothrombin), cholesterol transport (lipoproteins), immune function (globulins), colloid osmotic pressure (albumin), copper bioavailability (ceruloplasmin)
Production of bile	Digestion, gastrointestinal antimicrobial
Blood sugar balance	Storage of glycogen

1.3.1 Structure and cellular components

In 1957, Claude Couinaud described the concept of functional anatomy of the liver based on the segmental anatomy and location of the hepatic veins [30][32]. The so called Couinaud classification divides the organ into eight segments with individual inflow, outflow and biliary drainage [41]. This classification is guided by the location of the blood vessels (Figure 2). As a central metabolic coordinator, the liver is supplied with oxygenated blood though the hepatic artery (25 %) and nutrient-rich blood from the small intestine through the hepatic portal vein (75 %) [30][42]. The hepatic veins divide the right and left lobes into anterior and posterior segments, whereas the portal vein divides into upper and lower segments [41].

The lobes are made up of thousands of hexagonally shaped lobules forming the smallest functional unit of the liver (Figure 3). Oxygen- and nutrient-rich blood from both vessels flows through its capillaries, the sinusoids, eventually entering the central vein. [42][43][34]. The sinusoidal lumen contains *Kupffer cells* (KCs), the major phagocytic immune cells of the liver. As shown in Figure 3, the macrophage-like cells are in tight contact with *liver sinusoidal endothelial cells* (LSECs) and face the bloodstream [31].

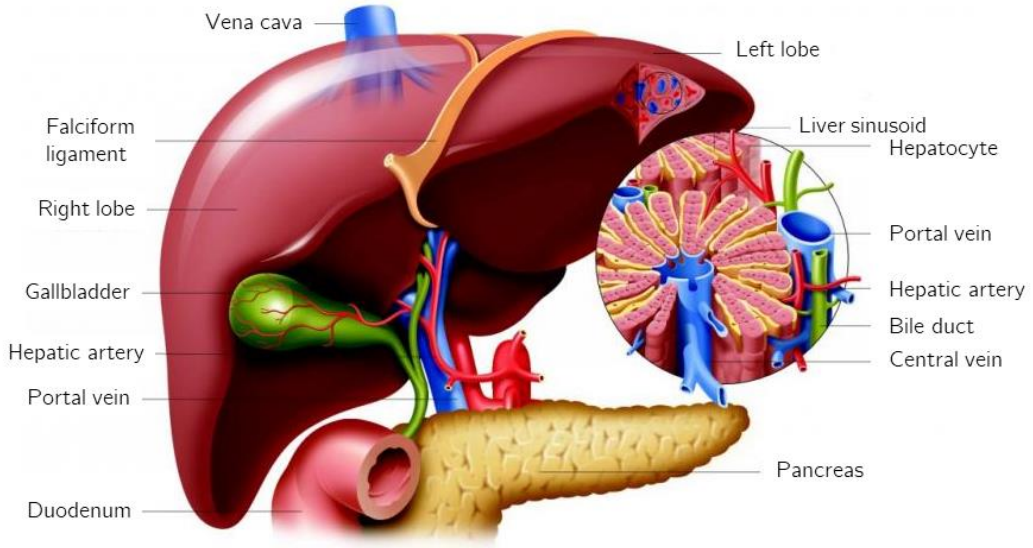

Figure 2: Anatomy of the liver.
[44]

The sinusoids consist of a single-layer epithelium of LSECs that lack a basal lamina. The area between the LSECs and the hepatocytes is called Space of Dissé (Figure 3 B). The Space of Dissé is the home of hepatic *stellate cells* (SCs), storing fat and 80 % of vitamin A in the whole body) [45]. Blood plasma, proteins or macromolecules up to 250 kDa, can pass directly through the Space of Dissé and come into direct contact with the basal side of the hepatocytes. [42]

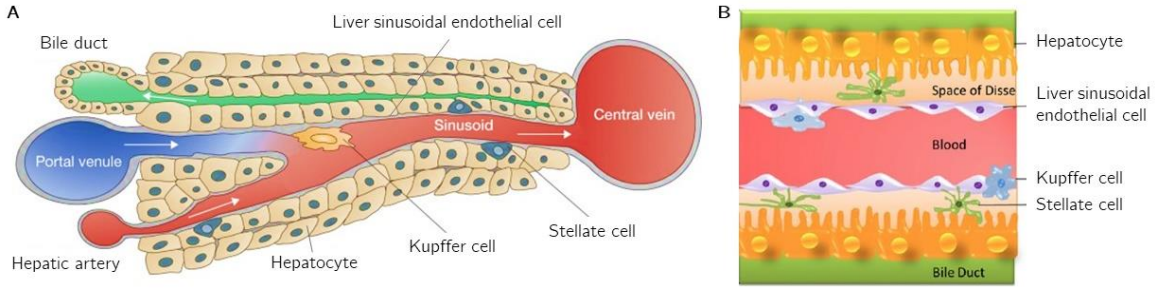

Figure 3: Cellular architecture of the hepatic sinusoid.
(A) Location of the liver cells within the hepatic sinusoid. **(B)** Enlarged structure of the sinusoid functional unit. LSECs surround the sinusoidal lumen. The Space of Dissé separates hepatocytes and LSECs and contains the SCs. KCs are in tight contact with LSECs and face the bloodstream. Cholangiocytes line the inner space of the bile duct tree. [31][46]

Table 2: Liver cells and their specific functions.
Cell specific functions of hepatocytes, LSECs, KCs, SCs, and cholangiocytes within the liver.

Liver cell	Function
Hepatocytes	Detoxification, synthesis of fatty acids, bile acids and proteins [47]
LSECs	Lining of the liver capillaries, formation of vessel walls, endocytic and scavenging function [48]
KCs	Resident macrophage, first line defense, phagocytic activity, release of various products, e.g. cytokines [49][31]
SCs	Fat and vitamin A storage, liver regeneration, expression of proinflammatory and profibrotic genes [45]
Cholangiocytes	Lining of the intra- and extrahepatic ducts of the biliary tree, modification of secreted hepatic bile, transport of bile along the bile tree [50]

Figure 3 A shows, that hepatocytes are arranged in cords which have the thickness of one cell. The basal sides of hepatocytes form the bile canaliculi, where bile is secreted in. The bile flow is arranged in parallel to the sinusoids flow, but in the opposite direction that the blood flows. It ends in the bile duct which is formed by cholangiocytes. [51] Cholangiocytes modify the hepatic bile by addition of, for example water and ions [50]. Together with LSECs, KCs and SCs, they are also called *non-parenchymal cells* (NPCs). The sinusoids consist of a single-layer epithelium of LSECs that lack a basal lamina. The area between the LSECs and the hepatocytes is called Space of Dissé (Figure 3 B). The Space of Dissé is the home of hepatic *stellate cells* (SCs), storing fat and 80 % of vitamin A in the whole body [45]. Blood plasma, proteins or macromolecules up to 250 kDa, can pass directly through the Space of Dissé and come into direct contact with the basal side of the hepatocytes. [42] Table 2 captures the major cell types of the liver and their specific functions within the hepatic sinusoid.

1.3.2 Hepatic drug metabolism

The human liver is essential for survival by managing the metabolism in the body, including glucose homeostasis, xenobiotic metabolism, and detoxification. However, its location, blood flow and functional role in the metabolism of xenobiotics make this organ particularly vulnerable to chemical injury. [52] Therefore, the liver is fully equipped with a broad range of DMEs. These DMEs can transform endogenous and exogenous substances, allowing the elimination of potentially toxic waste products. The excretion of hydrophilic derivatives occurs by two main routes of elimination - bile and urine. In contrast, the excretion of lipophilic products is difficult. To avoid the accumulation of these compounds, they must be transformed into a more hydrophilic product so that they can be removed via the normal excretory pathways (Figure 4). In order to minimize the potential injury caused by xenobiotics, the liver contains several drug metabolizing phase I and phase II enzymes and phase III uptake and efflux transporters, listed in Table 3 [53].

Table 3: Overview of the main phase I and II DMEs, and phase III transporters.
[54]–[58]

Phase I	Phase II	Phase III	
• Cytochrome P450 enzyme (CYP450) • Flavin-dependent monooxygenase (FMO) • Monoaminooxygenase (MAO) • Cyclooxygenase (COX) • Alcohol dehydrogenase (ADH) • Aldehyde dehydrogenase (ALDH) • Reductase • Esterase • Epoxydehydrolase (EH)	• Glutathione-S-transferase (GST) • Acyl-CoA aminoacid-N-acyltransferase (ACNAT) • Sulfotransferase (SULT) • Acetyltransferase (AT) • UDP-Glucuronosyl-transferase (UDP-GT) • Methyltransferase (MT)	ABC	• Multidrug resistance protein (MDR) • Multidrug resistance-associated protein (MRP) • Bile salt export pump (BSEP) • Breast cancer resistance protein (BCRP)
		SLC	• Na^+-taurocholate co-transporting polypeptides (NTCP) • Organic cation transporter (OCT) • Organic anion transporter (OATP) • Equilibrative nucleoside transporters (ENT) • Organic solute and steroid transporter (OST) • Multidrug and toxin extrusion protein 1 (MATE1)

The transformation of a xenobiotic starts with phase I. Phase I is also known as the functionalization phase. As shown in Figure 4, lipophilic compounds are chemically modified by oxidases, reductases and hydrolases which introduce functional groups into the compound [54]. Depending on the functional group, a nucleophilic or electrophilic metabolite is generated. The most common phase I enzymes belong to the *cytochrome P450-dependent monooxygenase* (CYP450) family, residing in the membrane of the endoplasmic reticulum (Figure 5). The human CYP450 catalyzes the oxidative biotransformation of most drugs and xenobiotics [59][60]. The nomenclature system is based on their amino acid sequence. If enzymes sharing <40 % of homology they belong to a family labeled by the first number (e.g., CYP1). However, enzymes sharing >55 % homology are denoted by the same letter (e.g., CYP1A). In the case of a lower consistency, a subfamily must be determined [61]. Finally, the isoform corresponds to the single gene of the subfamily and is labeled as a number (e.g., CYP1A1). [62] The isoforms, mainly responsible for drug metabolism are 1A2, 2C9, 2C19, 2D6 and 3A4 (circa 95 %) [63].

In phase II the active compound can be conjugated enzymatically or not enzymatically to polar endogenous ligands such as *glutathione* (GSH) or glucuronic acid (Figure 4). The major DMEs in this phase are *UDP-glucuronosyltransferases* (UGTs), *sulfotransferases* (SULTs), *N-acetyltransferases* (NATs), *glutathione S-transferases* (GSTs), thiopurine S-methyltransferases and catechol O-methyltransferases (Table 3). UGTs metabolize a broad spectrum of compounds, e.g., UGT1A6 is highly expressed and metabolizes bilirubin, certain phenols and estradiols or UGT2B7 which metabolizes opiates. [54]

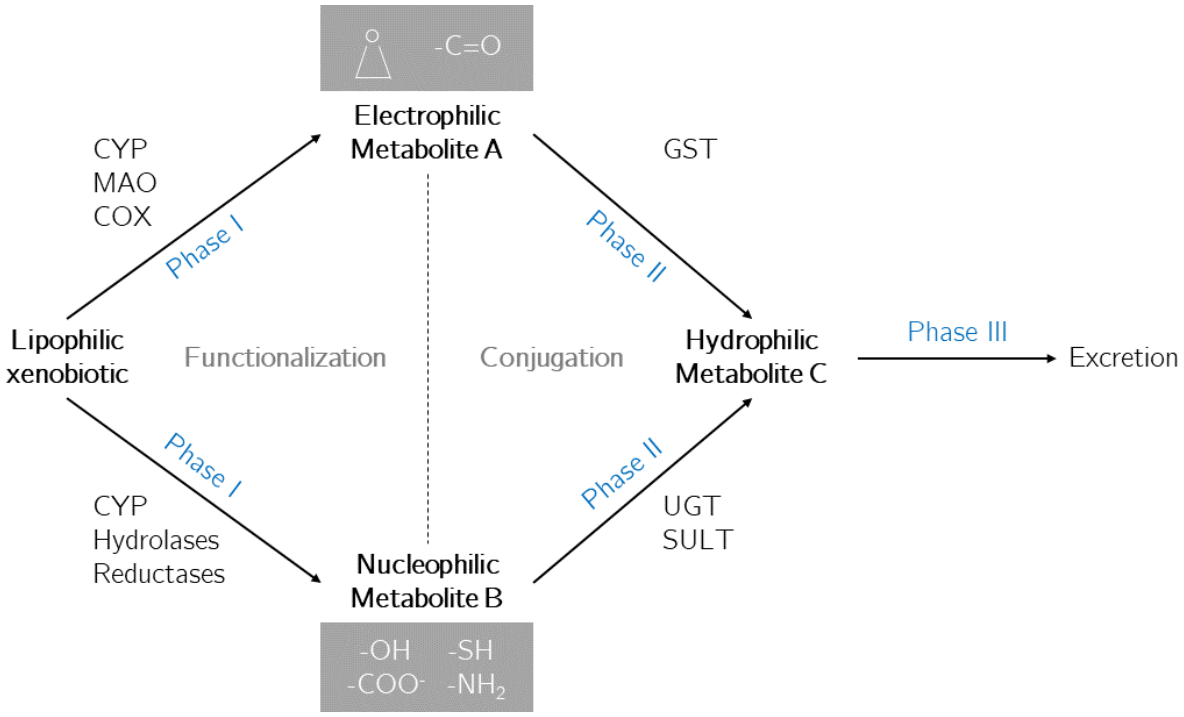

Figure 4: Phase model of xenobiotic metabolism.
A lipophilic compound is metabolized by phase I enzymes to a nucleophilic (e.g., hydroxyl-, sulfhydryl-, carboxyl-, acid-, amino groups) or electrophilic (e.g., epoxide function, carboxyl groups) metabolite. The functionalized metabolites are conjugated via phase II enzymes to polar molecules. In phase III the hydrophilic metabolite C can be eliminate biliary or urinary. [64][57]

After conjugation of the metabolite and thus generation of a hydrophilic product, the compound can be eliminated by phase III transporters from the hepatocytes. The transporters are classified by 2 main families: *Adenosine triphosphate* (ATP*)-binding cassette* (ABC) and *solute carrier* (SLC) transporters. As the name suggest, ATP transporters are dependent on energy consumption. Whereas SLC transporters are working against the electrochemical gradient. The main uptake transporter in the liver are *Na^+-taurocholate co-transporting polypeptides* (NTCP), *organic cation transporter* (OCT), and *organic anion transporter* (OATP). The main efflux transporters are ABCB1 (*multidrug resistance protein 1* (MDR1/P-gp)), ABCB11 (*bile salt export pump* (BSEP)) and ABCC2 (*multidrug resistance-associated protein 2* (MRP2)) (Figure 5). [54]

In pharmaceutical research, the drug metabolizing process is an essential aspect. Depending on the mechanism of metabolism, it can lead to an increased or decreased (adverse and/or efficacious) effect of the drug. In the following, two of these processes are described: Enterohepatic recirculation and first pass effect.

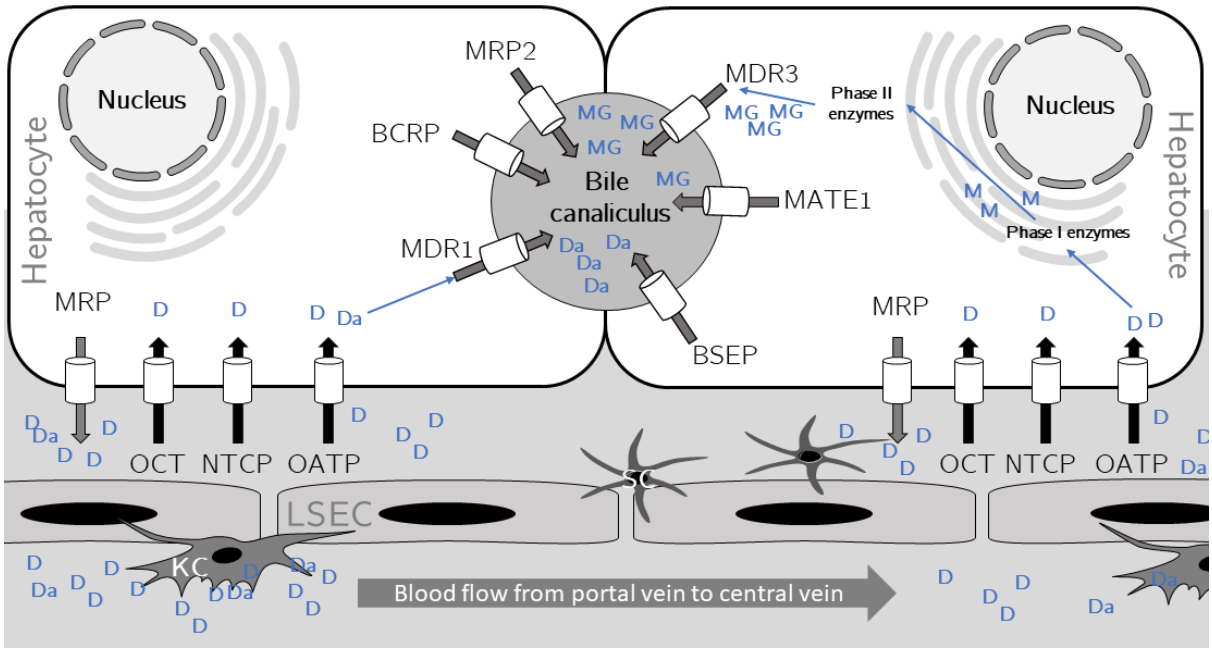

Figure 5: Hepatic uptake and efflux transporters in drug metabolism.
The drug D and Da are have different clearance pathways. Drug D is taken up by transporters then metabolized by phase I enzymes to a metabolite M. After, M is conjugated by phase II enzymes to glucuronide metabolite MG, which is finally discharged by phase III transporters into the biliary system. Drug Da is taken up by OATP directly and discharged by MDR1 without any chemical modification.

The transformation of enterally absorbed compounds into an active or inactive product is called first pass effect. The first pass effect can often become a major problem in pharmaceutical research, as it sometimes dramatically reduces the bioavailability of a compound upon reaching its site of action or the systemic circulation [65]. In contrast, in some cases phase I enzymes can produce a highly reactive metabolite. This metabolite can bind to intracellular structures such as proteins, nucleic acids, or lipids before conjugation by phase II enzymes. If the cellular concentration of such reactive metabolites exceeds the threshold of inherent repair mechanism, a drug-induced adverse effect may occur. Phase II reaction generally serve as detoxification step. However, they can also generate toxic metabolites such as unstable reactive electrophiles after acetylation [66].

Drugs can be secreted as active or inactive metabolites via bile and urine. In some cases, biliary secreted drugs can be reabsorbed from the intestinal lumen into the systemic circulation instead of being removed from the body. The process is called enterohepatic recirculation and results in a secondary adsorption process and potential increase in drug exposure. [67] In most cases enterohepatic recirculation is unwanted, as it increases the risk of adverse drug reactions due to decreased controllability of the concentration in the systemic circulation. In some cases, biliary eliminated phase II products are deconjugated by bacteria in the intestinal lumen to lipophilic phase I metabolites. These metabolites are reabsorbed again and become pharmacological active. [68]

Table 4: Transcription factors for DMEs and corresponding inducers
[56][69]

Transcription factor	Typical inducers	Target genes
Constitutive androstane receptor (CAR)	*Phenobarbital* (PB), *Rifampicin* (RIF), Carbamazepine, Efavirenz, Nevirapine	CYP1A1 and CYP1A2 [70]
		CYP3A4 [71]
		CYP2C9 and CYP2C19 [72]
		UGT1A1 and UGT1A6 [73]
		MDR1 [74]
		MRP2 [75]
		MRP4 [76]
Pregnane-X-receptor (PXR)	RIF (humans), Pregnenolone-16α-carbonitrile (PCN) (rodent)	CYP2B6 and CYP3A4 [77]
		UGT1A1 and UGT1A6 [73]
		MRP2 [75]
Peroxisome proliferator-activated receptor (PPAR)	Palmitic acid, Oleic acid, Linoleic acid, Arachidonic acid	CYP4A11 [78]
		SULT2A [79]
		UGT2B [80]
		MDR2 [81]
Aryl-hydrocarbon receptor (AHR)	TCDD, benzo[a]pyrene, Heterocyclic amines	CYP1A1/2 [78]

Commonly, DMEs are protecting the liver from toxic, foreign compounds which can lead to hepatic damage. The ability of xenobiotic metabolism is not constant and can be influenced by many internal and external factors. These factors include age, food, gender, pregnancy, disease state, organ transplantation, medication, or genetic polymorphism [54]. For example, adverse effects are 1.5 to 2 times more common in women which can be ascribe to, e.g., the impact of sex hormone, the body weight, fat amount, and limited volume of distribution of hydrophilic drugs due to the smaller size [82][83]. Children have a lower expression of DMEs and thus a decreased drug metabolism capacity [54]. The expression of DMEs is regulated mainly by the four transcription factors CAR, PXR, PPAR and AHR [84]. Table 4 gives an overview of transcription factors that influence the transcription of Phase I-III enzymes and transporters.

1.4 Drug-induced liver injury

The human liver is the first organ (after the gastrointestinal system) confronted with enterally applied xenobiotics. Hence, it is one of the initial target for medication-induced damage [85]. Still, new drug candidates fail due to unacceptable hepatotoxicity in pre-clinical or clinical phases. *Drug-induced liver injury* (DILI) is the most frequent cause for acute liver failure in the United States and Europe [86]–[89].

In Europe, liver damage is mostly caused by antibiotics [90]. In addition, a study of the Drug-Induced Liver Injury Network analyzed data of severe liver injury and identified antibiotics and antiepileptics as the main classes causing DILI [91]. In general, most of the medications causing DILI are older compounds that have been on the market for a long time. [90] Over all, as *Acetaminophen* (APAP) is the most commonly used drug for treatment of pain and fever, its overdose takes the largest rate for acute liver failures worldwide [92].

Today, over 1,000 compounds in nearly all medication classes have been categorized by the united States *Food and Drug Administration* (FDA) as causing DILI, e.g., anesthetics, anticancer drugs, antibiotics, antituberculosis agents, antiretrovirals, and cardiac compounds [93][94][85]. However, also phytotherapeutics, herb and dietary supplements can induce DILI [95]. Between 1953 and 2013, 81 drugs were withdrawn worldwide due to unexpected hepatotoxicity. This accounts for 18 % of total retractions, following by immune-related reactions (17 %) and cardiotoxicity (14 %). [96] Today, it is very difficult to predict DILI in pre-clinical phases. The occurrence of acute liver failure in clinical phases or post-marketing is a major economical and ethnical problem.

On the economical side, the development of a new drug is very costly [97]. Hence, a drug withdrawal in late phases or post-marketing, is extremely expensive for the pharmaceutical industry. If toxicity could be detected sooner, the saved money could be invested more effectively in other developing projects.

Most importantly, on the ethical side, patients affected mostly may be dependent on a liver transplantation to survive. Moreover, Hayashi et al. described that DILI leads directly or indirectly to mortality in 7.6 % of all cases [98]. After considering the serious ethical and costly economic reasons, it becomes clear, that it is essential to develop reliable, innovative techniques to predict hepatotoxicity during the early stages of drug development. Novel methods for the early assessment of DILI could save money, resources, working time, reduce the number of the animal experiments within the framework of the 3R animal welfare principles and, above all, save human lives.

1.4.1 Classification of DILI

The clinical presentation of DILI is very diverse. In most cases, toxic liver damage remains undetected for a long time. The diagnosis of DILI is based on an extensive clinical investigation, including a broad anamneses, detailed drug exposure inquiry and the exclusion of other hepatic injuries. [99]

Hyman Zimmermann developed the Hy's law to help the detection of severe DILI in patients. After exclusion of other liver diseases, it defines DILI as the combination of jaundice with hepatocellular damage evidenced by elevated serum levels of liver enzymes, but without existing cholestasis [100]. According, a three-fold evaluation of the serum *alanine aminotransferase* (ALT) level and a two-fold increase in *total bilirubin* (TBL) level remains the gold standard for DILI detection [101].

Today, DILI can be classified in three categories described in Table 5. First, the mechanism of hepatotoxicity, second, the clinical laboratory and third, the histologic findings.

Table 5: Classification of DILI.
[102]

Type of classification	Example
Mechanism of hepatotoxicity	Intrinsic
	Idiosyncratic Immune-mediated Metabolic
Clinical laboratory	Hepatocellular
	Cholestatic
	Mixed hepatocellular/cholestatic
Histological findings	Cellular necrosis or apoptosis
	Steatosis
	Fibrosis
	Phospholipidosis
	Granulomatous
	Sinusoidal obstruction syndrome

The classification based on the mechanism of hepatotoxicity, categorizes DILI into intrinsic and idiosyncratic (Table 5). The intrinsic DILI is dose-dependent and appears early after exposure (within days). It is commonly predictable at doses that exceed the therapeutic threshold levels and reproducible in animal models [103]. The best-known drug causing approximately 50 % of all intrinsic DILI is overdose with APAP, also known as Paracetamol [104][95]. Hence, APAP

is one of the best studied compounds. Plasma concentrations over 100 µg/L lead to acute liver injury in all individuals as the detoxification mechanisms are overburdened (Section 1.6) [105]. However, after withdrawal patients recovering from acute APAP toxicity mostly have no long-term consequential damages [85]. *Idiosyncratic DILI* (iDILI) is poorly understood and rare, but responsible for approximately 10-15 % of acute liver failures in the USA [87]. In contrast to intrinsic DILI, iDILI is dose-independent, occurs after a long latency period (from 5 days up to 12 months [106]) and is challenging to predict. Additionally, it does not arise in all individuals. It is reported, that iDILI is responsible for 13 % of all cases of acute liver failure of which more than 75 % result in liver transplantation or death [86].

The second classification type is defined according to the clinical presentation. DILI can be further classified into hepatocellular, cholestatic or mixed injury with an acute or chronic progress, based on the duration, the location of injury, and the affected target cells. [85] The classification was established using the ratio R [107][108][120][121][111]:

- $R \geq 5$ Hepatocellular pattern (Prevalence range: 52 – 59 %)
- $R > 2$ and < 5 Mixed pattern (Prevalence range: 6 – 23 %)
- $R \leq 2$ Cholestatic pattern (Prevalence range: 18 – 29 %)

R can be calculated by dividing the *upper limit of normal* (ULN) of serum ALT by the ULN of serum *alkaline phosphatase* (ALP) at the start of liver injury (Equation 1) [112]. Usually, the hepatocellular and the cholestatic pattern are related to a poor prognosis and an increased liver-related mortality. In contrast, the mixed pattern appears to have a lower mortality rate. [99][113][114]

Equation 1: Calculation of liver injury patterns.
Equation for calculating (A) the ALT activity, (B) the *alkaline phosphatase* (ALP) activity, and (C) the ratio R. [107]

$$(\mathrm{A})\ \mathrm{ALT\ acitivty} = \frac{\mathrm{patient's\ ALT}}{\mathrm{ULN}}$$

$$(\mathrm{B})\ \mathrm{ALP\ activity} = \frac{\mathrm{patient's\ ALP}}{\mathrm{ULN}}$$

$$(\mathrm{C})\ \mathrm{R} = \frac{\frac{\mathrm{ALT}}{\mathrm{ULN}}}{\frac{\mathrm{ALP}}{\mathrm{ULN}}} \text{ or } \mathrm{R} = \frac{\mathrm{ALT\ activity}}{\mathrm{ALP\ activity}}$$

In 1957, Fernando De Ritis described the de ritis ratio to characterize viral hepatitis [115]. It is calculated by dividing *aspartate aminotransferase* (AST) with ALT. Several studies described, that the ratio can also be used to classify DILI and distinguish from other liver injuries (>1.5 = worse prognosis) [106][117]–[119].

DILI can be further classified using a histological examination of a liver biopsy. Besides the well-defined patterns, such as chronic hepatitis or steatosis, a biopsy can depict multiple findings, such as inflammation, cholestasis, fibrosis, or necrosis. Nevertheless, the complexity of the pathology and the liver itself is often difficult to interpret. Each biopsy needs to be investigated systematically including the clear distinction between potential DILI and non-DILI liver diseases. Additionally, the classification of DILI in the known patterns can also be challenging. [119]

1.4.2 Epidemiology

In most countries, DILI is the most common cause of acute liver failure, black box warnings, and still the major concern for pharmaceutical and healthcare industries [90]. In the United States it is responsible for 15 % of all performed liver transplants [120]. Therefore, the FDA has recommended that industry should identify a drug's potential to cause DILI as early as possible [121][100]. Globally, DILI has a low clinical incidence and the major causative compounds can vary interregional [117][122]. The reason is, that some drugs are more frequently used in one country than in another. For example, in Europe DILI is mostly caused by antibiotics and disulfiram [90].

Table 6: Epidemiological studies.
Incidences and major causative compounds in different countries for DILI. Retrospective study (*), population-based study (**). [90][123]

Publication	Country	Incidence	Major causative compounds
**Björnsson et al. (2013) [124]	Iceland	19.1 per 100.000	Amoxicillin-clavulanate
**Vega et al. (2017) [125]	Delaware (USA)	2.7 per 100,000	Antibiotics
**Sgro et al. (2002) [126]	France	13.9 per 100,000	Non-steroidal anti-inflammatory drugs
*Abajo et al. (2004) [127]	United Kingdome	2.4 per 100,000	Chlorpromazine, Amoxicillin-clavulanate
*De Valle et al. (2006) [128]	Sweden	2.3 per 100,000	Antibiotics, Non-steroidal anti-inflammatory drugs

Since the early 1990s, DILI is epidemiological investigated [90]. Thenceforth, some studies have been conducted to determine the epidemiology and the major causative compounds across several countries (Table 6). These published studies show differences in the incidence rates because of the variety of the study methodology (e.g., usage of primary databases, the participation of specialists or the kind of patient recruitment (in- or out-patients)). Generally, retrospective studies show a low sensitivity and specificity, because of the usage of databases

and searching for codes of the International Classification of Diseases. Hence, population based studies show a higher incidence rate than retrospective studies [111][129].

1.4.3 Mechanism and pathogenesis

The mechanism of DILI is still poorly understood as it appears in different factettes in man. In the following, the five main hypotheses are described according to the numbering in Figure 6. As depicted, the starting point is the substance itself or its reactive metabolite, which causes a reaction in the cells.

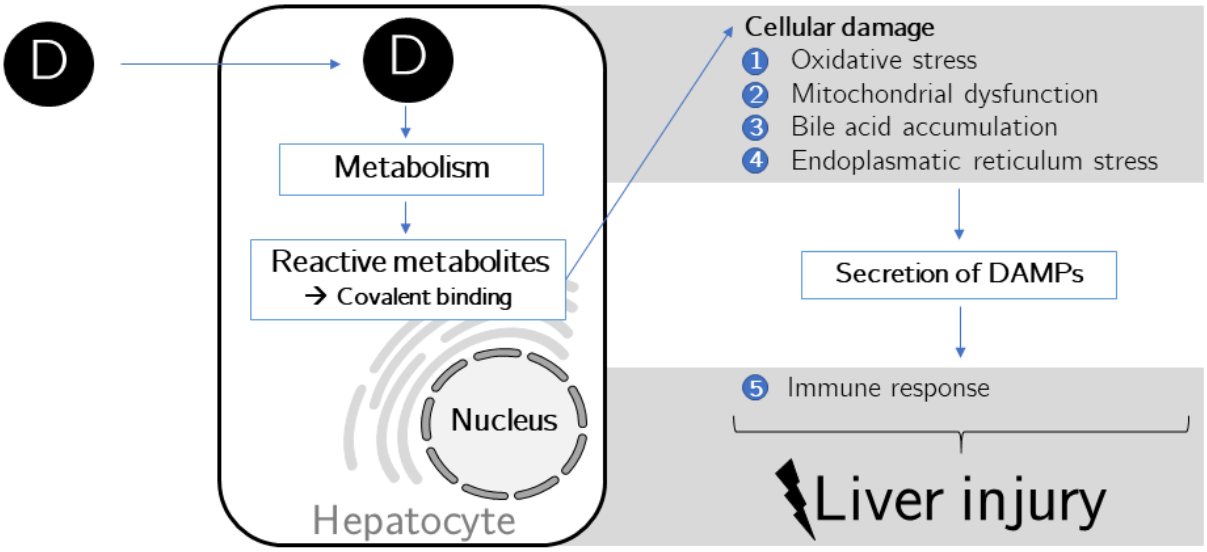

Figure 6: Mechanism of DILI.
[130]

Reactive metabolites (mechanism 1): Many drugs are lipophilic substances which are transformed via phase I enzymes and phase II enzymes into hydrophilic metabolites (Section 1.3.2). Mostly these metabolites are quickly excreted. However, DMEs can metabolize drugs into more active, electrophilic, *chemically reactive metabolites* (CRMs) or unstable reactive conjugates which bind to intracellular structures (Figure 6). Their electrophilic character promotes binding to electron-rich structures such as nucleic acids, lipids, or proteins. Consequently, the bound structures are inactivated or destroyed. Binding to hepatoprotective molecules, such as GSH, further enhances the hepatotoxic effect as another detoxification mechanism is inhibited. [131] The most familiar compound causing hepatotoxicity due to formation of CRMs is APAP. In overdose, APAP leads to acute liver injury due to metabolism to *N-Acetyl-p-benzochinonimin* (NAPQI) by CYP2E1, 1A2, 2D6 and 3A4. NAPQI is strongly electrophilic and is metabolized further by, e.g., GSH conjugation. In the case of overdose, the GSH depletes, and NAPQI increasingly reacts with macromolecules, leading to hepatic necrosis via, e.g., oxidative stress or mitochondrial dysfunction. [131]–[133]

Mitochondrial dysfunction (mechanism 2): The liver is densely packed with mitochondria for energy generation. The powerhouses also play a crucial role in cellular homeostasis including fatty acid oxidation or intracellular signaling. [134] Because of its variety of function, drugs can have different impacts on the mitochondria, such as oxidative stress, energy depletion, accumulation of triglycerides, and apoptosis [135]. For example, the release of pro-apoptotic factors into the cytosol can trigger necrosis or apoptosis of the cell. Likewise, the disruption of the mitochondrial permeability causes mitochondrial depolarization and lead to necrosis or apoptosis. The double-membrane-bound organelle contains specific genes, called *mitochondrial DNA* (mtDNA) which also can be depleted by drugs and their reactive metabolites, as described in mechanism 1. In summary, drugs can induce hepatotoxicity through mitochondrial dysfunction caused by membrane permeability, inhibition of fatty acid oxidation, impairment of oxidative phosphorylation, or mtDNA depletion. [131][135]–[137]

Inhibition of biliary efflux (mechanism 3): As described in Section 1.4.1, cholestatic and mixed DILI are two hepatotoxicity types which can occur in man. The biliary flow is highly regulated by transporters, such as NTCP, BSEP or MDRs (Section 1.3 and Figure 5). [135] Several drugs and/or metabolites can inhibit efflux transporters by covalent binding causing an increased intracellular concentration of bile acids. The accumulation within the hepatocytes lead to an impaired gastrointestinal performance as well as hepatocyte apoptosis and/or necrosis due to bile salt intoxication. [137] The release of hydrophobic, cytotoxic bile acids can lead to liver injury, cirrhosis and death due liver failure [138].

Endoplasmic Reticulum (ER) Stress and lysosomal dysfunction (mechanism 4): ER stress often is associated with liver diseases such as hepatitis, alcohol liver disease or DILI. The ER plays a significant role in many cellular processes, like protein synthesis, folding, trafficking, or intracellular calcium homeostasis. If its physiological function is disturbed, unfolded proteins accumulate. Consequently, a signaling cascade called unfolded protein response, is activated which upregulates the expression of genes involved in the folding process and quality control. [139][140][141] For example, APAP-induced liver injury causes an increased accumulation of reactive oxygen species leading to an calcium-imbalance and thus an activation of the unfolded protein response [142]. ER stress is an early event of the apoptotic cell death [143].

As recently described, some ER synthesized proteins are further modified in the Golgi. These proteins include nearly 60 different hydrolytic enzymes which are packed in transport vesicles [144]. The fusion of the vesicles with an endosome, containing foreign material, create a lysosome [145]. The hydrolytic enzymes degrade the foreign macromolecules taken up by endocytosis. For the optimal digestion conditions, an acidic milieu exists within the lysosomes, preventing an uncontrolled cytosolic digestion. The disruption of lysosomes by drugs or their CRMs lead to the formation of laminar bodies which result in, e.g., phospholipidosis. [146] Especially cationic amphiphilic drugs, such as *Amiodarone* (AMIO) are associated with the

intracellular accumulation of phospholipids as they become positively charged in the acidic milieu [147]. The phagocytosis of accumulated phospholipids by macrophages can induce an immune reaction [148].

Immune-mediated liver injury (mechanism 5): Drug-induced immune reactions have a prolonged latency, are diverse in all individuals and thus very challenging to detect until marketing of a new drug [149]. It is known that the involvement of the immune system may play a role in the development of DILI. The mechanisms behind are still unclear but there are different hypotheses that describe the drug-induced activation of the immune system. [142]

Many immune cells reside in the liver including KCs, dendritic cells, natural killer cells (innate immune cells) and natural killer T/B-cells (adaptive immune cells). In a healthy liver, these cells maintain a homeostasis between regeneration and immunity. [150] Cellular stress or injury (e.g., due to ER stress or BSEP inhibition) can lead to the release of extra- or intracellular danger molecules, named d*amage-associated molecular patterns* (DAMPs), by apoptotic and necrotic hepatocytes (“Danger Hypothesis”). DAMPs can activate innate immune cells and disturb the homeostasis. Consequently, proinflammatory cytokines and cytotoxic mediators, such as *interleukin* (IL)-10, IL-ß, and *tumor necrosis factor-alpha* (TNFα) can be produced and secreted by activated immune cells and influence hepatic mechanisms including transporter inhibition or oxidative stress [150][151]. In addition, small molecules, such as drugs and metabolites, can bind covalently to hepatocellular structures and form neoantigens which can be recognized by B-cells as foreign (“Hapten hypothesis”) [152]. Activated B-cells can produce and secrete antibodies against the neoantigens. This reaction may further enhance B-cell activation and antibody production [151]. The presence of antibodies directed against native or drug-modified hepatic proteins (neoantigens) in DILI patients, provides convincing evidence of the involvement of the adaptive immune system [142]. Chemical molecules can activate T cells directly though interaction with the T cell receptor (“Pharmacological interaction (p-i) Hypothesis”) [153]. This hypothesis is based on the observation, that some T cells rather recognize sulfamethoxazole itself instead of the reactive metabolite-protein adduct [154].

1.4.4 Risk factors

A variety of risk factors can increase the probability for DILI, such as a pre-existing disease, the chemical properties of a drug, environmental factors, or genetic predisposition.

Regarding pre-existing diseases, the human liver can suffer from hepatitis (liver inflammation), cholestasis (impairment of bile secretion), steatosis (fatty liver), liver fibrosis and cirrhosis (liver scarring) and/or a liver tumor (hepatocellular carcinoma) [85]. The pathologies can be triggered by infections (hepatitis), hypertriglyceridemia or alcohol consumption. People having a damaged or diseased liver also have an increased susceptibility for DILI. [155]

The physicochemical properties of a drug affect the cellular uptake and metabolism. The combination of a high daily dose and the lipophilicity of a compound can enhance the DILI risk [156].

Moreover, gender, age, pubertal development, sex hormones, pregnancy and growth hormone levels influence DMEs and the DILI risk [157]. For example, due to higher glucuronidation rates, men have a higher clearance rate of APAP than women [158]. Overall, women seem more vulnerable to toxin-mediated liver diseases and have a more rapid progression to fibrosis [86]. This can be attributed to the sex differences in drug bioavailability, metabolism, and excretion [157].

Several genes that control the metabolism of a drug can be altered by mutations and increase the DILI risk. GST protects the hepatocytes from oxidative stress [159]. Mutations in the GSTM1 and GSTT1 loci impacts the activity of the enzyme and thus the susceptibility to xenobiotic-induced toxicity [160]. ABC transporters are essential for the transport of bile acids and drugs (Section 1.3). Variations in these genes have been associated with cholestatic DILI due to intracellular accumulation of bile and compounds [161].

1.4.5 Prediction and new biomarkers

DILI is a common cause for the termination of multiple drug development programs in the last decades [155][162]. Especially the idiosyncratic nature of DILI is challenging to predict because it is host-dependent, dose-independent, and appears after a latency period. Furthermore, it occurs in a small number of patients at doses that are usually well tolerated [100]. In addition, it is diverse in clinical symptoms and individual regarding the patients' predispositions. These factors, describing the complexity of DILI compared with its unknown pathomechanism and the lack of human data, may explain the difficulty of prediction.

Today, DILI is diagnosed in patients with the help of a detailed anamnesis and the measurement of the traditional biomarkers ALT, AST, ALP, *glutamyl transpeptidase* (GGT), and TBL (Section 1.4.1) [122]. However, ALT, AST, ALP, and GGT are also present in other tissues, such as heart, skeletal muscle, brain, or kidney [163]. Thus, also other diseases are associated with elevated serum levels (for example, myocardial damage, skeletal muscle diseases). Nevertheless, the biochemistry marker ALT mainly is present in the liver and thus more liver-specific than AST [164]. The increased AST/ALT concentration is associated with hepatocyte necrosis and increased ALP levels with damaged biliary cells [122][165]. In addition, TBL is liver-specific but only appears after a latency period. [166][167][105] However, if an increase in liver enzymes can be measured in the serum, the patient is already suffering from liver damage. For the pharmaceutical industry as well as the patients' health it is crucial to identify hepatotoxicity in preclinical studies. However, current preclinical studies including 2D *in vitro* tests

and regulatory-based toxicity studies in animals, are insufficient to reliably predict DILI in patients [162]. Therefore, advanced computational capabilities, *in vitro* human test models, and novel specific and sensitive biomarkers are needed [166].

Computer-based methods ("*in silico*" methods) enable rapid and cost-effective screening of numerous chemicals. A machine learning software can calculate the potential hepatotoxicity risk based on the chemical structure and other known parameters from recent studies, such as pre-existing diseases, biochemistry, and environmental/genetic predispositions of DILI-patients [168][169]. *Quantitative structure–activity relationship* (QSAR) methods already are integrated in toxicology to measure and predict toxicity based on the chemical structure of a compound. Other machine learning methods are combined with human cell-based *in vitro* data sets allowing the quantitative assessment of the potential DILI risk (Bayesian machine learning) [170][171]. The combination of a data-rich machine learning software with convincing experimental data would be a promising tool. However, due to the low incidence, the poor understanding of the mechanism, and the lack of reliable biomarkers, the amount of data currently is insufficient to adequately "teach" the software to predict DILI.

Current *in vitro* and animal-based biomarkers have not been accurate enough for the detection of hepatotoxicity in drug development. While *in vitro* studies only give an indication of the potential DILI risk of a drug (< 25 % sensitivity [9]), local exposure levels measured in *in vivo* animal studies allow suggestions about the toxicity in humans. Nevertheless, only about half of the new drugs that cause hepatotoxicity in clinical trials are concordant with animal toxicity studies [9]. Reason for this are species differences (Section 1.1). Recently, different biomarkers have been described to predict DILI in preclinical phases (Table 7). According to the 3R principles (Section 1.1), the focus is based on novel DILI-biomarkers for *in vitro* studies. More precisely, for advanced human cell-based systems to avoid interspecies variation and possibly reduce the number of tested animals.

The traditional biomarkers ALT, AST, ALP, GGT, and TBL can be measured in the supernatant of *in vitro* cultured and treated *primary human hepatocytes* (PHHs). They are released from damaged hepatocytes and can help to identify liver damage. However, as described before, they are not entirely liver-specific and do not allow a mechanistic understanding of the damage. Thus, the entire reliance on these biomarkers is not meaningful to understand and predict the development of DILI [172]. Another protein, which is released from damaged hepatocytes is *glutamate dehydrogenase* (GLDH). GLDH is mainly liver-specific and involved in amino acid oxidation and urea production [122]. It is expressed in the mitochondrial matrix of hepatocytes and described as a marker for mitochondrial disorders [173]. However, as mitochondrial protein the prediction of DILI is limited to the mechanism of mitochondrial dysfunction (Section 1.4.3). The cytosolic enzyme GST is a biomarker for hepatotoxicity and released from damaged hepatocytes. In addition, it is a DME and specific gene polymorphisms are associated

with DILI (Section 1.4.4) [160]. During hepatotoxicity, its isoenzyme *alpha-GST* (αGST) reaches measurable levels faster than ALT and AST [174]. Hence, αGST allows the detection of an early hepatic damage [174].

The “Omics” technology describes a new approach based on the detection of genes (genomics), mRNA (transcriptomics), proteins (proteomic), and metabolites (metabolomic) [175]. Due to the broad number of analyzed molecules, it becomes more and more popular fur studying DILI and potential novel biomarkers [176]. For example, *micro ribonucleic acids* (miRNAs) are small non-coding sequences concerned in post-transcriptional regulation of gene expression [123][177]. The miRNAs mir122 and mir192 are enriched in hepatic tissue. An elevation of both in the plasma could be detected in the context of APAP-induced toxicity and was described as biomarkers for early hepatocellular damage [177][172][178]. The intermediate filament *keratin 18* (K18) and its cleaved form *caspase-cleaved keratin 18* (ccK18) are markers for damaged cells. Necrotic cells release K18 whereas ccK18 is derived from apoptotic cells. [179]

Table 7: List of biomarkers for the detection and prediction of DILI.
Traditional biomarkers (*). [180][122]

Biomarker	Liver specificity	Physiological function	Potential DILI utility	References
αGST/ GSTA	High in liver and other tissues	Drug-metabolizing Phase II enzyme (Section 1.3.2)	Involved in injury/death/recovery	[181][182][183] [184][185]
Albumin	High in liver and blood	Transport	Most sensitive marker for liver function	[186][183]
AFP	High in liver progenitors	Liver regeneration, hepatocyte proliferation	Involved in regeneration	[180][187]
Arginase-1	High in liver	Converting arginine into urea and ornithine	Involved in injury/death	[180][184]
ALT*	High in liver	Converting proteins into energy	Released from liver during injury/death	[166][188][189]
AST*	Liver and other tissues	Metabolize amino acids	Released into the bloodstream from injured tissues	[166][188][189]
ALP*	High in liver	Hydrolysis of phosphate monoesters	Released from liver during injury/death	[122][165]
Bile acids	High in liver and other tissues	Digestion, excretion	Impairment of cell membrane integrity	[190][191][192] [193]
Cadherin 5 (CDH5)	Liver and other tissues	Integrity and adhesion	Elevation during injury	[122][194]
CSF1	Liver and other tissued	Regulates differentiation	Increased in patients undergoing liver surgery	[195]

Fatty acid-binding protein (FABP1)	High in liver	Regulation of fat/lipid metabolism	Involved in injury/death	[122][194][196]
Fas ligand (FASLG)	Liver and other tissues	Induction of apoptosis	Induction of liver cell death	[197][198]
GGT*	Liver and other tissues	Transport molecule	Increased concentration during injury (canalicular damage)	[122][195]
GLDH/ GLUD1	High in liver	Oxidative deamination of glutamate	Loss of mitochondrial integrity (mitotoxicity, necrosis)	[93][199][179] [200][201]
High mobility group protein B1 (HMGB1)	Liver and other tissues	Regulatory functions, DNA replication/repair	Released from damaged cells → induction of inflammatory pathways	[202][203][195] [204][172]
Integrin Subunit Beta 3 (ITGB3)	Liver and other tissues	Cell adhesion and movement	Unknown	[205][206][207] [199][208]
K18/ccK18	Liver and other tissues	Structure and integrity	Involved in injury/death	[209][199][204] [172][179]
Lactate dehydrogenase (LDH)	Liver and other tissues	Cellular respiration	Monitoring of cytotoxicity/DILI	[188]
LECT2	High in liver	Recruitment of neutrophils	Recruitment protein, involved in regeneration	[180][187][210]
Macrophage colony-stimulating factor receptor (MCSFR)	Liver and other tissues	Receptor for the cytokine CSF (proliferation/differentiation regulation)	Macrophage receptor, involved in inflammation process	[180][202]
mir122	High in liver	Posttranscriptional regulation of mRNA involved processes	Involved in injury/death	[211][178][188] [202][199]
mir192	High in liver	Posttranscriptional regulation of mRNA involved processes	Involved in injury/death	[202][122]
Osteopontin (OPN/SPP1)	Liver and other tissues	Migration/infiltration of inflammatory cells Regulation of IL-12, IL-12 and IFγ	Involved in inflammation/regeneration	[122][202][195] [212][213]
Paraoxonase 1	High in liver	Protection against liver impairment	Increased concentration during injury	[180][200] [214]
Succinate dehydrogenase subunit A (SDHA)	High in liver and other tissues	Carbohydrate metabolism	Involved in injury/death	[122][215][180]
TBL*	High in liver	Antioxidant	Marker for cholestatic DILI, increased during injury	[122][166][167] [105]

In addition, *succinate dehydrogenase* (SDH) is highly concentrated in the liver and a sensitive indicator for acute and mild liver damage as it can be detected already during mild liver injuries. HMGB1 is primary involved in transcriptional regulation and released from damaged cells [122]. Extracellularly it binds to cell-surface receptors of immune cells and activates pro-inflammatory pathways [216]. The adhesion protein CDH5 can be found in many tissues as it is important for endothelial adhesion [122]. In the liver, an increased expression of CDH5 and sinusoidal dilatation was observed after treatment with oxaliplatin [217]. In addition, elevated levels were detected in serum samples of DILI patients. Hence, it is also described as a marker for DILI. [194] Bile acids are produced in the liver and excreted via the BSEP into the canaliculi network. Several compounds can inhibit the function of BSEP causing an intracellular accumulation of bile acids. Due to amphiphilic and emulsifying characteristic, they can induce a cytotoxic effect by disturbing the integrity of the cell membrane. Consequently, bile acids are also described as biomarkers for cholestatic disorders causing DILI. [122]

1.5 Hepatotoxicity testing

Toxicity testing of potential new drug candidates is essential for the drug development process [218]. *In vivo* and *in vitro* models can be used to simulate human diseases in preclinical safety studies. Safety studies in two or more animals species provide a good insight under physiological conditions whether a candidate will function in the body in the same way as in the artificial environment [219]. Animal-based experiments provide important information about the PK*/pharmacodynamic* (PD) and toxicological property of a compound. Retrospective analyses, however, determine poor concordance rates to human toxicity with 63 % for non-rodent and 43 % for rodent species [9]. Likewise, animals are more sensitive to drugs that are already administered in doses that are harmless to humans, such as APAP in mice or ibuprofen in dogs [220]. As already known, the preclinical prediction of clinical hepatotoxicity is poor [219][220]. Hence, the presence of a toxicity in animals does not typically stops the entering of a compound into the clinical phase unless clear dose-dependent effects are observed [223]. The poor predictivity may be due to the inter-species differences in e.g., anatomy, liver enzyme expression, and specificity. Therefore, animals are not fully representative for the function in the human body [224]. Although data of animal studies allows suggestions about the toxicity in humans, the interpretation and transfer to humans remains challenging [225][226]. In addition, infrequent and unpredictable adverse effects, such as iDILI are not easily identified in animal models, as the necessary number of animals makes it difficult to detect this rare hepatotoxic effects [227]. Due to concerns about animal welfare the establishment of reliable *in vitro* models for toxicologic investigations become a priority for the toxicology community [218]. This is also supported by organizations such as the National Research Council, the United States Environmental Protection Agency, and the United States National academy of Science [228].

1.5.1 Hepatic cell sources for *in vitro* hepatotoxicity testing

In 2007, the United States National academy of Science published recommendations for toxicity testing urging a shift from the extensive usage of *in vivo* to *in vitro* models. This should not only reduce the use of animals, but also lead to greater efficiency and a better mechanistic understanding of the side effects in humans [228]. Today, a variety of different *in vitro* human liver models have been developed, including immortalized cell lines and primary liver cells (Table 8) [229].

HepG2 is a hepatic cell line obtained from a human hepatoma. Due to their unlimited use, the cells are widely used in *in vitro* culture models. As displayed in Table 8, HepG2 are highly proliferative, reproducible, cheap, and easy to handle [230]. Hence, they are suitable for early screening tests or cytotoxicity assessments. However, many functions are turned off, including important metabolic activities, which makes them impractical for more detailed studies and challenges the detection of different adverse effects, such as DILI [231].

HepaRG is a bipotent cell line established by Gripon and colleagues [232]. The unique property of these cells is that they are able to proliferate as progenitor in the presence of *fetal bovine serum* (FBS) but also can differentiate into hepatocyte-like and cholangiocyte-like cells by adding *dimethyl sulfoxide* (DMSO) into the medium [233]. Once differentiated, the coculture has a comparable metabolic activity to PHH [234]. HepaRG express various CYP enzymes (CYP1A2, 2B6, 2C9, 2E1, 3A4) and nuclear receptors (CAP, PXR) at comparable levels like PHH [235]. Consequently, they represent the hepatic functionality better than HepG2 and are an alternative for PHH for specific issues (e.g., phospholipidosis, steatosis, cholestasis, inflammation, lipid metabolism, and mitochondrial and genetic toxicity) (Table 8) [100][236]. However, the cells derive from a single individual with poor CYP2D6 metabolization activity, which is one of the major enzymes involved in phase I drug metabolism (30 % of all approved drugs [100]) (Section 1.3.2). They also lack urea secretion in monolayer cultures, which is one of the major liver-specific function [237]. [100]. In summary, HepaRG cells are a potential alternative to study specific metabolic aspects but their response to xenobiotics is not quite comparable to that of PHH [234].

Table 8: Hepatic cell sources of human origin for in vitro toxicology testing.
(↑: high/ →: moderate/ ↓: low) [238]–[242]

	HepG2	HepaRG	Upcyte	iPSC	PHH
Proliferation	↑	→	↑	→	↓
CYP activity	→	→	→	→	↑
Metabolism	↓	→	→	→	↑
Easy handling	↑	→	→	↓	→
Cost	↑	↓	→	↑	↑
Batch differences	↓	↓	→	→	↑
Source	Tumor		Healthy human		

Upcyte® hepatocytes are PHHs with modified genes to promote proliferation. The basal expression levels of CYP enzymes are reported to be comparable to PHH. For example, it has been shown that CYP-activities can be measured and induced/inhibited, and key liver functions can be detected (e.g., albumin and urea secretion) [243][244]. In contrast, other publications reported controversial data. For example, a proteomic study has shown that Upcyte® hepatocytes express metabolizing enzymes at levels comparable to HepG2 and thus significantly lower than PHH [245]. Therefore, further optimization and more studies are needed to closer characterize these cells. However, as these cells are genetically modified, they are limited in the application for therapeutic and routine studies within the drug development process. The Ucpyte® technology was also performed with other primary cells, such as LSECs. Upcyte

LSECs are also genetically modified to promote proliferation without losing functional and phenotypic characteristics (up to 40 passages) [246]. Upcyte® hepatocytes, Upcyte® LSECs and Upcyte® mesenchymal stem cells can form 3D hepatic organoids in Matrigel® with stable phenotype [247]. Although, some published data show the potential of this technology, it needs further optimization and investigation regarding their suitability and use in drug development studies.

Human *induced pluripotent stem cells* (iPSCs) could provide a suitable cell source with unlimited supply. Their intrinsic proliferative capacity and potential to divide into almost all cell types make them an attractive tool for the development of new advanced *in vitro* cell models [248]. Moreover, they are able to form organ-specific architecture, self-renew and self-organize, revealing their great potential for studying the response of human organs to xenobiotics in preclinical phases [249]. *IPSC-derived human hepatocyte-like cells* (iHeps) already were generated from several groups [250][108][248][253]. They own several functions comparable to PHHs, however, currently to PHH monolayers after 24-72 h in culture [226][254][210][211]. That means that several functions are severely down-regulated [251]. Among other aspects, such as cost and time intensity, this still prevents the integration into the routine and the widespread use of iHeps [251]. Recently, the focus is increasingly directed towards organoids. 3D iPSC-derived liver models provide closer cell-cell interactions of more relevant liver cell types with proliferative and self-organizing properties. Today, several publications can be found regarding the differentiation of iPSC-derived liver organoids and their functional characterization [257]. Nevertheless, this cell source is still in the early stages of development. Further optimization and characterization is needed to establish a model reliable for mechanistic and toxicological studies. [100][241]

PHH are the predominant cell type of the liver and the gold standard for *in vitro* hepatotoxicity and ADME studies. In contrast to other cell sources, they completely reflect the functionality of the liver *in vivo*, as they were actively part of it (Table 8) [258]. Donor pooling can minimize batch-to-batch variability which may improve predictability [259]. However, a clear advantage over the reaction of a single donor is controversially discussed and reported to be indistinguishable [260] In addition, cells usually have to be thawed and refrozen again to mix different donors, which can cause severe stress to the cells and affect the reaction to xenobiotics [261]. PHHs show limited growth activity, although hepatocytes are capable of renewal *in vivo*. In addition, they have high donor-to-donor variability and quality. [235][262] Suspensions are useful to study metabolic clearance and CYP inhibition-mediated drug-drug interactions in high-throughput. However, due to their limited lifetime of a few hours, drug hepatotoxicity and CYP induction studies needs to be performed in 2D seeded PHHs [263]–[265]. In 2D, PHHs undergo dedifferentiation and lose their physiological function within 24-72 h [226][254][210][211]. This is attributed to the isolation method which disrupts the cells' polarity,

integrity and differentiation [266][267]. The isolation process damages the cell junctions (contact with ECM and other hepatocytes/cell types), cytosolic contents, and cell membrane, including surface receptors and antigens [229]. The oxidative stress to the cells lead to a great loss of for example, enzyme activities within 4-8 h [260][261]. Additional reasons for the rapid loss of physiological function can be explain in the culture form. PHHs are monocultured in 2D on optimized plastic surfaces, at static conditions without any contact to other liver cell types. The reconstitution of the liver-specific architecture in so-called advanced liver models can preserve the physiological function long-term by reconstructing cell polarity and promoting model robustness (Section 1.5). Several publications have already described that advanced culture models allow longer viability and functionality of PHHs for up to four weeks [270][271][33].

1.5.2 Non-parenchymal cells and their role in hepatotoxicity

Liver parenchymal and NPCs closely interact with each other to fulfill a variety of functions [272]. NPCs, such as LSECs, KCs, and SCs comprise approximately 20 % of the total liver mass. They represent the minority of liver cells compared to hepatocytes, but are essential for communication and liver homeostasis [273]. There is an increasing evidence that LSECs are also involved in various metabolic activities and are the primary target for some hepatic toxins [274]. LSECs form a selective barrier that proteins and large molecules must pass to reach the hepatocytes (Section 1.3.1) [275]. Thus, LSECs are one of the first cell type meeting xenobiotics in the liver. The barrier prevents hepatocytes from vascular shear stress, and during inflammation, LSECs are involved in immune cell recruitment [276].

Although they have a significant role in drug exposure and toxicity, they have limited use for drug screening besides hepatocytes [277].The coculture of hepatocytes with LSECs or SCs stabilize CYP activity and the phenotype in long term [32][274]–[278]. In addition, it provides a more realistic toxicity model [33]. KCs are reported to play a central role in modulating CYP450 due to the exposure of several regulatory factors such as cytokines [283][284]. Thus, the creation of an *in vivo*-like microenvironment is useful for examining the metabolic function and xenobiotic toxicity in a more realistic way.

In case of DILI, NPCs are described to be directly targeted by DAMPs secreted from damaged hepatocytes [226]. Liu et al. described that the immune system plays a critical role in the progression of APAP-induced liver injury by triggering a secondary reaction after the initial damage of hepatocytes, that can increase the initial damage [285]. In contrast, NPCs also play a major role in the regulation of the hepatic functions and can prolong their physiological functionality *in vitro* [286][287]. To understand the development of DILI it is crucial to understand the communication between hepatocytes and NPCs. Therefore, the establishment of liver cell cocultures needs to be further investigated and optimized. A robust coculture model may be a useful tool to study the first and second response in the hepatic xenobiotic metabolism.

1.5.3 2D cultures

Several *in vitro* assays using primary cells or hepatic immortalized cell lines are integrated in the routine assays for toxicological screening. The experiments are cost efficient, easy to handle, less time-consuming, controllable, have high-throughput potential, and can be performed with different species with less ethical concerns. [288] In order to examine the impact of a chemical to the human liver, PHHs cultured in 2D are the gold standard for hepatotoxicity testing. Short-term studies can be performed examining enzyme induction and inhibition in an interspecies and inter-individual manner [237][238]. However, long-term studies are not possible as PHH in 2D rapidly lose their physiological function, such as phase I and II enzyme activities (within 48 – 72h). [225][259]–[261]

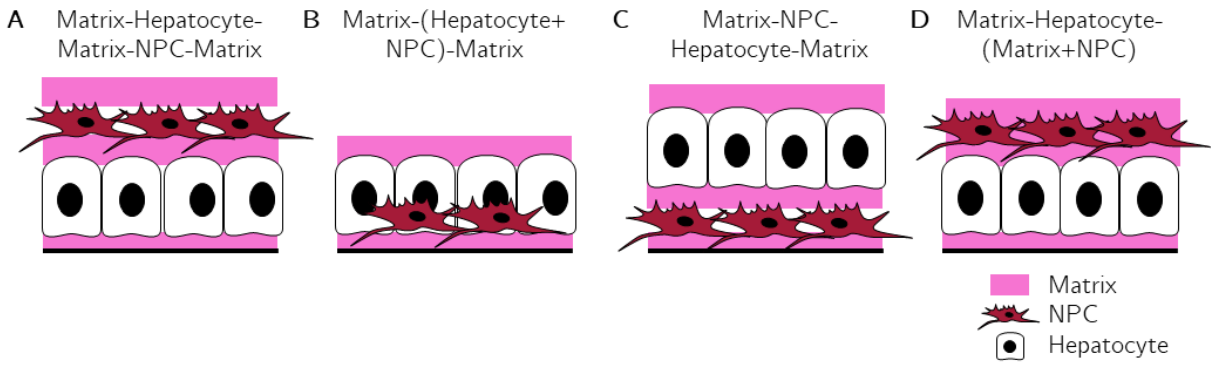

Figure 7: Schematic overview of hepatocyte and NPCs sandwich configurations.
Graphics show different sandwich formats including **(A)** Matrix-Hepatocyte-Matrix-NPC-Matrix, **(B)** Matrix-(Hepatocyte + NPC)-Matrix, **(C)** Matrix-NPC-Hepatocyte-Matrix, and **(D)** Matrix-Hepatocyte-(Matrix + NPC).

Next to the damage of the cells during the isolation process (Section 1.5.1), also the flat monoculture on optimized plastic surfaces, at static conditions, without any contact to other liver cell types, influences the maintenance of the physiological function. A partly reconstitution of the liver-specific architecture, by including ECM and other cell types, can prolong the physiological functions of the PHH [229][291]. For example, in a simple sandwich configuration, hepatocytes are growing with NPCs (e.g., LSECs) on/under or within a matrix (e.g., collagen or Matrigel®) (Figure 7). This advanced coculture model maintains the hepatocytes functions, such as albumin/urea secretion and CYP activity for up to 4 weeks [292].

1.5.4 3D cultures

Despite of the positive aspects of sandwich models (Section 1.5.3), the liver-specific functions decreased over time [229]. The *in vivo* microenvironment of the human liver has a big impact on the maintenance of the function including the response to endogenous and exogenous molecules [229]. Therefore, *in vitro* models are further developed to closer mimic the liver-specific architecture by the establishment of so-called 3D culture systems. The aim is, to create a cellular microenvironment which enables the long-term maintenance of the physiological

functions due to the recreation of the cellular polarity [291]. 3D cell culture models can be either spheroids or organoids (Figure 8). A spheroid is an aggregate which means that the cells are not organized as in an organ (Figure 8, left). It can be formed using primary cells or cells from a cell line, representing a partial tissue compartment. The long-term maintenance is difficult as a spheroid comprises several layers (on the surface or in the center) differently supplied with nutrients and oxygen. In cell line-based spheroids, the surface-near cells continuously proliferate. Consequently, the central cells get necrotic due to the low supply of nutrients and oxygen. In contrast, primary cells are limited proliferative and thus longer culture periods are possible.

An organoid mostly is derived from stem cells differentiated into organ-specific cell types [293]. It can self-organize and thus recapitulates an organ-like organization (Figure 8, right). Organoids can be expanded *in vitro* and thus cultured long-term. [294] However, the differentiation of a fully functional organoid, comprising all cell types of the organ of interest, is challenging. In addition, the maintenance and handling require further organ-specific optimization and standardized protocols for integration into the drug development process. Nevertheless, the organoid-field becomes more and more attractive and thus several differentiation methods are yet published [30][291]–[294].

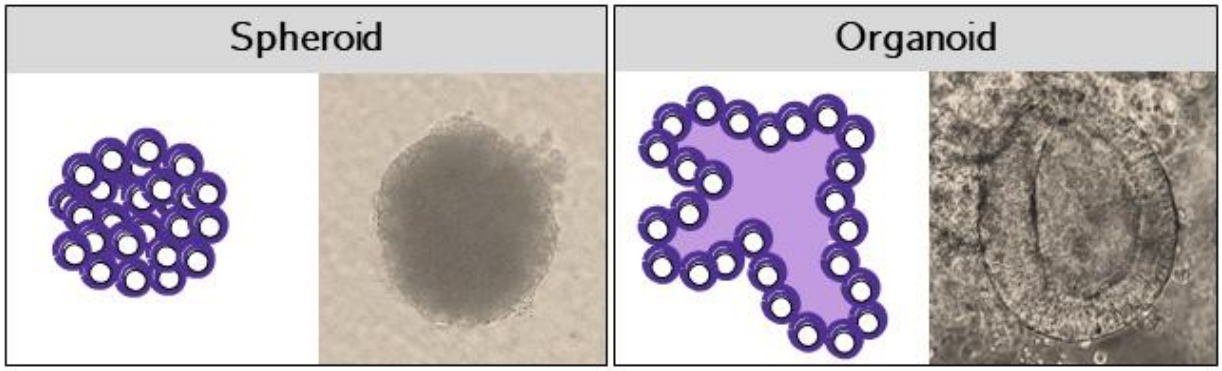

Figure 8: Schematic illustration and microscopical image of a spheroid and an organoid.
Graphic shows schematically the difference between spheroidal and organoidal structure with a microscopic example image.

Current advanced 3D models range from scaffold-free to scaffold-rich technologies (Figure 9). The formation of spheroid, or differentiation of organoids can be performed using these methods. A scaffold-free method is for example the optimization of the cell culture surfaces with a non-adhesive coating. Consequently, cells attach tightly to each other and form round aggregates (Figure 9). Depending on the cell type and the donor, the formation differs between 24 h and several days [299]. Likewise, scaffold-free spheroids can be generated by the hanging drop method. Therefore, a cell suspension-drop is dibbled onto a surface, such as the underside of a petri dish. Due to the surface tension of the liquid the drop remains intact, and cells can attach to each other as described before. A third scaffold-free method is the use of a

bioreactor. The principle of a bioreactor is that the medium is moved continuously so that the cells cannot settle down and aggregate within the circulating liquid. The formation using a bioreactor can result in a large number of spheroids, however, with different sizes since the number of cells that aggregate with each other cannot be controlled. For toxicological screening, different spheroid sizes are inconvenient because smaller aggregates might respond different to chemicals than large ones. In addition, very large spheroids can form a necrotic core. This means that the inner cells cannot be supplied sufficiently with nutrients and oxygen and waste products cannot be released efficiently. Consequently, the cells become necrotic [300]. Necrotic cells release pro-inflammatory DAMPs that can trigger a reaction of the surrounding cells. Then it is challenging to determine whether an effect was triggered by a chemical or by the cells themselves.

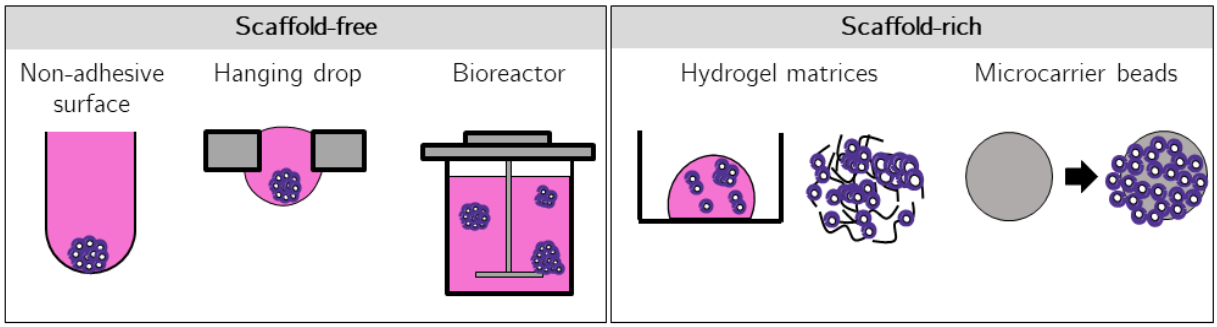

Figure 9: Different methods for the generation of 3D spheroids.
Spheroids can be generated using a scaffold-free and scaffold-rich method. Scaffold-free methods include non-adhesive surfaces (e.g., *ultra-low attachment* (ULA) coatings), hanging drops, and bioreactors. Scaffold-rich methods form spheroids within a hydrogel/matrix or using microcarriers.

In vivo the ECM plays an important role in intracellular scaffolding and communication [301]. Therefore, several scaffold-rich technologies were developed based on hydrogels or carriers (Figure 9). Natural or synthetic hydrogels, such as laminin, collagen or Matrigel®, have gelation characteristics that mimic the *in vivo* three-dimensionality. However, the choice of the appropriate biomaterial can vary depending on the analysis. A hydrogel can vary in the mechanical property, source (e.g., synthetic or animal-based), and composition (e.g., with/without growth factors or proteoglycans) [302]. All this must be considered in the selection process, as various additives or properties of the gel can affect the viability and function of the cells. Biopolymer-based microcarriers can also be of natural or synthetic origin. Cells can adhere and proliferate on the surface. Compared to full cell aggregates, the transport of nutrients, oxygen and waste products within the microcarriers is easier [303]. However, due to the different composition of the biopolymers, the choice of the right microcarrier must be adjusted depending on the assay. In addition, surrounding of a microcarrier does not mimic the physiological *in vivo* architecture of the cells. [304]

1.5.5 Microphysiological systems

Static cell culture models mimic the complex liver physiology only to a limited extent. Recently, so-called *microphysiological systems* (MPS) or *organ-on-a-chip* (OOC) system have rapidly emerged in biomedical research and have the potential to offer a promising alternative for *in vivo* and static *in vitro* systems [305]. The integration of microchannels to set up a flow, mimicking the “blood flow”, changes the static *in vitro* culture into a dynamic one. The, MPS allows an *in-vivo*-like consistent distribution of nutrients, oxygen, and compounds. Likewise, a constant elimination of waste products is possible. In addition, cells can be treated with chemical gradients [306]. Hence, the experimental possibilities closer mimic the dynamic microenvironment *in vivo*.

MPS consists of one or more channels, mostly connected to an external pump system. In this work, the Emulate OOC system was used, schematically illustrated in Figure 10 2D. Different cell types can be seeded into the top and the bottom channel. Both channels are separated by a porous membrane which allows cultivation with different media and communication between both cell types without direct contact.

Today, the OOC market is continuously growing. Many companies and start-ups have already developed, enhanced, and marketed their MPS techniques and models. Some of them are for example Mimetas, Tissuse, AlveoliX, and inSphero. The OOC of inSphero enables for example the cultivation of 3D cell constructs, such as spheroids or organoids (schematically shown in Figure 10 3D). Therein, the 3D cellular models can be transferred or formed directly within microwells which are supplemented continuously by the flow stream above.

However, the handling of the systems is complex as mostly specialized equipment, such as external pumps, are necessary. The specialized equipment also limits the number of possible simultaneous experiments and treatments, due to the defined number of connections. Together with the high cost, MPSs are currently not suitable for high-throughput screening but a promising tool for the mechanistic understanding of biological processes. Further, the most common material for MPS is *polydimethylsiloxane* (PDMS), due to its biocompatibility and ability of gas permeabilization. Nevertheless, the soft polymer is known to undergo easily structural changes at higher pressures. Deformation of the microfluidic channel can affect the flow rate. In addition, PDMS can absorb small molecules such as drugs [307]. Compounds with high hydrophobicity ($\log P > 2.67$) show high absorption by PDMS [308]. Consequently, for toxicological studies, the application of PDMS-based MPS is limited to the individual physicochemical property of the compound.

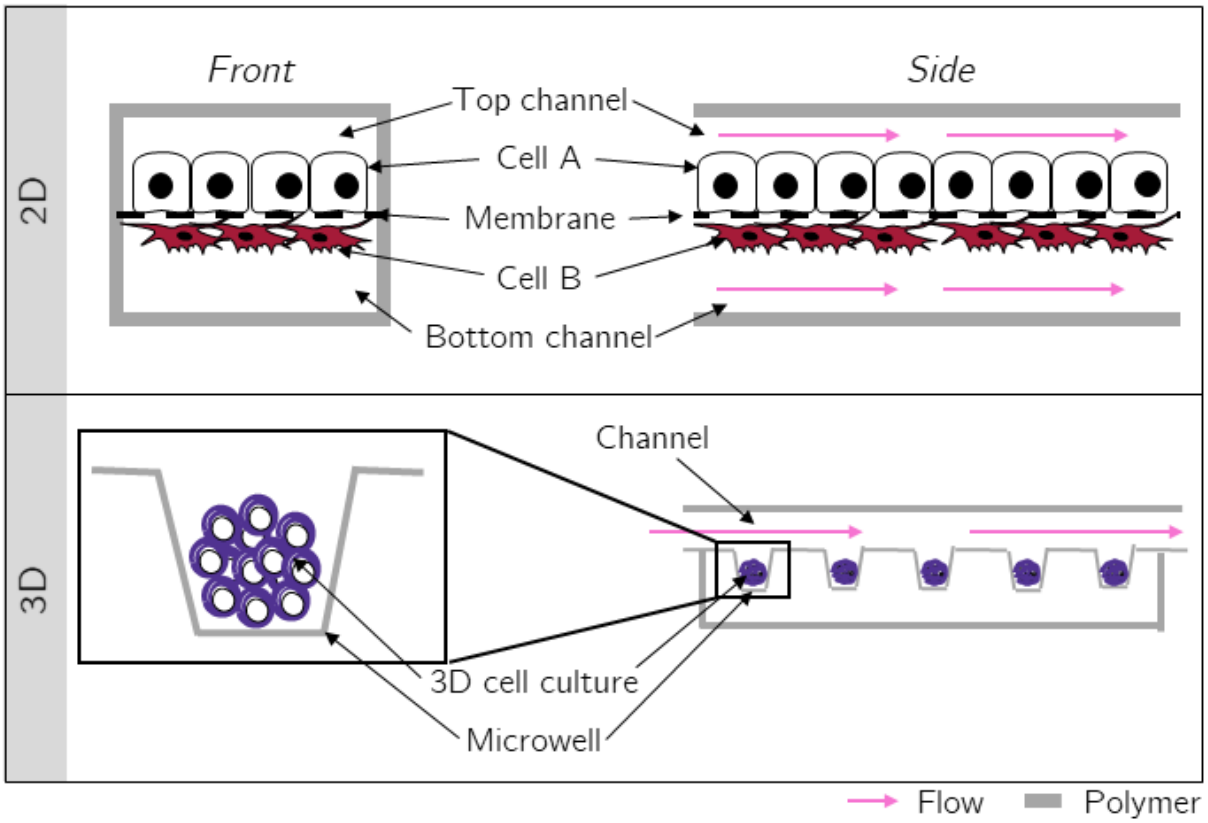

Figure 10: Illustration of different microfluidic systems.
Graphic shows two types of organ chip models seeding a 2D monolayer or integrating 3D spheroid/organoids.

1.6 Test compounds

In this work, several advanced *in vitro* liver models were assessed and treated with marketed or formerly marketed compounds known to cause or not cause DILI (Table 9). In the following, the selected compounds are briefly described according to their hepatotoxic mechanism.

The hepatotoxicity of APAP is one of the most extensively studied mechanisms. In humans, APAP is either glucuronidated or sulfated to intermediates that are excreted in urine. A part of the drug is metabolized by CYP2E1, 1A2, and 3A4 to the toxic CRM NAPQI. [309] In general, NAPQI is rapidly bound by GST to prevent a toxic effect. Nevertheless, APAP overdose leads to an increased NAPQI formation that exceeds GST binding capacity. Consequently, NAPQI binds covalently to proteins and macromolecules and causes hepatocyte death. [85]

AMIO is a very potent antiarrhythmic drug. It accumulates preferentially in lipid-rich regions. Consequently, it firstly inhibits phospholipase activity by forming non-covalent complexes and secondly, its metabolites accumulate in lysosomes, leading to phospholipidosis. [310][131]

The endothelin receptor antagonist *Bosentan* (BOS) is taken up from blood by OATP1B1 and OATP1B3 followed by the metabolization via CYP3A4 and 2C9 to three main metabolites. [311] The drug inhibits the efflux transporters BSEP and MRP2 leading to an intrahepatic accumulation of bile acids which cause liver damage. [312][313]

Diclofenac (DIC) is a nonsteroidal anti-inflammatory drug metabolized by CYP2C9, 3A4 or peroxidase-mediated oxidation to different quinone-imine reactive metabolites [314]. These reactive metabolites can form adducts with proteins and macromolecules [315]. In addition, DIC disturbs the mitochondrial function, such as rapid and concentration-dependent ATP depletion in very high doses [131]. However, the clear mechanism for diclofenac-induced liver injury in patients is still poorly understand.

Fialuridine (FIA) is an antiviral drug for the therapy of hepatitis B. It failed in clinical phase II studies due to unexpected hepatotoxicity. 7 out of 15 patients suffered from irreversible acute liver failure after FIA exposure [316]. In preclinical *in vitro* and animal studies the hepatotoxicity potential could not be predicted [317]. As described in Section 1.5, FIA is an excellent example of the essential problem of the interspecies differences between animal and human. In contrast to mice, human express the equilibrative nucleoside transporter 1 in the mitochondrial membrane. FIA and its metabolites are predominantly located in the mitochondrial membrane and are metabolized to triphosphorylated products. These products have a high affinity to the mitochondrial DNA polymerase γ. Hence, mitochondrial toxicity occurs due to gradual depletion of mtDNA. [318]

Levofloxacin (LVX) is a third-generation fluoroquinolone. In short term studies, abnormal elevations of serum ALT and AST could be observed in 2-5 % of patients after levofloxacin exposure. The mechanism of fluoroquinolone-induced liver injury is poorly understood. However, it seems to be associated with a hypersensitivity reaction leading to hepatitis-like signs and symptoms which can results in hepatic injury. [319][320]

Similar to LVX, *trovafloxacin* (TVX) is a third-generation fluoroquinolone associated with dose-dependent DILI [321]. It was withdrawn from the market in 2001, three years after marketing [322]. Abnormal hepatic serum levels were recognized in 2-3 % of patients after 2 – 3 weeks of trovafloxacin exposure [323]. It was not possible to detect the hepatotoxicity in preclinical studies [324]. A potential mechanism of the development of TVX-induced liver injury is a hypersensitivity manifestation. This assumption is based on the data generated in rodent experiments in which an inflammation was induced with lipopolysaccharides prior to trovafloxacin treatment [325]. The inflammatory reaction is thought to be due to activated Kupffer cells. However, also LSECs and SC are able to produce inflammatory cytokines [324].

Tolcapone (TOL) inhibits the catechol-O-methyl transferase reversible in the treatment of Parkinson's disease. It was already withdrawal from the market in 1998 due to hepatotoxicity. However, it was reintroduced in Europe in 2006 for the treatment of Parkinson's disease, on the condition that liver enzymes are determined regularly during the first six months of therapy [326]. The clear mechanism is poorly understood. Nevertheless, TOL seems to cause mitochondrial uncoupling of OXPOS and disrupt the energy-generating cycle, resulting in decreased ATP production and an increased oxygen consumption. [327][328]

Troglitazone (TRO) was withdrawn from the market due to elevated serum ALT levels [329]. Hepatotoxicity due to TRO is diverse. Biotransformation of the drug results in the formation of reactive metabolites, although it is reported that this is not the primary mechanism for liver injury [330]. Furthermore, it interacts with mitochondrial structures and leads to ATP depletion and cytochrome C release [331]. In addition, TRO accumulated in lipid-rich regions, promoting the development of fibrosis [332]. The inhibition of the biliary efflux, leading to bile acid accumulation, cholestasis, and consequently to the death of hepatocytes via the Fas death receptor signaling pathway, has also been demonstrated in several studies [333][334].

Ximelagatran (XIM) is an orally administered direct thrombin inhibitor that was withdrawn from the market due to liver enzyme evaluations in long-term treatment (> 35 days) [335]. The mechanism of hepatotoxicity is attributed to an immune-mediated effect due to a genetic association between elevated ALT and the major histocompatibility complex alleles DRB1*07 and DQA1*02 [336].

The non-DILI listed compounds in Table 9 are classified in the DILI rank list of the FDA as being of “low DILI concerned” [337]. *Dabigatran* (DAB) is a potent direct thrombin inhibitor and

did not cause DILI in several studies [338]. The antihyperglycemic drug *metformin* (MET) is not metabolized in the liver and does not cause DILI, although it had caused cholestasis in some patients [339][340]. In case of TOL and TRO-induced liver injury, *entacapone* (ENT) and *pioglitazone* (PIO) serve as negative controls [131].

Table 9: Compound selection used in described investigations and DILI mechanisms.
(RM: Generation of reactive metabolites, IM: Immune-mediated toxicity, MD: Mitochondrial dysfunction, BEI: Biliary efflux inhibition, LD: Lysosomal dysfunction)

Drug	**Therapeutic function**	**DILI mechanism**	**FDA black box/ severity class** [337]	**Reference**
APAP	Analgesic	RM, MD, IM	Most-DILI-concern/5	[309][85]
AMIO	Antiarrhythmic	MD, LD	Most-DILI-concern/8	[310][341]
BOS	Antihypertensic	BEI	Most-DILI-concern/7	[311][312][313]
DAB	Anticoagulant	No DILI	No item	[338]
DIC	Analgesic	RM, MD	Most-DILI-concern/8	[314][342][315]
ENT	Parkinson's disease	No DILI	Less-DILI-concern/0	[131]
FIA	Hepatitis B therapy	MD	Most-DILI-concern/8	[343][317][316][344]
LVX	Antibiotic	IM	Most-DILI-concern/8	[320][344][319]
MET	Antidiabetic	No DILI	Less-DILI-concern/0	[339][340]
PIO	Antidiabetic	No DILI	Less-DILI-concern/3	[131]
TOL	Parkinson's disease	RM, MD	Most-DILI-concern/8	[327][328]
TRO	Antidiabetic	RM, MD, BEI, LD	Most-DILI-concern/8	[329][332][331]
TVX	Antibiotic	IM	Most-DILI-concern/8	[321][322][323][324]
XIM	Anticoagulant	IM	Most-DILI-concern/8	[335][338][339][340]

1.7 Aim of the thesis

DILI is a common reason for the termination of multiple drug development programs in the last decades [155][162]. Unexpected hepatotoxicity is one of the major causes. Current preclinical *in vivo* and *in vitro* test models are limited in predicting hepatotoxicity in human. Due to concerns about animal welfare, there is an urgent need for advanced *in vitro* liver models and reliable biomarkers to study and predict the development of DILI in the human liver.

The first aim of the thesis was the establishment of four advanced *in vitro* liver cell culture models (2.5D sandwich, 3D spheroids, OOC, liver organoids) for the preclinical assessment of DILI (AIM_1). As primary human liver cells rapidly lose their physiological function in monoculture, the advanced cell culture models should consist of two or more hepatic cell types. A cocultured 2.5D sandwich, cocultured 3D spheroid, and quadcultured OOC model were chosen to recapitulate the liver physiology closer to *in vivo* and prolong the functionality of the cells *in vitro*. The second goal of this work was the differentiation of iPSC-derived liver organoids to create a proliferative 3D preclinical test model with functional and structural aspects of the human liver (AIM_2).

The third aim was to characterize the establish advanced cell culture models and test their long-term functional stability using microscopical techniques (bright-field and immunofluorescence staining) and multiple OMICs analysis (metabolomics, proteomics, genomics, secretomics). To get an insight into the impact of the culture system to the primary liver cells, the microscopical images, OMICs data, and additional pathway analyses should be compared between 2.5D, 3D, and OOC (AIM_3).

Currently, DILI is very challenging to predict *in vitro*. One reason is attributed to the lack of biomarkers to reliable determine and detect DILI. A further objective of this work was to research and test clinically used and potential new biomarkers, in all advanced *in vitro* liver models, to detect DILI. Therefore, the fourth goal was to select high-DILI-concern compounds and low-DILI-concern drugs according to the FDA DILIrank dataset (AIM_4). As DILI is known to develop after a latency period, the treatment should be performed in a repeated-dose manner for 14 days. The resulting fifth aim was to study the reaction of the cells in the advanced liver models to the selected compounds by analyzing the specific genes and secreted proteins which are described as potential *in vitro* DILI biomarkers (AIM_5). The sequential sampling of secreted proteins on days 2, 7 and 14 should show potential time-dependent responses. The gene expression was determined on day 14 to study the consequences of a prolonged *in vitro* treatment. The statistical analysis should identify a biomarker or a set of biomarkers which are significantly different between high-DILI-concern and low-DILI-concern treated cells. The final objective was to demonstrate the suitability of the tested biomarkers in the established advanced liver cell culture models for early *in vitro* detection of DILI using statistical analysis.

Summary: The main objectives were to

AIM_1 Establish and optimize advanced cell culture models using primary human liver cells for long-term culture (2.5D sandwich, 3D spheroids, OOC)

AIM_2 Generate iPSC-derived liver organoids using a self-developed differentiation protocol

AIM_3 Study the differences between the 2.5D sandwich, 3D spheroids, and OOC for long-term culture using microscopical techniques (brightfield and immunofluorescence staining) and multiple OMICs analysis (metabolomics, proteomics, genomics, secretomics)

AIM_4 Select and treat the advanced cell culture models with compounds known to cause and not to cause DILI in humans

AIM_5 Study the response of treated cells in all systems to assess their suitability for the early detection of DILI using known and potential (novel) biomarkers

2 Material

2.1 Consumables

Name	Manufacturer
15 mL tubes	Becton Dickinson GmbH
50 mL tubes	Becton Dickinson GmbH
24-well cell culture plates, white/clear, collagen-I-coated	Corning
96-well cell culture plates, white/clear, collagen-I-coated	Corning
96-well cell culture plates, black/clear, collagen-I-coated	Corning
96-well deep well plate 600 µL	Starlabgroup
96-well deep well plate 1.1 mL	Starlabgroup
Adhesive PCR foil seals, Axygen®	Corning
ART 10, disposable tips	Thermo Fisher Scientific
ART 20, disposable tips	Thermo Fisher Scientific
ART 100, disposable tips	Thermo Fisher Scientific
ART 200, disposable tips	Thermo Fisher Scientific
ART 300, disposable tips	Thermo Fisher Scientific
ART 1000, disposable tips	Thermo Fisher Scientific
Cell counting chamber (Fuchs-Rosenthal)	LO-Laboroptik
Cell culture Dish 150mm (353025)	Corning
Disposable hypodermic needle 100 Sterican 20-gauge	B. Braun
Emulate Organ Chips (Chip carrier, POD reservoirs, organ chip, reservoir lid)	Emulate Inc.
MicroAmp Fast Optical 96-well reaction plate	Applied biosystems
Optical adhesive covers	Applied biosystems
Parafilm ®	Brand
Pipette tips 0.5 – 20 µL	Brand GmbH&Co. KG
Pipette tips 2 – 200 µL	Brand GmbH&Co. KG
Pipette tips 5 – 300 µL	Brand GmbH&Co. KG
Pipette tips 50 – 1000 µL	Brand GmbH&Co. KG
Safe lock tubes 1.5 mL	Eppendorf
Safe lock tubes 2.0 mL	Eppendorf
Serological pipettes 1 mL	Corning Inc.
Serological pipettes 5 mL	Corning Inc.
Serological pipettes 10 mL	Corning Inc.
Serological pipettes 25 mL	Corning Inc.
Serological pipettes 50 mL	Corning Inc.

Single use syringes 1 mL Norm-ject	Henke Sass Wolf GmbH
T12.5 Cell culture flask	Corning Inc.
T25 Cell culture flask	Corning Inc.
T75 Cell culture flask	Corning Inc.
ULA U-bottom plate	Costar
ULA U-bottom plate	FaCellitate

2.2 Chemicals and reagents

Name (Cat.no.)	**Manufacturer**
Acetic acid, 96 %	Merck KGaA
Amiodarone	Sigma-Aldrich
Ampicillin (A1593)	Sigma-Aldrich
Ascorbic Acid (5960)	Millipore Sigma
Attachment Factor™ (4Z0-201)	CellSystems
B27 Supplement	Gibco
Basic human growth factor (bHGF) (100-39)	PeproTech
Bosentan	Sigma-Aldrich
Bovine Serum Albumin	Millipore Sigma
CMFDA (C2925)	Thermo Fisher Scientific
Collagen lyophilizate, from rat tail (354249)	Corning
CSC Medium 4Z0-500	CellSystems
Culture Boost 4CB-500	CellSystems
Dabigatran	Sigma-Aldrich
RNase-free/DEPC treated water, Ambion™	Thermo Fisher Scientific
DEF 500 CS (Thawing medium, culture medium, COAT-1, GF-1, GF-2, GF-3)	Takara
DEX (D4902)	Sigma
Diclofenac	Sigma-Aldrich
DMSO	Millipore Sigma
Entacapone	Sigma-Aldrich
Ethanol gradient grade of liquid chromatography	Merck KGaA
ER-1 Solution	Emulate Inc.
ER-2 Solution	Emulate Inc.

FBS (F4135)	Sigma
Fibronectin (33010-018)	Thermo Fisher Scientific
Fibroblast growth factor (FGF) 100-18B	PeproTech
Fialuridine	Sigma-Aldrich
Fungin™ (ANT-FN-1)	InvivoGen
GlutaMAX (35050-061)	Thermo Fisher Scientific
Hoechst 33342	Thermo Fisher Scientific
ITS+ premix (354352)	Corning
Knockout™ SR	Gibco
Levofloxacin	Sigma-Aldrich
Lysis Mixture	Thermo Fisher Scientific
Matrigel® GFR (354234)	Corning
Methanol	Sigma
Metformin	Sigma-Aldrich
Omeprazole	Thermo Fisher Scientific
Oncostatin M	StemCell
$PBS^{-/-}$, 1x, pH 7.4	Corning
$PBS^{-/-}$, 10x, pH 7.4	Corning
Penicillin/Streptomycin 100 U, 100 µg/mL (P4333)	Millipore Sigma
Percoll® solution (P4937)	Sigma
Resazurin	Sigma-Aldrich
Paraformaldehyde Solution, 4 % in PBS	Thermo Scientific
Phenobarbital	Sigma-Aldrich
Pioglitazone (0503032)	Cayman Chemical
Proteinase K	Affymetrix®
Rifampin	Sigma-Aldrich
RNase away	Molecular BioProducts
ROCKi	StemCell
RPMI 1640 medium 21875034	Gibco
Tolcapone	Sigma-Aldrich
Triton X-100	Sigma-Aldrich
Troglitazone (0513242)	Cayman Chemical

Trovafloxacin	Sigma-Aldrich
Trypan blue solution (93595)	EuroClone S.p.A.
TrypLE™ Express	Gibco
Trypsin-EDTA (T3924)	Sigma
Williams medium E (-), no glutamine (W1878)	Sigma
Williams medium E (+), no glutamine (W4128)	Sigma
Ximelagatran	Sigma-Aldrich

2.3 Kits/Assays

Name (Cat.no)	**Manufacturer**
Albumin Smiple Step ELISA (ab179887)	Abcam
Alpha GST ELISA activity assay (TE1056)	TecoMedical
ALT Activity assay (Mak055)	Sigma
AST Activity Assay (Mak052)	Sigma
CellTiter-Glo ® assay	Promega
CellTiter-Glo 3D ® assay	Promega
LDH-Glo™ Assay (J2380)	Promega
QuantiGene plex gene expression assay	Thermo Fisher
QuantiGene® 2.0 miRNA assay	Thermo Fisher

2.4 Cells

Name	**Supplier (Product number/ LOT)**
Cryopreserved Primary human hepatocytes	AXOLbio (ax3750-1/ 37501ZMC)
Cryopreserved Female human Hepatocytes	Celsis (F00995/ AKB)
Cryopreserved Female human Hepatocytes	Celsis (F00995/ HJK)
Cryopreserved Male human Hepatocytes	Celsis (M00995/ XQD)
Cryopreserved Primary Human Hepatocytes	Gibco (HU1880)
Cryopreserved Primary Human Hepatocytes	Gibco (HU1591)
Cryopreserved Primary Human Hepatocytes	Gibco (HUM4235)
Cryopreserved Primary Human Hepatocytes	Gibco (LOT HU1951)
Cryopreserved Primary Human Hepatocytes	Gibco (LOT HU8305)
Cryopreserved Primary Human Hepatocytes	Gibco (LOT HU8148)
Cryopreserved Primary Human Hepatocytes	Gibco (HU4248)
Primary human Liver Sinusoidal MVEC	Cell Systems (ACBRI 566/ 566.01.02.05.0M)
Primary human Liver Sinusoidal MVEC	Cell Systems (ACBRI 566/ 566.01.03.05.0M)

Primary human Liver Sinusoidal MVEC	Cell Systems (ACBRI 566/ 566.04.02.05.0M)
Primary human Liver Sinusoidal MVEC	Cell Systems (ACBRI 566/ 566.04.03.05.0M)
Primary human Liver Sinusoidal MVEC	Cell Systems (ACBRI 566/ 566.05.02.05.0M)
Human Liver Sinusoidal Endothelial Cells	AXOLbio (ax3777-1/ 37771ZMC)
Human hepatic Stellate Cells - Adult	iXCells (10HU-210/ 3000075-3)
Human Kupffer Cells	SAMSARA (HLKC/ HL180076KC)
Human Kupffer Cells	Gibco (HUKCCS/ HK8373)
Cellartis ® Human iPSC (ChiPSC18)	Takara (Y00300/ AK20001S)
Upcyte LSECs	BioIVT (CLS002/ 444-200501.1)
Upcyte LSECs	BioIVT (CLS002/ 462-20190701.1)

2.5 Equipment

Name	**Manufacturer**
Autoclave Varioklav 300E	HP Medizintechnik GmbH
Bioanalyzer 2100	Agilent
Centrifuge Multifuge 3 S-R	Heraeus
Centrifuge Megafuge 1.0R	Heraeus
Confocal microscope CX-7	Thermo Fisher
Emulate ZOE CM-1™ Culture Module	Emulate Inc.
Emulate Chip Tray	Emulate Inc.
Emulate Chip Cradle	Emulate Inc.
Emulate Orb-HM1™ Hub module	Emulate Inc.
Eppendorf pipettes (10 µL, 100 µL, 200 µL, 300 µL, 1000 µL)	Eppendorf
FLEXMAP 3D™ instrument	Luminex Corporation
Fume hood	Thermo Fisher Scientific
Incubator HeraCell®	Heraeus
Lumistar	Omega
Microplate shaker TITRAMAX 101	Heidolph instruments
Microscope IX70	OlympusDeutschland GmbH
Microscope camera	OlympusDeutschland GmbH
Mr. Frosty freezing container	Thermo Fisher Scientific
Integra Viaflo electronic pipettes	Intagra Bioscience
NanoDrop 2000	Thermo Fisher Scientific
Pipet boy accujet® pro	Brand GmbH&Co. KG
Spectrophotometer Discovery HT-R	MWG AG Biotech
StepOnePlus ™	Thermo Fisher Scientific

Sterile bench HeraSafe®	Heraeus
Tecan Infinite 500	Tecan
Thermomixer comfort	Eppendorf
UV Light box	Emulate
VorTemp 56 incubator	Labnet International Inc.
Vacuum pump	Thermo Fisher Scientific
Vortex Genie 2	Scientific Industries Inc.
Waterbath 1002	GFL Gesellschaft für Labortechnik mbH, Burgwedel

2.6 Software

Name	**Manufacturer**
GraphPad Prism v5.0.4	GraphPad Software
xPONENT	Luminex Corporation
Microsoft Office 2016	Microsoft Corporation
Lumistar galaxy	BMG Labtech
KC4	MWG AG Biotech
ImageJ	Wayne Rasband (NIH)
I control	Tecan
HCS Studio	Thermo Fisher Scientific

2.7 Antibodies

Primary antibody	**Cat.no.**	**Manufacturer**
Anti-albumin rabbit pAb	sc50535	Santa Cruz Biotechnology
Anti-CYP3A4 mouse mAb	sc53850	Santa Cruz Biotechnology
Anti-CD31 mouse mAb	MA5-13188	Thermo Fisher Scientific
SE-1 mouse mAb	NB110	Novus Biologics
Anti-BSEP mouse mAb	sc74500	Santa Cruz Biotechnology
Anti-BSEP rabbit pAb	ab256536	Abcam
Anti CD68 mouse mAb	333809	BioLegend
Anti OCT4 rabbit pAb	ab181557	Abcam
Anti-SOX17 mouse mAb	ab84990	Abcam
Anti-F-Actin mouse mAb	AB130935	Abcam
Anti-LYVE1 rabbit pAb	ab14917	Abcam
Anti-AFP rabbit mAb	ab169552	Abcam
Anti-HNF4α mouse mAb	SAB1412164	Sigma Aldrich

Anti-CYP450 rabbit pAb	MFO-100	Stressgen
Anti-MDR mouse mAb	P7965	Sigma Aldrich
Anti-MPR2 rabbit pAb	sc20760	Santa Cruz Biotechnology
Anti-MPR2 rabbit pAb	sc20766	Santa Cruz Biotechnology
Anti-CK7/17 mouse mAb	sc8421	Santa Cruz Biotechnology
Anti-MDR1 mouse mAb	sc55510	Santa Cruz Biotechnology

Secondary antibody	**Cat.no.**	**Manufacturer**
Donkey anti rabbit AF488	ABCAAB	Abcam
Goat anti mouse AF647	ab150115	Abcam
Donkey anti mouse AF647	A315711	Invitrogen

2.8 Media composition

Table 10: Composition of the CSC medium.
For LSECs culture.

CSC medium	**Volume [mL]**
CSC Medium (4Z0-500, Cell Systems)	43.5
FBS	5
Culture Boost 4CB-500, CellSystems	1
Penicillin/Streptomycin [100 U; 100 µg/mL]	0.5

Table 11: Coculture medium with 10 % FBS.
For PHH/LSEC spheroids formation.

Coculture medium 10	**Volume [mL]**
William's Medium E (W4128, Sigma)	43.445
FBS	5
GlutaMAX (350500-61, Gibco™)	0.5
Penicillin/Streptomycin [100 units; 100 µg/mL]	0.5
ITS + premix (354352, Corning®)	0.5
Ascorbic Acid [50 mg/mL]	0.05
DEX [1 mM]	0.005

Table 12: Coculture medium with 2 % FBS for the long-term cultivation.
Coculture of PHHs/LSECs in 2.5D and in 3D spheroids after formation.

Coculture medium 2	Volume [mL]
William's Medium E (W4128, Sigma)	47.445
FBS	1
GlutaMAX (350500-61, Gibco™)	0.5
Penicillin/Streptomycin [100 units; 100 µg/mL]	0.5
ITS + premix (354352, Corning®)	0.5
Ascorbic Acid [50 mg/mL]	0.05
DEX [1 mM]	0.005

Table 13: Coculture medium without FBS.
For PHHs culture.

Coculture medium	Volume [mL]
William's Medium E (W4128, Sigma)	48.445
GlutaMAX (350500-61, Gibco™)	0.5
Penicillin/Streptomycin [100 units; 100 µg/mL]	0.5
ITS + premix (354352, Corning®)	0.5
Ascorbic Acid [50 mg/mL]	0.05
DEX [1 mM]	0.005

Table 14: Composition of the PHH maintenance medium.
For the cultivation of PHHs in the Emulate OOC.

PHH medium	Volume [mL]
William's Medium E (W4128, Sigma)	48.445
GlutaMAX (350500-61, Gibco™)	0.5
Penicillin/Streptomycin [100 units; 100 µg/mL]	0.5
ITS + premix (354352, Corning®)	0.5
Ascorbic Acid [50 mg/mL]	0.05
DEX [1 mM]	0.005

Table 15: Composition of tested coculture media.
For PHH/LSEC coculture.

Coculture medium Test 1 [345]	**Coculture medium Test 2 [33]**	**Coculture medium Test 3** [346]	**Coculture medium Test 4** [347]	**Coculture medium Test 5 [InVitroCue collaboration]**
William's Medium E (W4128, Sigma)	DMEM (high glucose 4.5 g/L)	DMEM	DMEM (high glucose 4.5 g/L)	Advanced DMEM
2 mM L-Glutamine	2 mM L-Glutamine	1 mM Natriumpyrovate		0.292 g/mL L-Glutamine
100 U/mL Penicillin/ Streptomycin	2 % Penicillin/ Streptomycin	1 % Pen/Strep	1 % Pen/Strep	1 % Pen/Strep
10 µg/mL Insulin	500 U/L Insulin	4 µg/mL ITS		10 µg/ml Insulin
5.5 µg/mL Soldium Selenite	0.02 mg/L EGF	5 ng/mL EGF	40 ng/mL rVEGF	6.7 µg/mL Selenite
100 mM DEX				0.1 µM DEX
5.5 µg/mL Transferrin	7.5 mg/L Hydrocortisone	5 µg/mL Hydrocortisone		5.5 µg/mL Transferrin
	0.01428 mg/L Glucagon			15 mM HEPES
10 % FBS	10 % FBS	10 % FBS	10 % FBS	5 % FBS

Table 16: Composition of the NPC maintenance medium.
For the cultivation of NPCs in the Emulate OOC.

NPC medium	**Volume [mL]**
CSC Medium (Table 10)	24.5
PHH Medium (without DEX) (	24.5
FBS	1

3 Methods

3.1 Advanced 2.5D and 3D cell culture

The advanced cell culture models were generated and handled under sterile conditions. Cells were incubated in an incubator maintained under humidified atmosphere of 5 % *carbon dioxide* (CO_2), 95 % air and at an environmental temperature of 37 *degree Celsius* (°C).

In this work, primary human liver cells were used. In contrast to cell lines, they are fully differentiated and only a minor proportion undergo cell division [348]. The cultivation of PHHs as a monolayer in 2D, only allows short-term maintenance of maximum 24 - 72 h [226][254]–[256]. Longer cultivation results in dedifferentiation processes and PHHs lose their liver-like phenotype and function [349][350]. An advanced culture configuration, such as a sandwich (2.5D), spheroid (3D) or within an organ chip (OOC) enables longer viability and functionality for up to 4 weeks [270][271][33]. In the following section, the establishment and set-up of these advanced cell culture models is described. Prior to cell seeding, various PHH donors were tested once (N=1) for their suitability, including the possibility of spheroid formation, the gene expression of liver-specific markers and the secretion of hepatic proteins.

3.1.1 Thawing and pre-cultivation of liver sinusoidal endothelial cells

LSECs are highly specialized cells, located between the blood cells on the one side and the hepatocytes and SCs on the other side [276]. PHHs and LSECs account for the largest share of liver cells in the liver [33]. Therefore, LSECs were selected in this work to build a 2.5D and 3D coculture model.

For recovery and proliferation, LSECs were precultured for 3-4 days until the coculture with PHHs was set up. Until cell seeding, a T75 flask was coated with 5 *milliliters* (mL) Attachment Factor™ (4Z0-201, CellSystems) at 37 °C. Cryopreserved LSECs (LOT 566.01.02.05.0M, Cell Systems) were thawed in a 37 °C water bath and transferred into a 15 mL falcon with 3 mL CSC medium (4Z0-500, Cell Systems) supplemented with 10 % FBS, penicillin/streptomycin, and 2 % Culture Boost (4CB-500, CellSystems) (Table 10). The volume of the falcon was brought up to 15 mL with CSC medium. Cells were centrifuged for 5 *minutes* (min) with 250 *times gravity* (xg) at *room temperature* (RT). The supernatant was discarded, and the pellet was resuspended in 10 mL fresh CSC medium. Afterwards, the Attachment Factor™ was aspirated from the T75 flask. Immediately, the cells were seeding into the flask and cultivated at 37 °C, 5 % CO_2. The medium was changed daily until the coculture was set up.

3.1.2 Thawing of primary human hepatocytes

Hepatocytes represent the greatest population of cells in the liver and are currently the gold standard for *in vitro* testing of hepatotoxicity [351][352]. Different donors of cryopreserved

PHHs were purchased from BioIVT, Thermo Fisher, and other suppliers (Section 2.4). Cryopreserved cells were thawed in a 37 °C water bath and transferred into a 50 mL falcon with 3 mL of prewarmed Williams E Medium (W4128, Sigma) supplemented with 1x GlutaMAX (350500-61, Gibco), penicillin/streptomycin, ITS+, 50 µg/mL ascorbic acid, and 10 % FBS. The vial was rinsed twice with 1 mL medium to ensure that all hepatocytes were transferred. Subsequently, the volume was brought up to 50 mL and cells were centrifuged (5 min, 90 xg, RT). Afterwards, 45 mL of the supernatant was aspirated, and the pellet was resuspended gently. The cell number was determined according to the protocol in Section 3.1.3.

3.1.3 Determination of the cell count and the cell viability

The cell number was counted using a Fuchs-Rosenthal counting chamber. The viability of the cells was determined by incubating them with a trypan blue solution. The blue dye cannot pass the cell membrane of vital cells, thus live cells appear white under the microscope. In contrast dead cells are stained blue due to their membrane permeability.

To count the cells and control the viability, 500 *microliters* (µL) of medium and 500 µL trypan blue solution were mixed with 50 µL of the resuspended cell suspension. Afterwards, 20 µL of the mixture were pipetted into the Fuchs-Rosenthal counting chamber. Under a microscope, live and dead cells of at least four of the 16 squares were counted to determine a mean value. The number of viable cells per mL (Equation 2) was calculated to seed the right number of cells for following experiments.

Equation 2: Calculation of viable cells per milliliter cell suspension.

$$\frac{\text{cells}}{\text{ml}} = \text{viable cells} \times \frac{\text{dilution factor}}{\text{chamber depth} \times \text{counted area}}$$

$$= \text{viable cells} \times \frac{21}{0.2\ \text{mm} \times (16 \times 0.0625\ \text{mm}^2)}$$

$$= \text{viable cells} \times \frac{21}{0.2 \times 10^{-3}\ \text{ml}}$$

$$= \text{viable cells} \times 21 \times 5000$$

3.1.4 Setup of the advanced 2.5D and 3D coculture models

PHHs rapidly lose their hepatic functionality when culturing on optimized plastic surfaced and in monoculture *in vitro* [271][270]. In order to prolong the physiological functions, they were cocultured with LSECs in two advanced cell culture formats [33].

For the 2.5D coculture model, PHHs were diluted with coculture-media-10 to a final concentration of $5x10^5$ cells/mL and 100 µL of the diluted cell suspension was seeded per well into a

collagen I-coated 96 well plate. 4 h post-seeding, the attachment of the PHHs was controlled via the microscope and the medium was changed to coculture medium without FBS.

The next day, an ice-cold solution of 0.25 *milligrams* (mg)/mL Matrigel® (*growth factor reduced* (GFR)) in coculture-medium-2 was prepared.

For both advanced coculture models, LSECs were detached from the surface of the T75 flask described in Section 3.1.1. Therefore, the media was aspirated, the cell layer was washed once with 10 mL *phosphate-buffered saline* $(PBS)^{-/-}$ following by treatment with 3 mL *Trypsin-ethylenediaminetetraacetic acid* (EDTA) 0.05 % (3 min, 37 °C). The Trypsin-EDTA solution was diluted four-fold with coculture-media-10 to inactivate the enzyme reaction. The cell count was determined according to the protocol in Section 3.1.3.

To set up the 2.5D coculture model, LSECs were diluted to a final concentration of $1x10^5$ cells/mL in the prepared Matrigel®/coculture-medium-2 solution. The medium of the PHHs was replaced with 100 µL/well of the LSECs/Matrigel/coculture-medium-2 suspension. As shown in Figure 11, the experiments with the 2.5D model were performed the next day.

To set up the 3D coculture model, PHHs and LSECs were diluted to a final concentration of $2x10^4$ cells/mL of each cell type in the coculture-medium-10. 50 µL of each cell suspension was pipetted into an ULA U-bottom plate. The plate was centrifuged to accumulate the cells at the bottom of the U-bottom plate (1 min, 90 xg). The formation of spheroids was observed daily (Figure 11). Until formation, the media was not changed as a medium change can disturb the aggregation.

3.1.5 Experimental schedule of the advanced 2.5D and 3D coculture models

As depicted in Figure 11, the medium was changed every 2-3 days. Medium samples were collected at days 0, 2, 7, and 14 to monitor the secreted proteins (Section 3.8). The cell lysate was collected after 14 days of treatment, to analyze the gene expression (Section 3.4).

In the 2.5D coculture model, the medium was aspirated out of the wells and replaced with 100 µL of fresh medium. For the 3D coculture model, 50 µL of the medium were aspirated very gently and replaced with 50 µL of fresh media.

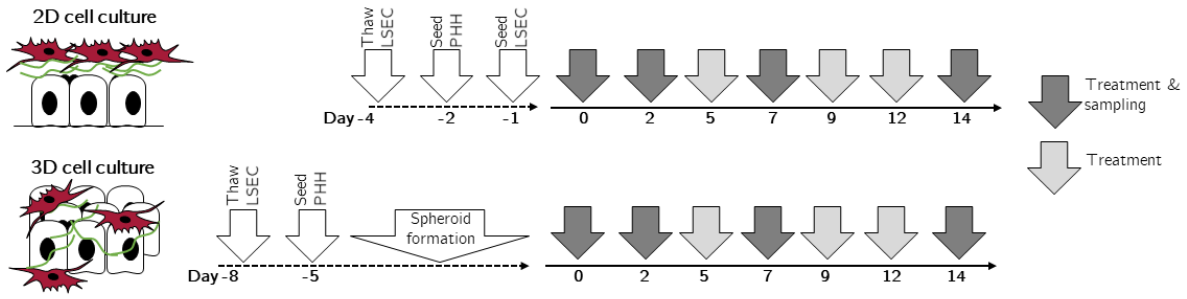

Figure 11: Experimental timeline for the advanced 2.5D and 3D models.
Timeline includes cell culture preparation, treatment, and sampling time points.

Compounds were selected from the FDA DILI rank list and grouped into most-DILI-concern and less-DILI-concern based on their known ability to induce DILI in humans. In order to select treatment concentrations which provoke a cellular response but maintain the viability predominantly, the *half-maximal effective concentration* (EC_{50}) was investigated using different concentrations (Table 17). Afterwards, cells were treated with most- and less-DILI-concern compounds (Section 1.6) (Table 18). BOS served as positive control and MET as negative control. All compounds, except of MET, were dissolved and diluted 200-fold in DMSO to the final treatment concentrations. MET was dissolved 200-fold in medium. The stock concentrations were diluted with medium to 1-fold for the 2.5D model and 2-fold for the 3D model to achieve a final DMSO concentration of 0.5 %. Higher concentration of DMSO is known to have a negative impact on the cellular function. DMSO of 0.5 % served as vehicle control. Dilutions were done within a deep well plate. At day 0, the depleted medium of the 2.5D model was aspirated completely and replaced with 100 µL of medium with the 1-fold concentration of compound (Figure 11).

To treat the 3D spheroids, 50 µL of the depleted medium were aspirated and replaced with 50 µL of fresh medium supplemented with a 2-fold concentration of the compound. Together with the 50 µL of remaining medium, a 1-fold concentration was created. For all subsequent treatments, 50 µL were replaced with a 1-fold medium concentration to maintain the target concentration.

Table 17: Compounds and examined dose ranges used to study the EC_{50} value.
14 compounds were selected for the evaluation of EC_{50} values in the 2.5D and 3D model.

Compound	Tested concentrations [µM]	Solvent
APAP	10 - 5000	DMSO
AMI	1 - 300	DMSO
BOS	30	DMSO
DAB	1 - 300	DMSO
DIC	1 - 300	DMSO
ENT	1 - 300	DMSO
FIA	1 - 300	DMSO
LVX	1 - 300	DMSO
MET	750	Medium
PIO	1 - 300	DMSO
TOL	1 - 300	DMSO
TRO	1 - 300	DMSO
TVX	1 - 300	DMSO
XIM	1 - 300	DMSO

Table 18: Final concentrations of most-DILI-concern and less-DILI-concern test compounds.
Compounds were selected for treatment of the advanced 2.5D and 3D model. Substances marked with (*) are less-DILI-concern (non-DILI) drugs.

	Final concentration per well [µM]		
	Low dose	Mid dose	High dose
MET*	750	750	750
BOS	30	30	30
XIM	10	100	200
DAB*	10	100	200
TRO	10	100	200
PIO*	10	100	200
TOL	10	100	200
ENT*	10	100	200
DIC	10	100	200
FIA	10	100	200
APAP	100	2500	5000
AMI	100	100	100

Cells were treated every 2 - 3 days for 14 days. Medium samples and cell lysate was collected during the treatment period, to measure different endpoints described in Section 3.4-3.9.

3.2 Thawing and cultivation of iPSCs

IPSCs can differentiate into other cell types, including the different liver cells. They have been used to study diseases *in vitro* and develop new drugs [31]. The ability of organoids to self-renewal and self-organization, can provide an unlimited and accurate tool for clinical and basic research [31][241]. Liver organoid differentiation was performed as a side project. Therefore, results are N=1. In this work, liver organoids were differentiated from iPSCs using three different methods (Figure 12) described in the following.

The cell line Cellartis® human ChiPSC18 (Y00300, LOT AK20001S, Takara) and the DEF CS 500 culture system (Y30017, Takara) were used. The COAT-1 solution was diluted 1:20 in $PBS^{+/+}$ and a T12.5 culture flask was coated for 30 min at 37 °C with 0.1 ml/cm^2 of coating solution. In the meantime, the DEF CS 500 thawing medium was supplemented with DEF CS GF-1 1:333, DEF CS GF-2 1:1000 and DEF GF-3 1:1000. The cryopreserved iPSCs were thawed in a 37 °C water bath and transferred into a falcon with 4 mL of thawing medium (RT). The vial was rinsed with 1 mL of medium. After centrifugation (1 min, 300 xg, RT), the supernatant was discarded, the cells were resuspended in 3 ml thawing medium and transferred into the coated T12.5 flask.

The next day, the confluency of the cells was controlled under the microscope and the medium was changed daily with DEF CS 500 culture medium supplemented with DEF CS GF-1 1:333 and DEF CS FG-2 1:1000.

3.2.1 Passaging of iPSCs

For passaging of iPSCs, the gentle dissociation reagent TrypLE Express (Gibco, 12605-010) was used. To detach the cells, the medium was removed, cells were washed once with $PBS^{-/-}$ and incubated with 20 µL/cm^2 TrypLE Express (37 °C, 5 min). After incubation, the cells were resuspended in 30 mL of thawing medium and counted as described in Section 3.1.3. 50.000 cells /cm^2 were seeded into a new, fresh coated flask. The following days, the medium was changed daily using culture medium until the confluency of circa 90 % was achieved again.

3.2.2 Cryopreservation

For cryopreservation, cells were detached and counted as described before. After centrifugation (5 min, 200 xg, RT), iPSCs were diluted to $1.5x10^6$ cells/mL with DEF CS 500 cryopreserving medium, supplemented with 10 % DMSO and 20 % FBS. 1 mL of the cell suspension was transferred into a cryovial. Cells were frozen overnight at -80 °C using a Mr. Frosty™ freezing container (Thermo Fisher) following the manufacturer's usage instructions. After 24 h, the cryovials were transferred into liquid nitrogen storage.

3.2.3 Generation of iPSC derived liver organoids

To differentiate iPSCs into liver organoids, three different methods were tested based on already published protocols [31][296]–[299]. As shown in Figure 12, the chosen methods differ in the time of pre-cultivation and the shape in which the cells were embedded into the Matrigel® (GFR) dome. In method 1 (25 days) and 2 (20 days), single iPSCs were seeded into the Matrigel® (GFR) dome. Using the method 3 (29 days), embryoid bodies were formed before embedding. Medium and lysate samples were taken at day 0, 5, 10, 15, and 20 to track the changes in gene expression (Section 3.4) and secretion (Section 3.8). The viability of the cells was monitored 24 h after the addition of a new differentiation medium to make sure they tolerate it well. Therefore, the Resazurin assay was used (Section 3.8.4).

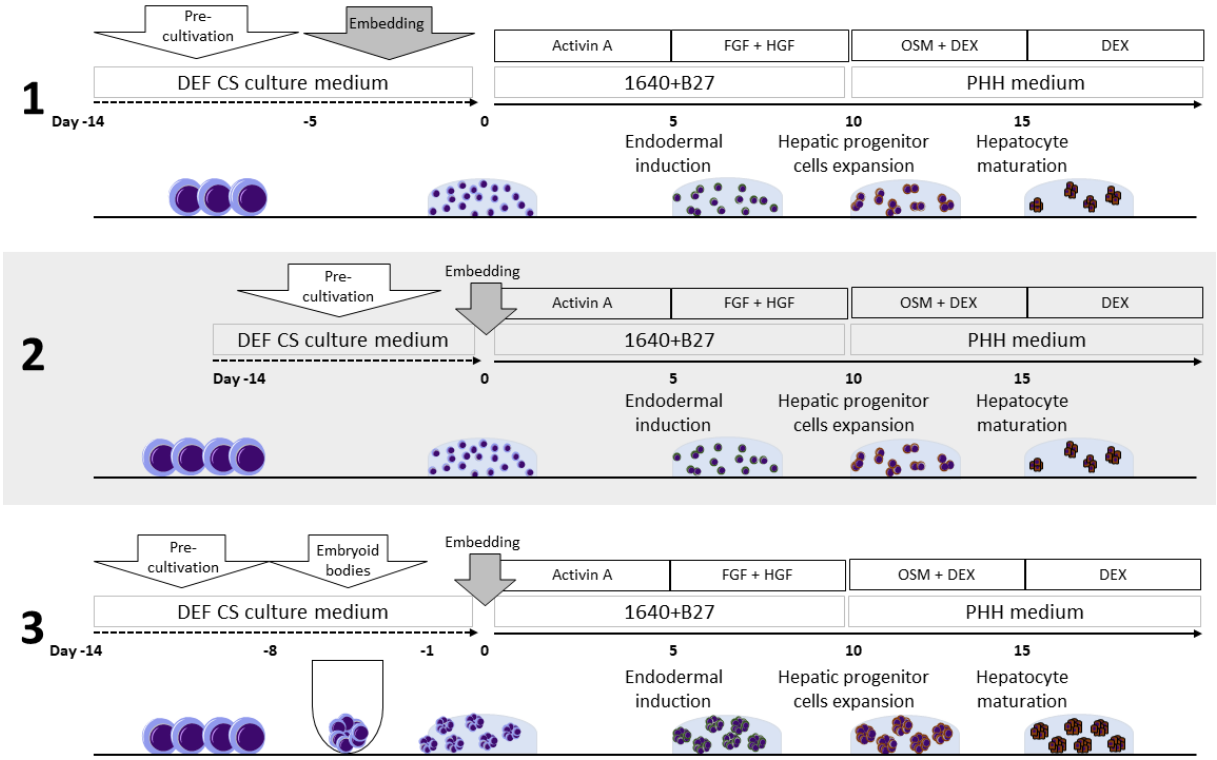

Figure 12: Schematic overview of the differentiation methods.
Panel 1 shows the overview of the first differentiation method. IPSCs were embedded into a Matrigel dome as single cells and pre-cultivated for 5 days before the differentiation started. Panel 2 shows the overview of the second method, where iPSCs were also embedded as single cells into the Matrigel dome, but the differentiation started direct after embedding. Panel 3 described the third method, where iPSCs were seeded into a U-bottom plate to form embryoid bodies over several days. This embryoid bodies were embedded into Matrigel®. Afterwards the differentiation protocol was started.

To embed the single iPSCs into a Matrigel® (GFR) dome, the cells first were detached from the culture flask and counted as described before. Moreover, Matrigel® was thawed on ice. To achieve 5.000, 10.000, and 15.000 iPSCs per Matrigel dome, 80.000, 160.000, and 240.000 cells were transferred into a separate tube and centrifuged (1 min, 300 xg, RT). After centrifugation, the supernatant was discarded, and the cells were resuspended with ice-cold tips in 400 µL cold Matrigel® on ice. Small droplets of 25 µL were pipetted into the middle of a 24 well

plate. The plate was incubated for 10 min at 37 °C to make the Matrigel® solid. Subsequently, 700 µL medium were added to the domes. In method 1 DEF CS culture medium and in method 2 700 µL of differentiation medium I (Table 19) were added to the domes. After 5 days of pre-cultivation, the medium of the iPSCs described in the first panel (Figure 12) was also replaced with differentiation medium I.

Table 19: Composition of the differentiation medium I.
This medium was generated to achieve endodermal induction.

Differentiation medium I	Volume [ml]
RPMI 1640 medium (21875034, Gibco™)	23.5
B27 50x, serum-free (17504044, Gibco™)	0.5
Penicillin/Streptomycin 100 U, 100 µg/ml	0.25
GlutaMAX (350500-61, Gibco™)	0.25
Knockout™ SR (10828010, Gibco™)	0.25
Activin A 10 µg/mL	0.25

To conduct method 3, cells were detached from the flask surface and counted as described before. Afterward, four different concentrations of iPSCs (500, 1.000, 1.500 and 2.000 cells/well) were seeded in DEF CS culture medium into an ULA U-bottom plate (BIOFLOAT™, FaCelliate). The formation of embryoid bodies was observed daily. Every second day, 50 µL of the depleted medium was discarded and replaced very gently with 50 µL of fresh DEF CS culture medium, not to disturb the aggregation process. When embryoid bodies were formed, eight wells were pooled into a separate tube. After embryoid bodies settled down, the supernatant was discarded, and the cells were resuspended with cold pipette tips in 200 µL ice-cold Matrigel®. Next, small droplets of 25 µL were pipetted into the middle of a 24 well plate. The plate was incubated for 10 min at 37 °C to make the Matrigel® solid. Thereupon, 700 µL of the differentiation medium I was added to the domes (Table 19).

The differentiation medium I was changes daily for 5 days to achieve endodermal induction [31][295]. After 5 days, the next differentiation step was performed by replacing the differentiation medium I with the differentiation medium II (Table 20). Again, the medium was changes daily for 5 days.

The incubation with medium supplemented with *fibroblast growth factor* (FGF) and *basic human growth factor* (bHGF) (Table 20) achieve hepatic progenitor cell differentiation [31]. After 5 days, the differentiation medium III (Table 21), supplemented with *Oncostatin M* (OSM) was added to the cells for another 5 days with daily medium exchange. OSM induced the expression of hepatic differentiation and mature markers [353].

Table 20: Composition of the differentiation medium II.
This medium was generated to induce hepatic progenitor differentiation.

Differentiation medium II	Volume [ml]
RPMI 1640 medium (21875034, Gibco™)	30.3936
B27 50x, serum-free (17504044, Gibco™)	0.64
Penicillin/Streptomycin 100 U, 100 µg/ml	0.32
GlutaMAX (350500-61, Gibco™)	0.32
Knockout™ SR (10828010, Gibco™)	0.32
FGF 100 µg/mL (100-18B, Peprotech)	0.032
HGF 100 µg/mL (100-39, Peprotech)	0.032

Table 21: Composition of the differentiation medium III.
This medium was generated to promote further hepatic differentiation and maturation.

Differentiation medium III	Volume [ml]
William's Medium E (W4128, Sigma)	18.41
FBS	0.93
Penicillin/Streptomycin 100 U, 100 µg/ml	0.2
GlutaMAX (350500-61, Gibco™)	0.2
ITS+ premix (354352, Corning®)	0.2
Ascorbic Acid 50 mg/mL	0.02
DEX 1 mM	0.02
Oncostatin M 10 µg/mL (StemCell)	0.02

In the last step of the differentiation protocol, cells were incubated for 5 days with coculture medium (Table 13) supplemented with *dexamethasone* (DEX) which promote further differentiation and maturation of the hepatic cells [295].

3.2.4 Passaging of liver organoids

The confluence during the differentiation process and of the liver organoids were controlled daily under the microscope. To passage the cells, the medium was aspirated and the Matrigel® dome was dissolved by pipetting up and down with 500 µL of ice-cold $PBS^{-/-}$. The suspension was then transferred into a 15 mL falcon and centrifuged (3 min, 100 xg, 4 °C). After centrifugation, the cell pellet was controlled. If a second phase of cloudy Matrigel® was still visible, the supernatant was aspirated to the cloudy phase. The ECM was dissolved again by pipetting up and down with 5 mL of ice-cold $PBS^{-/-}$. Afterwards, the cells were centrifuged as described before. The process was repeated until the cloudy phase was gone. In later differentiation phases, the organoids were dissociated by treatment with 1 mL of TrypLE Select and ROCKi (1x) for 5 min in a 37 °C water bath. Every 1 - 2 minutes the falcon was taken under the sterile bench and the cells were dissociated by pipetting up and down 5-10 times. Subsequently, the

dissociation process was stopped by adding medium and the cell number was determined as described in Section 3.1.3. In earlier differentiation states, the cells could be counted right after the centrifugation. Approximately 1.000 cells were seeded into a new Matrigel® dome as described before.

3.2.5 Cells lysis for genetic analysis

To monitor the changes in gene expression, the cells were lysed after each differentiation step. Therefore, cells were detached from the ECM, centrifuged, and counted as described before. 1 µL of *working lysis mixture* (WLM) described in Section 3.4 was added per 400 cells. Cells in WLM were incubated for 30 min at 55 °C and stored at -80 °C.

3.2.6 Treatment of liver organoids

To determine the metabolic activity and the response of the liver organoids to different compounds, the differentiated organoids were treated with test substance listed in Table 22 for 72 h. For that, cells were detached, counted, and seeded in the same density in a Matrigel® dome in a 24 well plate. The treatment was performed by diluting the prepared 200-fold stock solutions with medium as described in Section 3.1.5. After the treatment, medium and cell lysate samples were collected and analyzed using the methods described in Sections 3.4-3.9.

Table 22: Final concentrations of CYP-inducing compounds.
Compounds were selected for the treatment of the generated liver organoids to determine the metabolic activity.

	Final concentration per well [µM]	Determined function
MET*	750	Negative control
BOS	30	CYP3A4 and 2C9 induction [354]
RIF	25	CYP3A4 induction [355]
APAP	100	CYP1A2 and 2E1 induction [356]

3.2.7 Cryopreservation of liver organoids

Cell in all differentiation stages were partly cryopreserved in liquid nitrogen for long-term storage. Therefore, they were removed from the Matrigel® dome and counted as described before. Cells were diluted to $1x10^6$ cells/mL with medium, supplemented with 10 % DMSO and 20 % FBS. 1 mL of the cell suspension was transferred into a cryovial. Cells were frozen overnight at -80 °C by using a Mr. Frosty™ freezing container (Thermo Fisher) and following the manufacturer's usage instructions. After 24 h, the cryovials were transferred into liquid nitrogen storage.

3.2.8 Thawing of liver organoids

Cells were thawing quickly from liquid nitrogen in a 37 °C water bath. The suspension was transferred into a 15 mL falcon supplemented with 4 mL of the appropriate medium, depending on the status of the cells at the time of freezing. The medium was previously supplemented with ROCKi (1x) to avoid dedifferentiation processes. The falcon was centrifuged (3 min, 100 xg) and cell pellet was resuspended in ice-cold Matrigel®. Subsequently, a dome of 25 µL was placed into the middle of a 24 well plate and incubated for 10 min at 37 °C to become solid. The cells were incubated in medium supplemented with ROCKi (1x) for 24 h. Afterwards, ROCKi was omitted.

3.3 Microphysiological system

To compare the advanced 2.5D and 3D models with a MPS, the Emulate liver chip was established and tested. Emulate Inc generated one of the first organ-chips commercially available. It consists of a clear, flexible PDMS polymer with two internal channels, separated by a porous membrane (Section 1.5.5).

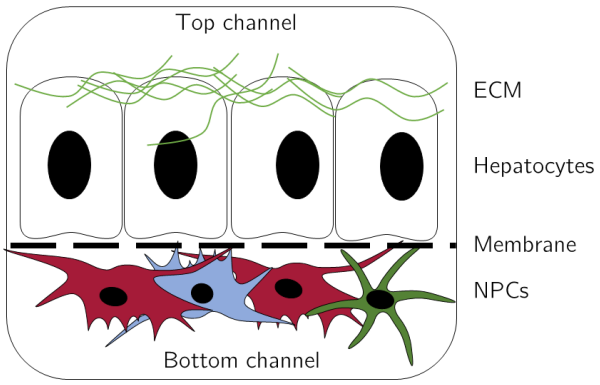

Figure 13: Schematic cross section of the liver chip.
Top and bottom channels are separated by a porous membrane. PHHs are growing in the top chancel, overlayed with an ECM. NPCs, such as KCs, SCs, and LSECs were seeded into the bottom channel.

As depicted in Figure 13, the separated channels within the chip allow the cultivation of two or more different cell types with its specific culture medium. PHHs can be seeded in the top channel and NPCs in the bottom channel. It is described that they can communicate via the pores in the membrane, but do not have direct cell contact. The chip is positioned in a chip charier, which can be clipped into the POD (Figure 14). The POD can then be positioned on a Tray to insert the chips into the Zoe culture module. Using the Zoe, a specific flow rate can be adjusted for each channel. As recommended by Emulate, the liver cells were incubated with a flow rate of 30 µL/h [357].

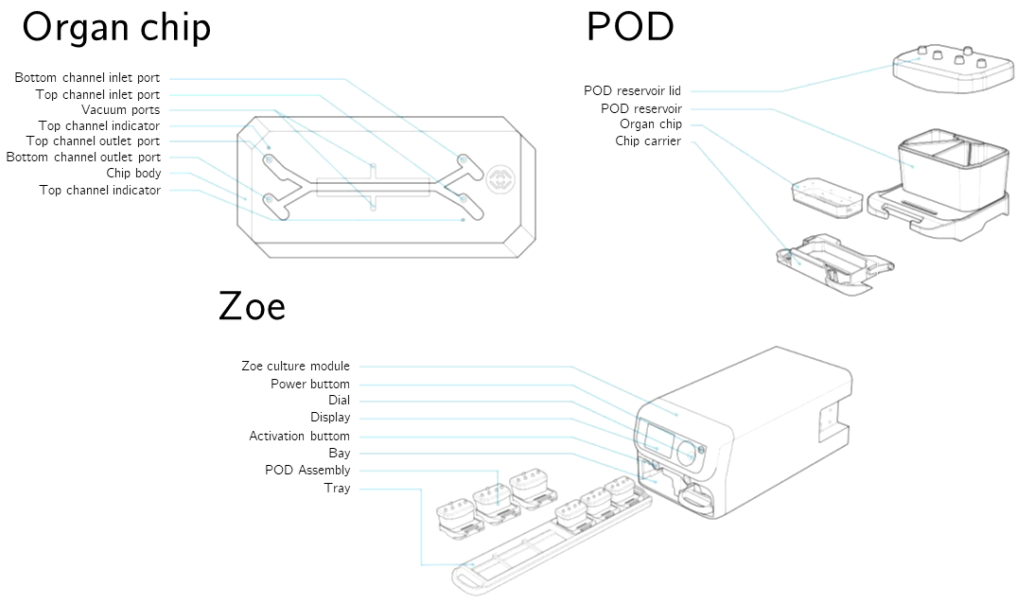

Figure 14: Components of the Emulate organ chip system.
[358] Components of the system include the organ chip, the POD, and the ZOE culture module.

3.3.1 Activation and coating of the liver chip

On the day of activation, LSECs were thawed and pre-cultivated (Section 3.1.1).

For the activation of the organ chips, the chemicals ER-1 and ER-2 were equilibrated to RT and ER-2 was dissolved stepwise with ER-1 according to the protocol. The prepared activation solution was pipetted into both channels and activated for 20 min under UV light. Afterwards, the activation solution was aspirated, the channels were washed once with 200 µL of ER-2 following by 200 µL of sterile cold $PBS^{-/-}$.

Next, the ECM coating solution was prepared composed of collagen I (final concentration 100 µg/mL) and fibronectin (final concentration 25 µg/mL) in $PBS^{-/-}$. The PBS inside the channels was aspirated and 100 µL of ECM solution was pipetted into both channels. Chips were incubated overnight at 4 °C and for 1 h at 37 °C the following day. [357]

3.3.2 Thawing and seeding of primary human hepatocytes

Complete hepatocyte seeding medium was prepared according the to Emulate protocol [357]. Cryopreserved PHHs were thawed in a 37 °C water bath and transferred into a 50 mL falcon prepared with 3 mL of warm seeding medium. The volume was brought up to 35 mL with seeding medium. 15 mL of a 90 % Percoll solution was added to the falcon. The cells were inverted carefully 2-3 times and centrifuged (96 xg, 6 min, RT). Upon, the supernatant was discarded, leaving 3-5 mL, and cells were resuspended in the remaining medium. Hereon, the medium was brought up to 50 mL again and the cells were centrifuged again (4 min, 72 xg, RT). The supernatant was aspirated, leaving 1-2 mL to resuspend the cells. The cell number

was determined according to the protocol in Section 3.1.3. [357] PHHs were diluted to a final concentration of $3.5x10^6$ cells/mL. The channels were washed once with seeding medium and 35 µL of cell suspension was quickly pipetted into the top channel. 3 h post seeding, a gravity wash was performed by dropping 200 µL of fresh medium on the top inlet which cause a flow through the channel. The outlet medium was aspirated, and the chips were cultivated overnight at 37 °C. [357]

The next day, PHHs were overlayed with a Matrigel®-medium solution. Therefore, maintenance hepatocyte medium was prepared according to the Emulate protocol. Matrigel® (354235, Corning ®) was diluted to 0.25 mg/mL in ice-cold maintenance medium. The cells were washed once with 200 µL of warm maintenance medium to remove cell debris. After, 200 µL of ice-cold Matrigel®-medium solution was pipetted in the top channel. Cells were incubated overnight at 37 °C. [357]

3.3.3 Thawing, detachment, and seeding of non-parenchymal cells

On the fourth day, the NPCs were seeded into the bottom channel. The NPC seeding medium was prepared according to the manufacturers protocol. [357]

First, LSECs were detached from the T75 flask by washing the layer once with 10 mL of PBS $^{-/-}$ and treatment with 3 mL of Trypsin/EDTA 0.05 % (3 min, 37 °C). The Trypsin/EDTA reaction was stopped by adding 4-fold NPC medium. The cells were transferred to a 15 mL falcon and centrifuged (5 min, 200 xg, RT). The supernatant was discarded, the cell number was determined as described in Section 3.1.3, and cells were diluted to a final concentration of $9x10^6$ cells/mL. The LSEC-suspension was kept on ice until the rest of the cells were ready.

Second, cryopreserved SCs were thawed in a 37 °C water bath and transferred into a 15 mL falcon prepared with 1 mL of warm NPC medium. The volume was brought up to 15 mL with ice-cold NPC medium and cells were centrifuged (5 min, 250 xg, RT). After centrifugation, the supernatant was discarded, and cells were counted (Section 3.1.3). The cell number was diluted to $0.3x10^6$ cells/mL in ice-cold NPC medium. Cells were kept on ice until seeding.

Third, cryopreserved KCs were thawed in a 37 °C water bath and transferred into a 15 mL falcon prepared with 1 mL of cold NPC medium. The volume was brought up to 15 mL with ice-cold NPC medium and cells were centrifuged (5 min, 500 xg, 4 °C). After centrifugation, the supernatant was discarded, and cells were counted (Section 3.1.3). The cell number was diluted to $1.5x10^6$ cells/mL in ice-cold NPC medium.

Before seeding, LSECs, KCs, and SCs were mixed in a ratio 1:1:1 to final density of $3x10^6$ LSECs/mL, $0.1x10^6$ SCs/mL, and $0.5x10^6$ KCs/mL. 15 µL of the mixed cell suspension was pipetted into the bottom channel. Directly after seeding, the chip was turned upside down on a chip carrier so that the cells adhere to the membrane. 4 h post seeding, cells were washed

once with maintenance medium in the top channel and NPC maintenance medium in the bottom channel. Chips were incubated overnight at 37 °C with filtered tips inserted in the inlet and outlet ports to avoid mixing of the different media.

3.3.4 Connecting of the chip to POD and ZOE

The next day, maintenance PHH medium (Table 14) and maintenance NPC medium (Table 16) was prepared according to the Emulate protocol [357]. The medium was warmed up and equilibrated 5 min using a Steriflip-connected tube and a vacuum source with at least -70 kPa. 3 mL of maintenance medium was added to each inlet reservoir and 300 µL to each outlet reservoir. Using the “Prime” program on the Zoe culture module, a small drop of medium is pressed through the channels to the bottom of the POD – four small droplets can be observed. Small droplets of the appropriate medium were also placed on the inlet and outlet ports of the chips. The chip and the POD can then be clipped together. Using the “Regulate” program, the cultivation of the chips with the specific flow rate of 30 µL/h was started.

3.3.5 Experimental schedule of the liver chip

As depicted in Figure 15, Medium was changed every 2-3 days completely in all reservoirs. Medium samples were collected at days 0, 2, 7, and 14. The cells were lysed after the treatment period at day 14.

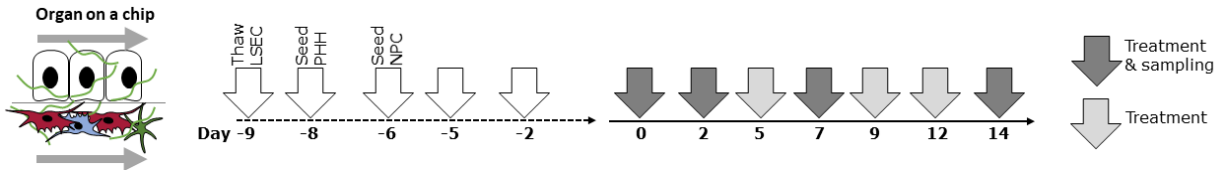

Figure 15: Experimental timeline for the Emulate liver chip.
Timeline includes cell culture preparation, treatment, and sampling time points.

For the first media exchange, the chip and the POD were put out of the Zoe. The lid of the POD was opened, and the medium was aspirated from each reservoir. 3 mL of fresh, equilibrated medium were pipetted into the inlet reservoirs. After 5 days of pre-cultivation, the chips were ready for experimental testing. As described in Section 3.1.5, compounds listed in Table 25 were dissolved 200-fold in DMSO to the final treatment concentrations. MET was dissolved 200-fold in medium. In contrast to the advanced 2.5D and 3D treatment, compounds such as DAB, TRO, and PIO need to be excluded from the experiment. The reason for this is, that the chip is composed of PDMS. This polymer is known to have high absorption capacity for small molecules, such as drugs, which impacts the bioavailability. The molecular weight and the hydrophobicity of a compound determined the absorption by PDMS [307]. Therefore, all substance were tested before using the *compound distribution kit* (CDK) of Emulate (Section 3.3.6). All compounds listed in Table 25 show moderate or no absorption and thus could be

used for the experiments. The stock concentrations were diluted to 1-fold in the submitted medium in the top channel reservoir by adding 15 µL. Every 2-3 day the medium was changed, and fresh compound was added.

Table 23: Final concentrations of DILI and no DILI test compounds.
Compounds were selected for treatment of the liver chip. Substances marked with (*) are no DILI risk compounds.

Compound	Final concentration per well [µM]
MET*	250
BOS	30
XIM	100
TVX	10
LVX	100
TOL	80
ENT*	80
DIC	100
FIA	300
APAP	2500
AMIO	80

3.3.6 Compound distribution kit

To determine the absorptive character of a compound, the CDK of Emulate was used. Empty chips, without cells, were prepared. Hepatocyte maintenance medium and NPC medium were equilibrated and 100 µL were pipetted into each reservoir of the POD and each channel of the chip. As described before, the PODs were “Primed”, and one drop of medium was pipetted on the inlet and outlet ports. Upon, the chip and the POD were clipped together to achieve a connection. Table 24 listed the tested compounds. All other substances, described in Section 3.3.5, that are not tested in the kit, have already been successfully tested by Emulate.

For each POD, 3 mL of hepatocyte maintenance and NPC medium were supplemented with the listed compounds. The inlet ports of the PODs were aspirated completely, and 3 mL of the medium/compound solution was pipetted into the inlet ports. The chip was cultivated for 5 min, 37 °C and 500 µL/h to flood the channels with the substance. Subsequently, the medium of the outlet reservoir was aspirated completely. Afterwards, the chips were cultivated for 72 h without medium change at 30 µL/h, 37 °C. Every day, medium samples were taken from the top and bottom channel outlet reservoirs and stored at -80 °C. The concentration of the compound in the inlet reservoirs at day 0 and in untreated chip serve as reference controls. The media samples were diluted 1:10, 1:100, and 1:1000 and analyzed using *liquid chromatography–mass spectrometry* (LC-MS) by Anindya Siddharta.

Table 24: List of compounds and concentrations tested in the CDK.
The samples were diluted 1:10, 1:100, and 1:1000 for LC-MS analysis.

	Final concentration per well [µM]	Dilutions prepared for LC-MS				Timepoints [h]
XIM	20	undiluted	1:10	1:100	1:1000	0 24 48 72
DAB	40					
TOL	20					
ENT*	40					
TRO	3					
PIO	20					
MET	250					
BOS	30					

3.4 Gene expression assay: QuantiGene™ Plex Assay

Using the QuantiGene™ Plex Assay multiple RNA targets in one sample can be quantified simultaneously. The method is based on two different approaches, namely the *branched DNA* (bDNA) signal amplification and the multi-analyte profiling beads ® technology. In contrast to target amplification methods like *quantitative polymerase chain reaction* (qPCR), the bDNA assay directly measures nucleic acid molecules and amplifies the reporter signal. [359] This signal amplification uses labeled DNA probes hybridized to RNA of interest via extenders. One of these extenders is a so-called *capture extender* (CE). This distinguishes between the different capture beads and hybridizes with a specific target RNA (Figure 17). This differentiation of different capture beads enables multiplexing with the multi-analyte profiling ® technology. For bead identification, each capture bead has its own specific dye concentration detected by the Luminex™ FLEXMAP 3D™ instrument. The Luminex™ FLEXMAP 3D™ system is based on a flow cytometer. Each bead passes through two lasers measuring the specific bead signal and the amplified reporter signal resulting in a fluorescence signal, associated with each capture bead. A 532 nm green laser excites the probe bound to SAPE. The 635 nm red laser excites the dyes inside the beads and is also used to measure the light scatter for doublet discrimination (Figure 16). [360] This signal is than reported as the *median fluorescence intensity* (MFI) which is proportional to the number of target RNA molecules in the sample [361].

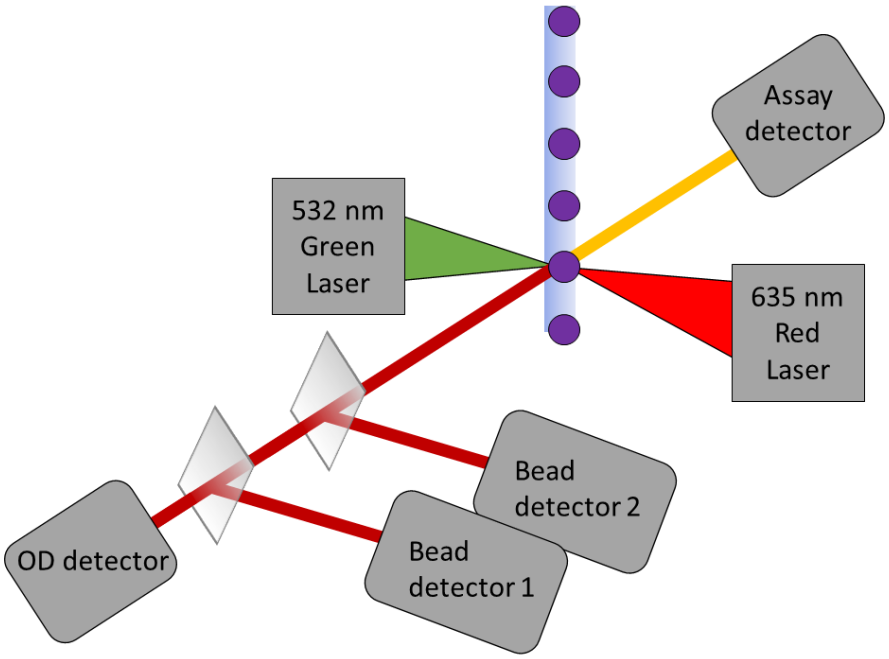

Figure 16: Principal of bead detection in a Luminex™ instrument.
The detection method is based on flow cytometry. Each bead in discriminated by its specific fluorescence signal by the red laser. The green laser excites SAPE, bound to every sample via extenders. [360]

To analyze and compare the gene expression in all culture models, cell specific markers, metabolizing enzymes and potential DILI markers were measured using the QuantiGene™ Plex Assay (ThermoFisher Scientific).

As depicted in Figure 17 and mentioned before, the assay is based on hybridization of a target sequence to magnetic beads and signal amplification by bDNA technology. In this work, B2M, EIF4F, PPIB, PPIA, and POLR2A serve as housekeepers. These housekeepers were previously selected in a separate experiment to be suitable for the present samples.

Before lysing of the cells, the lysis mixture was pre-warmed for 30 min at 37 °C to dissolve possible precipitated salts. Cells in the 2.5D culture system were lysed by aspirating the medium and adding 1 µL of WLM per 400 cells per well, which composed of one-part lysis mixture, two parts culture medium, and 10 µl Proteinase K per mL of WLM. For the 3D model, 16-24 spheroids were pooled into a 1.5 mL tube. The supernatant was discarded, and cells were lysed with 1 µL per 400 cells per tube with the WLM. For the OOC, the depleted medium was aspirated from the channels. The cells were lysed with 1 µL per 400 cells WLM with inserted pipette tips in each inlet and outlet port. Samples were lysed by pipetting 15-20 x up and down and incubation for 30 h at 55 °C. Lysates were transferred into a 96 well plate and stored at -80 °C until further use.

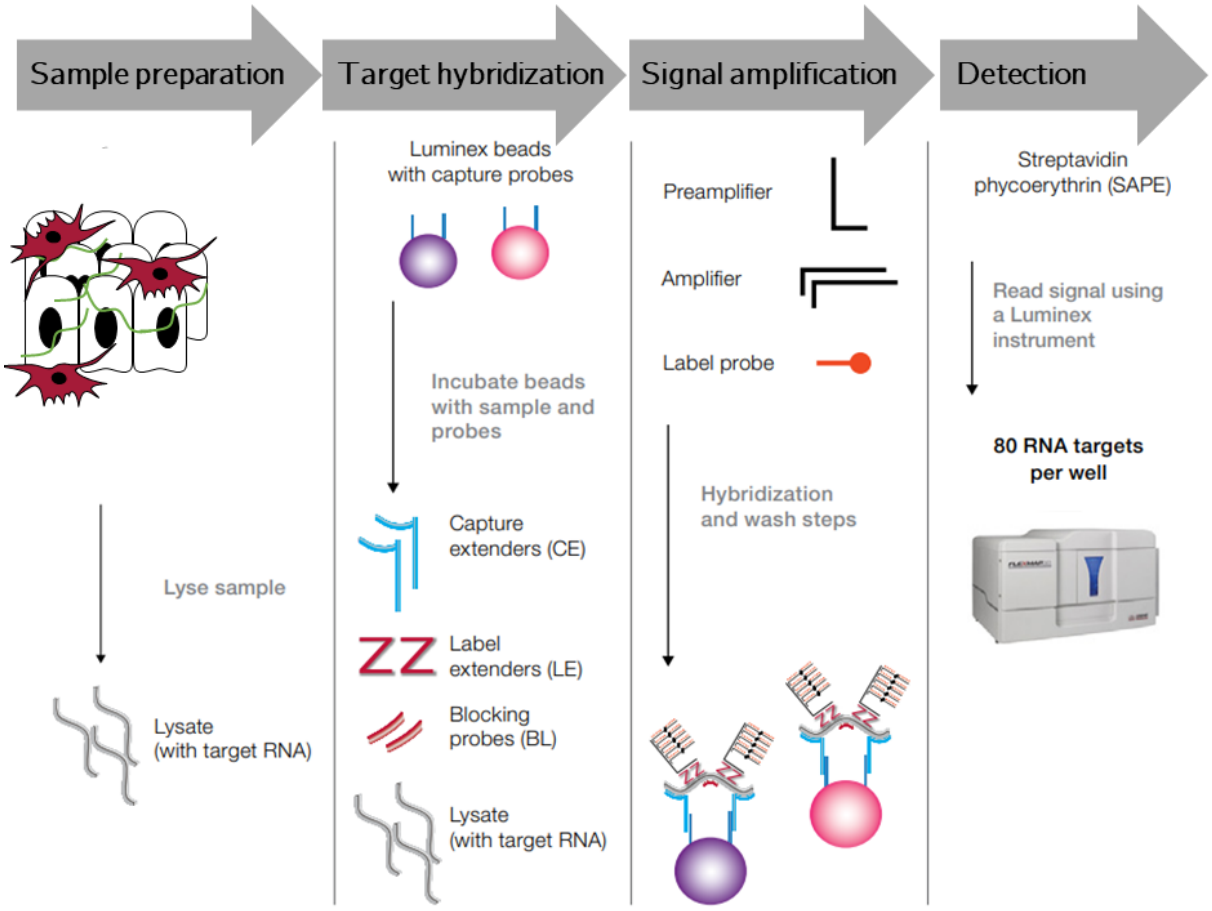

Figure 17: Procedure of QuantiGene™ Plex Gene Expression Assay.
This assay is divided into four stages: Sample preparation, target hybridization, signal amplification, and detection. First, the sample is lysed, and the target sequence is hybridized to the bead-bound CE. Second, the signal amplification tree is built in successive hybridization steps. Finally, SAPE is used as a fluorescence-based indicator for signal generation allowing the quantification of the target RNA present in the sample. [362]

3.4.1 Hybridization

Samples were thawed at RT following by 30 min incubation at 37 °C. The lysis mixture was pre-warmed for 30 min at 37 °C. The Probe Set was thawed at 4 °C. For hybridization of the target RNA to the capture beads, two working plex sets, one for the samples and one for the total liver RNA control, were prepared as shown in Table 25.

The right sample dilutions were examined for each separate plex panel in a preliminary test with four different concentrations. Accordingly, samples were diluted with the diluted lysis mixture (1:1 with RNase free water). The total liver RNA serves as assay control and was diluted to 50 ng per well.

The hybridization was performed in a hybridization plate. 80 µL of the Working plex set total liver was pipetted to the 20 µL diluted total liver RNA. Conversely, 20 µL of the Working plex set samples was pipetted to the 80 µL of diluted samples or 80 µL of nuclease free water as blank control. The plate was sealed with a pressure seal and incubated for 18-22 h at 54 ± 1

°C at 600 rpm. The temperature was monitored twice with a separate thermometer, as the success of the assay is very temperature sensitive.

Table 25: Pipetting scheme for the working plex sets.
The volumes of the working plex set were abstracted from the QuantiGene™ Plex protocol.

Reagent	Working Plex Set sample	Working Plex Set total liver control
	Volume/well [µL]	Volume/well [µL]
Nuclease free water	4.2	387.7
Lysis mixture	6.6	33.3
Blocking reagent	2.0	2.0
Proteinase K	0.2	-
Capture beads	1.0	1.0
Probe set	6.0	5.0

3.4.2 Signal amplification

The next day wash buffer was prepared by combining 189 mL nuclease free water with 10 mL of wash buffer component 2 and 0.6 mL of wash buffer component 1. After incubation, the hybridization plate was centrifuged for 3 min at RT, and 240 xg. Samples were pipetted up and down several times and transferred to the magnetic bead plate. The plate was placed into a hand-held magnetic 96 well separator and a minute was spent waiting for all beady to be magnetically attracted. The supernatant of each well was decanted and tap gently against clean paper towels to remove excess liquid. The plate was removed from the separator and 100 µL of wash buffer were added per well. Next, the plate was placed into the separator again and the steps described above were repeated two times. Afterwards, 100 µL/well of pre-amplifier mix were added, the plate was sealed with an adhesive foil and shaken for 1 min at 800 rpm to resuspend beads. The plate was incubated for 1 h at 50 ± 1 °C and 600 rpm. After incubation, the plate was washed again three times as described above. Hereafter, 100 µL/well of amplifier were added, the plate was sealed with an adhesive foil, and shaken for 1 min at 800 rpm to resuspend beads. Subsequently, the plate was incubated for 1 h at 50 ± 1 °C and 600 rpm following by 3 washing steps described before. Thereupon, 100 µL/well of label probe mix were added, the plate was sealed with an adhesive foil and shook for 1 min at 800 rpm to resuspend beads. The plate was incubated on a shaking incubator for 1 h at 50 ± 1 °C and 600 rpm and washed again as described above. 15 mL SAPE diluent and 36 µL SAPE were mixed and 100 µL/well of this SAPE mix were added to each well. The plate was sealed with a foil and shook for 1 min at 800 rpm to resuspend the beads and afterwards incubated at RT and 600 rpm for 30 min. After incubation, the beads were washed again as described above but with SAPE wash buffer. Finally, 130 µL/well SAPE wash buffer were added to each well,

the plate was shaken for 5 min at 800 rpm and measured with a the Luminex™ FLEXMAP 3D™ instrument.

3.4.3 Data analysis

The Luminex™ FLEXMAP 3D™ instrument was used to measure the fluorescence produced by SAPE. The fluorescence signal was measured, and the MFI was calculated by the xPonent software and used for further analysis. The online Dashboard of Thermo Fisher calculated the average gene expression of the sample corrected against the blank and normalized to the housekeepers. Statistical analysis between DILI- and non-DILI treated cells was performed by Julian Kreis using the software R statistic.

3.5 Mir122 expression assay: QuantiGene® 2.0 miRNA Assay

Similar to the QuantiGene™ Plex Assay (Section 3.4), the miRNA assay is a hybridization-based method. The cells were lysed as described in Section 3.4 (400 cells/µl of WLM) and the lysate could either be examined directly or stored temporarily at -80 °C. Samples were diluted in sample diluent (2:1 nuclease-free water and lysis mixture) according to the results of a preliminary concentration finding experiment using this assay.

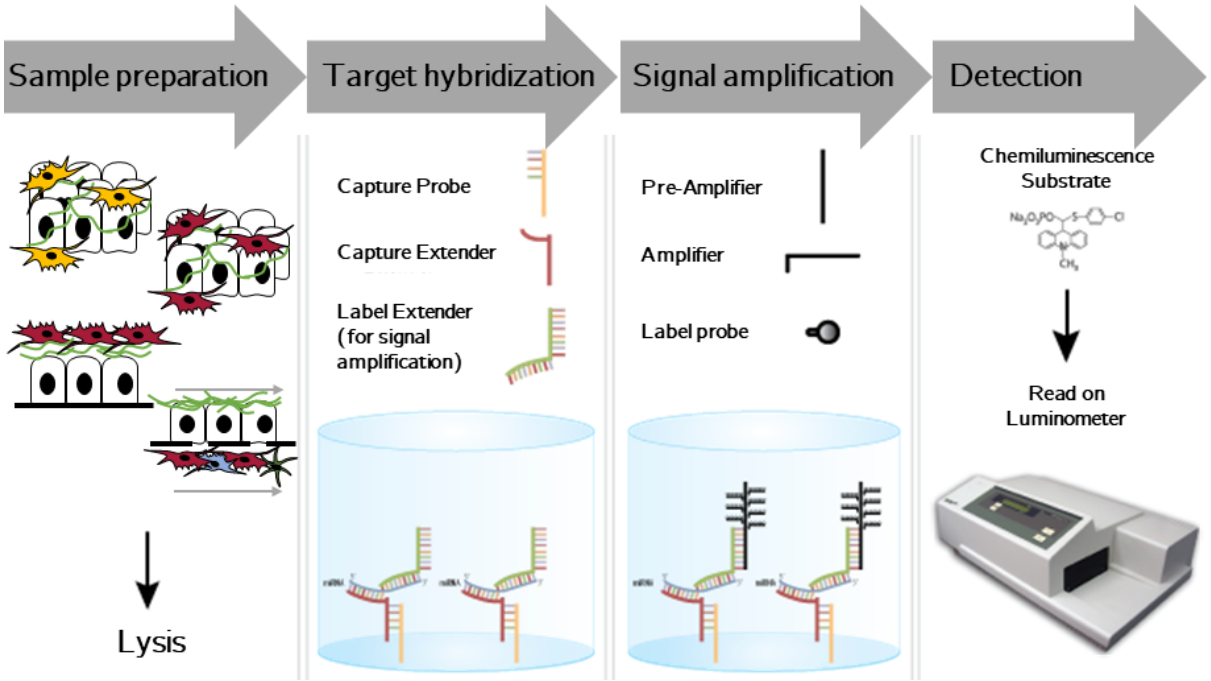

Figure 18: Procedure of QuantiGene® 2.0 miRNA Assay.
This assay is divided into four stages: Sample preparation, target hybridization, signal amplification, and detection. First, the sample is lysed, and the target sequence is hybridized to the plate-bound capture probe, *capture extender* (CE), and *label extender* (LE). Second, the signal amplification tree is built in successive hybridization steps. Finally, a chemiluminescence substrate is used allowing the quantification of the miRNA amount present in the sample. [363]

The probe set was prepared according to the pipetting scheme in Table 26. After the capture plate reaches RT, 20 µL of the probe set were pipetted into each well. Subsequently, 80 µL of the diluted samples were added. The plate was sealed tightly, centrifuged (240 xg, 20 sec), and incubated for 16-20 h at 46 ± 1 °C.

Table 26: Pipetting scheme for the working plex sets for the miRNA assay.
Volumes for the working plex sets were abstracted from the QuantiGene™ Plex protocol.

Reagent	Volume [µL] per well
Nuclease-free water	11.7
Lysis mixture	6.7
Blocking reagent	1
CE	0.3
LE	0.3

The next day, the plate was removed from the incubator and 200 µL of wash buffer were added per well. The wash buffer previously was prepared according to the manufacturer's protocol [363]. The capture plate was inverted over a suitable vessel, and the contents were forcibly expelled. Subsequently, the inverted plate was tapped on clean paper towels to dry. The washing step was repeated two more times using 300 µL of wash buffer followed by invert centrifugation (240 xg, 1 min) to dry the plate. Next, 100 µL of the pre-amplifier were added per well and incubated for 1 h at 46 ± 1 °C. After incubation, the washing procedure was repeated, and the samples were incubated with 100 µL amplifier for 1 h at 46 ± 1 °C. In the meantime, the label probe reagent was prepared as described in the protocol [363]. The capture plate was washed with the procedure described before and incubated for 1 h at 46 ± 1 °C with 100 µL of the label probe reagent. After an additional washing step, 100 µL of the 2.0 substrate were added per well, incubated for 5 min at RT followed by analysis using a luminometer. The intensity of the luminescence signal was either directly compared between samples in *relative luminescence units* (RLU) or as fold changes normalized to the vehicle controls after a treatment.

3.6 Proteomics analysis

In order to analyze the level of expressed proteins, a proteomics study was performed once (N=1). PHHs and LSECs were thawed as described in Section 3.1.1 and 3.1.2. Cells were counted (Section 3.1.3) and $1x10^5$ cells were transferred into a separate 1.5 mL vial. The vials were gently centrifuged for several seconds using a benchtop centrifuge. The supernatant was discarded, and the cell were flash-freezed in liquid nitrogen. Until analysis cell pellets were stored at -80 °C.

The remaining cells were seeded in 2D, 2.5D, and 3D in mono- and coculture according to Table 27. After 1-, 7-, and 14-days, cells in 2D and 2.5D were detached and transferred into a separate vial. After centrifugation and aspiration of the supernatant, cell pellets were flash-freezed in liquid nitrogen and stored at -80 °C until analysis. In 3D cultured cells, day 1 was when a round spheroid was observed under the microscope. Subsequently, cells were harvested on day 7 and 14. Therefore, 24 spheroids were pooled for each condition and stored as described before.

Table 27: Timepoints of sample collection and sample types for proteomic analysis.
Primary liver cells were thawed, seeded, and cultured in different culture formats. Media and lysate samples were collected regularly and stored at - 80 °C until analysis.

Sample type	Number of cells per well	Collection of the cell lysate sample			
LSECs from freezing vial	-	Day 0	-	-	-
PHHs from freezing vial	-		-	-	-
2D monoculture LSEC	40.000	-	Day 1	Day 7	Day 14
2D monoculture PHH	50.000	-			
2.5D coculture PHH/LSEC	50.000/10.000	-			
3D monoculture LSEC	2.000	-			
3D monoculture PHH	2.000	-			
3D coculture PHH/LSEC	1.000/1.000	-			

3.6.1 Sample preparation

Expressed proteins were analyzed using the tandem mass tag-based quantitative method. The following protocol was prepared and carried out by Thomas Wild.

The cell pellets were thawed and lysed in lysis buffer (10 µL per 10.000 cells). The lysates were incubated for 10 min on ice, followed by sonicating for 5 min in a water bath, and additional 5 min incubation on ice. After centrifugation (5 min, 16.000 xg), the supernatant was transferred into a fresh 1.5 mL tube. The samples were rebuffered into 50 mM Hepes (pH 7.81)/1M urea, using seven kilodalton Zeba spin columns (Thermo Scientific, 89882) according to the manufacturer's guidelines. Next, samples were reduced with dithiothreitol (5 mM, 55 °C, 30 min) and cooled down to RT. Subsequently, samples were alkylated with iodoacetic acid (15 mM, RT, 30 min, dark) and 0.2 *micrograms* (µg) trypsin was added per 10 µL of sample. The samples were incubated overnight at 37 °C and 700 rpm. The next day, 25 µL of each sample was transferred into a new 1.5 mL vial. For tandem mass tag-labelling, nine tandem mass tag labels (126N, 127N, 128N, 129N, 130N, 131N, 132N, 133N and 134N) of a 16plex (Thermo Scientific, A44521) were used. Of each label 0.5 mg were solved in 60 µL acetonitrile, and 10 µL of the appropriate label was added to the samples. The samples were incubated at

RT for 60 min. Afterwards, the labelling reaction was quenched by the addition of 4 µL 1M Tris. Again, samples were incubated at RT for 15 min followed by multiplexing though combining 34 µL of each appropriate sample into a new 1.5 mL vial. Subsequently, samples were dried using a SpeedVac Vacuum Concentrator and dissolved in 200 µL of 20 mM Hepes. The detergent (NP-40 present in the lysis buffer) was removed from the sample using a Detergent Removal Kit (Thermo Scientific, 87777) according to the manufacturer's guidelines. Next, samples were frozen at -20 °C overnight. The next day, 10 µL of 10 % trifluoroacetic acid and 90 µL of 0,1 % trifluoroacetic acid were added to the samples. The pH was confirmed to be < 3 using pH indicator strips. The sample was fractionated with the High pH Reversed-Phase Peptide Fractionation Kit (Thermo Scientific, 84868) according to the manufacturer's guidelines except for using the following acetonitrile concentrations for eight fractions (7,5 %, 10 %, 12.5 %, 15 %, 17.5 %, 20 %, 30 %, and 50 %). The volume of the obtained fractions was reduced to 25 µL using a SpeedVac Vacuum Concentrator. The eight fractions were transferred into HPLC vials and stored at -20 °C till analysis on the *mass spectrometer* (MS).

3.6.2 Mass spectrometry

Samples were thawed and analyzed by coupling a nanoflow liquid chromatography system to a *trapped* ion mobility spectrometry quadrupole time of flight spectrometer. From each sample 2 µL were injected for MS analysis. The peptides were separated on a reversed phase C18 column using a 100 min gradient of 2-37 % buffer (0.1 % FA in acetonitrile) at a constant flow rate of 400 nanoliters/min (column temperature, 50 °C). MS data was collected over a *mass to charge* (m/z) range of 100 to 1700.

3.7 Metabolomics analysis

A metabolomics study was performed to analyze the impact of the culture conditions to the level of intra- and extracellular metabolites. PHHs and LSECs of the same donor were used for all culture systems to avoid donor differences. The cells were thawed as described in Section 3.1.1 and 3.1.2. Cell lysate and supernatant samples were collected according to Table 28.

Table 28: Timepoints and collected samples for metabolomics analysis.
Primary liver cells were thawed and cultured long-term in four advanced cell culture models. Media samples were collected at three time points, and lysate samples at two time points.

Culture model (name)	Supernatant sample			Cell lysate sample	
2.5D coculture (2D)	Day 1	Day 3	Day 6	Day 1	Day 6
3D coculture (3D)	Day 1	Day 7	Day 14	Day 1	Day 14
OOC coculture (OOC-bi)	Day 1	Day 7	Day 14	Day	Day 14
OOC quadculture (OOC-quad)	Day 1	Day 7	Day 14	Day	Day 14

100 µL of each fresh medium (PHH medium (Table 14), NPC medium (Table 16), and coculture medium (Table 12)), and a mixture of freshly thawed PHHs/LSECs (50.000/50.000) serve as baseline. The vials were gently centrifuged for several seconds using a benchtop centrifuge. Subsequently, the supernatant was discarded, and cells were washed once with $PBS^{-/-}$ and lysed with 50 µL of ice-cold methanol/water (9:1). All samples were stored at -80 °C until analysis.

For the 2.5D culture model (in this experiment also named 2D), $3x10^5$ PHHs were seeded into a collagen coated 24 well plate. 4 h post seeding, cells were coated with Matrigel® (Section 3.1.4). At the next day, $6x10^4$ LSECs were seeded on top of the ECM. At day 1, 2 and 6, the medium supernatant was collected. At day 1 and 6, cells were washed one with $PBS^{-/-}$ and lysed with 200 µL ice-cold methanol/water (9:1). Cells were detached from the surface using a cell scraper. The lysate was transferred into a fresh tube and stored at -80 °C.

For the 3D model, $1x10^3$ PHHs and $1x10^3$ LSECs were mixed and seeded per well into a 96 well ULA U-bottom plate according to Section 3.1.4. The formation was observed daily. Day 1 was determined as soon as a round spheroid could be observed. The supernatant of ten wells was pooled at day 1, 7, and 14. At days 1 and 14, eight spheroids were pooled into a fresh tube, washed once with $PBS^{-/-}$, and lysed with 50 µL ice-cold methanol/water (9:1). The samples were stored at -80 °C.

For the OOC samples, the Emulate OOC was activated and prepared as described in Section 3.3. For the OOC-bi model, only LSECs were seeded into the bottom channel at a concentration of $4x10^6$ cells/mL. At days 1, 7, and 14, 250 µL of the top channel outlet reservoir and 250 mL of the bottom channel outlet reservoir were pooled together in a separate tube. At days 1, 14, cells in the OOC were washed once with $PBS^{-/-}$ and lysed with 25 µL ice-cold methanol/water (9:1) per channel. The cells within the chip were attempted to lyse by pipetting up and down. The supernatant of both channels was pooled in a fresh tube and both samples were stored at -80 °C until analysis.

Table 29: List of collected lysates for the metabolomics analysis.
Lysate samples of primary liver cell cultures were collected at days 0, 1, and 14.

Cells	Number of cells per well	Culture system	Time points [days]	Lysate volume [µL]
PHH/LSEC	50.000/50.000	Freshly thawed	0	50
PHH/LSEC (2D)	50.000/10.000	2.5D	1, 14	200
PHH/LSEC (3D)	1.000/1.000	3D	1, 14	50
PHH/LSEC (OOC-bi)	98.000/22.400	OOC	1, 14	50
PHH/LSEC/SC/KC (OOC-quad)	98.000/16.800/ 560/2.800		1, 14	50

Table 30: List of collected media sampled for the metabolomics analysis.
Media samples were collected at days 0, 1, 2, 6, 7, and 14, depending on the culture model.

Cells	Media supernatant	Culture system	Time points [days]	Volume [µL]
-	PHH medium	-	0	500
-	NPC medium	-	0	500
-	Coculture medium	-	0	500
PHH/LSEC (2D)	Coculture medium	2.5D	1, 2, 6	500
PHH/LSEC (3D)		3D	1, 7, 14	500
PHH/LSEC (OOC-bi)	PHH medium/NPC medium	OOC		500
PHH/LSEC/KC/SC (OOC-quad)				500

The samples were analyzed by Biocrates, a company which provides services for quantitative, reproducible and standardized mass spectrometry-based metabolomics analysis [364]. Lysate and media were analyzed using the MxP® Quant 500 Kit. The statistical analysis was performed by Alex Rolfe using the software R statistic.

3.8 Colorimetric and luminescence assay

3.8.1 AST activity assay

The pyridoxal phosphate-dependent enzyme AST catalyzes the conversion of aspartate and α-ketoglutarate to glutamate and oxaloacetate. In clinic, the AST level in the blood are a marker for liver function [365]. For determining the liver function in the three models, the AST Activity Assay of Sigma (MAK055) was used. Therefore, the media samples were diluted 1:3 with AST Assay Buffer in a white, clear bottom plate. The prepared standard series and positive control were pipetted into the plate as described in the protocol. The reaction mix was pipetted in all sample or control wells. Subsequently, the plate was incubated for 2-3 min at 37 °C. Upon, the absorbance was measured at 450 nm at the initial time. The incubation of the plate was continued, and the absorbance was measured every 5 min until the value of the most active sample is greater than the value of the highest standard. For the calculation of the AST amount and activity, the penultimate reading before the most active samples is near or exceeds the end of the linear range of the standard curve was used. The activity was calculated as described in the protocol [365]. Statistical analysis between DILI- and non-DILI treated cells was performed by Julian Kreis and Dilafruz Juraeva using the software R statistic.

3.8.2 ALT activity assay

The pyridoxal phosphate-dependent enzyme ALT catalyzes the transfer of an amino group from alanine to and α-ketoglutarate, generating glutamate and pyruvate. Evaluations of the

ALT level are a marker for hepatocellular injury [366]. For determining the hepatocellular injury, in the 2.5D, 3D, and OOC, the ALT Activity Assay of Sigma (MAK052) was used. Therefore, the media samples were diluted 1:3 in ALT Assay Buffer in a white, clear bottom plate. The standard series and positive control were pipetted into the plate as described in the protocol. The reaction mix was prepared and pipetted in all sample or control wells. Subsequently, the plate was incubated for 2-3 min at 37 °C. Upon, the absorbance was measured at 570 nm at the initial time. The incubation of the plate was continued, and the absorbance was measured every 5 min until the value of the most active sample is greater than the value of the highest standard. For the calculation of the ALT amount and activity, the penultimate reading before the most active samples is near or exceeds the end of the linear range of the standard curve is used. The activity was calculated as described in the protocol [366]. Statistical analysis between DILI- and non-DILI treated cells was performed by Julian Kreis and Dilafruz Juraeva using the software R statistic.

3.8.3 LDH-Glo assay

LDH is widely used as cytotoxicity marker. It is present in many cells and rapidly released into the culture medium upon disruption of the plasma membrane [367]. To determine the viability of the cells in each culture system, the LDH-Glo assay of Promega (J2380) was used. The principle of the assay is depicted in Figure 19. The released LDH catalyzes the oxidation of lactate with reduction of *oxidized nicotinamide adenine dinucleotide* (NAD^+) to *reduced nicotinamide adenine dinucleotide* (NADH). Using NADH and Reductase Substrate, the Reductase generates luciferin which is converted to a bioluminescence signal. The signal is proportional to the amount of LDH.

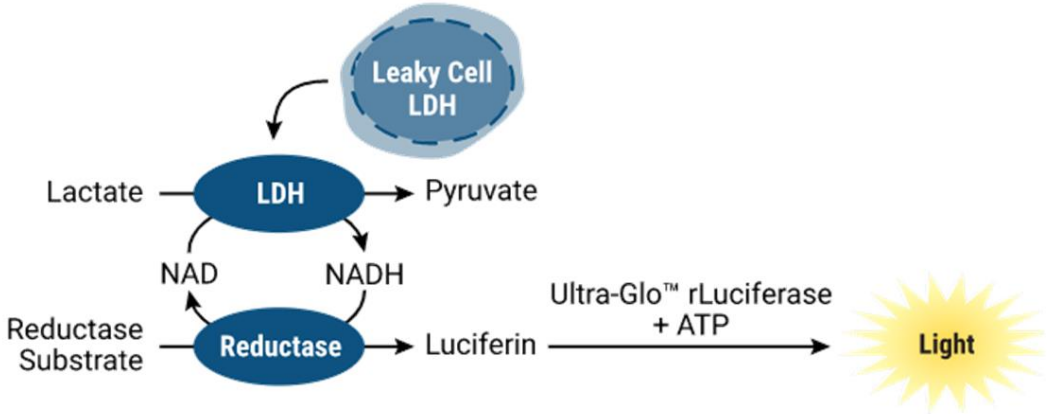

Figure 19: Principle of the LDH-Glo™ Cytotoxicity Assay.
(J2380, Promega)

2 µL of each medium sample were collected and diluted in a white clear bottom 96 well plate in 48 µL of LDH Storage Buffer according to the protocol [367]. The LDH Detection Regent

was prepared by combining the LDH Detection Enzyme Mix with the Reductase Substrate. Furthermore, a standard series was prepared. 50 µL of the LDH Detection Reagent were added to each well, composing 50 µL of diluted samples or standard. The plate was incubated for 1 h at RT. Afterward, the luminescence was measured. The amount of LDH was calculated by plotting the standard concentration on the x-axis against the RLU of the standards on the y-axis. The LDH concentration could then be read off the standard curve. Statistical analysis between DILI- and non-DILI treated cells was performed by Julian Kreis and Dilafruz Juraeva using the software R statistic.

3.8.4 Resazurin assay

Resazurin is a blue dye (Figure 20), and irreversibly reduced in the presence of NADH of metabolically active cells. The reduced product, Resorufin, in pink and highly fluorescent. The fluorescent signal can be detected at 590 nm and is proportional to the number of metabolically active cells.

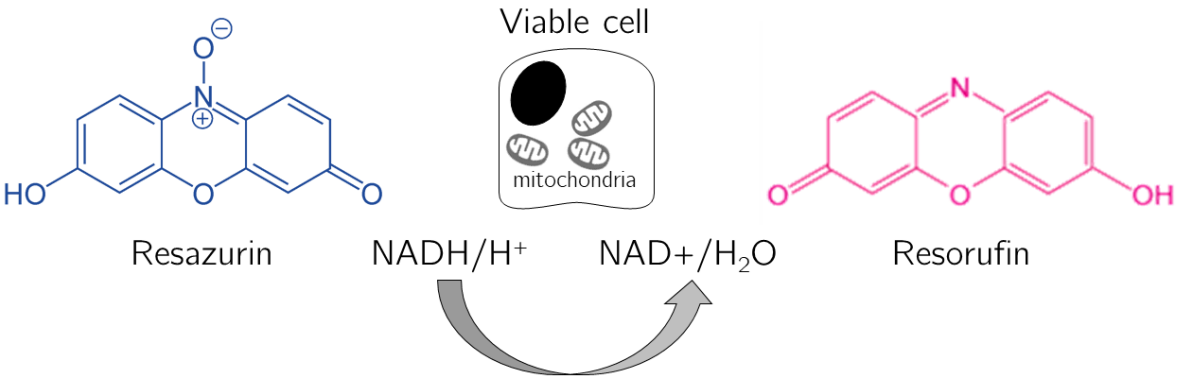

Figure 20: Schematic overview of the principle of the Resazurin assay.
[368]

To determine the cell viability, a Resazurin stock solution (4.5 mM) was prepared and diluted 1:10 with medium. It was then added to the cells (100 µL for 96 well and 700 µL for 24 well) and incubated for 1 h at 37 °C. After incubation, the solution was transferred into a black 96 well plate with clear bottom and the fluorescence was detected at 580 nm with the Tecan microplate reader, using the software I control. Afterward the cells were washed 2-3 times with PBS -/- until the blue color was washed out. After adding the appropriate medium, the cells can now be cultivated further.

3.8.5 Albumin SimpleStep ELISA

Albumin is high soluble, stable, and the most abundant plasmatic protein with approximately 30-50 g/L on humans. With 150 mg/kg/day it is predominantly synthesized in the liver. An increase or decrease in albumin synthesis and secretion can indicate liver injury [369]. To determine the secreted amount of albumin in 2.5D, 3D, and OOC, the Albumin SimpleStep

ELISA Kit from Abcam (ab179887) was used [370]. Therefore, the media samples were diluted 1:5-1:10 with Sample Diluent NS. Next, the standard series and the antibody cocktail was prepared according to the protocol. 50 µL of each sample and standard were pipetted into each well of the anti-tag coated microplate. Afterwards, 50 µL of the antibody cocktail were added into each well. The plate was incubated for 1 h at 400 rpm at RT. After incubation, each well was washed three time with Wash Buffer PT. Subsequently, 100 µL of the TMB Development Solution were pipetted into each well and incubated in the dark (10 min, 400 rpm, RT). Subsequently, the reaction was stopped with 100 µL Stop solution. After another 1 min incubation at 400 rpm, the OD was measured at 450 nm. The amount of albumin was calculated by plotting the standard concentration on the x-axis against the absorbance of the standards on the y-axis. The albumin concentration could be read off the standard curve. Statistical analysis between DILI- and non-DILI treated cells was performed by Julian Kreis and Dilafruz Juraeva using the software R statistic.

3.8.6 αGST ELISA activity assay

AGST is a cytosolic phase II detoxification enzyme [371]. The quantification of αGST is one of the most sensitive biomarkers for the early detection of liver damage [372]. To determine hepatic injury in the 2.5D, 3D, and OOC, the Human Alpha GST ELISA of TECO Medical (TE1056) was used [373]. Therefore, the media samples were diluted 1:5 in Sample Diluent. A standard series was prepared according to the protocol. 100 µL of all samples, standards, and controls were pipetted into the αGST antibody coated microtiter plate and incubated for 1 h at 500 rpm at RT. After incubation, the wells were washed four timed with diluted Wash Buffer. Subsequently, 100 µL Enzyme Conjugate was added per well and incubated for 1 h at 500 rpm at RT. Next, all wells were washed again four times with Wash Buffer. Upon, 100 µL of TMB substrate was pipetted in each well followed by further incubation (15 min, 500 rpm, RT). The reaction was stopped by adding 100 µL of stop solution. The absorbance was measured at 405 nm. The amount of αGST was calculated by plotting the standard concentration on the x-axis against the absorbance of the standards on the y-axis. The αGST concentration could be read off the standard curve. Statistical analysis between DILI- and non-DILI treated cells was performed by Julian Kreis and Dilafruz Juraeva using the software R statistic.

3.9 Fluorescence staining

To visualize the expression and location of liver specific markers and structures, the advanced cell culture models were stained with specific antibodies and fluorescent dyes.

2.5D, 3D, and OOC were setup and cultured as described in Section 3.1, 3.2, and 3.3. At specific time points, the cells were fixed, permeabilized, and stained. Therefore, the medium of the 2.5D, 3D organoid, and OOC model was aspirated, cells were washed 2x with $PBS^{-/-}$

and fixed for 15 min with 4 % PFA at RT. Afterward, cells were washed again 2x with $PBS^{-/-}$ and permeabilized with 0.5 % triton X-100 in blocking buffer (3 % BSA in $PBS^{-/-}$) for 15 min at RT. Subsequently, cells were washed again twice with $PBS^{-/-}$ and blocked with blocking buffer for 30 min at RT.

For the 3D spheroid model, 8-16 spheroids were pooled into a tube and washed twice with $PBS^{-/-}$. Liver spheroids where fixed with 4 % PFA for 1 h followed by two washing steps with $PBS^{-/-}$. Upon, cells were permeabilized with 0.5 % triton X-100 in blocking buffer (3 % BSA in $PBS^{-/-}$) for 2 h at RT [374]. After permeabilization, cells were washed again twice with $PBS^{-/-}$ and blocked with blocking buffer overnight at 4 °C [375][376].

After fixation, permeabilization, and blocking, cells of the 2.5D, 3D organoid, and OOC model were incubated with the primary antibody diluted in blocking buffer overnight at 4 °C. 3D spheroids were incubated for 48 h with the primary antibody in blocking buffer at 4 °C [377]. Primary antibody solution was removed after incubation and cells were washed twice for 10 min with $PBS^{-/-}$. The appropriate secondary, fluorescence labeled antibody was diluted according to the manufacturer's recommendation. Cells were incubated overnight with the diluted secondary antibody and 1:1000 diluted Hoechst 33342 in blocking buffer at 4 °C [374].

To visualize the formation of bile canaliculi, a live cell staining with the fluorescent Green *5-chloromethylfluorescein diacetate* (CMFDA) dye (C2925, Thermo Fisher) was established. After 14 days of cultivation, the medium in 2.5D and 3D organoids was replaced with medium containing 1:1000 CellTracker Green CMFDA and 1:1000 Hoechst 33342. For the 3D model, eight spheroids were pooled into a tube and the medium was replaced with medium containing the same amount of CMFDA and Hoechst 33342 as described before. Cells were incubated in the dark (37 °C, 45 min). After incubation, cells were washed three time with $PBS^{-/-}$ and imaged by confocal microscopy.

3.10 Statistical Analysis

Statistical analyses were conducted by experts of the bioinformatic department of Merck KGaA. Heatmaps and statistical analysis, comparing the untreated expression of liver specific genes in the 2.5D, 3D, and OOC model, were generated by Dilafruz Juraeva (Section 4.4.2). Dilafruz Juraeva used the software R to check the data for normal distribution and perform a *linear model for microarray* (limma) data analysis. Data points not comparable to other data replicates were excluded from the analysis. Accordingly, some analyses contain 3 or 4 technical experiments (N=3/4). The expression values were log2 transformed before differentially expressed genes analysis. Limma is a R software package for analyzing gene expression data which enables a stable analysis even for experiments with small data sets [378][379]. Heatmaps are clustered based on spearman correlation and annotated with nominal p-value

groups: *P ≤ 0.1; **P ≤ 0.05; ***P ≤ 0.01; ***^P ≤ 0.001. In addition, Dilafruz Juraeva provided graphs and statistical analysis of the secreted hepatic levels during the 14-day cultivation (Section 4.4.3). The raw data was processed as described above. The Kruskal-Wallis test is a non-parametric method for comparing two or more independent samples with the same or different sample size, for testing whether samples come from the same distribution. In this work, it was chosen to assess the long-term stability of the advanced cell culture systems *in vitro*. It showed the changes in secretion from day 2 until day 14 with nominal p-value groups: *P ≤ 0.1; **P ≤ 0.05; ***P ≤ 0.01; ***^P ≤ 0.001.

The analysis of the proteomic data set from one experiment (N=1) was performed by Thomas Wild. The raw MS data was analyzed with Peaks Studio 10.6. The output was further analyzed using R. For analysis, proteins were collapsed into protein groups. A mixed sample present in all five 9plexes (tandem mass tag-label 134N) was used to normalize the intensities between the five 9plexes. The mean of the mix sample over the different plexes was calculated and for each protein and plex a normalization factor was applied to obtain the mean mix intensity in the mix sample. The *principal component analysis* (PCA) analysis was performed using the prcomp() function in R with scale = TRUE (Figure 44). Hierarchical clustering shown in Figure 45 was performed with the pheatmap package in R. The generated heatmap and pathway analysis give a deeper inside into the metabolic differences between freshly thawed and cultures PHHs. The heatmap was generated using the euclidean distance clustering method (Figure 45). Clusters for the pathway analysis were selected by me and analyzed by Nicholas Geraci using JEPETTO. JEPETTO uses multiple webservers and enrichment values (KEGG, Gene Ontologies, and Wiki Pathways) from STRING which is a protein interaction database source. Heatmap shown in Figure 46 was created by myself using a heatmapper website and the clustering method euclidean distance, as used by Thomas Wild [380]. The data set generated by Thomas Wild was used for this purpose.

PCA and bile acid heatmap of the metabolomic data set from one experiment (N=1) was conducted by Alex Rolfe using R. Raw data was normalized to the blank medium (for supernatant samples) or values detected in freshly thawed cells (for cell lysate samples). The PCA was performed using the prcomp() function in R with scale = TRUE (Figure 48). As mentioned before, the hierarchical clustering was performed with the pheatmap package in R to visualize the differences between intra- and extracellular detected bile acids during 14-day cultivation.

The statistical analysis of the data set after treatment (Section 4.5.5and 4.5.6) was performed by Julian Kreis using R. Background corrected expression data was normalized by housekeeping gene expression (2D and 3D using *B2M*, *EIF4E2*, *POLR2A* and *PPIA* and OOC using *EIF4E2*, *POLR2A* and *PPIA*). *PPIB* and *B2M* were removed from individual normalization procedures due to lower correlation coefficients. Before analyzing differentially expressed genes,

the data was quantile normalized between each replicate and each system respectively. Quality control indicated a lack of signal in two replicates. Thus, these replicates were removed from analysis. Accordingly, some analyses contain 3 or 4 technical experiments (N=3/4). Additionally, the genes *FASLG* and *CDH5* did not show any signal across all platforms and replicates and was also removed. For the identification of differentially expressed genes, the background, housekeeping and quantile normalized data was log2 transformed data analyzed using limma, described before.

4 Results

PHHs in 2D monocultures are the current gold standard for hepatotoxicity testing. However, in this culture format, they often fail to predict chemically-induced hepatotoxicity due to the rapid loss of the hepatocyte-specific phenotype and function [381]. The culture of primary cells in 2D is one discussed reason why many toxicological effects, such as DILI, cannot be predicted in preclinical studies. Consequently, for a several years, advanced cell culture models have come more and more into focus. They reflect the *in vivo* situation more reliably than conventional 2D models so that PHHs retain their physiological functions longer (up to four weeks, depending on the model) [382]–[384]. In this thesis, three advanced liver cell culture models were established: An advanced PHH/LSEC 2.5D sandwich, a 3D spheroid model and the Emulate OOC quad-culture system with NPCs (PHHs, LSEC, KC, and SC) (AIM_1).

The phenotype and physiological function of these three culture models were characterized and compared up to 14 days in culture. The measured endpoints include the secretion of hepatic-specific proteins, cell viability, cell morphology, and the expression of cell specific markers, genes, proteins, and metabolites (AIM_2).

Furthermore, these liver models were treated for 14 days with ten most-DILI-concern and four less-DILI-concern compounds (Section 1.6) (AIM_4) in order to evaluate potential sensitive biomarkers for the early detection/prediction of DILI (AIM_5).

4.1 Generation of the liver coculture models

PHHs exhibit donor-to-donor differences in their functionality and ability to form spheroids [345]. In order to generate realistic human 2.5D and 3D coculture liver models, several PHH donors were tested in two different ULA U-bottom plates (Costar and FaCellitate) (Section 3.1.4). The formation was documented daily until a round spheroid could be observed (D4-D14).

As depicted in Figure 21 A, in Costar U-bottom plates a spheroid was observed for the donors 37501ZMC and HUM4235 after 5 and 14 days of cultivation. The donors HU1591, HU1881, HU8284, and HU1951 formed multiple unequal aggregates and additionally showed some scattered single cells. In Figure 21 B, the donors HJK and XQD formed raggedly shaped spheroids after 4 days in the FaCellitate U-bottom plate. Below, the images for the batches AKB, HU1880, HU8284, and HU1951 showed round shaped spheroids after 6-10 days.

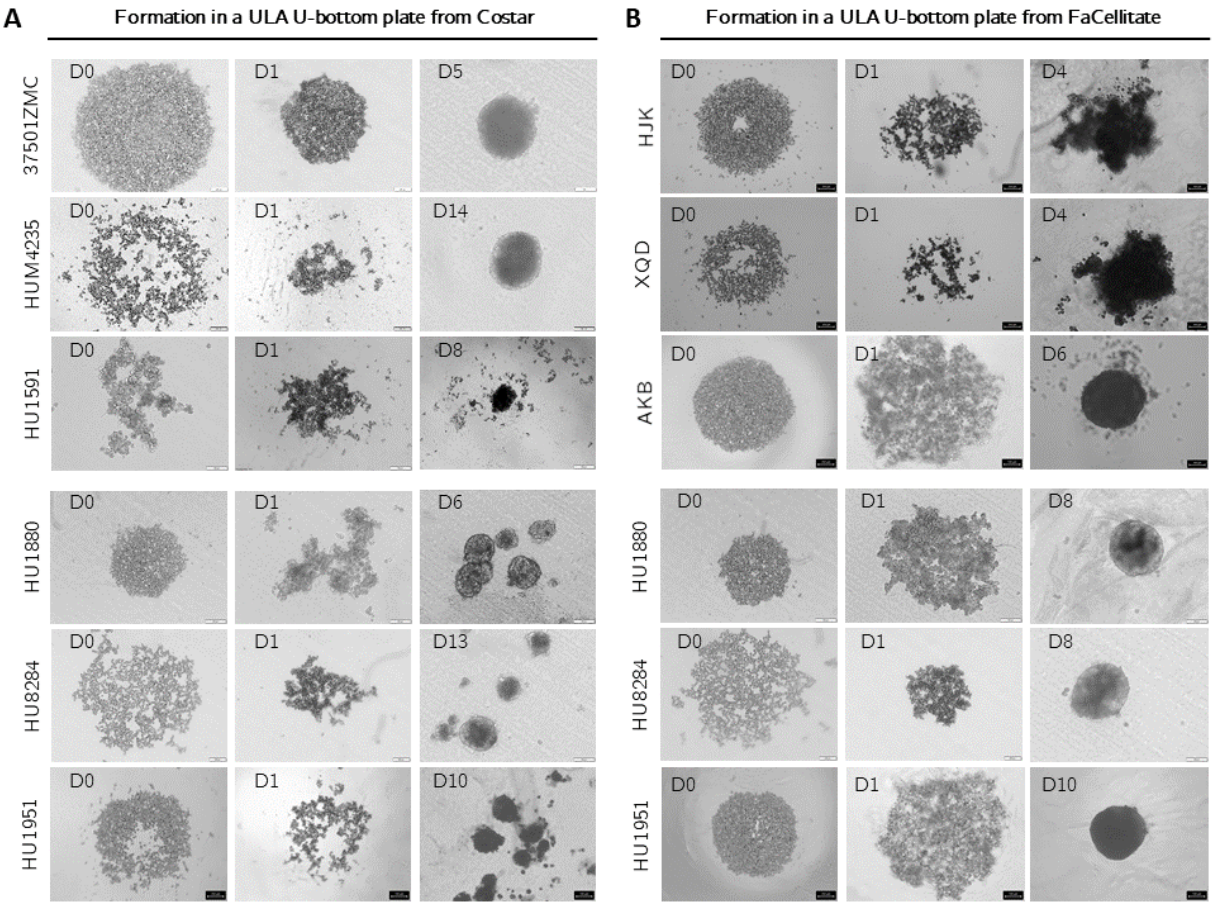

Figure 21: Spheroid formation of nine PHH donors in monoculture.
Time series shows the progressing spheroid aggregation in two different ULA U-bottom plates. 2000 PHHs were seeded per well and centrifuged down. D0 shows the state after centrifugation. After 24 h (D1), spheroids were imaged daily until a round aggregate could be observed (D4-D14) in **(A)** Costar and **(B)** FaCellitate plates.

Each cell type has specific needs depending on its function and therefore requires a suitable media composition [385]. To establish an appropriate media to coculture PHHs and LSECs, five coculture media (M1-5) were created and tested in the 2.5D culture system (Table 15). The cell viability was measured after 24, 72, and 120 h using the Resazurin assay. As shown in Figure 22 A, after 24 h the viability was stable for media M1, M2 and M3, and decreased for M4 and M5. After 72 h, the viability first increased and subsequently decreased after 120 h for all media, with M1 showing the least variability.

In Figure 22 B, the morphology of PHHs and LSECs can be seen after 24 h. Hepatocytes in the M1 and M2 medium showed a typical shape. Due to the sandwich format and the different heights at which the cells are arranged, the LSECs are difficult to see. However, they do also show their typical elongated shape. PHHs and LSECs cultured in media M3, M4s and M5 showed an increasing number of round shaped cells. The total number of attached cells in M3, M4, and M5 also decreased.

Albumin is an indicator for functional liver cells [292]. To analyze if the composition of the media does not affect the expression of PHH and LSEC specific markers, the cells were fixed and immunofluorescently stained. For PHHs an anti-Albumin-antibody and for LSECs a SE-1-antibody was used. Nuclei were stained using Hoechst 33342. Figure 22 C shows the fluorescence images of the stained liver cells. The highest signal was observed for M1, followed by M2 and M5 for both cell types. A reduced number of cells (Hoechst 33342) and decreased fluorescence signal (Albumin and SE-1) was seen for M3 and M4.

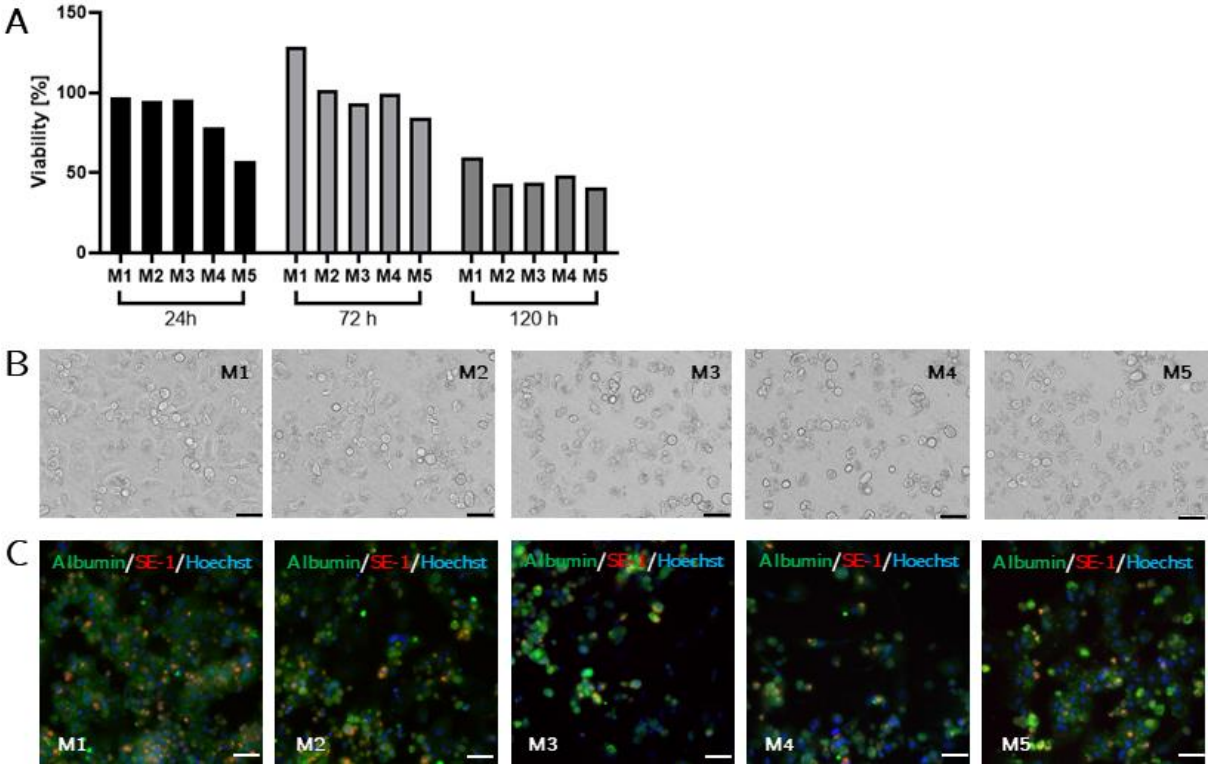

Figure 22: Characterization of cocultured PHHs and LSECs in five culture media.
PHHs (donor 37501ZMC) and LSECs (donor 566.05.02.05.0M) were thawed and cocultured in a sandwich format. **(A)** The viability was measured after 24 h, 72 h, and 120 h with the Resazurin assay. Values were normalized to the control media (1:1 ratio of specific PHH media and LSEC media). **(B)** Morphology of the cells after 24 h. **(C)** Expression of cells specific markers Albumin (PHH) and SE-1 (LSEC) after 120 h. Nuclei (blue) were stained with Hoechst 33342. Scale bar 50 µm.

Further experiments were performed with the FaCellitate U-bottom plate and M1. M1 is called coculture medium in this work and included two improvements over ITS+ instead of insulin, selenite, and transferrin separately and adjusted amount of FBS according to the cells in culture (e.g., PHHs in monoculture were cultured without FBS and in coculture with 2 %).

In the next step, the ability of PHHs and LSECs to form spheroids in M1 was investigated. Therefore, eight hepatocyte donors were cocultured with the LSEC donor 566.05.02.05.0M. The spheroid formation was documented daily (Figure 23). Compared to PHHs in monoculture (Figure 21), a more efficient spheroid formation was observed. In addition, donors in Figure 23 A show a faster formation and more roundish shaped aggregates compared to spheroids in Figure 23 B.

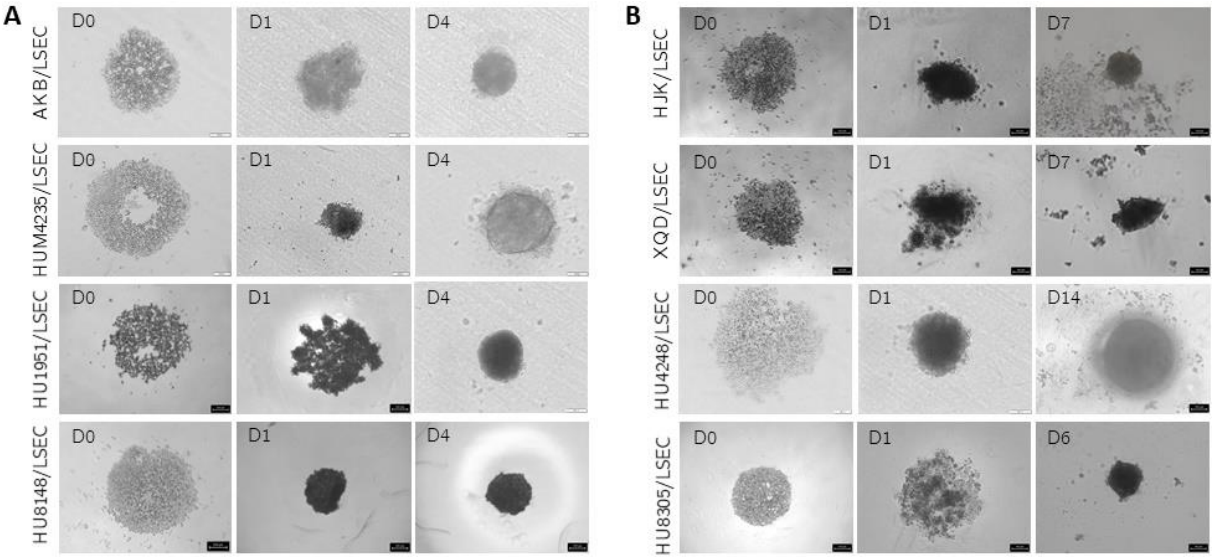

Figure 23: Spheroid formation of eight PHH donors in coculture with LSECs.
Time series shows the progressing spheroid aggregation. PHHs and LSECs (donor 566.05.02.05.0M) were seeded in a ratio of 1:1 and centrifuged down. D0 shows the state after centrifugation. Spheroid formation was documented after 24 h (D1) and daily until a round shaped aggregate could be observed (D4-D7). **(A)** Coculture of LSECs with AKB, HU4235, HU1951, HU8148 and **(B)** with HJK, XQD, HU4248 and HU8305. White scale bar 200 µm, black scale bar 250 µm.

The long-term stability of the cocultured cells was investigated in the established coculture medium (M1). Therefore, PHHs and LSECs were cultured in 2.5D, 3D, and OOC for 14 days, fixed, and immunofluorescently stained with the previous mentioned anti-Albumin- and SE-1-antibodies. Cells cultured in its specific media within the OOC served as control. As shown in Figure 24, albumin was observed in an equal intensity in all systems. In addition, a SE-1 signal was seen in all systems. In 2.5D and 3D, the albumin and SE-1 signals were randomly distributed and showed no specific expression pattern.

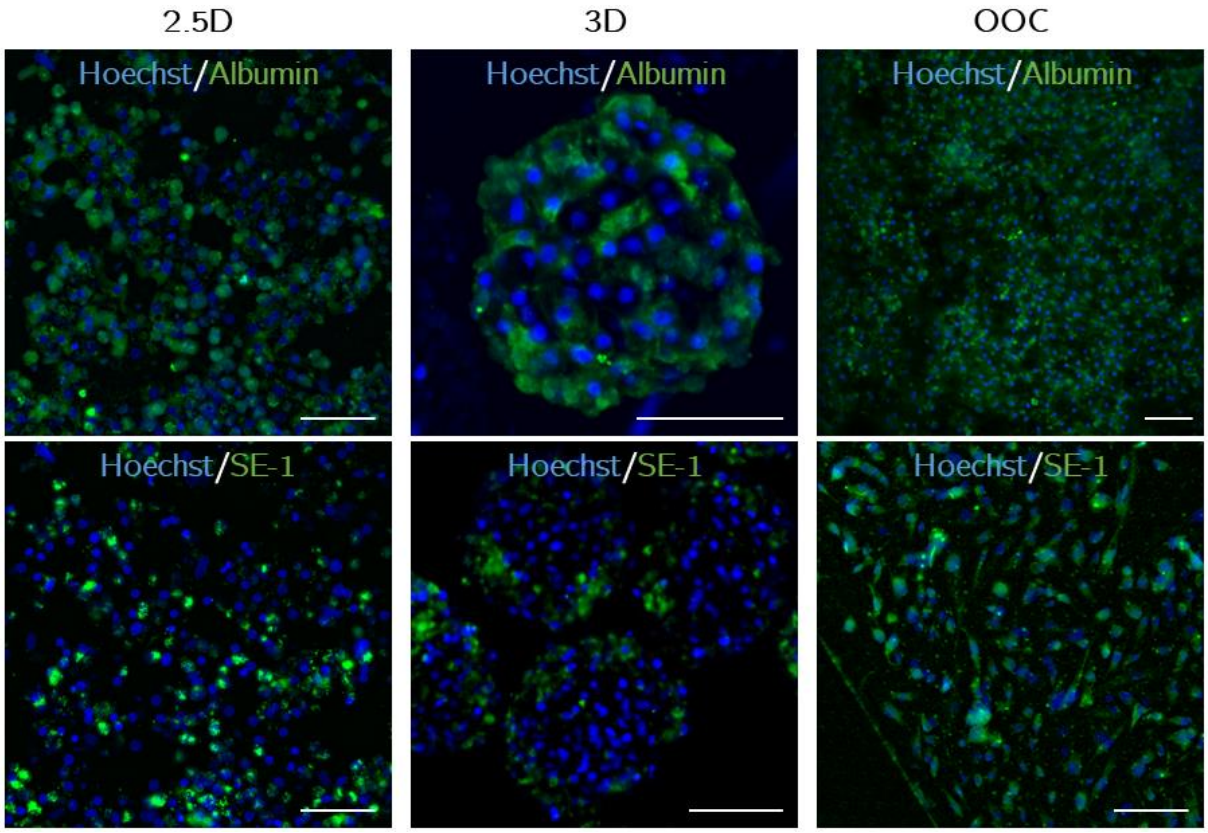

Figure 24: Immunofluorescence staining of albumin and the SE-1 antigen.
PHHs and LSECs were cocultured for 14 days in 2.5D and 3D spheroids in M1 (donor AKB and 566.05.02.05.0M). Both cell types were also seeded into the OOC in its specific media as control (donor HUM4235 and 566.05.02.05.0M). At day 14, cells in all systems were fixed, permeabilized, and stained with the anti-Albumin-antibody (PHH) and SE-1-antibody (LSEC). Nuclei (blue) were stained with Hoechst 33342. Scale bar 100 µm.

4.2 Functional and metabolic activity of PHHs

Based on the superior spheroid formation capacity, the gene expression of the cocultured PHH donors AKB, HUM4235, HU1951, and HU8148 (Figure 23 A) was characterized to determine the most suitable donor for the subsequent experiments. The gene expression was analyzed using the QuantiGene™ Plex method (Section 3.4). Figure 25 shows the relative gene expression of phase I (A), II enzymes (B), phase III transporters (C) and albumin (D). In Figure 25 A, the relative gene expression of the five CYP450 enzymes 1A2, 2C9, 2C19, 2D6 and 3A4 are shown (Section 1.3.2). A low to moderate expression of *CYP1A2* (blue) and *2C19* (red) was detected for all donors, except of HU8148 which lack CYP1A2. The relative expression level of *CYP2C9* (green) and *2D6* (violet) was over 10 in all tested donors. *CYP2C9* was approximately threefold lower in HU8148 compared with the other donors. *CYP3A4* (orange) was weakly expressed in HU1951 and HUM4235, and absent in AKB and HU8148.

Phase II enzymes were detected in all donors, except for *SULT1E1* (red) which was absent in AKB and HU8148 (Figure 25 B). A high expression was seen for *UGT2B7* (violet) in HU1951 and HUM4235. All other relative gene expressions were below 10. The phase III transporters

ABCB11 (BSEP, red) and *ABCC2* (MRP2, violet) were detected in all donors (Figure 25 C). *ABCB1* (MDR1, blue) was very low in three donors and absent in HU8148. The transporter *ABCC1* (MRP1, green) could not be detected in any donor.

As described before, albumin is an indicator for functional liver cells [292]. Figure 25 D depict the relative gene expression of *ALB*. The expression was on a similar level for AKB, HU1951, and HUM4235 and twice as high in HU8148.

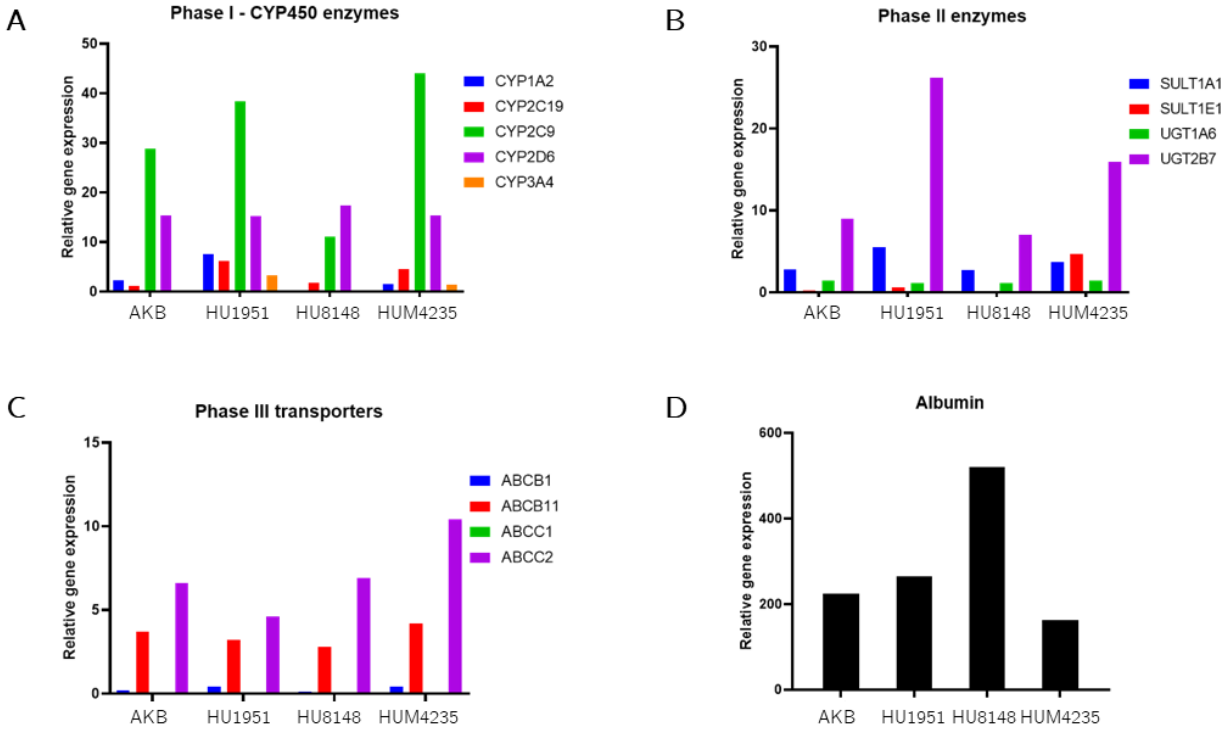

Figure 25: Relative gene expression of four PHH donors.
Cells were thawed, lysed directly, and analyzed using the QuantiGene™ Plex method. **(A)** Relative gene expression of phase I enzymes *CYP1A2*, *2C19*, *2C9*, *2D6*, and *3A4*, **(B)** phase II enzymes *SULT1A1*, *SULT1E1*, *UGT1A6*, and *UGT2B7*, **(C)** phase III transporters *ABCB1* (MDR1), *ABCB11* (BSEP), *ABCC1* (MRP1), and *ABCC2* (MRP2), and **(D)** *ALB*. Gene expression was normalized to housekeepers *PPIB*, *POLR2A*, *PPIA*, *EIF4E2*, and *B2M*. N=1

The donor HUM4235 showed high expression values and formation capacities. However, cells were supplied by Emulate for the OOC system and therefore had limited availability for 2.5D and 3D experiments.

In order to analyze the viability and functionality of hepatocytes growing in 3D spheroids, three PHH donors were analyzed regarding their secretion of LDH, albumin, AST, and ALT. The concentration was measured at days 2, 7, and 14 after spheroid formation.

The elevation of the LDH release is an indicator for cellular injury. Figure 26 A shows the LDH release, normalized to the secreted concentration at day 0, for three different donors. All donors showed a decrease in LDH release from day 2 to 7. The donors HU1951 and HU8148 showed a further decrease from day 7 to 14, whereas donor AKB remained stable over this time. The albumin secretion was on a comparable level for HU1951 and HU8148 (Figure 26

B). The secretion by AKB was slightly lower. Increasing ALT and AST levels are signals of liver injury [386]. The AST and ALT levels of all donors were comparable (Figure 26 C and D), except of ABK which showed a slightly decreased AST level at day 2.

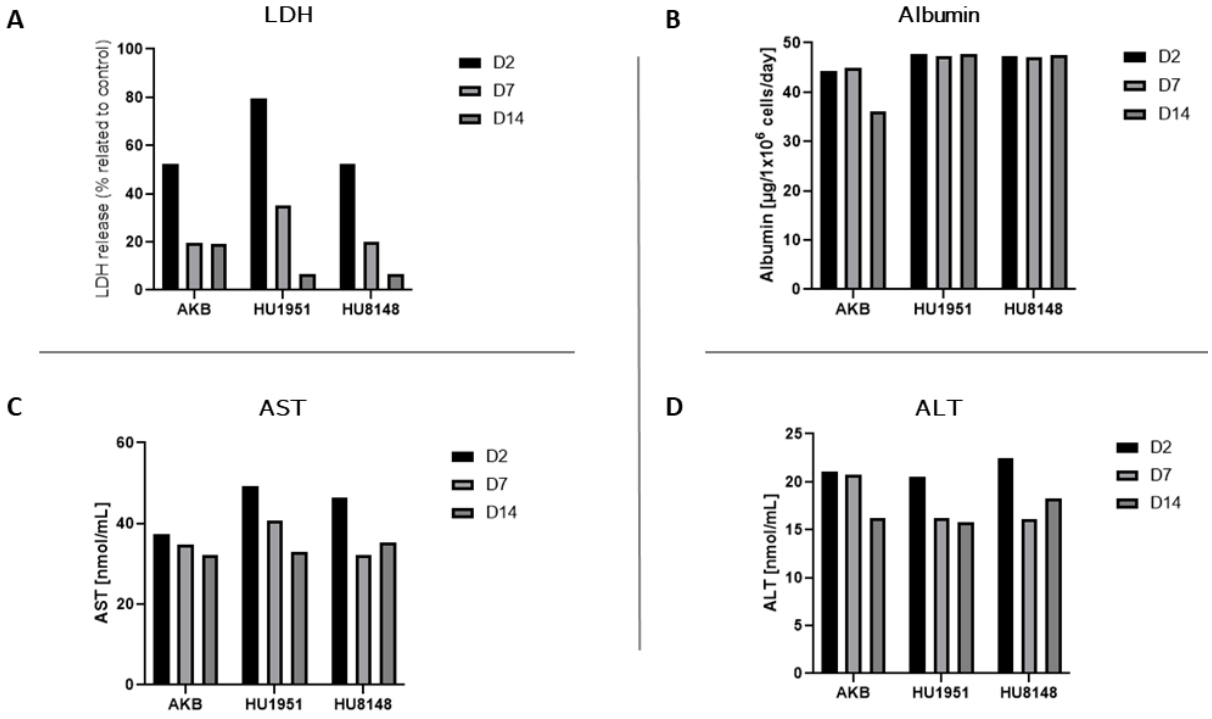

Figure 26: Viability and functionality of tested PHH donors cultured in 3D.
Albumin, LDH, AST, and ALT concentrations were determined in untreated spheroids. Media samples were collected at days 2, 7, and 14. **(A)** LDH release normalized to the secreted LDH level at day 0. **(A)** Albumin concentration normalized to $1x10^6$ cells per day. **(C)** AST, and **(D)** ALT in the untreated 3D culture system. N=1

HU8148 had an increased albumin level and additionally lacked some metabolizing enzymes and transporters. Therefore, this donor was excluded from the further experiments (Figure 25 D). Donor HU1951 showed higher release of LDH and some overexpressed genes which also strongly differed in the expression level. Hence, this donor was also excluded from the further experiments. Based on the appropriate expression level of drug metabolizing enzymes and transporters, as well as the stable secretion of specific hepatic proteins, the 2.5D and 3D experiments in this work were performed with the donor AKB.

4.3 IPSC-derived liver organoids

Liver organoids are a very promising tool that can retain hepatocyte function long-term and deliver a model for the better predictability of hepatotoxicity [248]. Their self-renewal and self-organization reveal their big potential for the preclinical study of xenobiotics [249][31]. In this work, a liver organoid differentiation protocol was generated based on different publications (Figure 12) [31][296]–[299] (AIM_3).

4.3.1 Generation of liver organoids

The differentiation status was tracked on days 0, 5, 10, 15, 20, and 25 by examining the expression of cell specific markers and the secretion of hepatic proteins. For Method 1 and 2, the iPSC cell line ChiPSC18 was thawed, cultivated, and embedded into a Matrigel® dome as depicted in Figure 27. Cells were evenly distributed within the dome. For Method 3, EBs of ChiPSC18 cells were formed prior to embedding (Appendix 8.1). The EB size was nearly equal and independent of the number of seeded cells. Thus, all aggregates were pooled and embedded into domes as described in Section 3.2.3.

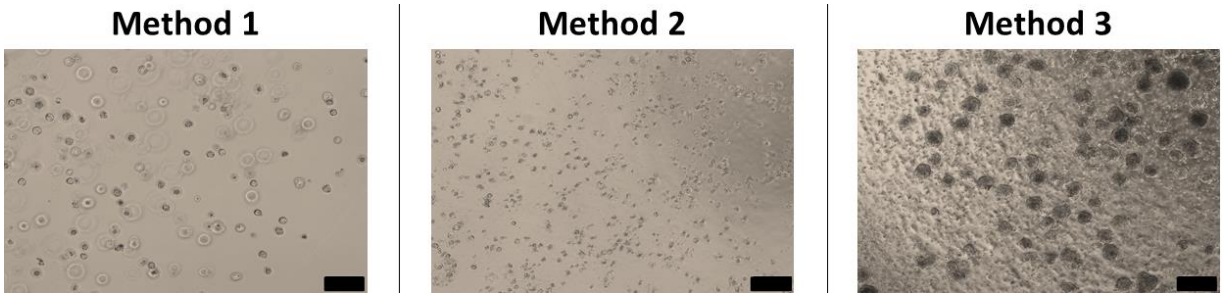

Figure 27: IPSCs embedded in Matrigel® at D0.
IPSCs were thawed, expanded, and seeded into a Matrigel® dome as single cells (Method 1 and 2) and EBs (Method 3). Immediately after embedding, the cells were imaged microscopically. Scale bar 100 µm.

According to the differentiation protocol in Figure 12, the shape of the organoids was documented at each state. Figure 28 shows the morphology of the progressive liver organoid differentiation in three stages. The preparation by Method 1 resulted in spheroid-like cell aggregates, which were observed immediately after endodermal induction with Activin A. The progress of differentiation was evident in the formation of liver organoids having an outer and an inner circle. These clear structures were observed in Method 3. In Method 2, the formation of cell aggregates was delayed, and the two distinguishable circles were not clearly visible.

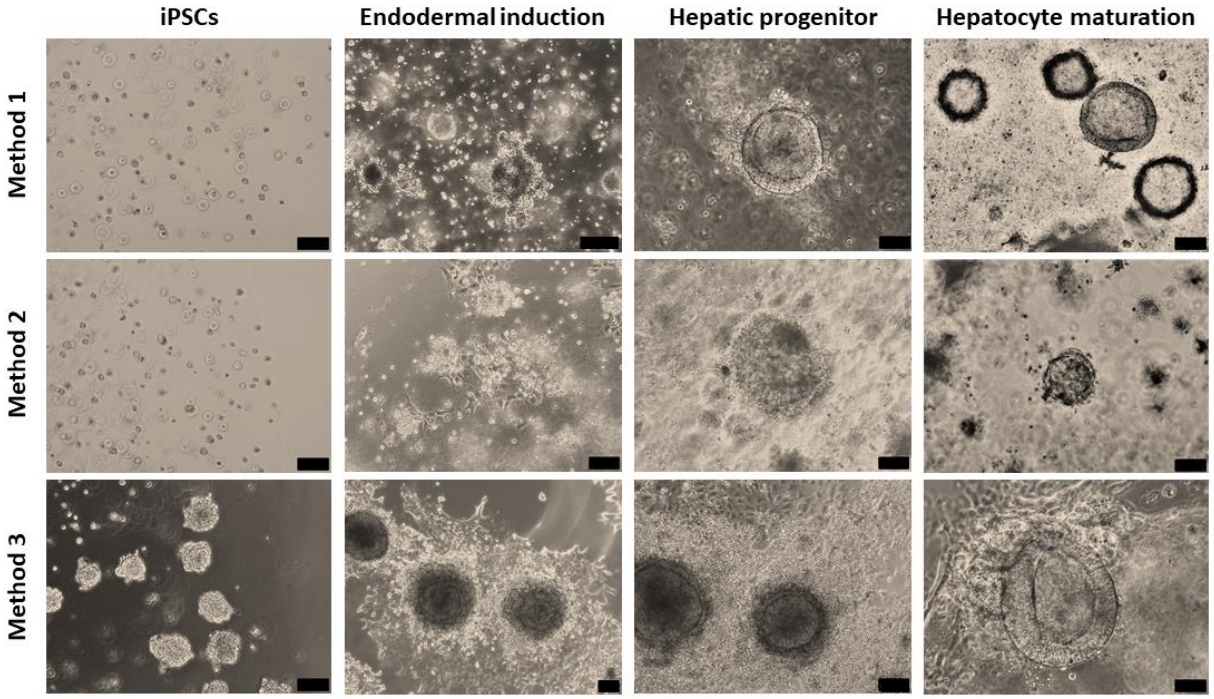

Figure 28: Illustration of the three-stage differentiation for all three methods.
IPSCs were embedded into a Matrigel® dome before starting the three-stage differentiation protocol. The differentiation comprises the endodermal induction, the generation of hepatic progenitor cells, and hepatocyte maturation. Scale bar 100 µm.

4.3.2 Localization of cell specific markers and cellular polarization

The differentiation of the iPSCs into liver organoids was tracked by examining the expression and secretion of cell-specific markers. At day 5 and 20, cells were isolated, fixed, and stained to visualize the localization of cell specific features. Figure 29 A shows the developing liver organoids at day 5 (Method 3). The expression of the pluripotent marker OCT4 and the endodermal marker SOX17 both exhibited a clear signal. The OCT4-positive cells were distributed toward the center of the organoid, whereas the SOX17-positive cells were in the outer part of the cell aggregates. At day 20, liver organoids from Method 3 were stained. An expression of liver-specific markers albumin, HNF4α, MDR1, MRP2, and CYP3A4 was observed (Figure 29 B). Albumin, HNF4α, and CYP3A4 were distributed throughout the whole organoid.

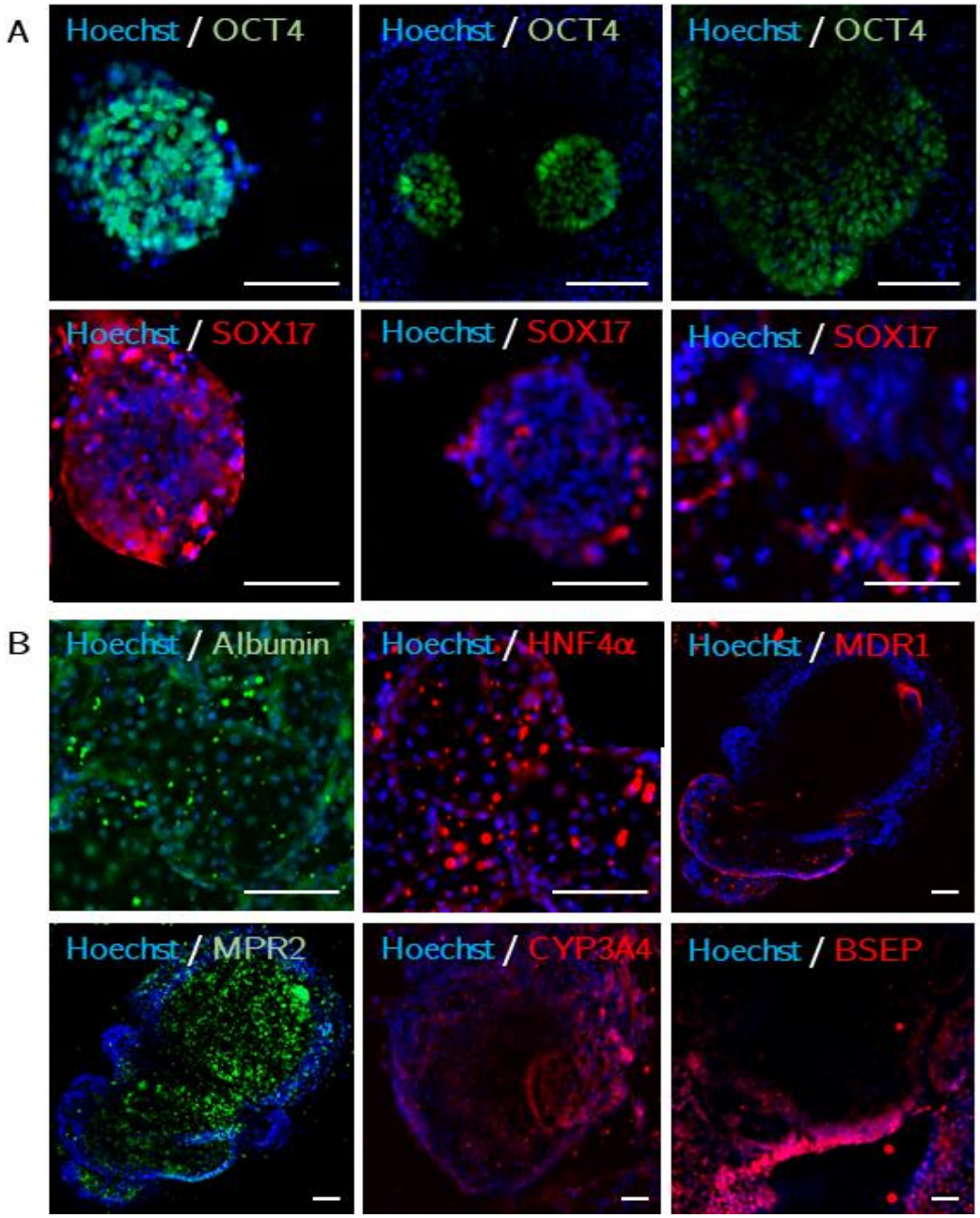

Figure 29: Expression of specific markers during the liver organoid differentiation.
(A) Immunofluorescence staining of the pluripotent marker OCT 4 (green) and the endodermal marker SOX17 (red) at day 5 (method 3). **(B)** Visualization of the hepatocyte markers Albumin (red) and HNF4α (green), liver phase III transporters MDR1 (red), BSEP (red), and MRP2 (green) and phase I enzyme CYP3A4 (red) at day 20 (method 3). Nuclei (blue) were stained with Hoechst 33342. Scale bar 100 µm.

In order to determine the formation of bile canaliculi-like structures, the ability of liver organoids to metabolize CMFDA was investigated at day 20 (Figure 30). The fluorogenic substrate CMFDA actively passes through the cell membrane of hepatocytes and is degraded to produce fluorescein, which accumulates in biliary tissue. Accumulation of fluorescein in a tract-like manner was observed in the Method 1 derived liver organoids at day 20 (green), suggesting functional bile canaliculi-like structures.

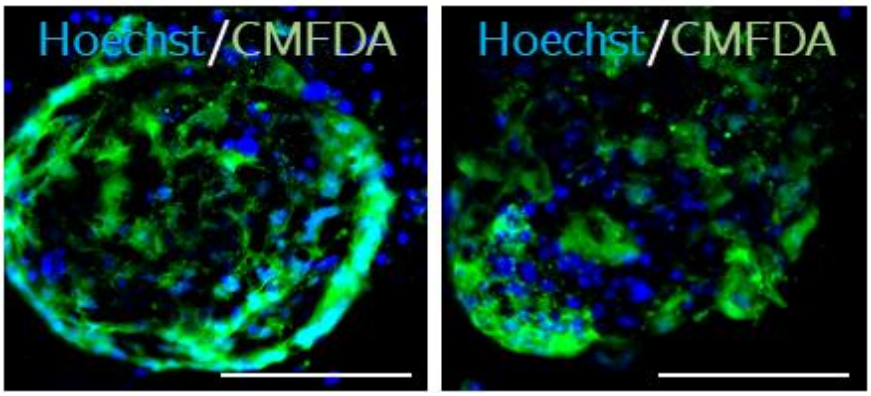

Figure 30: Live cell fluorescence microscopy of bile canaliculi-like structures in liver organoids. Organoids were incubated at day 20 with the CMFDA dye for 45 min (method 1). Nuclei (blue) were stained with Hoechst 33342. Scale bar 100 µm.

4.3.3 Gene expression during the differentiation process

To examine the progress of the liver organoid differentiation, cells were collected at days 0, 5, 10, 15, and 20 and the gene expression was analyzed using the QuantiGene™ Plex assay. The gene expression of iPSCs growing in 2D and iPSCs embedded in Matrigel®, before starting the three-stage differentiation, served as controls. The expression of the pluripotent marker *NANOG* decreased from day 0 to 20 (Figure 31 A). Additionally, the endodermal markers *FOX2* and *SOX17* (Figure 31 B) increased, starting from day 5 and decreased again at day 15. The gene expression levels of the hepatic progenitor *alpha fetoprotein* (*AFP)* and hepatocyte marker *ALB* increased steadily from day 10, except for organoids derived by Method 2, which showed a decreased expression at day 20. Similarly, the SC marker *ACTA2* and the cholangiocyte markers *CK7* and *CK19* showed an increased expression level from day 10. However, the expression level of *ACTA2* was lower in Method 1 and 2 as well as the level of *CK7* in Method 1.

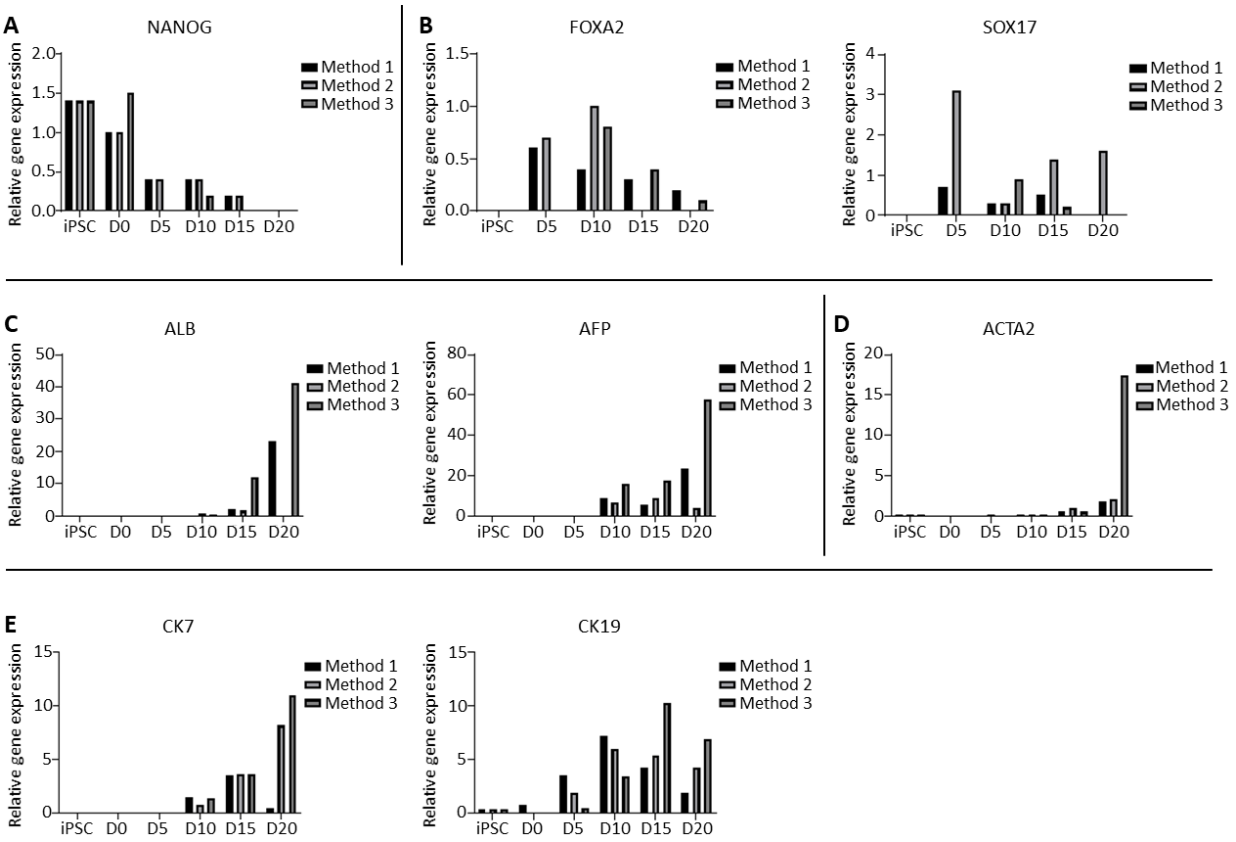

Figure 31: Relative gene expression of liver organoids during the differentiation process.
IPSCs were expanded and embedded into a Matrigel® dome. Cells were harvested at days 0, 5, 10, 15, and 20. Undifferentiated iPSCs served as control. Graphs show the relative mRNA level of **(A)** the pluripotent marker *NANOG*, **(B)** endodermal markers *FOXA2* and *SOX17*, **(C)** hepatic progenitor *AFP* and hepatocyte marker *ALB*, **(D)** SC marker *ACTA2*, and **(E)** cholangiocyte markers *CK7* and *CK19*. The expression was normalized to housekeepers *PPIB*, *POLR2A*, *PPIA*, *EIF4E2*, and *B2M*. N=1

4.3.4 Functional characterization of liver organoids

The functional properties of the liver organoids during the differentiation process were also examined. Mature hepatocytes can secrete albumin and αGST into the extracellular space. Therefore, the secretion levels of albumin and αGST were measured. In addition, the AST and ALT enzyme activity was determined. Medium samples were collected at each differentiation stage to analyze the secretion of these hepatic proteins (Figure 32). In addition, cells were treated with four compounds to study the response of the organoids to DILI-causing drugs.

In Figure 32 A, albumin was detected at a level of 600 ng/mL/day in the supernatant. In addition, 100 ng/mL/day αGST was measured from day 20. The AST activity increased from day 10 to a constant level of approximately 25 nmol/mL/day, whereas the ALT activity was detectable from day 25 at approximately 3 nmol/mL/day.

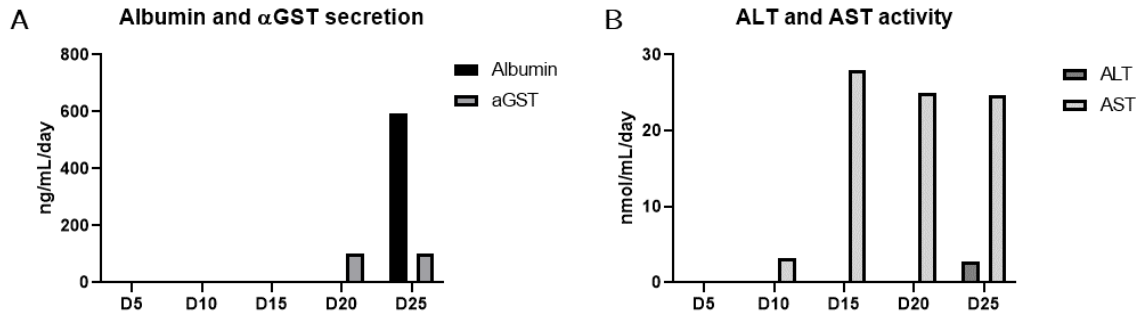

Figure 32: Secretion of albumin, αGST, ALT, and AST during liver organoid differentiation. Supernatant was collected at days 5, 10, 15, 20, and 25 of differentiation. **(A)** Concentration of albumin and αGST was measured using an ELISA, and **(B)** the ALT and AST activity was examined using a colorimetric assay. N=1

The second part of the functional investigation was to test the reaction of the organoids to four different drugs. The elevation of LDH release is an indicator of cell injury. In this experiment, the treatment with APAP and BOS lead to an increased release of LDH (Figure 33 A). Organoids treated with MET showed a slight increase in LDH release, whereas RIF-treated organoids secreted lower amount of LDH compared to the vehicle controls.

As mentioned before, the synthesis and secretion of albumin is an important marker for functional liver cells, However, abnormal secretion is associated with tissue damage [186]. In Figure 33 B, the gene expression of albumin was decreased after treatment with MET, RIF, and BOS.

The expression of CYP450 enzymes is essential for drug metabolism. Hence, the levels of *CYP3A4* and *CYP1A1* were analyzed after treatment. As depicted in Figure 33 C, the expression of *CYP3A4* decreased after treatment with MET, RIF, and APAP, but increased with BOS. In addition, *CYP1A1* showed a decreased expression after BOS treatment, but an increased expression after treatment with MET, RIF, and APAP.

Hepatic tissue is characterized by enriched mir122 expression. In addition, several publications have described mir122 as biomarker for hepatocellular damage. Part of the liver organoid characterization was the detection of the mir122 level during the differentiation process as well as after treatment with the four compounds, MET, RIF, APAP, and BOS. Figure 34 A shows the RLU of detected mir122 during the differentiation process. The signal increased from day 10 to day 15 and decreased until day 20. After 72 h treatment with four compounds, the *mir122* expression level increased 1.35-fold with BOS, 2.64-fold with APAP, and 1.48-fold with RIF. With MET a slightly decreased was observed.

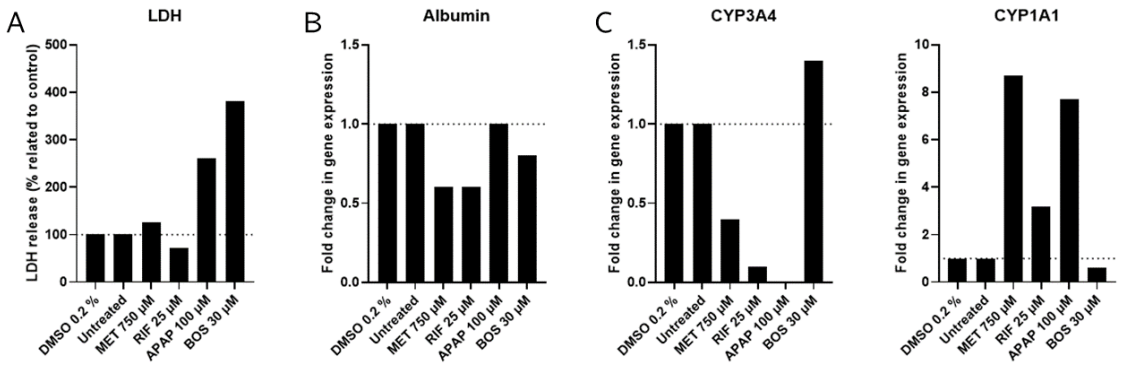

Figure 33: Viability and fold change in gene expression after 72 h treatment.
Liver organoids were thawed, pre-cultured for 5 days and treated with 750 µM MET, 30 µM BOS, 100 µM APAP, and 25 µM RIF. Media samples and cells were collected after 72 h. **(A)** The viability of the cells was analyzed by measuring the LDH amount in the supernatant. LDH release was normalized to the vehicle controls DMSO 0.2 % (for RIF, BOS, and APAP) and untreated (for MET). Fold change in gene expression of **(B)** *ALB*, **(C)** *CYP3A4* and *CYP1A1* was measured using the QuantiGene™ Plex assay. Gene expression was normalized to the housekeepers *PPIB*, *POLR2A*, *PPIA*, *EIF4E2*, and *B2M*. Following by normalization to the vehicle controls DMSO 0.2 % (for RIF, BOS, and APAP) and untreated (for MET). N=1

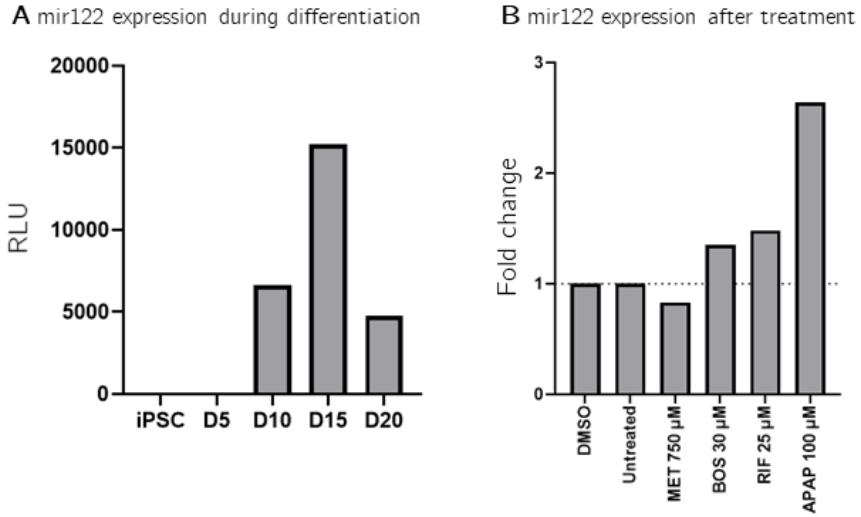

Figure 34: Mir122 expression in liver organoids.
Mir122 expression was detected **(A)** during the differentiation process in RLU, and **(B)** after 72 h treatment with four compounds normalized to the vehicle controls. The cell lysate was analyzed using the QuantiGene® 2.0 miRNA Assay. The baseline in (B) is set on the controls at 1. N=1

4.4 Characterization and comparison of the advanced cell culture models

In order to analyze the benefits and limits of PHHs cultured in an advanced cell model, multiple fluorescence stainings of specific biomarkers and an OMICs profile (including genomics, secretomics, proteomics, and metabolomics) was performed (AIM_2). Additionally, the expression of cell specific markers, using (immune-) fluorescence staining after 14 days in culture, was determined in the 2.5D and 3D system to visualize the stability of the expression of specific cell and functionality markers.

4.4.1 Expression of cell specific markers in advanced cell culture models

To analyze the expression and location of cell specific markers, an immunofluorescence staining was performed with PHHs and LSECs cocultured in 2.5D and 3D spheroids. As depicted in Figure 35, The PHH and LSEC specific markers albumin and LVYE1 showed a signal in both culture formats. However, the signal in 2.5D was weaker and a greater background fluorescence was observed. As primary liver cells lose their metabolic function in 2D very fast, metabolic enzymes and transporters were analyzed after 14 days of culture. A clear fluorescence signal of the phase I enzymes CYP450 and the phase III transporters MRP2, MDR1, and BSEP was seen in stained cells (Figure 35).

A key function of hepatocytes is the formation of bile canaliculi at their apical side, where bile is secreted in (Section 1.3.1). To visualize and compare the formation of canaliculi structures in the advanced 2.5D and 3D model, cells were stained with CMFDA at day 14. In Figure 36, a channel-like CMFDA accumulation was observed in monocultured PHHs. In the cocultured PHH/LSECs models, the fluorescent signal was mainly seen in the intracellular space in 2.5D and selectively distributed in 3D spheroids.

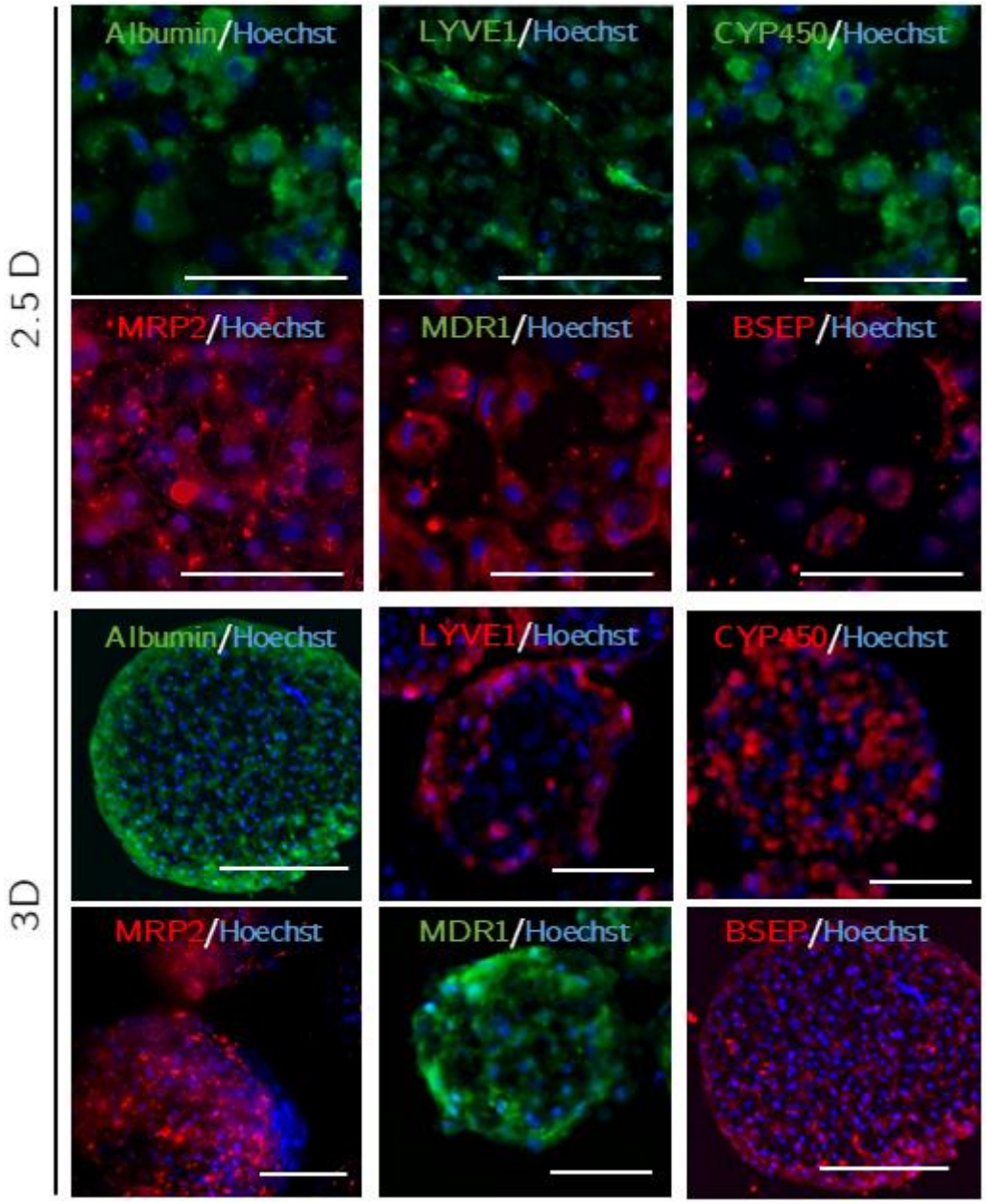

Figure 35: Immunofluorescence staining of cell specific markers.
Primary liver cells were cultivated in 2.5D and 3D. After 14 days, cells were fixed, permeabilized, and stained with specific antibodies. Albumin was stained to visualize PHHs and LYVE1 for LSECs. Phase I enzymes (CYP450) and phase III transporters (MPR2, MDR1, and BSEP) were stained with specific antibodies. Nuclei (blue) were stained with Hoechst 33342. Scale bar 100 µm.

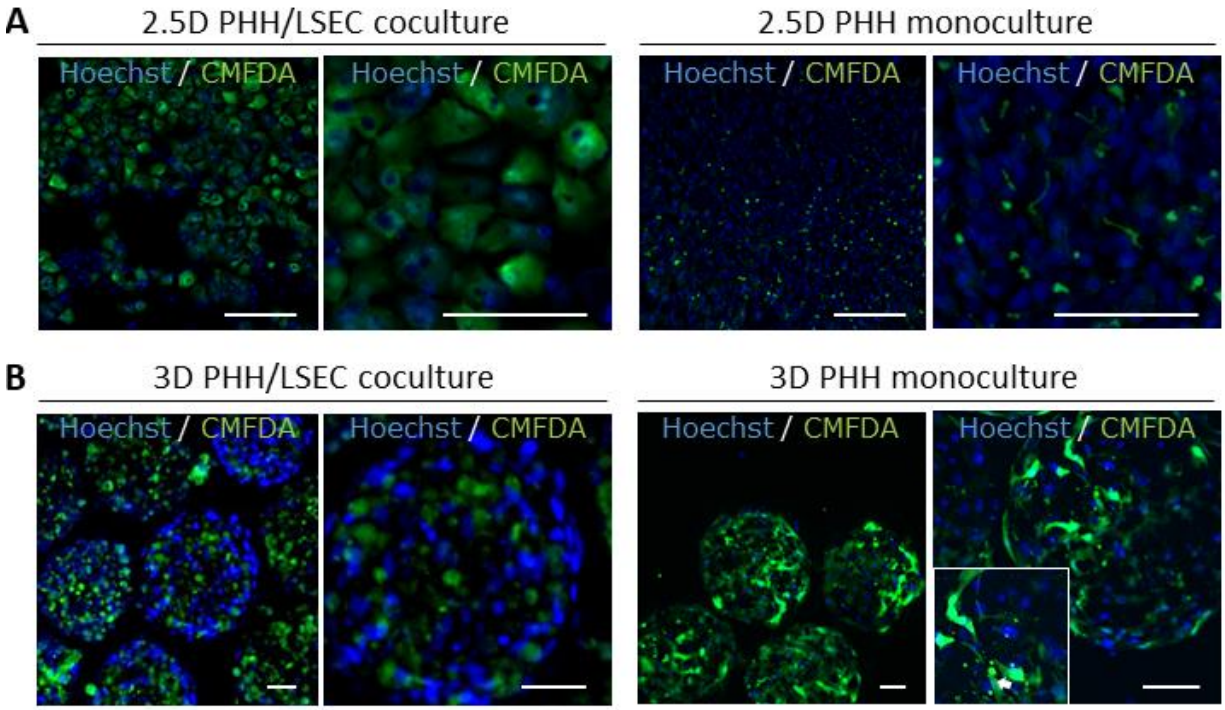

Figure 36: Live fluorescence microscopy of bile canaliculi-like structures.
PHHs were cultured in **(A)** 2.5D, and **(B)** 3D mono- and coculture with LSECs. At day 14, canaliculi-like structures were visualized using the Green CMFDA day, incubated for 45 min. Subsequently, cells were imaged live. Nuclei (blue) were stained with Hoechst 33342. Scale bar 100 µm.

4.4.2 Genomics

To examine the level of cell specific markers after 14 days in culture, the gene expression was measured using the QuantiGene™ Plex assay (Section 3.4). Figure 37 depicts the relative expression of specific PHH, LSEC, KC, and SC marker genes, normalized to the housekeepers in 2.5D, 3D, and OOC. In Figure 37 A, the expression of the PHH specific marker *ALB* showed the highest level in 3D, a more than three-fold decreased level in 2.5D and the lowest level in OOC. In Figure 37 B, a low expression of the two LSEC markers *ICAM1* and *PECAM1* were seen in all models, except for 3D, which lacked ICAM1 expression. The KC and SC specific markers were especially high in the OOC model.

The generated heatmap (Figure 38) visualizes the different expression of PHH and LSEC specific markers at day 14 across all systems. The expression of *ALB* was statistical significantly different ($p = 0.037$) between the 3D and OOC system. In addition, the LSEC marker PECAM 1 was significantly different ($P = 0.05$) between these systems. Comparisons of the 2.5D system with OOC or 3D revealed no significant chances in gene expression.

Drug metabolism plays an important role in the toxicity of many compounds [387]. Hence, the expression of DMEs and transporters was investigated in PHH cocultures after 14 days in culture. In Figure 39 A, seven CYP450 isoforms were investigated. In general, the expression of CYP450 enzymes decreased in all systems compared to freshly thawed PHHs. However,

the highest expression for most of CYP450 enzymes was observed for PHHs cultured in 3D, followed by the OOC system. In PHHs cocultured in 2.5D, only a weak expression of *CYP2C9* (orange) and *2C19* (violet) was observed.

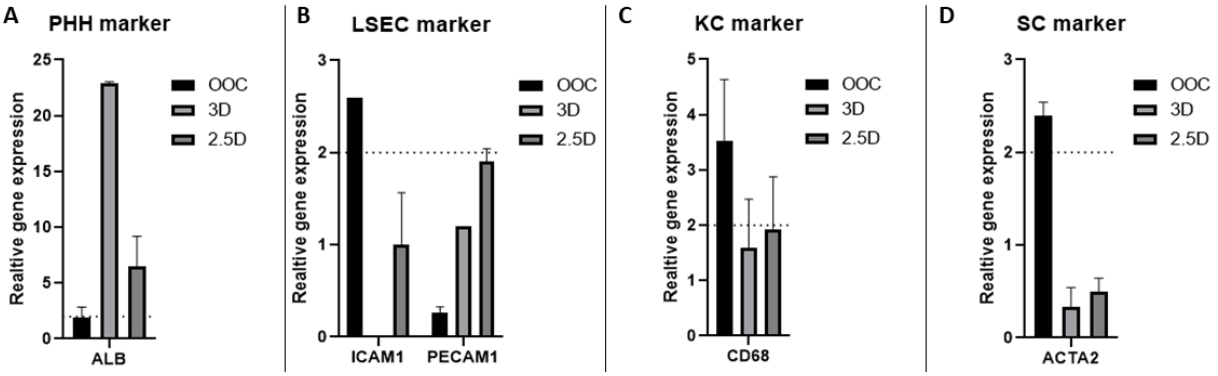

Figure 37: Relative gene expression of liver cell markers.
Primary human liver cells were cultivated for 14 days in the 2.5D, 3D, and OOC system. Afterwards, cells were lysed, and the gene expression was analyzed using the QuantiGene™ Plex method. Relative gene expression of **(A)** the PHH marker *ALB*, **(B)** the LSEC markers *ICAM1* and *PECAM1*, **(C)** the KC marker *CD68*, and **(D)** the SC marker *ACTA2*. Relative gene expression was normalized to the housekeepers *PPIB*, *POLR2A*, *PPIA*, *EIF4E2*, and *B2M*. N=3

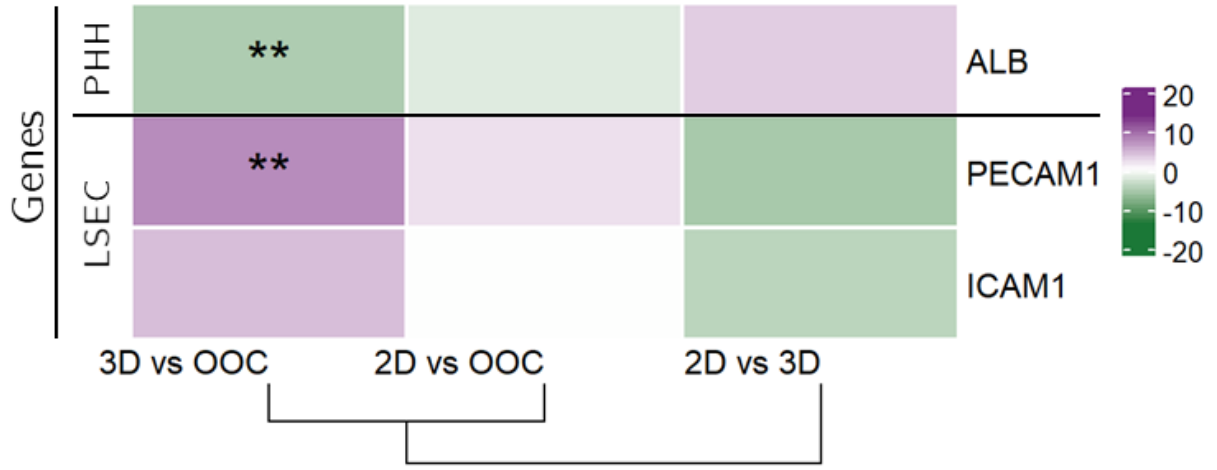

Figure 38: Heatmaps and statistical investigation of specific PHH and LSEC markers.
Primary human liver cells were cultivated in the 2.5D, 3D, and OOC system. At day 14, cells were lysed, and the gene expression was analyzed using the QuantiGene™ Plex method. The relative gene expression was normalized to the background and the housekeepers *PPIB*, *POLR2A*, *PPIA*, *EIF4E2*, and *B2M*. The heatmap shows the Log2 fold change values of differentially expressed genes across systems. Values derived from limma analysis. Heatmaps annotated with nominal p-value groups: **P ≤ 0.05. N=3

Similar to the observation in Figure 39 A, the highest relative gene expression of the phase II enzymes was observed for freshly thawed PHHs (Figure 39 B). In 3D and OOC all investigated enzymes were also detectable after 14 days in culture. The 2.5D cocultured PHHs expressed the lowest level of phase II enzymes overall.

When examining the relative gene expression of phase III transporters, the highest expression was observed in freshly thawed PHHs, followed by the OOC system (Figure 39 C). In addition, PHHs cultured in 3D showed a moderate expression level for the examined transporters and in 2.5D an even further reduced expression was seen.

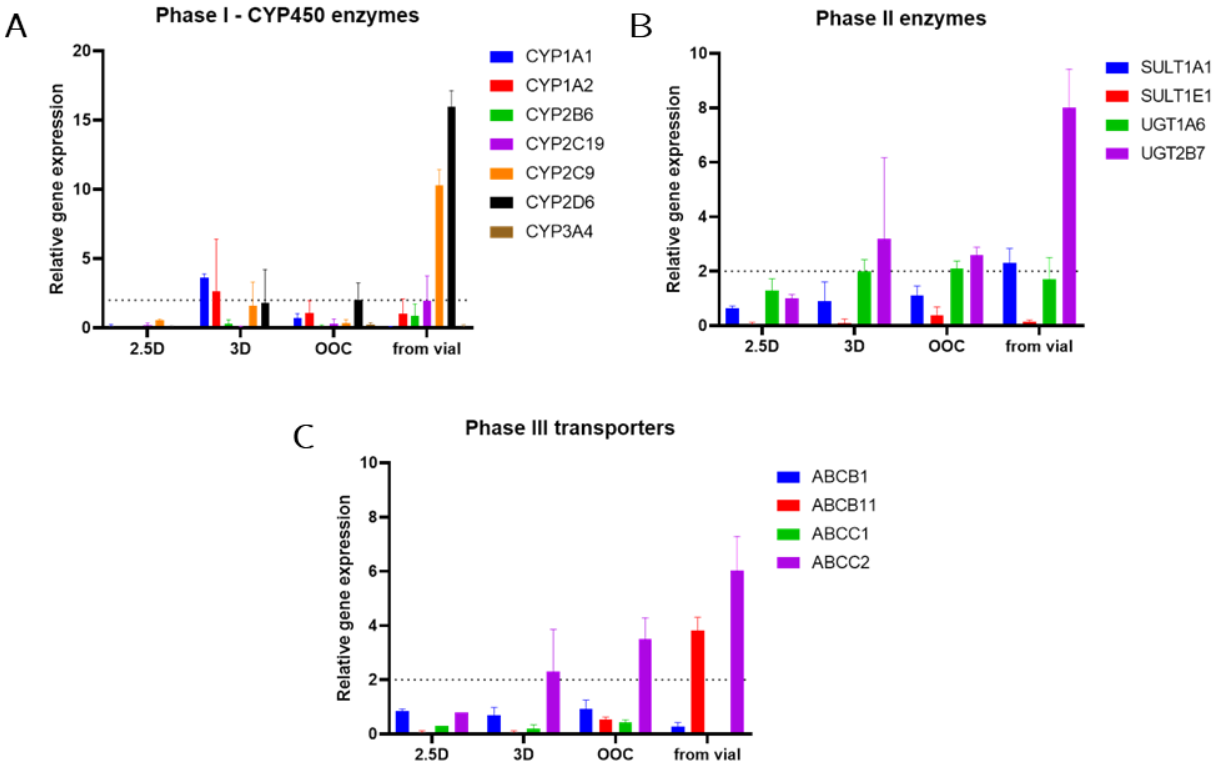

Figure 39: Metabolomic functionality of PHHs cocultured in 2.5D, 3D, and OOC.
PHH were cocultured with LSECs for 14 days in different culture models, following by lysis and genetic analysis via the QuantiGene™ Plex assay. The same PHH donor, lysed directly after thawing, serve as control (from vial). Relative gene expression of **(A)** Phase I enzymes *CYP1A1, 1A2, 2B6, 2C19, 2C9, 2D6*, and *3A4*, **(B)** phase II enzymes *SULT1A1, SULT1E1, UGT1A6*, and *UGT2B7*, and **(C)** phase III transporters *ABCB1* (MDR1), *ABCB11* (BSEP), *ABCC1* (MRP1), and *ABCC2* (MRP2). N=3

In order to analyze if the detected differences in the relative gene expression levels are significant, the expression of DMEs was assessed statistically across all systems. The heatmap in Figure 40 A visualizes differently expressed CYP450 enzymes. The expression of five CYP enzymes were statistical significantly different when comparing the 2.5D and OOC system. In the 2.5D and 3D models, *CYP2D6* ($p = 0.072$), *CYP1A1* ($p = 0.005$), and *CYP2B6* ($p = 0.018$) were significantly different. The comparison of the relative gene expression levels of CYP enzymes in the 3D and OOC model resulted in *CYP3A4* ($p = 0.065$), *CYP1A1* ($p = 0.018$), and *CYP2C19* ($p = 0.031$) as significantly different.

Figure 40 B visualizes the different expression of phase II enzymes across all systems. In general, calculated log2 fold changes were lower than in Figure 40 A. *SULT1E1* was the only gene expressed differently in the OOC system, compared with the 2.5D ($p = 0.05$) and 3D (p

= 0.03) model. Analyzing the phase III transporters, *ABCB11* (p = 0.001) was significantly different in the 2.5D versus OOC system and *ABCC2* (P = 0.095) in the 2.5D versus 3D system (Figure 40 C).

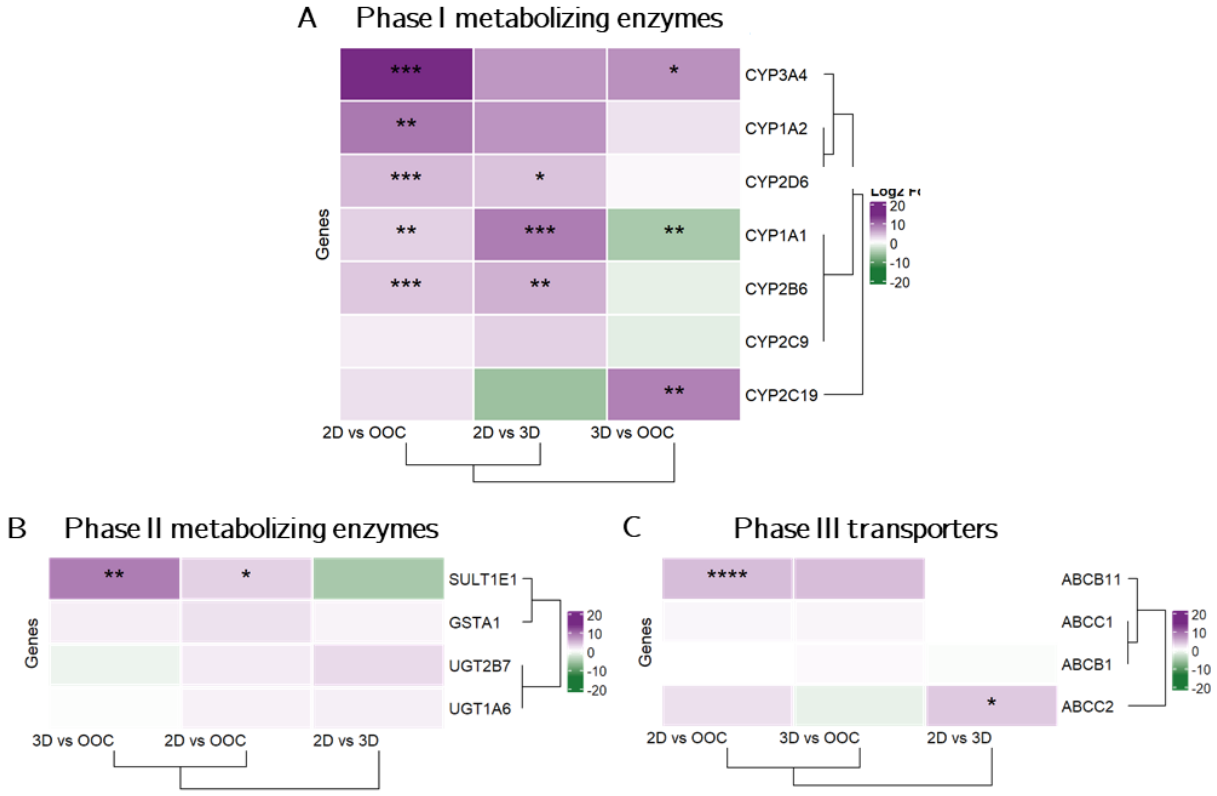

Figure 40: Heatmaps and statistical analysis of genes involved in drug metabolism.
Primary human liver cells were cultured in the 2.5D, 3D, and OOC system. At day 14, cells were lysed, and the gene expression was analyzed using the QuantiGene™ Plex method. The relative gene expression was normalized to the background and the housekeepers *PPIB, POLR2A, PPIA, EIF4E2,* and *B2M*. The heatmaps show the Log2 fold change values of differentially expressed genes across systems split into **(A)** phase I metabolizing enzymes, **(B)** phase II metabolizing enzymes, and **(C)** phase III transporters. Nominal p values derived from limma analysis. Heatmaps annotated with nominal p-value groups: *P ≤ 0.1; **P ≤ 0.05; ***P ≤ 0.01; ****P ≤ 0.001. N=3

4.4.3 Secretomics

To assess whether hepatocyte-specific functions were maintained in all culture models during the prolonged culture, media samples were collected at days 2, 7, and 14 to analyze the secretion of albumin, αGST as well as the ALT and AST activity. In addition, the elevation of LDH during the culturing time was measured in the supernatant.

In the 2.5D system, the albumin concentration fluctuated from day 2 to 14 (Figure 41 A). In contrast, the concentration remained stable in the 3D and OOC systems during the entire culture period. Furthermore, it was investigated whether the albumin concentrations would have changed significantly within the 14 days in one system using the Kruskal-Wallis test. The calculated p values for the 2.5D ($p = 0.55$), the 3D ($p = 0.19$), and OOC ($p = 0.84$) system do not indicate any significant change in secretion over the time in culture.

The cytosolic enzyme αGST is present in all cell types, but at high concentrations in hepatocytes [388]. In Figure 41 B, the concentration of secreted αGST was analyzed in all systems at three time points. In 2.5D, the αGST level was increased at day 2 and decreased strongly at day 7 and 14. The enzyme level measured in the 3D system was also increased at day 2. However, the concentration was clearly lower than in the 2.5D system. At days 7 and 14, the levels remained stable. In the 3D and OOC models, the measured αGST amount was stable from day 2 to 14 – although low. The calculated p values revealed a significant change in the secretion for the 2.5D ($p = 0.037$), and the 3D ($p = 0.018$) system. The αGST amount in the OOC ($p = 0.57$) model indicated no significant change.

In clinics, ALT and AST are biomarkers for liver damage [386][389]. Hence, the ability of PHHs to secrete ALT and AST is an important function and could be a potential predictive biomarker for DILI in preclinical phases [390]. The measured ALT and AST concentration in Figure 41 C and D showed a mainly stable secretion for all models. However, the measured values varied greatly between the technical replicates. The calculated p values indicate no significant change in the secretion of ALT nor AST.

To track the viability of the cells during 14 days in culture, the LDH amount was measured during 14 days in all models. As depicted in Figure 42, for the 2.5D and the 3D systems the mean measured LDH level was comparable at day 2. In the 2.5D model, the level decreased until day 7, but increased again at day 14 ($p = 0.095$). Cells in the 3D model showed a significant decrease in LDH release until day 14 ($p = 0.034$). In contrast, the level was stable in the OOC model ($p = 0.62$).

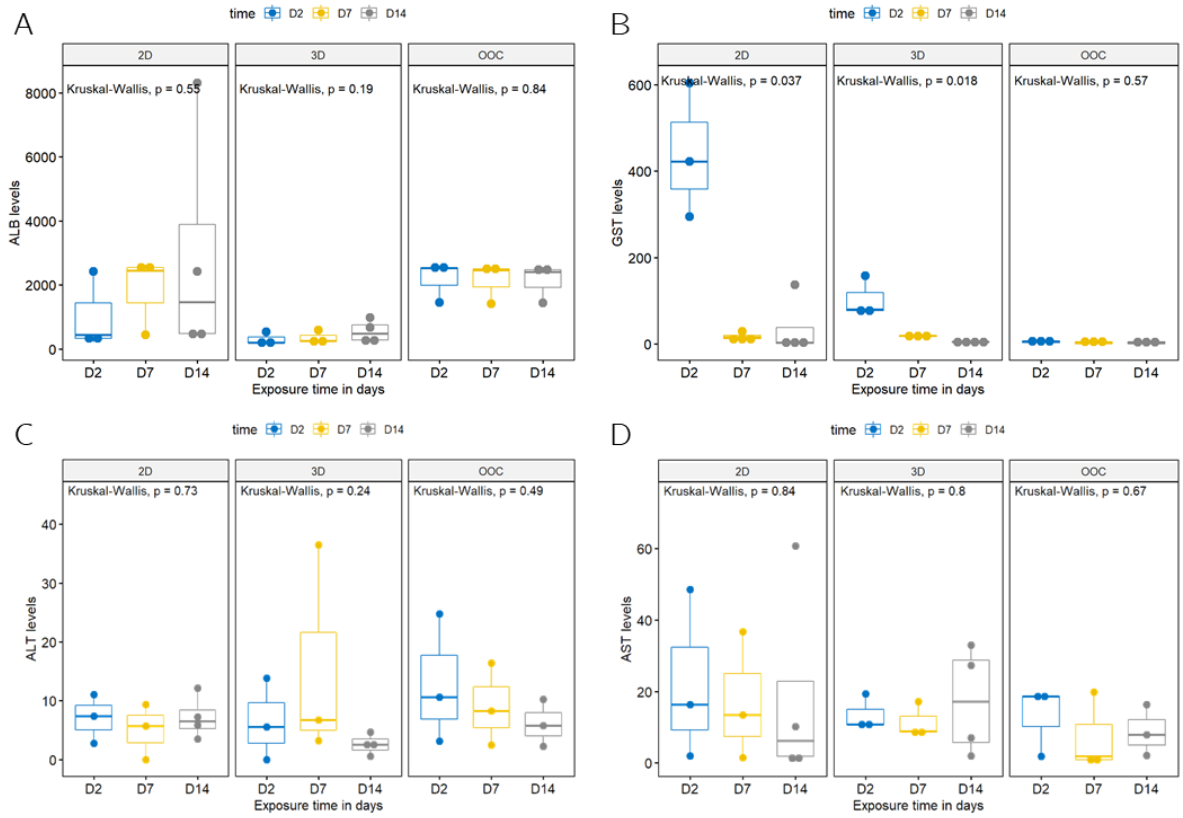

Figure 41: Secreted hepatic proteins in liver coculture models.
PHHs and LSECs were cocultured in 2.5D, 3D, and OOC for 14 days. At days 2, 7, and 14, the concentration of **(A)** Albumin (ALB), **(B)** αGST, **(C)** ALT, and **(D)** AST were measured in the supernatant. Differences in the secretion from day 2 to 14 were analyzed statistically for each system by Dilafruz Juraeva via the Kruskal Wallis test. Statistically significant $p < 0.05$; further significant $p < 0.01$; highly significant $p < 0.001$. N = 3/4.

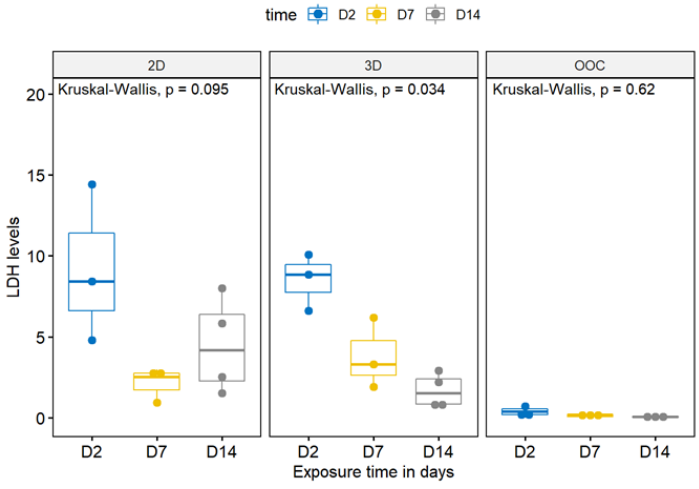

Figure 42: Measured LDH release within 14 days culture.
PHHs and LSECs were cocultured in 2.5D, 3D, and OOC for 14 days. At day 2, 7, and 14, the concentration of LDH was measured in the supernatant. Differences in the secretion from day 2 to 14 were analyzed statistically in each system by Dilafruz Juraeva via the Kruskal Wallis test. Statistically significant $p < 0.05$; further significant $p < 0.01$; highly significant $p < 0.001$. N = 3/4.

4.4.4 Proteomics

The level of expressed proteins provides an additional information on the altered molecular pathways in primary liver cells during long-term culture. To assess the differences between coculture and monoculture, the proteomic patterns were analyzed and compared in 2D, 2.5D, and 3D at time points according to Table 27.

To avoid donor specific differences, the experiments were performed with cells from the same donor. Cells out of the freezing vial served as a baseline. Proteomics analysis was performed by Thomas Wild (Section 3.6). The range of quantified proteins in the 9 plex was between 3000 and 6000. Overall, 2199 proteins were common across all samples.

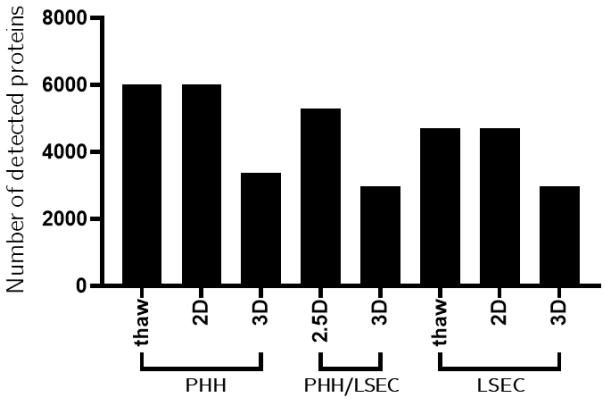

Figure 43: Number of detected proteins in the proteomics analysis.
PHHs and LSECs were thawed and cultivated in mono- and coculture in a 2D, 2.5D, and 3D model. Freshly thawed and cultured cells were harvested, lysed, and analyzed via MS. N=1

In this work, 6025 proteins were detected in freshly thawed PHHs and PHHs cultured in 2D (Figure 43). In 3D cultured PHHs, 3374 proteins were identified. In the PHH/LSEC coculture models, 5294 proteins were detected in 2.5D and 2975 in 3D. Freshly thawed and 2D cultured LSECs yielded in 4700 proteins. 2975 proteins were identified in LSECs cultured as 3D spheroids. In general, higher numbers of proteins were detected in freshly thawed and 2D/2.5D cultures.

To get a first insight into the impact of the culture system on the liver cells, a PCA was performed. The PCA plots in Figure 44 captures the most (PC1) and the second most (PC2) important parameters that caused this variation in the data. The PCA of all samples resulted in a clear separation according to the culture type. PHHs and LSECs analyzed directly after thawing differed most in the PC2 direction. In order to get an overview about the potential influence of the culture configuration on hepatocytes, Figure 44 B illustrates the generated data without the LSEC samples. A clear distinction between the 2.5D and the 3D samples was observed in the PC1 direction. PHHs after thawing differ most from cells in culture in the PC2 direction.

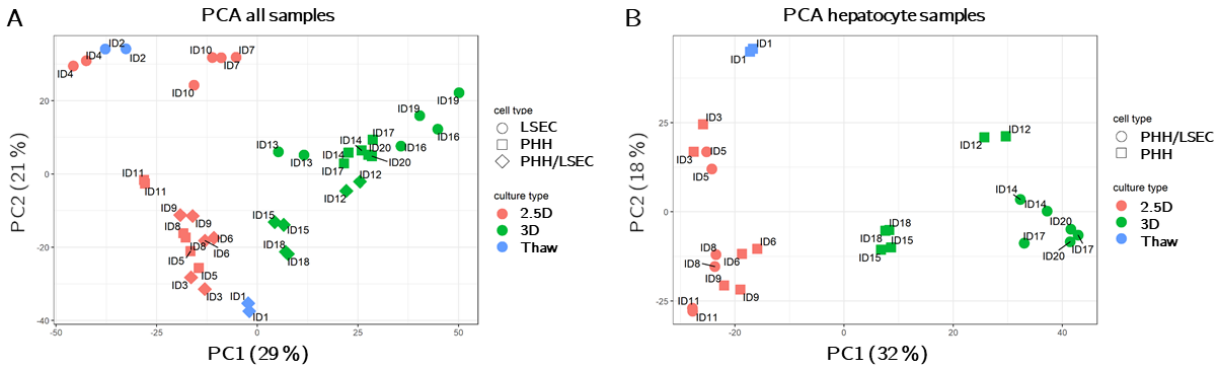

Figure 44: PCA of detected proteins.
PCA was performed by Thomas Wild with proteins detected in (A) all samples and (B) in hepatocyte-containing samples. N=1

The heatmap in Figure 45 shows the pathways with the highest association calculated with the three different web-based pathway tools KEGG, Gene Ontologies, and Wiki Pathways. The proteins of PHHs in 2D culture closely clustered with PHH/LSEC in 2.5D. Likewise, the expression of the 3D mono and coculture showed a predominantly similar pattern for the upper two clusters, but a different for the bottom clusters.

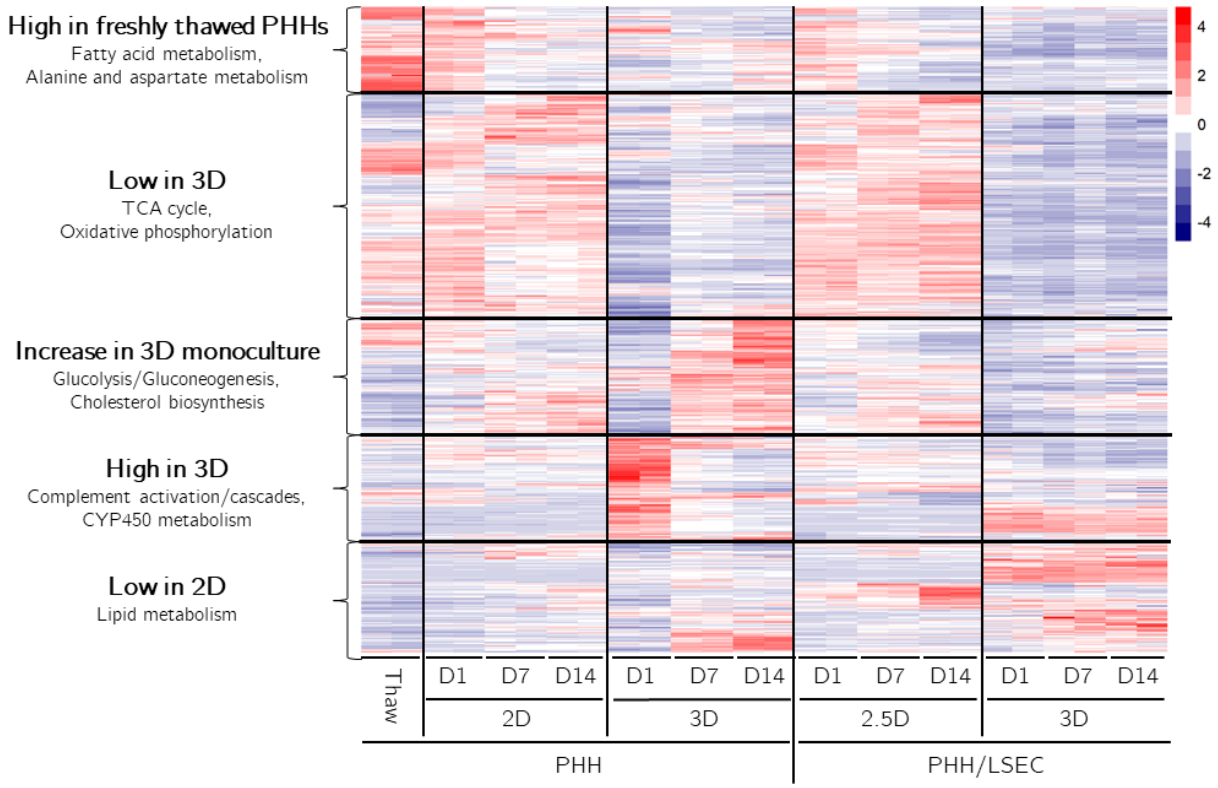

Figure 45: Proteomic profile and pathway analysis of *in vitro* liver models.
Proteomics analysis detected proteins in freshly thawed, mono- and cocultures liver cells (2D, 2.5D, and 3D). Heatmap (generated by Thomas Wild) shows the Z-score of found proteins clustered using the Pearson method. Pathway analysis was performed by Nicholas Geraci using the Cytoscape plugin JEPETTO. N=1

As seen in the first cluster, the proteins found in freshly thawed PHHs already differs to D1 in all culture models. The most associated pathways found for this cluster were fatty acid, and alanine and aspartate metabolism. Next, the second cluster shows a decreased proteomic profile in 3D associated with *tricarboxylic acid cycle* (TCA) cycle and oxidative phosphorylation. In the third cluster an increase in protein expression was detected for the 3D monoculture from day 1 to 14. According to the pathway analysis, glycolysis/gluconeogenesis and cholesterol biosynthesis were driving this change. The fourth cluster shows a decreased complement activation and CYP450 metabolism for the 2D culture models. In addition, pathway analysis of the fifth cluster revealed a reduced lipid metabolism in 2D cultures.

As mentioned previously, drug metabolism plays an important role in the toxicity of a number of compounds [387]. Hence, the stability of DMEs and transporters was investigated in the PHH mono- and cocultures at three time points (day 1, 7, and 14) (Figure 46). Only the proteins found in all systems were integrated into the heatmap. DMEs that did not reach the LOD in any one system were excluded.

The highest level of phase I enzymes was detected in freshly thawed PHHs. No cell system showed stable expression levels of CYPs during the studied period. In general, PHH monocultures exhibited a slightly higher level than the cocultures. Phase II enzymes seemed to increase during culturing, as the levels in freshly thawed cells was lower. In 2D mono- and cocultured PHHs, an increase was observed at day 1 and 7, followed by a decrease at day 14. In contrast, phase II enzyme levels increased in 3D cultured PHHs at day 7 and 14 whereas cocultured liver cells exhibit an overall low expression. Phase III transporters also increased in cultured PHHs, compared to the low levels in freshly thawed cells. However, the expression varied greatly from day 1 to day 14. The lowest levels were also observed in the 3D coculture model.

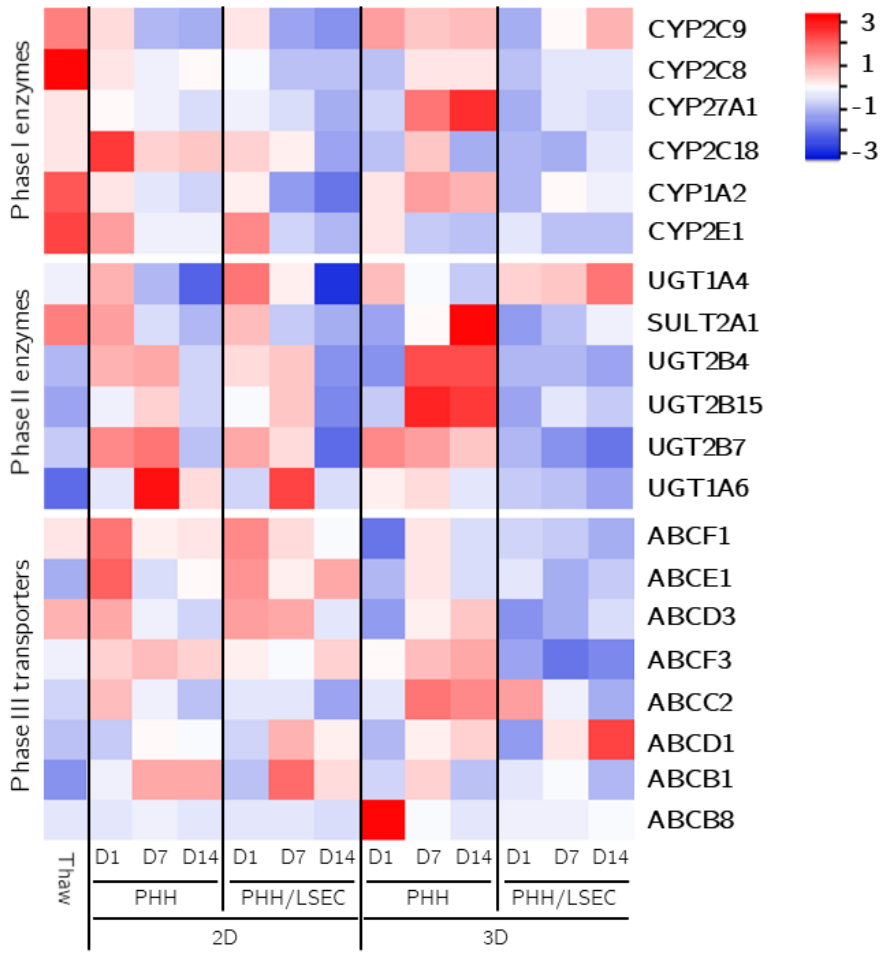

Figure 46: Proteomic analysis of DMEs in 2D/2.5D and 3D mono- and coculture.
PHHs and LSECs were thawed and seeded in 2D, 2.5D, and 3D in mono- and coculture. At days 1, 7, and 14, cells were lysed, and proteins were analyzed by MS (performed by Thomas Wild). Heatmap shows Z-scores calculated for each gene and clustered using euclidean distance. N=1

4.4.5 Metabolomics

Metabolites are substances that are formed as intermediates or as degradation products of metabolic processes of the organism. In this work, the metabolic patterns of primary liver cells cocultured in the three advanced cell culture systems were investigated and compared. As it was suspected that the functionality of liver cells decreases rapidly in the 2.5D system, the culture period was shortened to 6 days (twice as long as the described retention of metabolic activity in PHHs). To avoid donor-specific differences, the same PHH and LSEC donors were used in all models. Cells out of the freezing vial and fresh media served as the baseline.

Samples were analyzed by Biocrates using the MxP® Quant 500 assay. The MxP® Quant 500 kit covers up to 630 metabolites from 26 biochemical classes [364]. As shown in Figure 47 A, in total 625 metabolites were detected from an assay in this study. Of them, 274 metabolites were detected in the lysate and 436 in the supernatant. Figure 47 B illustrates the distribution of metabolites in lysates and supernatant. In total, eleven metabolite classes were found in the analyzed samples. The number of cholesteryl esters and phosphatidylcholines make up the

largest share. Followed by amino acids and ceramides. In addition, fatty acids, triglycerides, and bile acids could be detected.

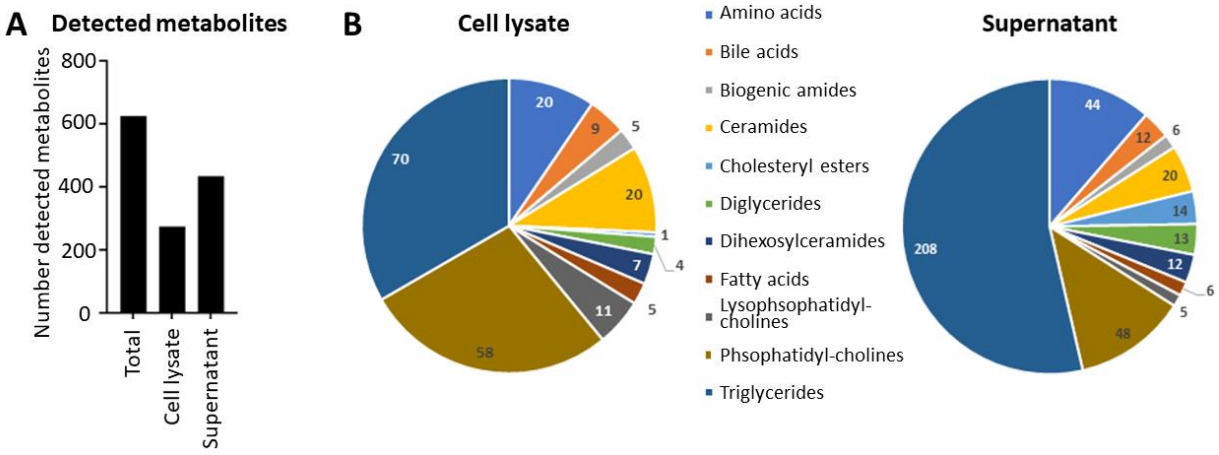

Figure 47: Data set overview of detected metabolites.
Liver cells from the same donor were thawed and cultured in different culture systems. Metabolites were measured in the supernatant and cell lysate for different time points using the MxP® Quant 500 assay. **(A)** Number of detected metabolites in total, lysate, and supernatant. **(B)** Pie chart of the distribution of detected metabolites in eleven metabolite classes. N=1

The raw data was cleaned to exclude analytes with too many concentration values missing or below the LOD. To assess the impact of the culture system on the liver cells a PCA was performed on the metabolic features for each sample type. The PCAs in Figure 48 were generated by Alex Rolfe and capture the most (PC1) and the second most (PC2) parameters that cause the variation in the data. The PCA of both sample types resulted in a strict separation between the culture systems. In Figure 48 A, cells cultured in the 2.5D, 3D, and OOC-quad systems differed most from the OOC coculture (OOC-bi) in the PC1 direction.

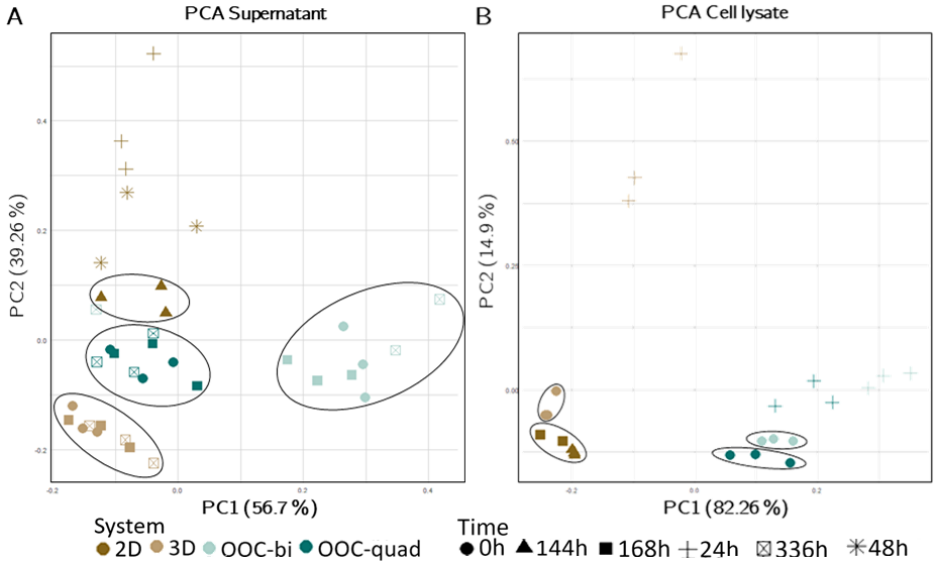

Figure 48: PCA of detected metabolites.
PCA was performed by Alex Rolfe with metabolites detected in the **(A)** supernatants and **(B)** cell lysates. N=1

For lysate samples in Figure 48 B, cells cocultured in 2.5D and 3D varied most in PC1 from the OOC model. The variation in PC2 direction was low. The highest and lowest inputs responsible for the shifts in Figure 48 are described in Table 31. Triglycerides, phosphatidylcholines, and cholesteryl esters were the metabolite classes predominantly responsible for the variations in the PCA plots.

Table 31: Metabolites with highest variation causing the shifts in the PCA plots.
Metabolites were analyzed in supernatant and cell lysate by Biocrates using the MxP® Quant 500 assay.

Comparator	Highest input (Supernatant)	Highest input (Cell lysate)
2D to OOC-Bi	Triacylglycerides, Phosphatidylcholine, Sarcosine	Triacylglyceride, Trihexosylceramide, Phosphatidylcholine
OOC Quad to. OOC-Bi	Lysophosphatidyl-choline, 3-Methylhistidine, Glycodeoxycholic acid, p-Cresol	-
3D to OOC-Bi	Triacylglyceride, Cysteine	Cystine, Triacylglyceride, Cholesteryl ester
3D to OOC-Quad	-	Cystine, 3-Methylhistidine, Cholesteryl ester, Arginine
2D to OOC-Quad	-	Taurine, Phosphatidylcholine, Triacylglyceride

In order to compare the impact of the culture system to the production of metabolites in 2.5D, 3D, and OOC, the detected metabolites were counted in both, cell lysate and supernatant (Figure 49). Subsequently, the number was compared with the total amount of metabolites studied (total = red bar) and the differences between the systems themselves. The bar graph in Figure 49 A showed no major changes in amino acids, bile acids, and fatty acids. In all systems, only half as many triglycerides were detected as were examined. For phosphatidylcholines, a lower number of metabolites was observed in 2.5D and 3D. Figure 49 B depicted the number of detected metabolites in the supernatant. 42/48 phosphatidylcholines were found in the OOC cocultured with PHHs and LSECs. For triglycerides, the lowest number was found in the 3D samples, with the number of metabolites almost doubling during cultivation (from 35 at day 1 to 68 at day 14). 18/19 amino acids were detected in the 3D sample at day 14. In contrast the number of amino acids in the supernatant was weak for all other systems (2-7/19). The largest number of bile acids and fatty oleic acids were found in the OOC coculture. A more detailed insight into the distribution of detected bile acids can be seen in Figure 50.

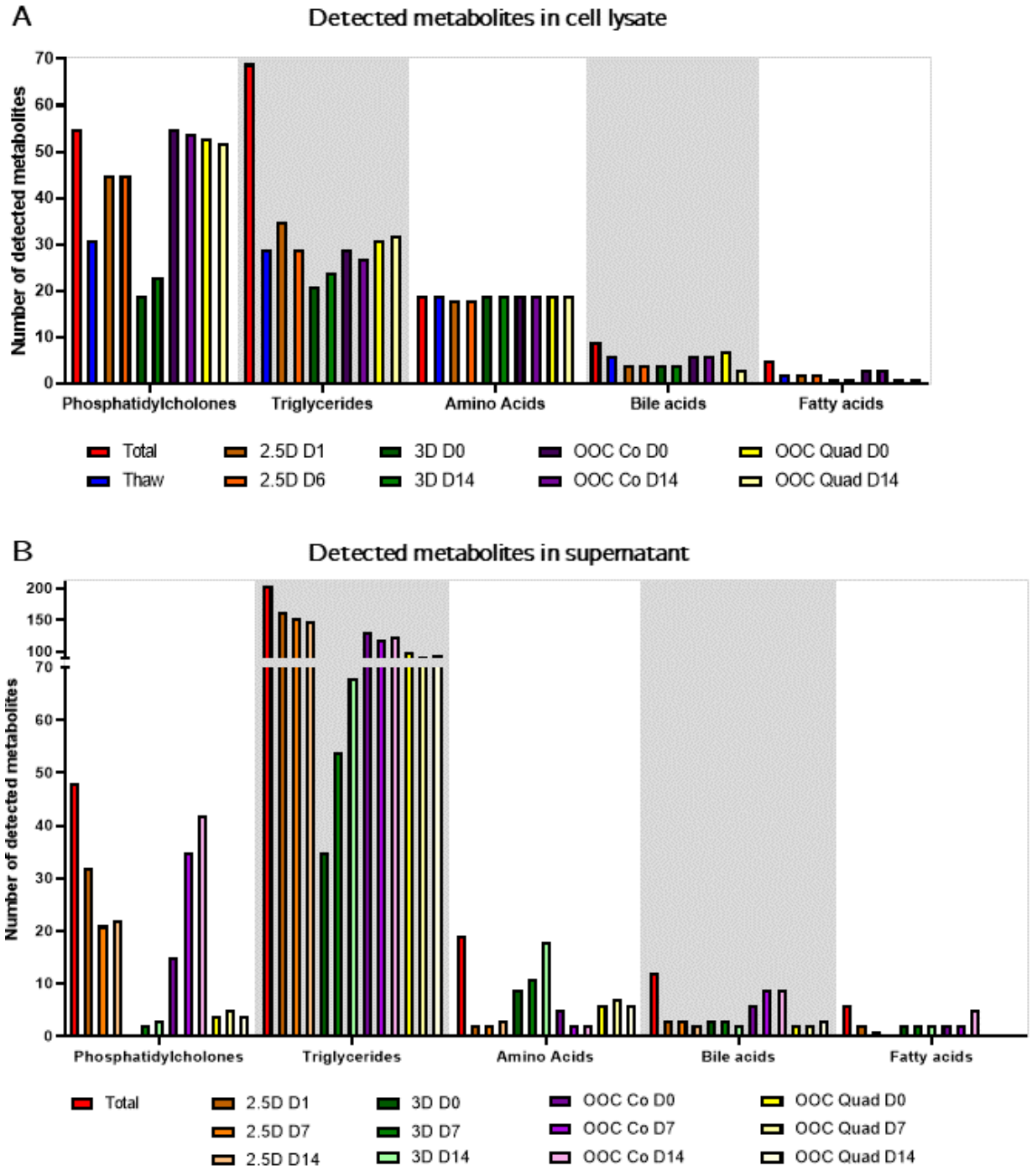

Figure 49: Number of detected metabolites in cell lysate and supernatant.
Liver cells of the same donors were cultured in different culture systems. Metabolites were detected at several time points in the cell lysate and medium supernatant. Bar graphs visualize the number of detected metabolites in **(A)** cell lysate and **(B)** supernatant. N=1

Bile secretion is an important function of hepatocytes. In addition, bile acids are crucial regulatory factors [193]. Therefore, the ability of PHHs to produce and secrete bile acids was analyzed and compared between the systems. In this present metabolomics study, twelve bile acids were analyzed in all systems and samples. No detection was possible in some samples or at specific time points. Bile acid levels were higher in the OOC systems than in 2.5D and 3D, in both, lysates and medium supernatant. Intracellularly, the amount of bile acids in the

OOC decreased from day 1 to 14. For the bile acids present in the medium, this was only seen in some cases. In general, it remained stable or even decreased during the study time. Lower levels of intracellular bile acids were observed in the 3D and 2.5D systems after quantification of the changes with freshly thawed cells. This was also observed for the supernatants in the 3D cultures which did not show an increased concentration of bile acid compared to fresh medium. In the 2.5D model, glycocholic acid, taurocholic acid, and glycolithocholic acid sulfate were detected in the supernatant after normalization to the fresh blank medium.

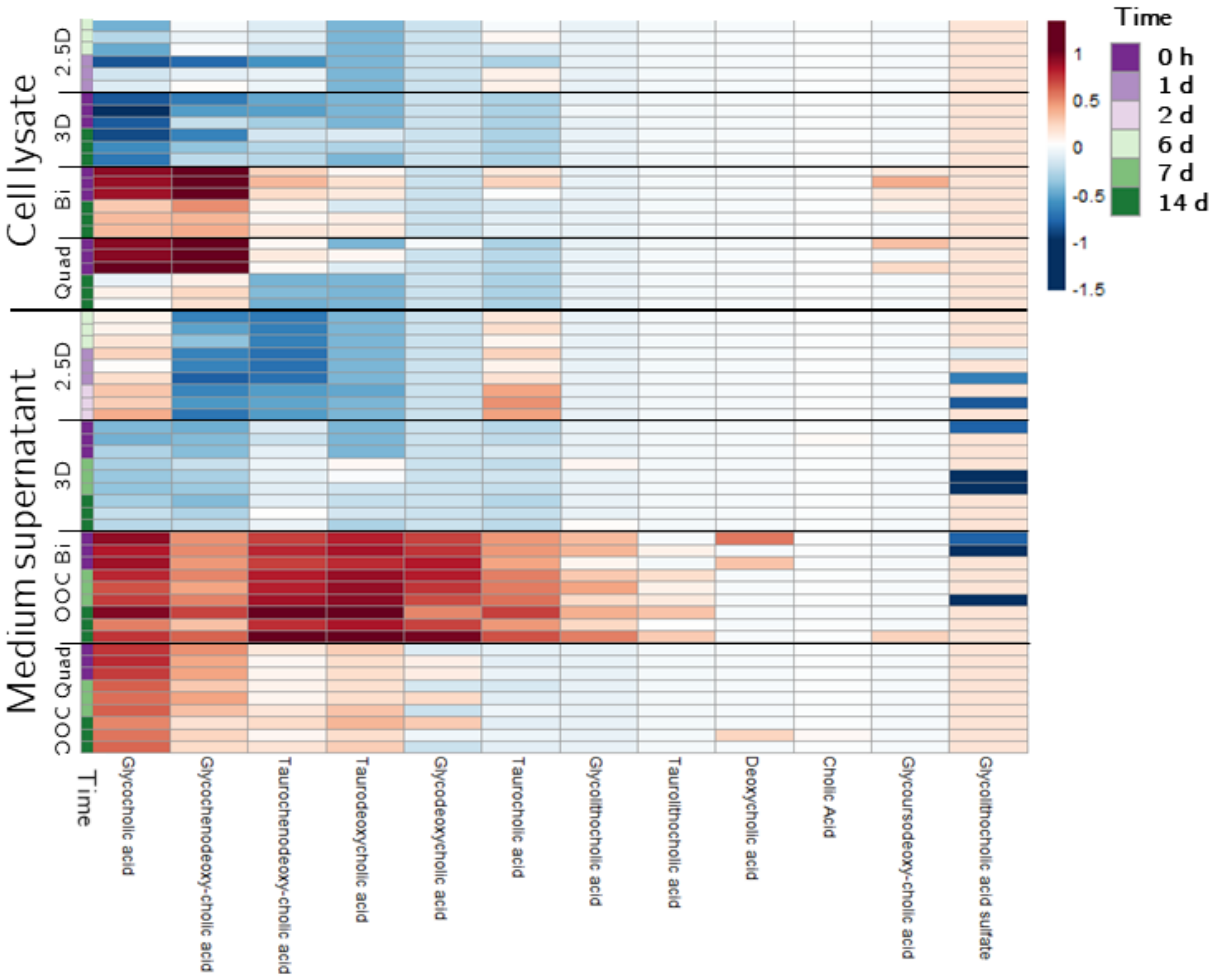

Figure 50: Heatmap of bile acids detected in 2.5D, 3D, and OOC cultured PHHs.
PHHs were thawed und cultured for several days in 2.5D (6 days), 3D (14 days), and OOC (14 days). Cell lysate samples were collected at the beginning and end of the study. The supernatant of the medium was analyzed at the beginning, middle, and end of the study. Freshly thawed PHHs and fresh culture medium serve as baseline. Heatmap was generated by Alex Rolfe and shows fold change of detected bile acids. N=1

4.5 Identification of novel DILI biomarkers

Today, DILI is very challenging to predict in *in vitro* cell culture studies. Beside the rapid decrease of functionality of 2D cultured PHHs, one reason is also attributed to the lack of biomarkers to reliable determine and detect DILI. To test and identify clinically used and potential novel biomarkers, the established advanced liver cell models were treated with compounds defined as “most-DILI-concern” and “less-DILI-concern” (AIM_4) for 14 days. The response of the cells to the compounds in 2.5D, 3D, and OOC was studied by analyzing specific genes and secreted proteins described in literature as “potential” *in vitro* DILI biomarkers (AIM_5).

4.5.1 *In vitro* dose finding study

Drug-induced cytotoxicity can be measured by the decrease in the total cellular ATP content.

A dose finding study was performed to define a suitable treatment concentration for the advanced *in vitro* models. The aim was to identify concentrations that provoke a response of the cells but maintain sufficient cell viability. The calculated EC_{50} values were examined in the 2.5D and 3D coculture models for twelve compounds in seven concentrations each (Table 17). For the most-DILI-concern-drugs DIC, APAP, and LVX, EC_{50} values could not be detected in the tested concentration range for both systems (Figure 51). For the less-DILI-concern-drugs, an EC_{50} could be calculated for each substance. In general, a higher EC_{50} value was detected in the 3D model, than in the 2.5D.

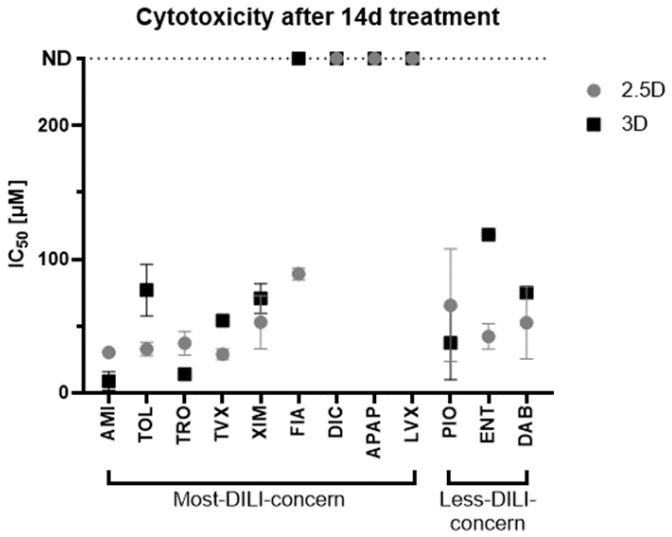

Figure 51: Examined EC_{50} values after 14 days treatment.
Both coculture systems were treated for 14 days with seven concentrations of drugs known to cause and not cause DILI. Cell viability was examined using the ATP CellTiterGlo® assay. Data is expressed as mean for multiple measurements. (ND: not detectable) 2.5D: N=2/5; 3D: N=1/3

4.5.2 Compound distribution within the Emulate OOC

The Emulate OOC is composed of PDMS. PDMS is known to absorb small molecules such as drugs [307]. Compounds with high hydrophobicity (log P > 2.67) show high absorption by PDMS [308]. Therefore, the physicochemical properties of the selected compounds were investigated for their application in the PDMS-based MPS. Chips without cells were cultured with PHH and NPC medium, supplemented with a specific compound concentration (Table 24).

Figure 52 shows detected initial concentrations in the inlet medium (0 h) compared to the flow through medium in the outlet reservoirs for three time points. The blue baseline visualizes the calculated target concentration. For XIM (Figure 52 A) and TOL (Figure 52 E) measured compound concentration was comparable to the initial concentration. For ENT (Figure 52 F) and PIO (Figure 52 D), a lower concentration was detected only in the top channel. In percentage terms, the difference was greater for PIO (~ 50 % decrease) than for ENT (25-50 % decrease). The bottom channel revealed minor changes. TRO (Figure 52 C) and DAB (Figure 52 B) differed strongly to the baseline in both media. Consequently, XIM, TOL, and ENT were included into the OOC experiments whereas TRO, PIO, and DAB were only tested in the 2.5D and 3D model.

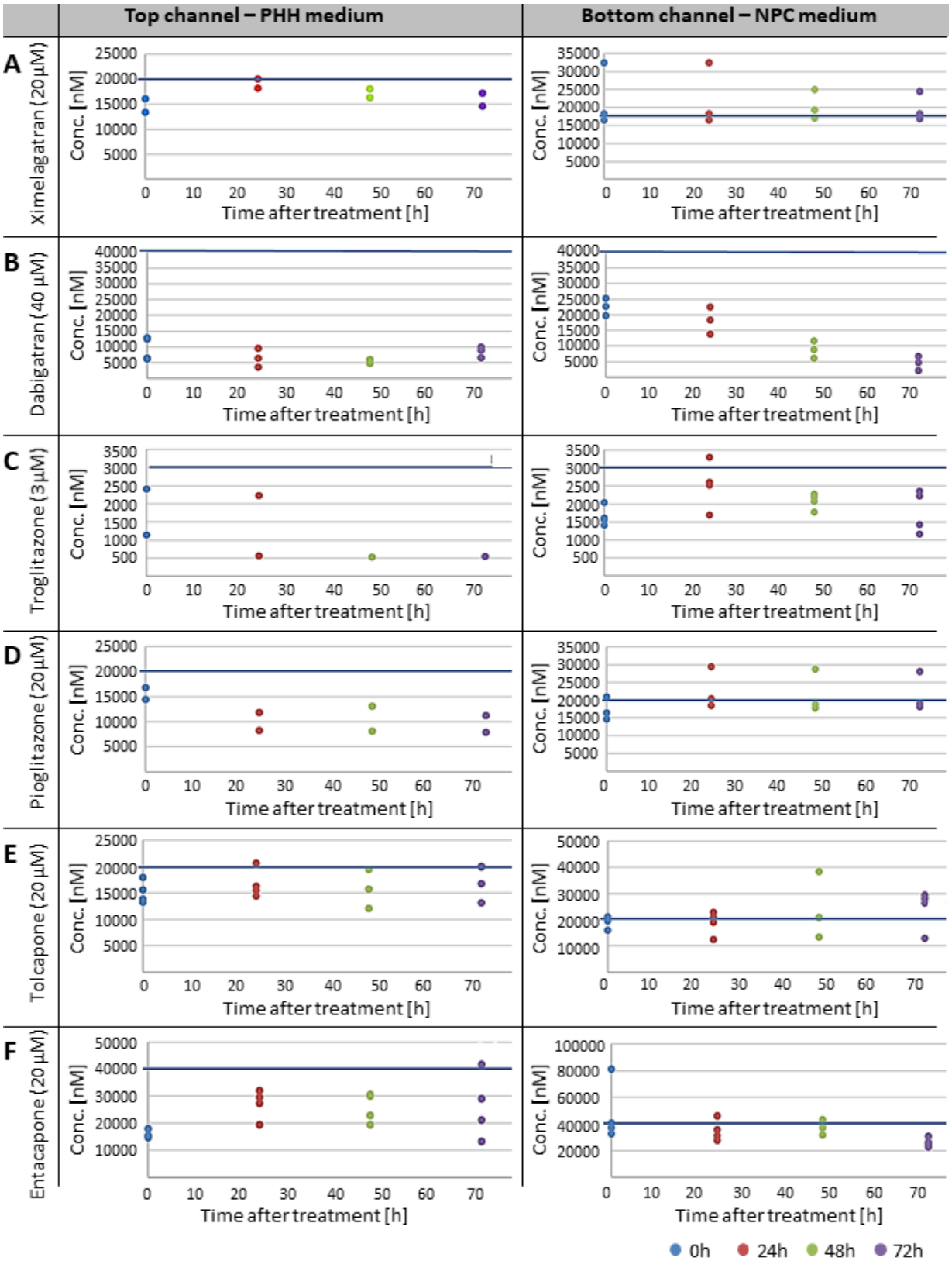

Figure 52: Detected compound concentrations in the OOC using the CDK.
Empty Emulate OOC were cultured with PHH and NPS medium supplemented with the target compound concentration (blue line). Concentrations from the inlet reservoir serve as control (0 h, blue). Media samples were collected from the outlet reservoir at time points 24 h (red), 48 h (green), and 72 h (violet), and analyzed via MS (by Anindya Siddharta). The undiluted samples and the 1:10, 1:100, and 1:1000 dilutions were analyzed and visualized in separate data points in the graph. N=1

4.5.3 Level of secreted hepatic proteins after during long-term treatment

The liver is the largest gland secreting a variety of compounds, such as bile acids and hormones. Specific secreted hepatic proteins can indicate hepatocellular damage. In the context of DILI, biomarkers such as ALT and AST are already routinely used for clinical diagnosis. *In vitro,* DILI cannot yet be predicted due to the lack of appropriate biomarkers. There is an increasing demand for new potential biomarkers for the early detection of DILI in preclinical studies. Recent publications have described potential biomarkers such as albumin, αGST, ALT, AST or LDH [186]. These biomarkers should be able to detect drug-induced hepatotoxicity *in vitro*. In this work, these biomarkers were tested in advanced cell culture models for their ability to specifically discriminate between most- and less-DILI-risk compounds (AIM_5).

Albumin is a universally used hepatocyte functionality marker. However, abnormal secretion is associated with tissue damage [186]. The reaction of the cells was investigated after 14 days treatment with the selected compounds (AIM_4). In Figure 53 A, a decreased albumin secretion was observed for ENT, XIM, TOL, APAP, and AMIO. In contrast, a slightly increased level was detected for MET-, PIO-, DAB-, and FIA-treated cells. The same pattern in decreased expression was also observed for the 3D spheroids (Figure 53 B). In 3D, an increase in albumin secretion was observed after treatment with FIA, DIC, and LVX. In contrast, the cells in the OOC showed little change in secretion during the treatment period (Figure 53 C). A slightly, but consistent decrease was seen for TOL, FIA, and APAP at days 7 and 14.

The enzyme αGST is quickly released from damaged hepatocytes in to plasma and thus is a promising *in vitro* biomarker for the detection of liver injury [181]. In Figure 53 D, eight compounds exceeded the set threshold value of 2, in the 2.5D model (MET, DAB, ENT, TOL, APAP, LVX, AMIO, BOS). These included compounds from both, the most- and less-DILI-concern groups. In the 3D model (Figure 53 E), four compounds exceeded the threshold, however, all were part of the most-DILI-concern test compounds (FIA, DIC, LVX, BOS). In the OOC model (Figure 53 F), an increase in αGST secretion was observed for TOL, DIC, and LVX.

The level of serum ALT and AST is the gold standard for *in vivo* detection of liver injury [181]. In this work, the enzymes were analyzed in the supernatant after treatment to determine whether they are suitable for the *in vitro* detection of DILI. Figure 68 shows the fold changes of the extracellular detected ALT concentration normalized to the vehicle control. The threshold value was exceeded in the 2.5D model (Figure 68 D). The elevation was unspecific, being observed in both, most- and less-DILI-concern compounds. The measured AST values did not exceed the threshold in any model (Figure 68 A - C).

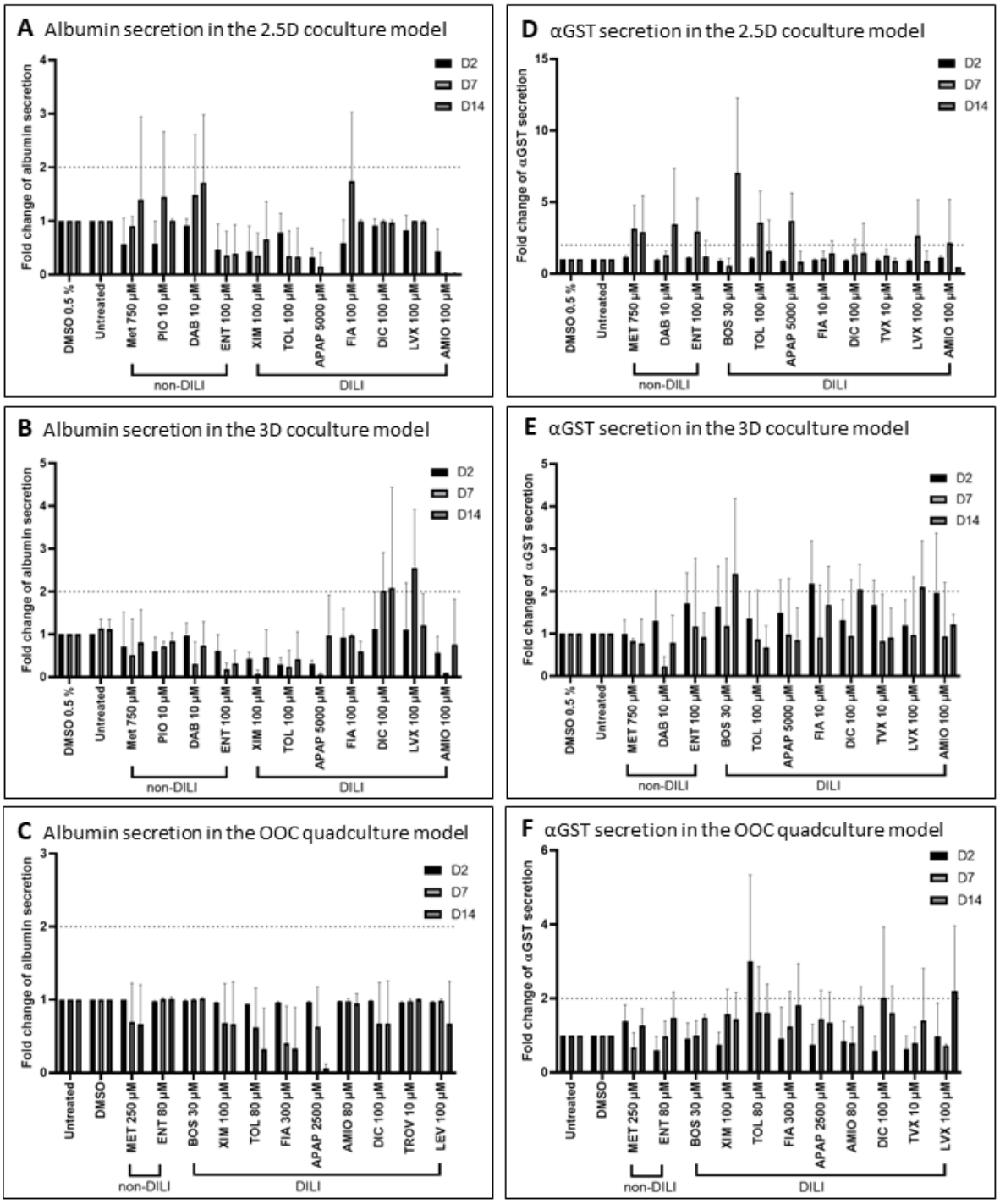

Figure 53: Fold change of albumin and αGST secretion in 2.5D, 3D, and OOC.
Primary liver cells were treated for 14 days in the advanced cell culture systems with most-DILI-concern (DILI) and less-DILI-concern (non-DILI) compounds. At days 2, 7, and 14, medium supernatants were collected: Albumin concentration was detected using the Albumin SimpleStep ELISA Kit from Abcam (ab179887). AGST concentration was detected using the Human Alpha GST ELISA of TECO Medical (TE1056). Left graphs show the fold change of albumin secretion normalized to vehicle control **(A)** in 2.5D **(B)** 3D, and **(C)** OOC (N=3/4). Right graphs show the fold change of αGST secretion normalized to vehicle control for **(D)** in 2.5D **(E)** 3D, and **(F)** OOC (N=3). The threshold value was set at 2.

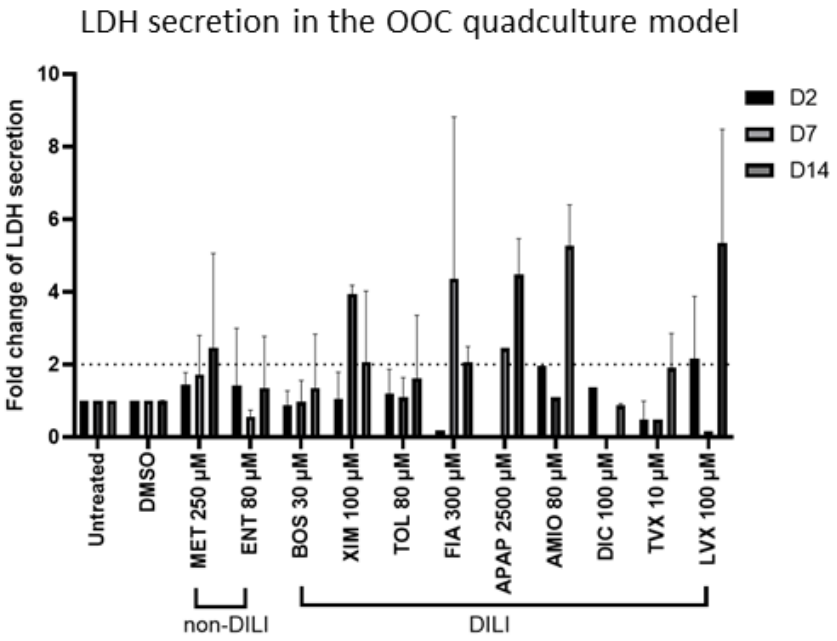

Figure 54: Fold change of LDH secretion in OOC normalized to vehicle control.
Primary liver cells were treated for 14 days in the OOC system with most-DILI-concern (DILI) and less-DILI-concern (non-DILI) compounds. At days 2,7, and 14, medium supernatants were collected, and the LDH concentration was detected using the LDH-Glo assay of Promega (J2380). Graphs show the fold change of LDH secretion normalized to vehicle control in the OOC model. The threshold value was set at 2. N=3.

Figure 54 and Figure 69 depicted the fold changes of the LDH concentration normalized to vehicle control. LDH is widely used as cytotoxicity marker and rapidly released into the culture medium upon disruption of the plasma membrane [367]. In this work it was used to assess the viability when measuring potential biomarkers. In the OOC model, cytotoxicity levels reached the threshold (Figure 54). In contrast, decreased LDH levels were observed in 2.5D and 3D after treatment with APAP (Figure 69).

4.5.4 Expression level of potential novel genetic biomarkers after 14 days treatment

Studying the gene expression profile is widely used to understand cellular mechanisms and the mechanism of toxicity, including the pathogenesis of DILI [391]. In addition, it is described as a promising tool for identifying potential new biomarkers for the early *in vitro* detection of DILI due to the broad range of data generated [93]. In this study, published potential novel DILI biomarkers were investigated in three long-term, drug-treated advanced cell culture models using known drugs that cause DILI or are safe from developing DILI.

The expression of eleven potential genetic DILI biomarkers was investigated after 14 days of treatment. Very low expression was detected for *CDH5* and *FASLG*, which was insufficient for comparison between 2.5D, 3D, and OOC. In addition, no treatment condition strongly induced an increase of the genes *CSF1*, *HMGB1*, *KRT18*, and *SDHA* (Figure 55). In Figure 56 A, an elevated gene expression was observed for 2.5D cocultured cells treated with BOS. Similarly,

SPP1 showed an increased level after treatment with AMIO and BOS (Figure 56 E). *SPP1* was also increased after treatment with AMIO in the 3D culture model, however, the expression was also elevated with TOL and APAP. Furthermore, *GLUD1* was increased in one condition in both, 2.5D and 3D (Figure 56 C). In 2.5D, two treatments (XIM, TOL) and in 3D, only cells treated with APAP reached the threshold value of 2. In addition, after treatment with PIO, DIC, and LVX, the expression of *FABP1* was increased in 2.5D and 3D (Figure 56 B). The gene expression level of *GSTA1* showed an increase for all advanced culture models. With DIC and TVX the threshold value was reached in all models. Furthermore, *GSTA1* was increased in 2.5D after MET and LVX, in 3D after APAP and LVX, and in OOC after ENT, BOS, and APAP treatment (Figure 56 D).

In general, liver cells cultured in the OOC showed no response to treatment in 10/11 studied potential genetic biomarkers. Highest fold changes, after 14 days treatment, were detected for the 2.5D and 3D culture model.

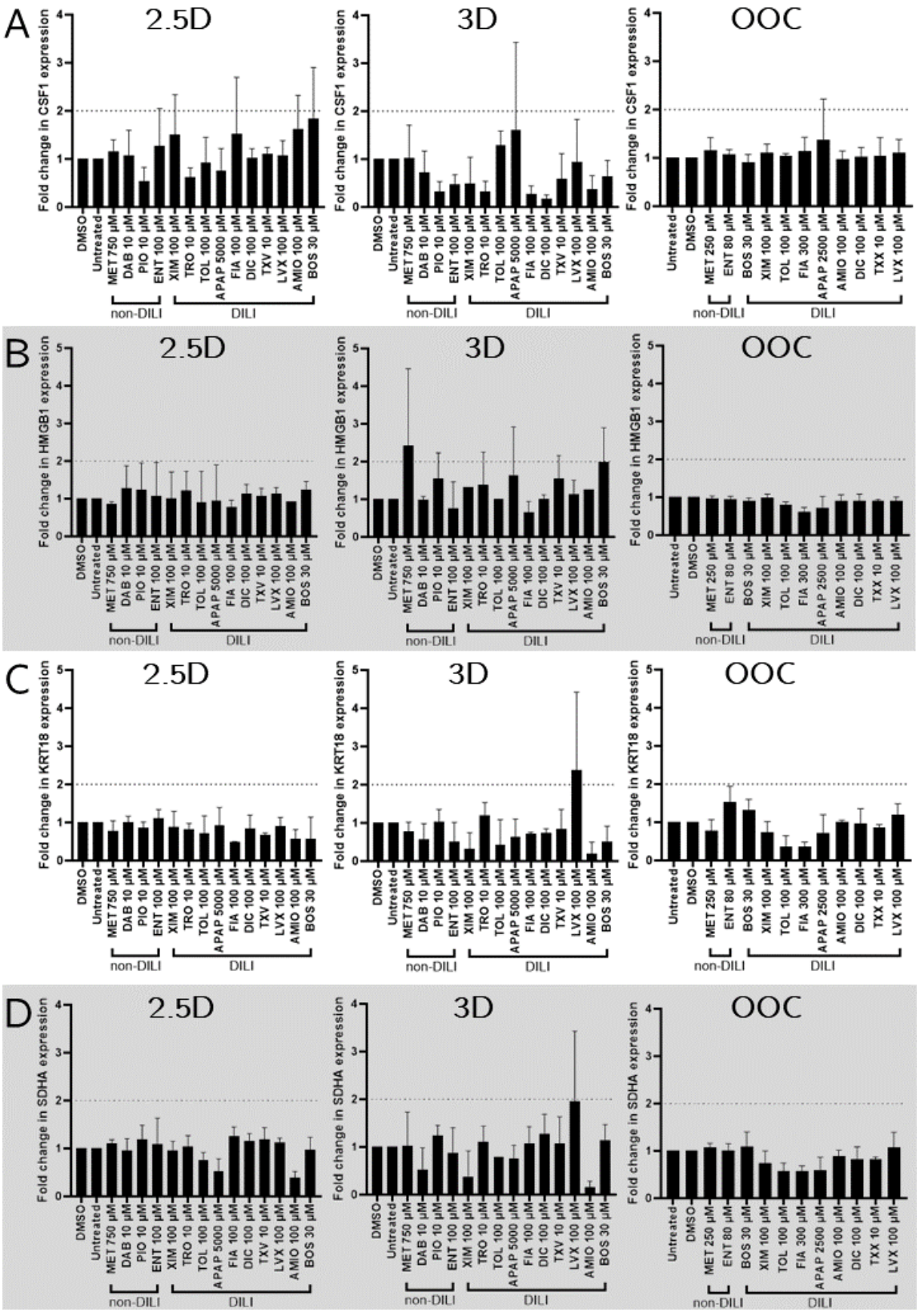

Figure 55: Fold change in gene expression of potential biomarkers *CSF1*, *HMGB1*, *KRT18*, and *SDHA*.
Primary liver cells were treated for 14 days in the advanced cell culture systems with most-DILI-concern (DILI) and less-DILI-concern (non-DILI) compounds. At day 14, cells were lysed, and gene expression was analyzed by the QuantiGene™ Plex assay. Graphs show the fold change of **(A)** *CSF1*, **(B)** *HMGB1*, **(C)** *KRT18*, and **(D)** *SDHA* expression normalized to vehicle control in 2.5D, 3D, and OOC. The threshold value was set at 2. N=3/4.

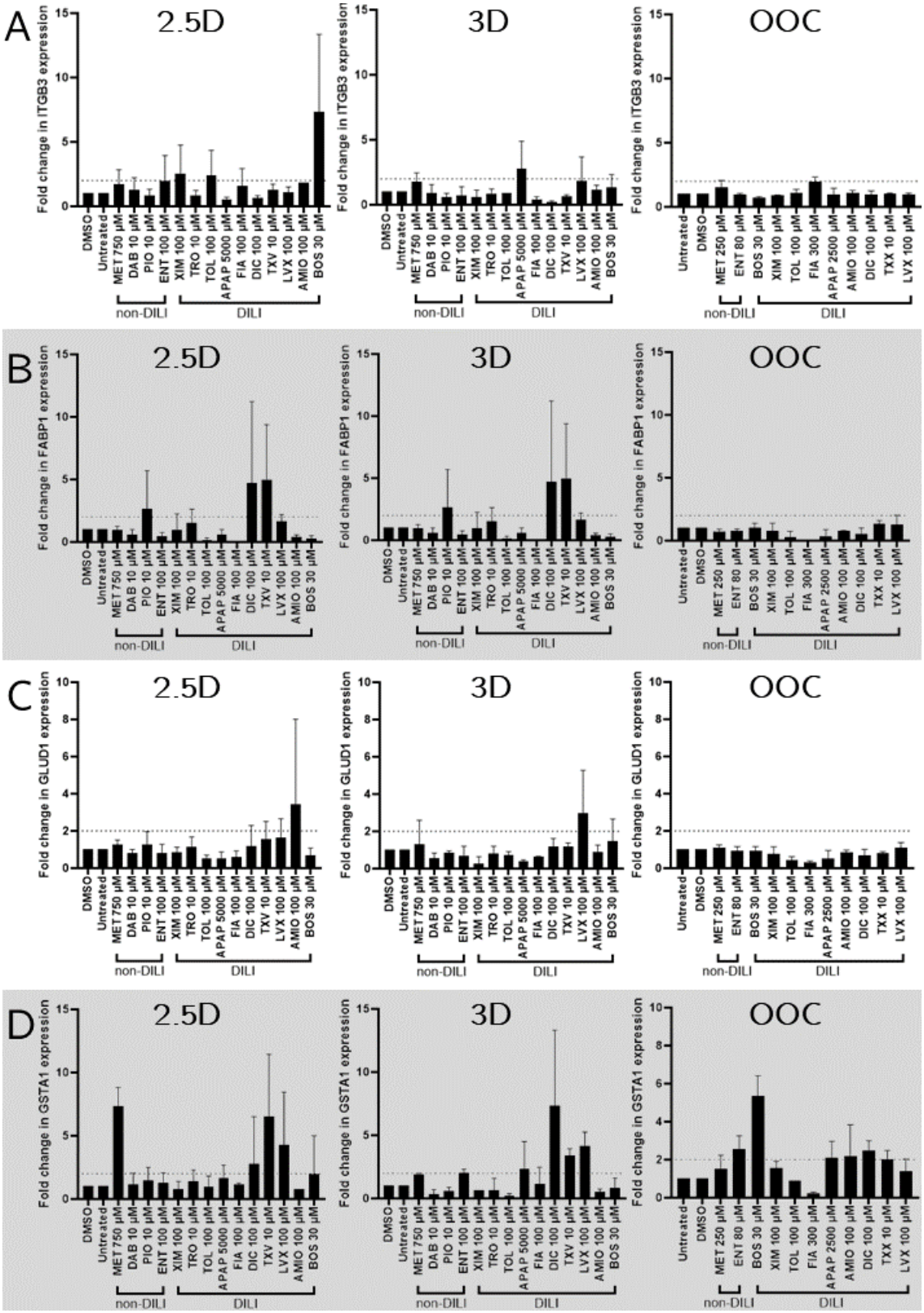
A
2.5D
3D
OOC
Fold change in ITGB3 expression
B
Fold change in FABP1 expression
C
Fold change in GLUD1 expression
D
Fold change in GSTA1 expression
DMSO
Untreated
MET 750 µM
DAB 10 µM
PIO 10 µM
ENT 100 µM
XIM 100 µM
TRO 10 µM
TOL 100 µM
APAP 5000 µM
FIA 100 µM
DIC 100 µM
TXV 10 µM
LVX 100 µM
AMIO 100 µM
BOS 30 µM
MET 250 µM
ENT 80 µM
BOS 30 µM
XIM 100 µM
TOL 100 µM
FIA 300 µM
APAP 2500 µM
AMIO 100 µM
DIC 100 µM
TXX 10 µM
LVX 100 µM
non-DILI
DILI

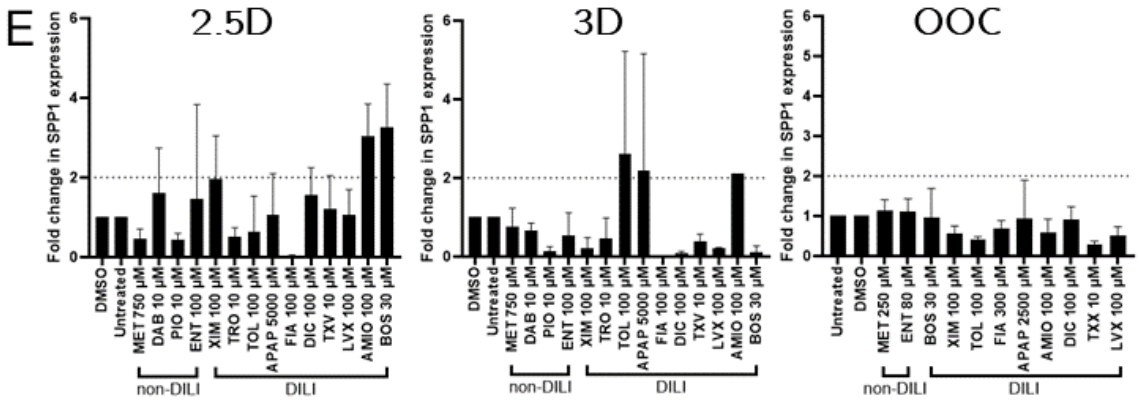

Figure 56: Fold change in gene expression of potential biomarkers *ITGB3*, *FABP1*, *GLUD1*, *GSTA1*, and *SPP1*.
Primary liver cells were treated for 14 days in the advanced cell culture systems with most-DILI-concern (DILI) and less-DILI-concern (non-DILI) compounds. At day 14, cells were lysed, and gene expression was analyzed by the QuantiGene™ Plex assay. Graphs show the fold change of **(A)** *ITGB3*, **(B)** *FABP1*, **(C)** *GLUD1*, **(D)** *GSTA1*, and **(E)** *SPP1* expression normalized to vehicle control in 2.5D, 3D, and OOC. The threshold value was set at 2. N=3/4.

4.5.5 Statistical comparison of gene expression between most- and less-DILI-concern treatment

Published potential novel DILI biomarkers were screened long-term in three advanced cell culture models. The liver cells were treated with drugs that are known to cause or are save from developing DILI. In this section the gene expression data was analyzed statistically to identify a biomarker or a set of biomarkers that significantly differ between the most-DILI-concern and less-DILI-concern treatments. Therefore, all less-DILI-concern and all most-DILI-concern compounds were combined and classified into “non-DILI” and “DILI”. Prior to the analysis, data normalization and cleaning were performed by Julian Kreis.

Figure 57 shows the statistical significance in gene expression between DILI and non-DILI treated cells. In the 2.5D model, a statistically significant p value was calculated for *GSTA1* ($p = 0.0365$) in the low-dose group (Table 18). Likewise, *GSTA1* ($p = 0.0416$) was statistically significantly different in the 3D model treated with high dose (Table 18). In addition, the expression of *FASLG* ($p = 0.242$) was significantly different between the DILI and non-DILI treatment in 3D low dose (Figure 75). All other examined potential biomarkers are depicted and listed in Figure 75 (Appendix 8.10), showed no statistically significant difference between DILI and non-DILI treatment. Moreover, no significant change was found in the OOC model.

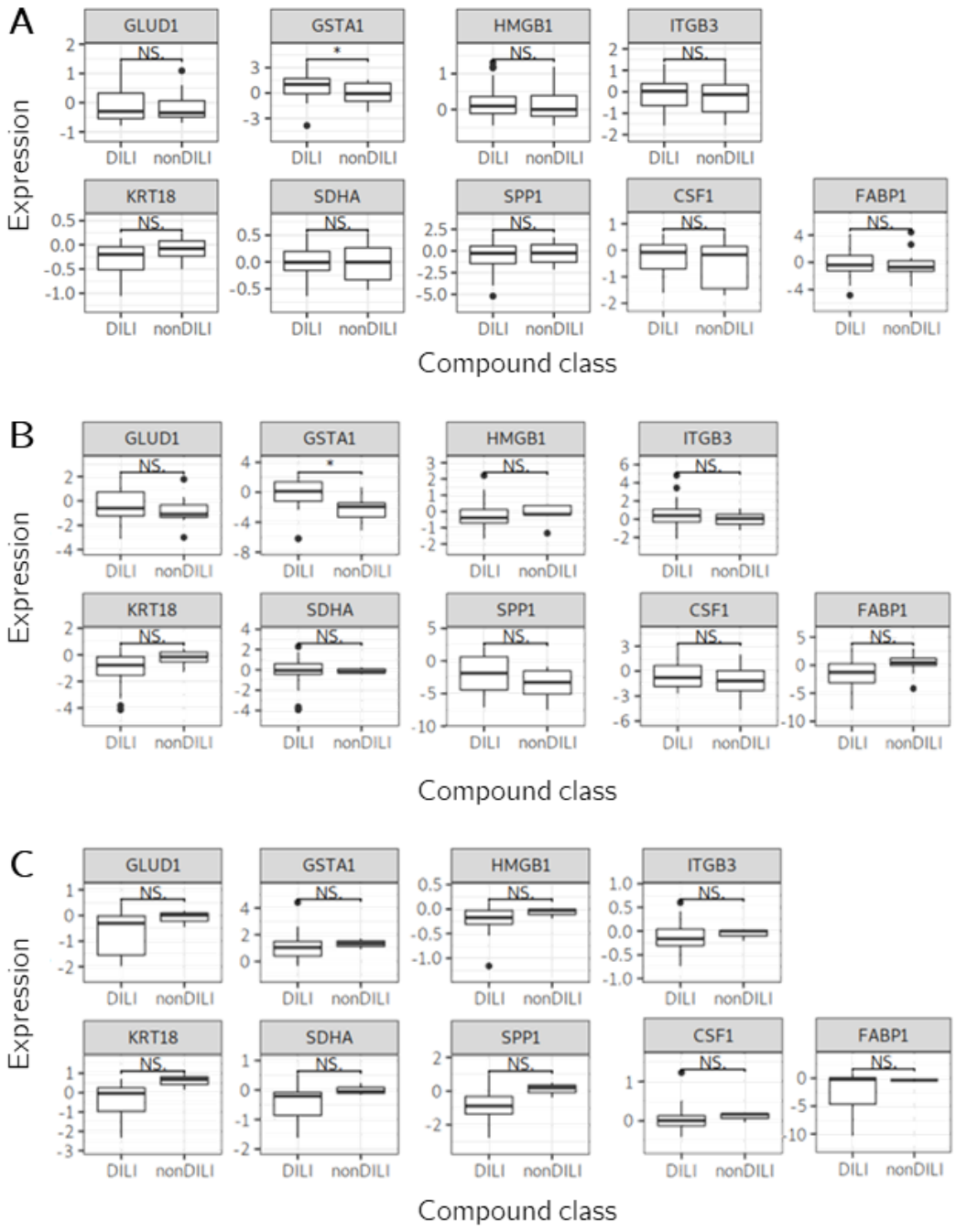

Figure 57: Statistically significant differences between DILI and non-DILI.
Primary liver cells were treated for 14 days in the advanced cell culture systems with most-DILI-concern (DILI) and less-DILI-concern (non-DILI) compounds. At day 14, cells were lysed, and gene expression was analyzed with the QuantiGene™ Plex assay. Graphs show statistically significance in **(A)** 2.5D low-dose, **(B)** 3D high-dose, and **(C)** OOC mid-dose treated models, normalized to vehicle control. Statistical analysis was performed by Julian Kreis using one-sides Wilcoxon test. Statistically significant *$p < 0.05$. N=3/4.

4.5.6 Statistical comparison of the secretion between most- and less-DILI-concern treatment

Secreted hepatic levels can indicate a hepatocellular damage. Therefore, the secreted level of the known and recent published potential biomarkers albumin, αGST, ALT, AST or LDH were statistically compared between DILI and non-DILI treated liver cells (AIM_5) [186]. Prior to the analysis, data normalization and cleaning were performed by Julian Kreis. Outliers were identified and removed from the calculation. A data point was defined as an outlier, if it was above Q3 + 1.5 *interquartile range* (IQR) or below Q1 - 1.5 IQ. Q1 and Q3 are the first and third quantile. The difference in secretion was compared for the three time points (D2, D7, and D14 (Figure 58)).

P values were calculated using the Wilcoxon test by comparing the time points separately and are listed in Figure 58. A statistically significant difference between the DILI and non-DILI treated was observed for the ALT secretion ($p = 0.0269$) in the 2.5D model in low dosage. In addition, there were three values that were < 0.1 (2.5D albumin high dose D14 ($p = 0.0859$), 3D albumin low dose D7 ($p = 0.0979$), and αGST low dose D2 ($p = 0.0963$)). Nevertheless, these and all other p values showed no statistical significance between DILI and non-DILI treatment in the advanced cell culture models.

After the evaluation of the time points separately, the progress of the measured concentrations from day 2 until day 14 was compared between DILI and non-DILI treated liver cells.

2.5D	low dose			mid dose			high dose		
	2	7	14	2	7	14	2	7	14
ALB	0.508	0.899	ND	0.383	0.865	0.787	0.22	0.949	0.0859
GST	0.404	0.756	0.897	0.834	0.461	0.643	0.826	0.702	0.411
AST	0.0269	0.418	0.947	0.492	0.953	0.964	0.263	0.791	0.891
ALT	0.98	0.998	0.867	0.879	0.542	0.875	0.979	0.817	0.473
LDH	0.54	0.624	0.509	0.964	0.362	0.554	0.801	0.947	0.54

3D	low dose			mid dose			high dose		
	2	7	14	2	7	14	2	7	14
ALB	0.185	0.0979	ND	0.662	0.548	0.819	0.683	0.452	0.675
GST	0.0963	0.412	ND	0.314	0.799	ND	0.207	0.48	ND
AST	0.233	0.209	ND	0.69	0.42	ND	0.329	0.382	ND
ALT	0.294	0.555	0.363	0.7	0.132	0.516	0.768	0.89	0.894
LDH	0.353	0.793	0.517	0.757	0.602	0.799	0.904	0.671	0.452

OOC	mid dose		
	2	7	14
ALB	0.767	0.972	0.799
GST	0.203	0.339	0.472
AST	0.275	0.472	0.528
ALT	0.648	0.583	0.324
LDH	0.467	0.231	0.101

Figure 58: Statistically significant differences in secreted hepatic levels between DILI and non-DILI.
Primary liver cells were treated for 14 days in the advanced cell culture systems with most-DILI-concern (DILI) and less-DILI-concern (non-DILI) compounds. At days 2, 7, and 14, the concentration of albumin, αGST, ALT, AST, and LDH in the supernatant was analyzed. Tables show calculated p values. Statistical analysis was performed by Julian Kreis using one-sides Wilcoxon test. *$p < 0.05$ (red). N=3/4.

4.5.7 Expression levels of mir122

Mir122 is enriched in hepatic tissue and described as a biomarker for early hepatocellular damage [177][172][178]. This study attempted to detect mir122 in the cell lysate and to compare the level between DILI and non-DILI treatment. In the 2.5D model the *mir122* expression was decreased by eight compounds and increased with MET and LVX. The highest fold change was detectable in the 3D model after treatment with MET, DIC, TVX and LVX. With five compounds the expression was reduced compared to the vehicle control. In the OOC, no significant increase in *mir122* expression was observed. However, decreased levels were detectable with six compounds, all belonging to the DILI group.

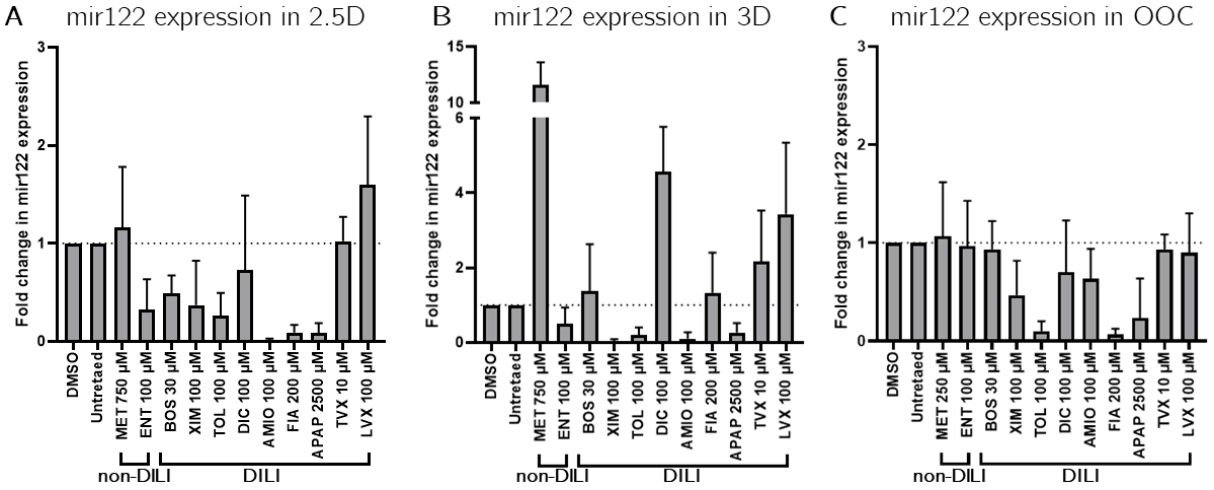

Figure 59: Fold change in mir122 expression.
Advanced cell culture models were treated for long-term with DILI and non-DILI compounds. At day 14, the mir122 level was detected in the cell lysate using the QuantiGene ® 2.0 miRNA Assay. Graphs show fold change in *mir122* expression after treatment in the **(A)** 2.5D, **(B)** 3D, and **(C)** OOC model. N=3

5 Discussion

DILI is still a significant challenge for the pharmaceutical industry due to the emerging hepatotoxicity in late phases and post-marketing. Between 1953 and 2013, hepatotoxicity was responsible for approximately 18 % of drug withdrawals [96]. In preclinical phases, it is investigated in *in vivo* and *in vitro* studies, however, with often limited predictivity. Although pharmacological and toxicity studies in whole animals are essential to predict adverse effects in humans, they are controversial because adverse effects are not always transferable. The reason lies mainly in species differences and the difficulty of transferring an observed reaction in animals to humans. As a result, if no dose-dependent effect is observed in preclinical animal studies, the new drug candidate can still pass to the clinical phases.

It is well documented that routinely used animal models are poor at predicting DILI [225][226]. In addition, animal testing should be reduced to a minimum for animal welfare reasons. Therefore, there has been an increasing focus on more advanced *in vitro* models in recent years. The current gold standard for *in vitro* studies of the liver are PHHs, which rapidly lose their physiological functions when grown in monoculture as a monolayer. However, to create a cell culture model that realistically mimics human drug metabolism and the different manifestations of liver toxicity (e.g., cholestasis, steatosis, etc.), it is necessary to maintain the phenotype of liver cells long-term. Recent studies have described the ability to maintain the PHH physiological function over a longer-term when the culture conditions are more closely adapted to the human *in vivo* physiological environment. This includes the integration of an ECM, other liver cell types, a 3D culture configuration, and/or dynamic flow.

In this work, four advanced *in vitro* liver cell culture models (2.5D sandwich, 3D spheroids, 3D organoids, and OOC) were established for the long-term maintenance of PHHs (AIM_1 and AIM_2). In addition, iPSC-derived 3D liver organoids were differentiated, characterized, and tested for their metabolic activity.

The 2.5D sandwich model was established through inspiration from papers by Bell et al., Bale et al. and others [291][378][386][387]. 3D spheroids were formed by the simple and scalable method using ULA U-bottom plates [292][394]. An enhanced ULA plate for microtissue formation was also launched in 2015 by InSphero, a company that sells “ready-to-use” spheroids as a platform for xenobiotic toxicity assessments [395][396]. The OOC model studied was from Emulate, one of the first commercially available organ chip system.

In this work, 2.5D sandwich, 3D spheroids, and OOC were treated with compounds to test their ability to develop DILI *in vitro*. The treatment of a test system over a longer period could be the essential factor to provoke the development of different types of DILI and hence better predict clinical outcome. For this purpose, the advanced cell culture models were treated long-term

with known DILI compounds (AIM_4). The detection of DILI should be better detected by examining potential new biomarkers, including the expression of specific genes and the secretion of proteins (AIM_5).

The data shown and described in Chapter 4 illustrated the generation and characterization of the 2.5D, 3D spheroid, 3D liver organoid, and OOC systems (AIM_1 and AIM_2). In addition, it revealed the impact on the maintenance of the PHH function by culturing them in advanced cell culture formats (AIM_3). These effects were compared in 2.5D, 3D spheroid, and OOC by examining different OMICs patterns, including genomics, proteomics, secretomics and metabolomics. Chapter 4 also addressed the reaction of the advanced cultured primary cells to known high-DILI-concern compounds (AIM_4 and AIM_5). Therefore, several well-known and potential novel biomarkers were researched and tested after 14 days treatment. The final Chapter (6) is a summary of the findings of this study, including new insights and future directions.

5.1 Significant differences between PHH donors regarding their ability to form spheroids

Today, various *in vitro* human liver models have been developed and some of them have already been integrated into toxicity studies. These models range from hepatoma cell lines, iPSC-derived hepatocyte-like cells, genetically modified cells, and primary cells. The HepG2 and HepaRG cell lines are known to vary greatly to the phenotype of PHHs [231][234]. They have disadvantages, such as the absence of important DMEs or other specific liver functions. Likewise, iPSC-derived hepatocyte-like cells do still need further development and optimization. Therefore, PHHs remain the gold standard for *in vitro* drug-induced hepatotoxicity and ADME studies [258]. They completely reflect the metabolic functionality of the liver and by culturing PHHs in an advanced cell culture model, the metabolic activity can be maintained for 30 days, providing clear advantages for toxicity testing [384][392]. Nevertheless, before PHHs can be integrated into an advanced cell culture model, a suitable donor must be determined. As individual as people are, their livers are also different and consequently the phenotype and functionality of the hepatocytes [397]. Due to the large donor-to-donor variability, multiple donors of PHHs need to be tested for *in vitro* suitability and response to xenobiotics before studies can be performed [345]. Depending on the indication, healthy male or female donors are often preferred for toxicological studies, since smoking, alcohol and/or drug consumption could affect the functionality and sensitivity of the DMEs. [398]. One example is cigarette smoking, which is known to significantly induce CYP1A2 and CYP2B6 [386][387]. In addition, alcohol consumption affects CYP2E1 levels [401]. Furthermore, their suitability for the specific application must be determined prior to testing. For example, in CYP induction assays, cells need

to be characterized according to their ability to respond to known CYP inducers, such as Omeprazole (CYP1A2), Phenobarbital (CYP2B6), or Rifampicin (CYP3A).

It is well known that not every PHH donor is able to form spheroids [345]. For this reason, many companies that supply cells already qualify their donors for their ability to form spheroids [402]. However, this information is not yet available for all donors and must be proven beforehand. Most companies, such as Gibco and BioIVT, isolate PHHs according to an internal protocol, which can lead to quality differences between providers [403]. Therefore, PHH donors from various suppliers were tested and compared with respect to their ability to form spheroids, secrete specific hepatic levels (e.g., albumin), and express cell-specific markers and DMEs.

Three donors were selected based on recommendations for appropriate spheroid formation (AKB, HJK, and XQD all from BioIVT). One donor was sent by Emulate as part of the ready-to-use culture kit (HUM4235/Lonza). An additional donor was ordered to test a further manufacturer (37501ZMC/AXOL), and four donors have already been integrated in 2D routine assays in the *in vitro* toxicology laboratory (HU1880, HU1951, HU1591, and HU8284 all from ThermoFisher).

In 2018, a study analyzed 39 different cryopreserved PHH donors and found that 79 % successfully aggregated into spheroids in ULA U-bottom plates [345]. In the present work, 66.6 % of the donors formed round spheroids in ULA U-bottom plates (37501ZMC, HUM4235, AKB, HU1880, HU8284, HU1951) (Figure 21). The difference to the published work could be justified by the fact that fewer donors were tested in this work. PHHs in monoculture self-assemble into spheroids in presence of FBS-containing medium in about 4-14 days. The formation of compact spheroids was faster in the FaCellitate ULA U-bottom plate compared to the Costar ULA U-bottom plate. This may be due to the special coating of the plate, which favors the formation of highly uniform spheroids [404].

5.1.1 Medium M1 maintains viability and expression of specific liver cell markers

Advanced culture configurations are reported to be crucial to preserve PHH functionality for extended periods. In addition, defined media compositions are important for maintaining the phenotype [405]. In this work, a coculture medium was optimized for PHHs and LSECs, based on several published compositions and recommendations from a collaboration with InVitroCue (from Mr. Kong Wai Mun) (Table 15) [32][341]–[343]. The generated media were tested in 2D cocultured PHHs and LSECs for 6 days. This was twice as long as the viability and functionality of hepatocytes reported in the literature.

Cell viability was investigated on days 1, 3, and 6 (Figure 22). A reduction in viability was observed from day 1 to 6 in all media, confirming the fact that primary liver cells lose their viability rapidly *in vitro*. Albeit the decrease was more slow in coculture compared to the known

data from monocultures (within 24-72 h) [225][259]–[261]. However, for media's M4 and M5 a decrease was already observed at day 1. For M4 it was probably due to the lack of glucocorticoids. Glucocorticoids, such as DEX and hydrocortisone, are important supplements in primary liver cultures as they enhance the viability and maintenance of the physiological functions [406]. By binding to the glucocorticoid receptor, they lead to its activation. The activated receptor translocated into the nucleus where it acts on anti-inflammatory and immunosuppressive pathways by, for example, inhibition of the NF-κB and activator protein-1 pathways [405]. The maintenance of viability and functionality was described for both PHHs and LSECs [407][408]. In media M5, the insulin concentration was increased by the 10 µg/ml. The glycemic homeostasis is a central function of the human liver. In a healthy state, insulin stimulates the glucose conversion in hepatocytes [409]. This leads to lipid and glycogen storage and affected the viability, attachment, and functionality of isolated PHHs [410][411]. Nevertheless, an increased insulin level can lead to an increased lipid content which is associated with inflammation, injury, and death [410][412]. This may explain the rapid decrease in viability observed when using M5.

In order to analyze the functionality of hepatocytes in each medium, albumin was investigated by immunofluorescence staining on day 6 (Figure 22). In addition, the LSECs phenotype was assessed by the SE-1 antibody [413]. The SE-1 antigen is expressed at the membrane and also associated with the LSEC fenestrae [414]. The highest signal for both albumin and SE-1, was observed for M1. In combination with the good viability, this medium was used for 2.5D and 3D spheroid long-term coculture (Figure 24). PHHs and LSECs cultured in its specific media in the OOC served as the control. Similar to 6 days, a clear signal for both markers was detectable after 14 days in culture in both 2.5D and 3D cultures. In addition, both signals were randomly distributed and showed no specific pattern of arrangement. In 2.5D, it was not possible to set both signals to a sharp position at the same time. Hence, two layers were observed during image acquisition, indicating successful establishment of the sandwich model. In 3D, no distribution pattern of PHHs and LSECs within the spheroid could be detected. This indicates that the cells aggregated randomly and did not reconstruct the livers' physiological structure. In conclusion, the successful detection of cell-specific markers led to the suitability of coculture medium (M1) for the long-term *in vitro* maintenance of PHHs and LSECs in 2.5D and 3D.

5.1.2 Coculture of PHH and LSECs promotes formation of 3D spheroids

As described, M1 was used for 2.5D and 3D cocultures, called coculture medium in the following. The donors that formed round aggregates in monoculture were studied in coculture with LSECs (Figure 23). These included donors AKB, HJK, XQD, HUM4235, and HU1951. In addition, one more donor was supplied by Emulate as part of the OOC kit (HU8305) and two

more donors were investigated from the standard *in vitro* toxicology laboratory (HU8148, and HU4248).

Despite LSECs representing the minority of cells in the liver, they are essential for liver homeostasis and can play a significant role in the development of DILI (Section 1.5.2) [273][226]. Consequently, LSECs were incorporated into the advanced liver models to create a tighter liver microenvironment. In coculture with LSECs, a round spheroid was observed for all PHH donors. In addition, a more efficient aggregation was seen for most PHH donors when compared to spheroids from PHH alone. For example, AKB formed a spheroid within six days in monoculture and within four days in coculture. Likewise, spheroid formation of HU1951 was six days faster in coculture. In addition, a more compact spheroid was observed when cocultured with LSECs (e.g., XQD and HJK). This leads to the assumption that the cultivation with LSECs promotes the positioning of the cells. This could be due to their key role in building the functional tissue structure *in vivo*, where hepatocytes orient themselves in the direction of the sinusoids. This was observed in 2010 by Kanebratt et al. who described the “hepatocyte-sinusoid alignment” where hepatocytes align along the closest sinusoid for liver regeneration after damage [415]. This process is also called hepatocyte-sinusoidal alignment. The alignment is essential for the restitution of the microarchitecture and thus the integration of LSECs in 3D cell culture probably contributed to a faster formation of the spheroids.

The selection of appropriate donors was based on the shape and time of formation. Due to the known rapid loss of physiological function and viability of *in vitro* cultured liver cells, donors with rapid aggregation were selected to minimize the time that cells must be in culture [33]. Fast aggregation was observed with the donors AKB, HUM4235, HU1951, and HU8148.

5.1.3 AKB shows robust expression of specific markers and long-term functionality

PHHs exhibit huge donor-to-donor variabilities (Section 5.1). They are known to lose their liver-specific phenotype and metabolic functionality during the isolation process and further during culturing *in vitro* [416]. To determine a suitable donor for the experiments at the earliest possible stage, prior to culture, freshly thawed PHH donors (AKB, HUM4235, HU1951, and HU8148) were analyzed. The measured relative gene expression levels of CYP enzymes in this work was compared with the proportion of each isoform described for the human liver in two publications (Figure 66). Since no direct comparison was possible between the percentages in the liver *in vivo* and the relative gene expression levels of thawed PHHs, in this study, the proportions of the respective CYP isoforms were compared to each other. As expected, Figure 66 A showed that the proportions of CYP enzymes differed between the publications especially for CYP2C19 and CYP2D6 [417]. This can be attributed to the different donors which were investigated and described by Prakash et al. in 2015 and Yeo et al. in 2004. As mentioned earlier, the expression of CYP enzymes is as individual as the donors themselves. Compared with the

relative gene expression of the tested donors, CYP2C19 was expressed at a lower level than CYP2D6 in all donors, consistent with the ratio found *in vivo* in Prakash et al 2015. In particular, donors HU1951 and HUM4235 showed similar levels of approximately threefold higher CYP2D6 than CYP2C19. With respect to CYP1A2, donor HU1951 also showed similarities to *in vivo* ratios, accounting for about half of CYP2D6. In this study, CYP2C9 had the highest relative gene expression level in three donors (AKB, HU1951, and HUM4235), whereas in the *in vivo* liver CYP3A4 accounted for the largest proportion. However, CYP3A4 was poor expressed in all thawed donors.

In general, the detected CYP enzyme levels found in freshly thawed PHH do not clearly match any of the published *in vivo* proportion. These large differences in CYP expression may be due to induced cellular stress. During the isolation process, significant metabolic changes occur in primary hepatocytes [416]. In 2017, Cassim et al. compared the metabolic profiles of primary murine hepatocytes before, during, and after isolation and found that levels decreased significantly immediately after the cells were removed from the liver and even more when cultured *in vitro* [418]. As freshly isolated hepatocytes are not unlimited and easily available, cryopreserved PHHs were used in this work. However, the process of cryopreservation and thawing can also contribute to changes in the basal CYP expression, as this procedure further induces cellular stress [416].

Phase II enzymes were also investigated as part of the selection of a suitable donor (Figure 25 B). SULT1A1 is one of the most important phase II enzymes for xenobiotic metabolism [419]. For example, APAP is sulfated by this sulfotransferase. It is predominantly expressed in the liver and the most expressed SULT (53 % [66]) in the liver [419]. SULT1E1 accounts for 6 % of all SULT enzymes in the liver [66]. In this work, the tested donors AKB, HU1951, and HU8148 showed a similar ratio, whereas HUM4235 exhibit higher expression of *SULT1E1* than *SULT1A1*.

UGT is also a key enzyme in metabolic processes, catalyzing 40-70 % of all drugs [420]. These enzymes are involved in the regulation of bile acids and other compounds [66]. In the human liver UGT2B7 accounts for 17 % and UGT1A6 for 9.4 % of all UGT enzymes [421]. In this study, UGT enzymes were found in all donors, however, HU1951 exhibit an increased expression of *UGT2B7* which is reported to be associated with increasing age (age of donor: 56 years) [422]. (Figure 25 B). In general, no tested donor showed a similar ratio as published for the human liver. The expression of *UGT2B7* was in all donors over sixfold higher than *UGT1A6*.

The phase III transporters *ABCB11* (BSEP) and *ABCC2* (MRP2) were found in a similar level for all donors (Figure 25 C). *ABCB1* (MDR1) was detectable in three donors (AKB, HU1951, and HUM4235) whereas *ABCC1* (MRP1) was absent in all. MRP1 is reported to be induced in

proliferating hepatocytes [423]. *In vivo*, hepatocyte proliferation is a remarkable property crucial for self-renewal after damage. *In vitro*, PHHs rapidly undergo dedifferentiation which is associated with the loss of physiological functions, including proliferation [424]. However, in coculture with other cell types, proliferation of hepatocytes was observed after disruption *in vitro* suggesting a positive influence on the phenotype maintenance [425][426]. This was also seen in the relative gene expression of cocultured PHHs with LSECs (Figure 39), where in all models *ABCC1* was detected.

The expression level of the PHH specific marker *ALB* was examined at day 14 (Figure 25 D). In a healthy liver, hepatocytes synthesize 10 - 15 g albumin per day [427][428]. An increased or reduced production and secretion can be associated with morbidity and mortality [427]. In this work, three of the four tested donors showed a comparable level of *ALB* (AKB, HU1951, and HUM4235). In contrast, a level twice as high was detected in HU8148. It is not clear from the relative gene expression level whether this is already a pathological increase. However, higher levels can be caused by infections, burns, and stress and the donor HU8148 suffered from a brain tumor, which is reported to be associated with elevated albumin level [429]. The albumin protein is known to be closely related to the *ALB* gene expression level [430]. However, in order to select a suitable donor for the long-term cultivation, the secretion of albumin was also investigated in the supernatant during 14 days in 3D culture for donors AKB, HU1951, and HU8148 (Figure 26 B). The measured albumin levels were similar among the three donors and the three timepoints. In addition, the level of secreted albumin was comparable to published values by Nudischer et al., Bale et al., and Paasonen et al. [431][292][432]. In addition, further functionality was investigated by measuring the secreted proteins LDH, AST, and ALT (Figure 26). The elevation of LDH release is an indicator for cell injury. Two days after thawing, the LDH levels were increased in all donors but highest for HU1951.It is well known that the thawing process puts primary cells under a lot of stress and therefore the viability may decrease due to dying cells [433]. This explains the high level on day 2. At day 7 and 14 the level decreased for all donors due to recovery of the cells after thawing and plating stress. A decreased LDH secretion was also observed by Paasonen et al. in 3D long-term cultured PHHs [432]. The measured ALT levels were comparable among the three donors. In addition, ALT is a traditional liver-specific marker used to detect hepatocellular damage [434]. Furthermore, AST is known to be released from damaged cells. In the supernatant of cultured donors HU1951 and HU8148 a slightly higher AST level could be detected, compared to AKB, suggesting more damaged PHHs.

In summary, due to the comparatively weak expression of DMEs (e.g., CYP2D6, CYP3A4), transporters (ABCB1), and the high expression level of albumin, HU8148 was excluded from further studies. HUM4235 showed a decreased expression level of *ALB* and in addition, it has limited commercial availability as this donor was supplied by Emulate as part of the OOC kit.

HU1951 had increased *UGT2B7* levels and AST secretion associated with hepatocellular damage. Therefore, this donor was also excluded from the performed experiments. Based on the successful detection of important DMEs and transporters, stable albumin secretion during 14-days culture, and reduced cell damage as reflected by lower AST, and decreased ALT and LDH levels, it was decided to use donor AKB for subsequent experiments. In addition, this donor formed round spheroids very well and quickly in monoculture and coculture and was commercially available.

5.2 Advanced coculture models show high potential for long-term maintenance of liver cell phenotype

Primary liver cells lose their phenotype *in vitro* rapidly, for example in suspension retain their metabolic activity for only six hours. PHHs cultured in 2D bring even more difficulties in predicting the long-term effect of a compound to the liver. The most common application of PHHs in 2D monoculture are short-term, single-dose assays to determine acute effects (cell health/viability) and mechanistic toxicity (e.g., mitochondrial toxicity, oxidative stress, etc.) [435][436].

However, models which can recapitulate the administration in humans are of increasing importance. This includes the possibility of long-term and repeat-dose studies. A very promising option to maintain the physiological functions long-term is by using advanced cell culture models. PHHs cultivated in 2.5D sandwich, 3D spheroids or within a MPS are reported to maintain their physiological function for up to four weeks [392][437][186]. In this work, advanced cell culture models were compared with each other according to their advantages and disadvantages for hepatotoxicity studies.

5.2.1 Advanced cell culture models exhibit a robust fluorescence signal of cell specific markers and increased cellular polarization in PHH spheroids

A fluorescence staining was performed in 2.5D and 3D to detect the expression and localization of cell specific markers (Figure 35). PHHs were characterized by the expression of albumin, and LSECs by LYVE-1 [413]. Liver cells, in both 2.5D and 3D, showed a positive immunofluorescence staining of albumin and LYVE-1 indicating the long-term maintenance of the required phenotype and is further supported by the expression of DMEs (CYP450) and transporters (MRP2, MDR1, and BSEP). It is known that the activity of CYP enzymes is lower in 2D compared to 3D [240]. In this study, a reduced expression and activity was observed between 2.5D and 3D. However, the sandwich configuration itself probably supported the maintenance of cell specific expression, when compared to traditional 2D cultures. The expression of drug transporters is also reported to be reduced in 2D monoculture [392]. Fluorescence images in this study also demonstrated the expression of transporters in 2.5D even after 14 days in culture. This is supported by the work of Bell et al. who also described increased expression of CYP enzymes and drug transporters in more advanced 2D sandwich cultures [392].

PHHs in advanced 2.5D and 3D cell culture systems were investigated according to their reconstruction of the apical-basal polarity (Figure 36). For the OOC the formation of canaliculi-like structures was already performed and confirmed by Emulate and therefore was not included in this assessment (Appendix Figure 63) [438][439].

A CMFDA staining was performed with live cells as a function of the MRP2. The cells were analyzed after 14 days in culture according to several publications describing this period as necessary for the formation of biliary-like structures [377][440]. An accumulated CMFDA fluorescence signal was observed in 2.5D and 3D mono- and cocultures. However, in monoculture the CMFDA accumulation was observed in channel-like structures. In particular, it was seen in 3D spheroids, indicating stable functional polarization of PHHs [270]. This is also consistent with the robust signal of the MRP2 signal depicted in Figure 35. In 2.5D, only a few smaller canaliculi were formed although a clear MRP2 signal was observed previously. The coculture with LSECs seems to disturb the channel-like formation of canaliculi-like structures in both 2.5D and 3D cultures, without affecting the expression of the MRP2 transporter. This was seen by a spot-like fluorescence signal (Figure 36). As mentioned before, LSECs play a key role in building the functional liver tissue structure (Section 5.1.2) [415]. PHHs in coculture with LSECs probably align along the closest sinusoid, which is described as “hepatocyte-sinusoid alignment” by Kanebratt et al. and therefore the canaliculi-like structures among themselves may be more spot-like rather than channel-like [415]. Thomas et al. also observed spot-like formation of canaliculi-like structures in 3D cocultured primary rat hepatocytes and SCs using transmission electron microscopy [441]. The ratio between PHHs and LSECs may also play a role. In this study a PHH/LSEC ratio of 1:1 was used for 3D spheroids. Perhaps a fewer number of LSECs in the spheroids would allow and promote canaliculi formation. A successful formation of canaliculi, visualized with CMFDA or comparable MPR2 substrates, was published for advanced liver culture models [377][442][439]. Ware et al. described the formation of functional bile canaliculi in a PHH/LSEC (5:1) and in a fibroblast triculture. However, LSECs and fibroblasts were cultured on micropatterned PHH colonies which is different from the method used in this work [347].

To date, most publications in which canaliculi-like structures were formed involved PHH monocultures but not cocultures. Therefore, further studies should be performed with cocultures to develop new methods enabling the formation of bile canaliculi in multicellular systems. For example, one possibility could be to pre-culture PHH spheroids so that channel-like structures can be formed, and then add NPCs. Furthermore, Turncliff et al. described the influence of the culture medium on the formation of the canalicular network [443]. Therefore, further optimization of the coculture medium could be also beneficial. Another possibility can be the demarcation between PHHs and NPCs as is the case in the Emulate liver-chip model. Since the NPCs

in the OOC model are not cultured between the hepatocytes, canaliculi-like structures can form unhindered as seen in a publication in the Emulate liver chip (Figure 63) [437].

5.2.2 3D cultured PHHs exhibit the highest relative *ALB* expression level

PHHs in 2D are the gold standard for *in vitro* liver models. However, when cultured flat on a plastic surface these cells dedifferentiate rapidly within 24-72 h [225][259]–[261]. A recent study described the downregulation of *ALB* and *CYP450* genes within three days in monocultures 2D PHHs [444]. Cultivation in an advanced cell culture model is reported to maintain the expression of specific markers, DMEs, and transporters. In this work, PHHs were cocultured for 14 days in 2.5D, 3D, and OOC followed by analysis of the gene expression. The relative gene expression of the hepatocyte functionality marker *ALB* was 3.5-fold higher in 3D spheroids than in 2.5D. This observation has already been described in other publications [445]. In addition, the *ALB* level was 12-fold higher than in the OOC. This may be due to the different culture condition as PHHs in the OOC are growing in 2D on a membrane and the 3D structure is reported to maintain hepatocyte functionality [445]. In addition, a different donor was used in the OOC, which may be related to lower albumin synthesis. As mentioned before, for 2.5D and 3D the same PHH donor AKB was used to avoid donor-to-donor variations. For the OOC, the donor HU8305 was used. This donor was supplied by Emulate as part of the OOC quad-culture kit.

ICAM1 and *PECAM1* are described as LSEC markers [446]. Since both are encoding for adhesion proteins, it is reasonable that they were damaged due to the isolation process and also the expression is downregulated in *in vitro* culture due to increased cell stress when losing polarity. Probably therefore, in this work, the expression of both genes was weak. Moreover, this indicates that no renewal took place during *in vitro* cultivation. The isolation, cryopreservation, and cultivation may have induced an inflammation-like state associated with decreased *PECAM1* expression [447]. KCs and SCs only were part of the OOC. Therefore, the relative gene expression of the specific genes *CD68* and *ACTA2* was highest in OOC.

Statistical analysis was performed to determine the impact of the cultivation conditions to the PHHs (Figure 38). According to the cell specific markers, the expression level of the 3D spheroid significantly differs from the OOC. This indicates that the expression of the cell specific markers *ALB*, *ICAM1*, and *PECAM1* is significantly higher when cells are cultured in a 3D configuration than growing flat, in 2D, on a membrane. The comparison between 2.5D and OOC and 2.5D and 3D showed no significant difference, indicating that the expression of cell-specific markers in the advanced sandwich culture was not statistically different from the 3D or OOC culture models. This suggests that the cultivation within a sandwich promotes the expression of important PHH and LSEC specific markers which was already described by Ware et al. and Bale et al. [293][348].

5.2.3 2.5D cocultured PHHs displayed weak long-term expression of DMEs and transporters

Drug metabolism is a key function of hepatocytes. In routine hepatotoxicity studies, metabolism related short-term experiments are performed as the physiological function is quickly lost. In this work, the maintenance of the expression of DMEs and transporters was analyzed in the advanced cell culture models and compared to the level of freshly thawed PHHs (Figure 39). The highest non-induced *CYP2C9* and *CYP2D6* expression was detected in freshly thawed PHHs. After 14 days in culture, the relative expression level of these two CYP enzymes was reduced in all systems. In general, the highest non-induced CYP expression at day 14 was detected in 3D spheroids, followed by OOC. This confirms the observation, that the 3D culture configuration promotes the expression of DMEs also described by Tostoes et al. who observed the maintenance of the expression of various phase I enzymes for at least two weeks [377]. In addition, this was seen in the statistical analysis where the comparison of 2.5D with 3D and 3D with OOC shows significantly different expressed CYP enzymes (Figure 40). All of them higher detected in the 3D model. The cultivation of PHHs in 3D advanced cell culture models is reported to increase metabolic activities and prolong the physiological function of primary hepatocytes [282]. Especially when PHHs are cocultured with NPCs in 3D, the functions and can be maintained for up to three months [282].

Significant differences were also found in CYP enzymes by comparing the 2.5D with the OOC model. Contrary to the PHH and LSEC specific markers, the cultivation within the OOC seems to maintain better the expression of DMEs compared to the sandwich culture (2.5D). This could be due to the dynamic flow, which, according to Allen and Bhatia, creates a consumption gradient, thus induces a metabolic zonation and promotes the expression of metabolizing proteins [448]. PHHs in 2.5D had only a weak expression of CYP enzymes after 14 days. According to a proteomic analysis by Thomas Wild, PHHs in sandwich culture showed decreased CYP enzymes during the first days in culture. A decreased transcriptomic and proteomic stability of DMEs was also observed in 2D cultures by Lauschke et al. and in 2.5D cultures by Bell et al. corresponding to the results in this study [384][392]. A higher expression of Phase II enzymes and Phase III transporter was measured in the 3D and OOC model than in 2.5D on day 14. *SULT1E1* was significantly induced in the OOC model compared to the 3D and 2.5D model (Figure 40). SULT1E1 expression has been reported to play a role in the pathogenesis of liver diseases such as cholestasis, but in this study, the difference may be due to the different donors rather than the culture configuration [449]. In addition, the phase III transporters ABCB11 (BSEP) between the 2.5D and OOC model, and ABCC2 (MRP2) between 2.5D and 3D were significantly different expressed (Figure 40). In 2006, Turncliff et al. described that the culture configuration of hepatocytes has an impact on the expression and function of transport proteins, which were assessed using a 2D sandwich model and optimized media [443]. However,

this study showed that culturing in an even more advanced 3D and OOC model further may increase the transporter expression as shown for spheroid by Bell et al. in 2018 [392].

The dedifferentiation process in 2.5D is reported to occur more slowly than in 2D [392]. Nevertheless, long-term studies are rather inappropriate when comparing the low expression of ADME proteins after 14 days. In 2.5D the formation of bile canaliculi and a robust short-term expression of metabolic transporters already were demonstrated [450]–[452]. Therefore, sandwich-cocultured PHHs are already successfully applied in short-term uptake and transporter studies [452]. However, the measured levels after 14 days suggest that 2.5D is not suitable for long-term hepatotoxicity experiments.

The higher level of relative gene expression in 3D and OOC highlighted that a three-dimensionality and flow establishment can improve the maintenance of the PHH functionality *in vitro*. 3D tissues and other MPS are reported to be promising tool to study metabolic and cytotoxic long-term effects [186]. The main benefits are described in the robust enzyme expression and functionality of phase I, II enzymes, and transporters compared to the simple 2D models [392]. For example, 3D coculture spheroids showed enhanced metabolic phenotypes with the cells from the same donor over 2D [269][386][449]. As mentioned above, these benefits were also observed in this study. In addition, the reconstruction of the hepatic sinusoid using the Emulate OOC also seems to be beneficial for the expression of key ADME proteins as the design of the chip mimics the structure of the smallest functional unit of the liver in combination with dynamic flow. [180][451].

5.2.4 Level of secreted liver-specific proteins is associated with the effort of the set-up of the models

The measurement of a stable albumin synthesis and secretion *in vitro* is used to identify functional hepatocytes. In this study, the secretion fluctuated strongly, but was not statistically significant in the 2.5D (Figure 41 A). The measured concentration in the 3D and OOC models remained stable over 14 days in culture. In several publications albumin is used to confirm the stability of cultured hepatocytes [292]. For example, compared to hepatocytes in a monoculture sandwich configuration, PHHs in 2.5D cocultured with LSECs produce albumin for up to 4 weeks [292]. In addition, a 3D coculture model composed of hepatocytes, SCs, KCs, and LSECs was described to maintain hepatocytes function for up to 3 months by measuring the albumin concentration [282]. Although albumin is a reliable marker to identify the functionality of liver cells, it is increasingly clear that it should not to be used as the only marker [455]. In addition, as the liver is a secretory gland, other secretory compounds, such as bile acids and the stability of expression of functional genes, should be investigated.

The aim of this work was the *in vitro* detection of DILI. Therefore, potential secretory biomarkers indicating liver injury (αGST, ALT, AST, and LDH) were investigated. Approximately

3–5 % of the total α-GST content in the body is present as soluble protein in hepatocytes, whereas ALT occupies only 0.6 % [456][457][458]. These proteins are released during injury in the extracellular space *in vivo*, and in this study the release was detected in the supernatant. ELISA assays were selected due to their high sensitivity for low abundance proteins (e.g., αGST_{LLOD} = 1.9 µg/L [373]). Firstly, the concentration of these marker was measured in the untreated models after 14 days in culture to find out whether the cultivation itself triggers a harmful response. The αGST protein is not liver-specific but is found in high concentrations in hepatocytes. Together with ALT and AST it is clinically used as a biomarker for liver damage. In this work, ALT and AST concentrations were detected in all systems on days 2, 7, and 14 (Figure 41 C and D). In addition, a significant decrease of the extracellular αGST concentration was detected in the 2.5D and 3D models (Figure 41 B). Further statistically significant changes were observed for the measured LDH concentrations (Figure 42). LDH is widely used as a cytotoxicity marker as it is rapidly released into the culture medium upon disruption of the plasma membrane [367]. The LDH concentration showed a high level for 2.5D and 3D systems on day 2, which subsequently decreased at later times (days 7, and 14). In the OOC the concentration of LDH remained stable from days 2 to 14. A possible reason for the different LDH levels in 2.5D, 3D, and OOC at day 2 may be explained by the experimental set-up of the different systems (Figure 11 and Figure 15). PHHs are only two days in culture, until the 2.5D sandwich is ready to use. In addition, the formation of 3D spheroids takes 3-5 days. In contrast, the OOC has the most elaborate set-up. The activation of the chip and seeding of the cells within the OOC took several days. In this process, PHHs have been in culture for 10 days until the LDH concentration was first examined at “day 2”. As already described, hepatocytes are severely stressed by the thawing process and many die shortly afterwards. This could also be the reason for the high LDH levels in systems that can be quickly set-up and used. However, after prolonged cultivation *in vitro*, the concentration decreases. This observation also supports the theory that the secretion of LDH level decreases when cells are cultured several days. In general, the fluctuations in 2.5D and 3D showed no statistically significant difference.

Since PHH lose their physiological functions rapidly *in vitro*, the timesaving set-up and use of the test model was an important factor. However, both investigations, the stable secretion of proteins and robust gene expression have shown that PHHs in the advanced cell culture models can be maintained for long-term. The advantages and disadvantages of a complex *in vitro* liver culture system are investigated in the subsequent sections.

5.2.5 Increased polarization and maintenance of functionality in 3D cultured PHHs

Long-term monocultured PHHs are reported to rapidly lose proteins involved in metabolic pathways [392]. In this work this observation was investigated in mono- and cocultured PHHs in a 2D, 2.5D, and 3D model. In the performed proteomics study, more than 6000 proteins were

detected in freshly isolated PHHs and almost 3000 proteins were present in all tested models. This variety of proteins also shows the great potential of the OMICs technology to investigate biomarkers and signaling pathways involved in multiple processes. The aim of this study was the investigation of the influence of the culture configuration on the protein expression and pathway regulation. Therefore, untreated PHHs and LSECs were examined during 14 days in culture. The PCA analysis showed a strict separation of 3D and 2D/2.5D cultured liver cells indicating that the culture configuration has an impact on the protein expression level. A more detailed analysis showed five clusters were delineated from the heatmap, which were used to perform a pathway analysis. The first cluster include proteins highly expressed in freshly thawed PHHs and moderate expressed in 2D/2.5D. These proteins were associated with the fatty acid and the alanine and aspartate metabolism. In monolayered PHHs a rapid down regulation of genes involved in fatty acid metabolism (right after 24 h) was already described by Richert et al. [459]. As depicted in the heatmap, PHHs in 2D/2.5D displayed a moderate expression on day 1. Thereafter, the signal continued to decrease until day 14. In the 3D culture, the proteins in the first cluster were weakly expressed. The reason for this could be the setup of the model, as the cells were already cultured for several days (until spheroid formation) before day 1 was analyzed.

Increase oxidative phosphorylation also raises the ATP level, which is, in part, required for improved polarization. After the cells are polarized, they shift to glycolysis-dependent ATP production [460]. As described previously, the isolation method disrupts the cells' polarity and integrity (Section 1.5.1) [266][267]. The repolarization process and maintenance is energy-dependent [461]. The process responsible is based on the activation of the *activated protein kinase* (AMPK) which can inhibit ATP-consuming pathways not crucial for survival [460]. Moreover, AMPK activates mitochondrial gene expression, resulting in enhanced mitochondrial bioenergetics that produces ATP very efficiently using the respiration oxidative phosphorylation mechanism [453][455]. Pathways related to the polarization were found in the second and third cluster. The second cluster includes proteins associated with the TCA cycle and oxidative phosphorylation. These proteins were weakly expressed in the 3D model. In contrast, the third cluster associated with cholesterol biosynthesis and glycolysis is highly expressed in the 3D monoculture but weaker in 2D/2.5D. The results of the proteomic analysis indicate that cells in 2D and 2.5D attempt to recreate cellular polarity by increasing the level of ATP required for structural restoration. The induced pathway of the TCA cycle supports this hypothesis as it reduces NAD^+ to NADH to generate CO_2 from acetyl-CoA and water. NADH is required for the oxidative phosphorylation pathway. [463] In contrast, 3D cultured PHHs seem to use the glycolysis-dependent ATP production pathway. The glycolysis pathway produces pyruvate, which is an intermediate product in the conversion of carbohydrates into fatty acids and cholesterol. Therefore, in addition to glycolysis, cholesterol biosynthesis is also upregulated. The increased

glycolysis-dependent ATP production pathway suggests that PHHs in 3D can either restore their cellular polarity more efficiently so that they do not have to rely on the increased ATP requirement, or that during the longer pre-cultivation period, until spheroid formation, the energy production pathway already converted again.

The fourth cluster deals with complement activation and CYP450 metabolism in the 3D models. The complement system is a central component of liver homeostasis as hepatocytes produce the major complement proteins [464]. In a healthy liver there is a balance between the synthesis and consumption of complement proteins. In contrast, a diseased state is associated with a decreased levels of complement proteins. [465] The proteomic analysis cannot exclude the possibility that complement activation is pathologically increased in the 3D models or reduced in the 2D/2.5D models. However, synthesis of complement proteins is an important function of hepatocytes, suggesting functional PHHs in the 3D models.

Another important function of PHHs is the CYP450 metabolism. Hepatocytes produce a variety of highly specific CYP450 enzymes that convert or inactivate hepatotoxic compounds [466]. Thus, metabolic activity is a sign that functional PHHs are present. In 3D monoculture the expression decreased at day 7, whereas cocultured 3D spheroids maintained a stable expression over 14 days. The fact that coculture of PHHs with NPCs promotes the stability of the metabolic activity has been already described in several publications and can also be confirmed in this study [467][434][281][375]. However, a closer look at the phase I, II enzymes and III transporters overall showed a higher expression in monocultured PHHs (Figure 46). It should be mentioned that the proteomics experiment was performed once. To statistically confirm this result, further studies including more replicates would have to be made.

Lipids are essential for cellular energy storage, structure, and signaling. Recent studies have demonstrated the role of altered lipids in the dedifferentiation process of PHHs in 2D. [444] In this work, lipid metabolism was decreased in 2D/2.5D cultured PHHs. In addition, an increased expression of proteins related to lipid metabolism were observed in cocultured PHHs. Not only PHHs but also LSECs play an important role in lipid metabolism [426]. According to the data, it seems to be beneficial to coculture PHHs together with LSECs, which maintains lipid metabolism.

In summary, the proteomic analysis showed an advantage of PHHs cultured in 3D in terms of induced polarization, maintenance of metabolic activity, and cell-specific functionalities such as lipid and cholesterol metabolism. More studies are needed to confirm the influence of the culture configuration on the liver cells. Nevertheless, in future it may be possible to select the advanced culture system according to the required scientific question (long-term/short-term testing, cytotoxicity, or metabolic activity studies).

5.2.6 Intra- and extracellular metabolome study examined condition-dependent differences, particularly in bile acid metabolism

The aim of the metabolomics study was to identify changes of the PHHs cultured in different advanced cell culture models. To account only for changes due to the culture configuration, the same donors were used for all systems. Freshly thawed cells and fresh medium serve as the baseline. Cell lysate and media supernatant samples were analyzed by Biocrates and resulted in over 600 metabolites found in eleven metabolite classes (Figure 47). Not surprisingly, triglycerides and phosphatidylcholines made up the largest share in both, cell lysate and supernatant. Phosphatidylcholines are the most abundant phospholipids in mammalian cells [468]. In this study, fewer phosphatidylcholines was observed for 3D cocultured spheroids in both, lysate and supernatant (Figure 49). The decrease of intracellular phosphatidylcholine-synthesis can affect the lipoprotein secretion and thus also the hepatic phospholipid composition which can lead to fatty liver disease and impaired regeneration [468]. In addition, a reduction of found metabolites was especially seen in the supernatant of the 3D model and the OOC quad culture. This may indicate impaired bile acid transport, as phosphatidylcholines are components of bile acids and are secreted by hepatocytes into the canaliculi network. Furthermore, a lower number of bile acids in the supernatant was observed in both culture systems. However, the intracellular amount of bile acids was not increased, so further studies should be conducted to investigate and confirm these results.

As already mentioned, the liver is the central organ for lipid homeostasis. This function also includes the storage of triglycerides which are the neutral form of fatty acids [469]. In healthy conditions, hepatocytes process a large number of fatty acids, but only store a small number of triglycerides [469]. This may be the reason for the different levels of detected triglycerides between cell lysate and supernatant. In addition, the performed PCA analysis filtered out triglycerides and phosphatidylcholines as the major metabolite classes responsible for most of the differences between 2.5D, 3D, and OOC cultured PHHs/LSECs (Figure 48).

The detection of fatty acids, triglycerides, and bile acids in all cell lysate samples assumes the presence of functional hepatocytes (Figure 49). Since amino acids are important components of protein synthesis and cellular metabolism, most of them can be found in the cell lysate compared to the supernatant. Cholesterol is degraded into bile acids and is catalyzed by CYP7A1 [470]. Bile acids are important regulatory factors of the liver as they serve for fat digestion and fat absorption. Clinical abnormalities can lead to inflammation and metabolic diseases [471]. In this study, twelve bile acids were investigated. A comparable amount was found between all systems in the cell lysate. However, in the supernatant, most of the bile acids were detected in the OOC coculture (Figure 49 B). A low level in the supernatant and a high level in cell lysate may be an indication of a disturbed bile acid circulation, which is also associated with cholestatic DILI [472][473]. Since bile acids are toxic to hepatocytes, impaired removal though the

BSEP transporter into the bile duct network may exceed the toxic intracellular threshold [472][474]. This leads to oxidative stress and mitochondrial damage, causing the release of inflammatory cytokines which trigger an inflammatory response in the liver [474]. However, it is difficult to say whether this decreased bile acid secretion already has a pathological character. In addition, it must also be mentioned that this study was performed only once and further repetitions are necessary to make more accurate statements.

5.3 Hepatic organoids are metabolically active and express liver-specific markers

Liver organoids are described as a promising tool for better predicting the efficacy and toxicity in *in vitro* preclinical studies [30][291]–[294]. In contrast to PHHs, they retain their phenotype long-term, are of unlimited supply, and are composed of different liver cell types, which enable studies in an more *in vivo*-related test model [248][248]. Moreover, they are arranged in organ-specific architecture within a functional unit [249].

For the differentiation of liver organoids from iPSCs. Three differentiation protocols were generated and tested based on the publication of Wang et al. and others [30][249][294]–[297]. The protocols differed in the preparation of the cells before differentiation began (Figure 12).

In humans, the development of the liver starts with the formation of hepatic cords by endodermal cells. These liver progenitor cells differentiate into hepatocyte-like and biliary-like cells which may develop into hepatocytes and biliary epithelial. [475] In this present work, liver organoids were differentiated from human iPSCs. Their capability to differentiate into nearly every cell type, coupled with their self-renewal, and self-organization potential, confirm their potential for studying the reaction of human organs to xenobiotics in preclinical phases [249]. The designed liver organoid differentiation began with the seeding of iPSCs as single cells and EBs into a Matrigel® dome, followed by endodermal induction, hepatic differentiation, and maturation (Figure 27). The endodermal differentiation was induced by Activin A. However, several studies reported that the differentiation into endoderm is affected by unspecific interactions of Activin A and other parameters, such as culture media and KnockOut Serum Replacement, which can influence the endodermal induction [476][477]. Nevertheless, the evidence of the expression of the reported endodermal markers *FOXA2* and *SOX17* (Figure 29 B), confirmed the success of the first differentiation step [478]. The microscopic documentation of the progress showed and outgrowth from the organoid center from endodermal induction in method 3 (Figure 28 A). One possible explanation is that the EBs were too heavy and fell to the bottom of the Matrigel® dome before it solidified. On the bottom, the cells then grew along the plastic surface in 2D. Immunofluorescence staining was performed at day 5 to visualize the location of differentiated cells within the organoids. The pluripotent marker OCT4 and the endodermal marker SOX17 both showed a positive signal. The OCT4-positive cells tended to be located in

the inner part of the organoid, while the SOX17-positive cells were found in the outer parts. This may be because the outer cells have more contact with the medium and the differentiation-leading substances then the organoid center. Therefore, these cells differentiated at different time.

Further differentiation into hepatic progenitor cells was promoted by HGF and bHGF, which have been shown to play a critical role in hepatic specification [479][252]. The progress of differentiation is evident in the formation of liver organoids having an outer and an inner circle, which has also been reported in several publications [480][481]. These clear structures were also be recognized in organoids from all methods, but most frequently and clearly in methods 1 and 3 (Figure 28). In addition, the increased gene expression of the hepatic progenitor *AFP* from day 10 confirmed the hepatocyte-directed differentiation (Figure 29 C).

The hepatocyte maturation was induced by the pleiotropic cytokine OSM and DEX which is reported to inhibit apoptosis and the proliferative response of mature hepatocytes [482][353]. The gene expression levels of the hepatocyte marker *ALB* increased steadily from day 10 but was absent in method 2 at day 20. Likewise, the stellate cell marker *ACTA2* and the cholangiocyte markers *CK7* and *CK19* showed an increased level from day 10. However, the expressed level of *ACTA2* and *CK7* was lower in method 1 and 2 derived organoids. Fluorescence staining on day 20 showed an overall clear signal of albumin, HNF4α, and CYP450. The expression of HNF4α is reported to be induced by DEX which was added to the media from day 10 on [483]. In addition, the staining of the transporter MDR1, showed a signal in the outer part of the organoid, suggesting the biliary membrane side. It is reported that the addition of HGF promotes the formation of biliary epithelium [483]. Bile canaliculi-like structures were investigated using the CMFDA dye visualizing clear canaliculi structures within the whole organoids.

After characterizing and confirming the differentiation of liver organoids, their functionality was investigated. Media samples were analyzed for liver-specific markers, such as albumin, αGST, AST and ALT. As mentioned before, αGST is present in many cell types but at very high levels in hepatocytes. The release of αGST can be an indication for hepatocellular damage. However, these concentrations are low compared to published literature [186][173]. Differentiated hepatocytes are able to self-renew after cell death and thus these concentrations may indicate a renewing system. [484]. ALT and AST were also increased from day 10/15 onwards. Both transaminases are primarily aggregated in the cytosol and can be detected in the serum at low levels (< 35 IU/L) [485][486]. The ability of liver organoids to produce and secrete ALT and AST showed an important hepatic function [201]. Slightly elevated values do not indicate a pathological condition and may be due to the cell renewal within the organoid, as mentioned before [390].

To examine the metabolic activity of differentiated liver organoids, cells were treated with MET, BOS, APAP, and RIF. Subsequently, the LDH, albumin, and CYP expression level were analyzed. The treatment with APAP and BOS lead to an increased release of LDH confirming that the correct concentrations were used here to induce cellular death (Figure 33). MET, a drug for type 2 diabetes, was used as negative control, as there is no reported toxic effect on hepatocytes [487]. However, a slight increase in LDH secretion was noted, which may be due to the experimental procedure rather than the substance itself as MET is known to not induce necrosis in primary hepatocytes by protecting against anion-induced caspase activation and *poly(ADP-ribose) polymerase* (PARP)-cleavage [488]. The slightly elevated LDH level could be due to a higher cell count in the MET-treated wells, as counting and evenly seeding of an accurate cell count was challenging in this study. RIF-treated organoids secreted lower amount of LDH compared to the vehicle controls. It is possible that the selected concentration of 25 µM was too low to cause cellular death. In literature this concentration is used to induce CYP3A4 protein levels, but not to induce cellular death. Furthermore, probably the number of cells per well could lead to the slightly decreased LDH level. In general, these experiments were performed once and would need conformation by more replicates.

As mentioned previously, the synthesis and secretion of albumin is an important marker for functional liver cells. However, abnormal secretion is associated with tissue damage [186]. In Figure 33 B, the gene expression of *ALB* was decreased after treatment with MET, RIF, APAP, and BOS. The treatment with 100 µM APAP showed no change of the *ALB* expression. Perhaps, the concentration was too low to induce a change in albumin secretion. In Forster et al., a reduced albumin secretion could be observed in PHHs after 10 days dosing with 1.5 mM APAP, which is 15-fold higher than used in this experiment [186]. Since the sensitivity of the differentiated liver organoids was not clear, a lower dose of APAP was used in this study. However, the results showed that the liver organoids seem to be robust to low APAP doses, so that a higher concentration could be used in future experiments. Treatment with MET, RIF, and BOS lead into a decreased *ALB* expression. With MET and RIF, the expression was inhibited 40 % and with BOS 20 %. This demonstrates that differentiated liver organoids are able to respond to drugs by altering ALB expression also described by Wang et al. [489].

The expression of CYP450 enzymes is essential for drug metabolism. Hence, the levels of *CYP3A4* and *CYP1A1* were analyzed after treatment with the four drugs. The expression of *CYP3A4* decreased after treatment with MET, RIF and APAP, but increased with BOS (Figure 33). RIF and BOS both are CYP3A4 inducers [69]. However, organoids treated with RIF showed decreased *CYP3A4* expression. In literature a concentration of 40 µM of RIF is used for primary hepatocytes to induce *CYP3A4* expression [490]. Therefore, it is possible that the used concentrations were too low to induce a reaction in the liver organoids. A further study with higher concentration could be performed to conform this assumption. In addition, liver

organoids may lack certain factors such as transcription factors and nuclear receptors that are required for the response to xenobiotics comparable to PHHs [491]. Therefore, further studies are needed to further develop robust differentiation protocols, characterize liver organoids and to compare their reaction with those of PHHs in more detail.

MET is reported to suppress *CYP3A4* expression in human hepatocytes by the major xenobiotic- and hormone-dependent nuclear receptor PXR [492]. The drug disrupts the coactivation of PXR with steroid receptor coactivator 1, which inhibits the transcriptional activity of PXR and thus the repression of its target genes [492]. Hence the reduced expression level in the differentiated liver organoids corresponds to the reaction observed in PHHs. Moreover, MET significantly induced *CYP1A1* expression in liver organoids, which was also observed by Chatuphonprasert et al. in mice after two weeks of treatment [493]. *CYP1A1* was also induced by RIF and APAP in this work. RIF is known to be a CYP1A1 inducer that activates the PXR receptor, which affects CYP450 activity [494]. Hence the respond of the liver organoids to RIF correspond to the reaction of PHHs to this compound. *CYP1A1* expression was also induced after APAP treatment. Casley et al. described an increased expression of CYP1A isoforms in mice hepatocytes after APAP treatment which also would correspond to the findings in APAP-treated liver organoids [495]. With BOS a slightly decreased *CYP1A1* expression was detected in liver organoids. BOS is an endothelin receptor antagonist, but its use is limited because of DILI [496]. It is mainly metabolized by CYP3A4 and CYP2C9 and can inhibit hepatic uptake and biliary efflux transporters such as BSEP which can lead to DILI [496][497]. However, a correlation between BOS and *CYP1A1* inhibition was not yet published. Therefore, further studies are needed to confirm the observation, as this experiment was conducted once, and this effect could also be an outlier. In general, these results confirm, that the differentiated liver organoids respond comparable to PHHs but are not completely equal which makes further optimizations necessary.

Hepatic tissues are characterized by enriched mir122 and mir192 expression [123][177]. Especially mir122 is described as essential for maintenance of the liver homeostasis including cholesterol, glucose homeostasis and lipid metabolism [499]. In mice, the absence of mir122 has been associated with the development of various liver diseases such as hepatosteatosis and fibrosis [499]. Furthermore, due to its stability and sensitivity the expression and circulation of mir122 is described as biomarker for hepatocellular damage [499][177][172][178]. In this work, the expression of the small non-coding mir122 was detected intracellularly during the differentiation process and after treatment with the four test compounds. From day 10 onwards, mir122 levels were detected which additionally confirms the organoids generated are hepatic-like. In Doddapaneni et al., the expression of mir122 was positively correlated with the expression of hepatocyte-specific genes during liver differentiation, which is consistent with the results of this study [500]. Treatment of liver organoids with various substances also showed that

the cells responded with altered concentrations of mir122. The mir122 level was increased after 72 h treatment with BOS, APAP, and RIF. An increase in mir122 associated with APAP-induced toxicity was previously reported *in vitro* by Forster et al, but the amount secreted was measured [186]. Evaluation of mir122 in response to BOS and RIF has not been completed, but both compounds are known to cause hepatocellular damage, and therefore, increasing intracellular mir122 may be an appropriate hepatic organoid response to prevent injury. Since the literature describes both expression and secretion of miRNA during cell destruction, further studies could address the correlation between released and intracellular mir122 concentration to further investigate this promising new biomarker for DILI [501].

The described investigations have confirmed the successful differentiation of liver organoids containing liver-specific features and functional activity. They show typically morphological shape and important hepatic characteristics, including the expression of cell specific markers and the secretion of albumin. Additionally, the liver enzymes αGST, ALT, and AST could be detected at comparable levels as in vitro PHH. The liver-like reaction to xenobiotics and the ability for long-term studies make liver organoids a robust model for the early assessment and mechanistic understanding of DILI.

However, liver organoids need to be further optimized with respect to standardized splitting and seeding protocols. In this project, it was not possible to dissociate the organoids into single cells without destroying many cells, which may also alter the properties of liver organoids due to cellular stress, such as the reformation of organoids. The dissociation was performed with the gentle TrypLE™ Select dissociation reagent, also used by Gao et al. for 2D differentiated hepatocyte-like cells [502]. Organoids were incubated with the reagent in a 37 °C water bath and additionally mechanically dissociated by pipetting up and down every 2-3 min, as incubation alone was not sufficient to separate them into a single cell suspension. Dissociation process and cell viability were continuously monitored under the microscope, and trypan blue staining was used to detect increasingly dead cells. Moreover, Wang et al. digested liver organoids using Accutase which in this study resulted in smaller organoids, but did not produce single cells with an appropriate viability [295]. Enzymatic dissociation is known to induce apoptosis and necrosis, for example, by disrupting intracellular connections responsible for maintaining cellular architecture and morphology, which are important for liver function and viability [503][504]. Thus, the dissociation process needs further optimization, to maintain cellular viability and achieve a single suspension which enables the seeding of an equal number of cells important for many experiments including hepatotoxicity tests. For example, Hannan et al. dissociated 2D hepatocyte-like cells using collagenase which was also used for hepatic organoids by Guan et al. [505][506]. Furthermore, Wu et al. described Dispase as dissociation regent for

liver organoids, however, only to achieve smaller organoids [296]. Recently, commercial reagents have become available, such as the 3dGRO™ Organoid Dissociation Reagent, which were also not tested in this work and could be investigated in a future study.

5.4 Advanced *in vitro* cell systems are suitable for the preclinical detection of DILI

During the isolation process, PHHs lose their polarity and undergo dedifferentiation. In 2D culture they lose their physiological function within 24-72 h. [225][259]–[261] This makes it impossible to study the effects of substances on cells in long-term. Several adverse effects, such as iDILI, may not be detected because many occur after a latency period. Therefore, the *in vitro* long-term maintenance of PHHs is essential to enable the development and study of different DILI mechanisms. In the previous chapters, it has already been shown that long-term cultivation is possible in advanced cell culture models while restoring the cellular polarity and maintaining metabolic activity (AIM_3). Subsequently, potential novel DILI biomarkers were screened in these models.

In the following sections, the suitability of advanced cell culture models for *in vitro* detection of DILI is discussed, based on a comparison of published biomarkers (Table 7). A panel of compounds was selected and grouped into most-DILI-concern (DILI) and less-DILI-concern (non-DILI) according to the FDA recommendation and the MIP-DILI project classification (Table 9, AIM_4) [337][135]. The advanced cell culture models were treated long-term with previously defined compound concentrations followed by the examination of secreted proteins and expressed genes (AIM_5).

5.4.1 Dose-finding study and PDMS compound sorption defines the range and concentration of substances that can be tested

AIM_4 of the present thesis was the selection of compounds known to cause and not to cause DILI in humans. An attempt was made to select substances covering each category of potential DILI mechanisms since a general DILI biomarker was sought (Table 9).

In this work, ten most-DILI-concern and four less-DILI-concern compounds were tested long-term in the 2.5D, 3D, and OOC systems. Attention was paid to the sensitivity of the selected biomarkers, since, for example, there were only 2000 cells per well in the 3D spheroid model [453].

In the Emulate OOC system, a limited number of chips can be cultured at the same time. Therefore, a dose-finding study was performed previously to evaluate the EC_{50} value of each compound in the 2.5D and 3D coculture model. The EC_{50} curve was then used to determine a safe $EC_{20\text{-}30}$ value for the long-term treatment of liver cells in the OOC. The goal was to provoke a cellular response to the compounds without large decrease in viability. If the cells would die

immediately in the first hours or days after the start of treatment, the long-term evaluation would show poor results. Therefore, safe concentrations for long-term treatment were tested. MET and BOS were excluded from this preliminary test as concentration recommendations for OOC already existed from Emulate [437].

In contrast to the OOC, there was no limitation on the number of possible concentrations for the 2.5D and 3D models. Therefore, three concentrations per compound were chosen with the perspective that it is not clear which concentration would induce DILI in the long-term *in vitro* experiments.

For three substances (DIC, LVX, and APAP), neither an EC_{50} in 2.5D nor in 3D could be calculated. Possibly, the concentrations chosen were too low (Table 17). A higher EC_{50} value was detected for most compounds in the 3D model, than in the 2.5D suggesting less cytotoxicity in 3D spheroids. However, this is not consistent with published observations that 3D spheroids are more sensitive to hepatotoxic compounds and should therefore be investigated in future studies with more compounds [392]. In addition, the EC_{50} values mostly correspond to already published data for 2D and 3D cultured PHHs for these test compounds (Appendix 8.11) [180][261][291][377][386]. For example, an EC_{50} of 8.9 µM (3D PHH/LSEC) was calculated for AMIO, which is very similar to the published value in Bell et al (11.9 µM in 3D PHHs) [386]. Furthermore, for TRO an EC_{50} was determined to be 14 µM, which is comparable to the value published by Proctor et al. (~10 µM) [377].

After a safe dose was determined, the *compound distribution kit* (CDK) was performed in the Emulate OOC as PDMS is known to have high absorptive properties. The compounds XIM, DAB, TRO, PIO, TOL, and ENT were investigated (Section 1.5.5). All other substances were excluded from this experiment as Emulate already had experience with their suitability in the OOC. The results of the CDK led to the exclusion of the substances TRO, PIO, and DAB as these were strongly adsorbed by the polymer. On this basis, a defined concentration within the chip could not be ensured and observed effects would be challenging to interpret.

According to the dose-finding study and the results of the CDK, the compounds and concentrations listed in Table 18 and Table 23 were used for the experiments in 2.5D, 3D, and OOC to provoke a reaction while maintaining a suitable viability.

5.4.2 Hepatocytes showed a dose-dependent secretion of albumin in 2.5D and 3D

Many circulating plasma proteins such as albumin, blood clotting factors, and modulators of immune complexes are produced in the liver by hepatocytes [434]. Therefore, the liver plays a central role in controlling homeostasis. The measurement of hepatic proteins, such as albumin is widely used to study and proof hepatocellular functionality [434]. It is known, that the synthesis of proteins is significantly downregulated during an inflammatory process [284][507]

[508]. In this study, the production and secretion of five proteins was investigated long-term in three advanced cell culture models while treatment with the set of test compounds (AIM_5).

In 2.5D, ≤ 50 % of the basal albumin level was observed on day 2 in the supernatant with 7/15 compounds compared to the control. After 7 days, a ≤ 50 % reduction was detected with six compounds and after 14 days with five compounds. This led to the assumption that cells cultured in 2.5D responded rapidly to treatment and for some compounds secretion recovered slightly over the 14-days cultivation period. In 3D, the albumin concentration was ≤ 50 % with 10/15 compounds on day 7. On day 2 and 14, this was the case in 6/15 compounds. Based on these observations, it appears that 3D-grown cells showed a delayed response to the selected compounds, but after a latency period a reduction with more compounds compared to 2.5D was observed. This would also be consistent with published observations that 3D spheroids respond more sensitively to hepatotoxic compounds [392]. The delayed reaction can be explained by the different zones of a spheroid. While in 2.5D the substance has direct contact with all cells at the same time, in 3D, mainly the outer cells come first into contact with the drug [509]. Therefore, it may take longer for a significant reduction in albumin secretion to occur. In addition, it appears that with increasing culture time, albumin synthesis and secretion recover in 2.5D and 3D. *In vitro*, the regenerative capacity is described as very low due to the loss of polarity and functionality [235][262]. Nevertheless, the stabilization of the albumin levels could be an indication for *in vitro* cellular regeneration, which is known to occur *in vivo* [427], [510].

In 2.5D and 3D, a dose-dependent response was observed for most compounds, including ENT, XIM, TRO, TOL, APAP, and TVX (Appendix 8.6). Due to the limited number of chips, only one concentration was examined in the OOC. Hence, a dose-dependent effect could not be examined. Nevertheless, a time-dependent decreased albumin concentration was detected from day 7 onwards with several drugs, including FIA and APAP. Both drugs were also tested in a recent study in which albumin was described as a sensitive biomarker for liver chips, as the secretion by hepatocytes decreased with increased treatment concentration [186]. Moreover, in Khetani et al., PHH cocultured with fibroblasts showed decreased albumin secretion after TOL treatment, which is consistent with the observation in this project [183]. Five substances (BOS, ENT, AMIO, TVX, LVX) resulted in no change in albumin secretion during 14 days of treatment. ENT served as a negative control in this study because it is known not to cause DILI in humans, which also correlates with the stable albumin secretion level over the treatment period [511]. BOS induces DILI by inhibiting the BSEP resulting in toxic intracellular bile acid accumulation [498]. The compound has been described by Emulate as a positive control for hepatotoxicity but seems to not affect albumin secretion [437]. TVX is a severe DILI compound that has been described to induce immune-mediated toxicity. This was confirmed by Li et al. by adding KC to PHH spheroids, resulting in an enhanced toxic response with lower

IC_{50} values after treatment, compared to PHH spheroid monocultures [512]. Based on the detected stable albumin concentration, the compound seems not to affect the secretion, however, Khetani et al. observed a significant reduced albumin level in micropatterned cocultures of PHHs and fibroblasts after TVX treatment [183]. Consequently, this observation should be investigated and confirmed again in a future study. LVX is a structural analog compound to TVX and can also cause DILI in humans. In a case report by Schloss et al. it was shown that LVX-induced hepatotoxicity is associated with elevated liver enzymes but stable albumin levels *in vivo* during and after treatment [513]. In addition, in *in vitro* micropatterned cocultures of PHHs with fibroblasts, the albumin secretion was not significantly reduced to the vehicle control after treatment with 15.7 µM LVX [183]. A stable albumin secretion after LVX-treatment could also be confirmed in this work. AMIO is also classified as severe DILI compound as it accumulated in mitochondria and disrupts the respiration [514]. Amiodarone-induced liver injury is defined in patients by elevated aminotransferases, however, it seems not to affect the albumin secretion in advanced hepatic models *in vitro* [515].

In all models, the cells responded to treatment with a reduced albumin secretion, although, not for every compound tested. With APAP and XIM, a reduction of $\leq$ 50 % was observed in all models. However, there was no clear demarcation between treatments with most-DILI-concern and less-DILI-concern compounds, suggesting that it is not a selective biomarker for DILI. In addition, further replication and testing with multiple compounds is needed to confirm the results of this study as only a small panel of compounds was tested.

5.4.3 The released level of αGST in 3D spheroids could be a potential biomarker for DILI

ALT and AST are the most common used clinical biomarkers for the detection of hepatotoxicity. However, these enzymes are known to be more elevated in the periportal region of the liver lobule than in the centrilobular region [371]. The uneven distribution within the liver can complicate the detection of a liver disease [174]. This was already observed in patients suffering from chronic liver diseases but having normal transaminase levels [481][482]. As αGST can be found consistent and in high cytosolic concentration throughout the liver, the enzyme is described as a more specific and sensitive biomarker for hepatocellular damage [518]. In treated male Wistar Han rats, αGST was increased more significantly than ALT and AST and therefore also was described as an appropriate biomarker for hepatotoxicity [174]. In addition, the evaluation of αGST has been described as a potential *in vitro* DILI biomarker by Foster et al. in the coculture Emulate liver chip (PHHs and LSECs) [186]. The enzyme is released from damaged hepatocytes and can be detected in the supernatant (Figure 60). In this work, the highest increase in αGST concentration was observed in 2.5D cultures with three non-DILI (MET, DAB, and ENT) and four DILI compounds (TOL, APAP, AMIO, and BOS) (Figure 53 D, AIM_5). In addition, a dose-dependent response was observed with some substances in 2.5D

and 3D (e.g., TVX and DIC) (Appendix 8.6). In the 3D model, the fold change values were lower, however, with five compounds the threshold of 2 was achieved (Figure 53 E). Importantly, all of them were part of the most-DILI-concern group. This confirms the published statement that αGST may be a potential DILI biomarker and can be used in preclinical *in vitro* models. However, the statistical analysis revealed no significance between the levels of DILI and no-DILI treated cells and therefore further compounds would need to be investigated to confirm the observation (Figure 58).

A similar observation was made in the OOC, where the threshold was reached with three compounds (TOL, AMIO, LVX), all belonging to the DILI group (Figure 53 F). In the Emulate liver chip, a significant fold caused by APAP and FIA was published by Foster and colleagues [186]. In this study, APAP and FIA did not reach the threshold. In the case of APAP, the lower concentration could be a potential reason as a large decrease in viability, precipitation, and clogging of the thin channels should be avoided. The clogging of the channels was already observed in this project after treatment with DAB and PIO (Appendix 8.7, Figure 73). These compounds precipitated during the treatment period in the medium. A decreased medium level was observed in the POD outlet medium reservoir, which is associated with a decreased supply of the cells with fresh nutrients, which in turn may affect the cellular viability. With FIA, the same concentration was tested as in the publication [186]. However, the evaluated fold change level of 1.8 in this study (on day 14) differed to the published data of a fold change circa 11, on day 10 [186]. The concentration of αGST in the supernatant was higher in this project, than in the published study, although the same assay from TECO Medical was used. In Foster et al., the highest level was detected on day 3 with circa 0.4 µg/1x10^6cells/day of αGST [186]. When converting the data generated in this study to µg/1x10^6cells/day, the level of secreted αGST was significantly higher for all time points (day 2 = 29.6 µg/1x10^6cells/day; day 7 = 29.5 µg/1x10^6cells/day, and day 14 = 26.5 µg/1x10^6cells/day) (Appendix Table 10). A potential reason for the large differences may be due to the known donor-to-donor variability. The publication does not describe which donor was used. Probably the donor used in this study response more sensitive to treatment than the donor used in Foster et al. Nevertheless, in this project, higher enzyme concentrations were also measured in the solvent control and in untreated liver chips, leading to lower fold changes after normalization. This may indicate an increased disruption of PHHs cultured in this study, although, under untreated conditions and therefore should be repeated with a further donor to confirm the observations and investigate the differences to the published data in more detail.

Together with αGST, ALT and AST are clinically used as biomarker for liver damage. The detected fold changes in AST were weak in all systems. However, a statistically significant difference in the low dose treated 2.5D model was calculated between the DILI and non-DILI

group (Figure 58). However, since the overall values were low, more replicates would need to be performed to confirm the results of this work.

The aminotransferases ALT and AST were measured in the supernatant after treatment. These enzymes are routinely used as biomarkers for liver damage in clinic and *in vivo* animal studies [519]. From clinical experience it is known that both aminotransferases cannot be stored stably at RT, 4 °C or -20 °C, due to rapid degradation of the enzymes and should therefore be measured rapidly after venipuncture [520]. A further study examined ALT loss of 8 % within 6 days storage in -80 °C [521]. Therefore, it is recommended to store the samples at - 80 °C to reduce the degradation rate. On day 2, a significant increase in ALT secretion was observed with 11/15 compounds in the 2.5D model, followed by a decrease on day 7 and 14. With two compounds (TOL, APAP) the decrease was already seen on day 2. The higher ALT concentrations on day 2 indicate a rapid response of the cells to the treatment. ALT is secreted by destroyed hepatocytes as this cytosolic enzyme is released from the cells into the extracellular space. Since ALT concentrations decrease significantly on days 7 and 14, this suggests that most PHH were initially damaged by the compounds. Hence, on the subsequent days lower fold changes were detected. With TOL and APAP, the lower fold-change values could indicate a weaker response of the cells or that there was a very rapid release of ALT, which was degraded during further cultivation and storage of the samples until measurement.

As mentioned in Section 3.8.3, LDH is widely used as cytotoxicity marker as it is rapidly released into the culture medium upon disruption of the plasma membrane (Figure 60) [367]. In this work, the highest fold changes in extracellular LDH levels were detected in the OOC model. Fold changes in LDH secretion were weaker for in the 2.5D and 3D models. In 2019, Riss et al. described that LDH has a half-life of approximately 9 h [522]. Therefore, cells may respond very quickly to the substance in 2.5D and 3D, but when the LDH concentration was measured after 2, 7, and 14 days, only minor levels could still be detected. Bell et al. and Li et al. already described the increased sensitivity of 3D cultured PHHs [271][435]. Possibly, PHHs in 3D and 2.5D are more sensitive due to the advanced culture configuration, which is more similar to the liver *in vivo*.

In 2.5D, also a weak dose-dependent increase of LDH was seen for some compounds (TVX, TOL, XIM, ENT) (Figure 69 A). In 3D, no dose-dependent changes in LDH were detected, except for APAP, which induced a reduction. High APAP concentrations can damage liver cells shortly after treatment initiation, resulting in elevated enzyme levels in less than 8-12 hours [523]. Since the LDH level was not determined until day 2, it is possible that the unstable protein is degraded by the time of measurement. Normalized and compared to the vehicle control, the measured LDH levels were therefore much lower than for the other compounds.

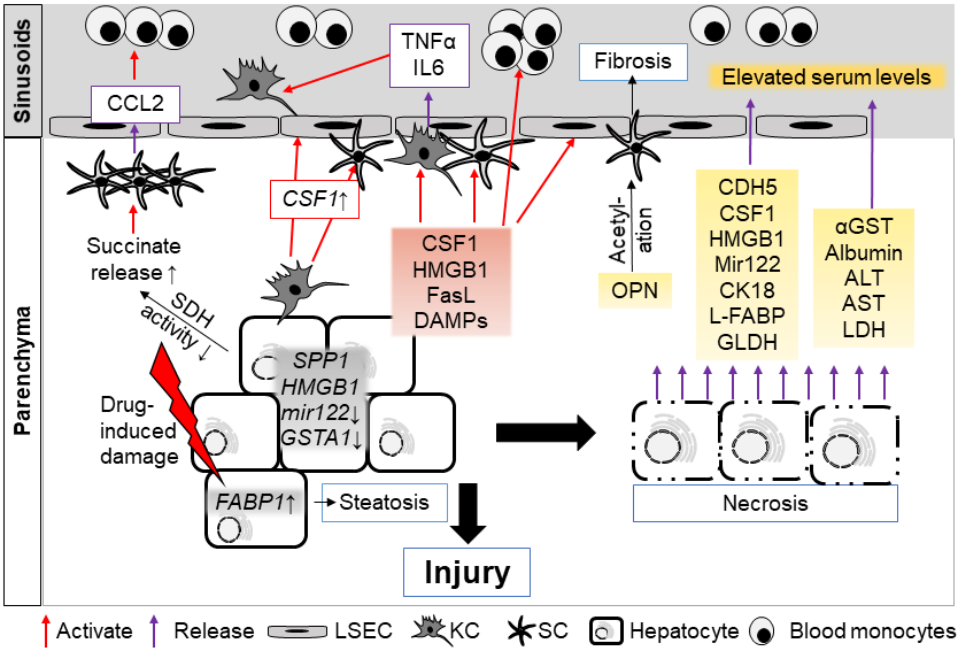

Figure 60: Schematic overview of genes and proteins involved in the development of DILI. Drug-induced damage of hepatocytes lead to release of DAMPs, HMGB1, FasL, CSF1, and other molecular danger molecules. NPCs, such as KCs, SCs, and LSECs become activated and release inflammatory cytokines (e.g., TNFα, IL6, *CCL2* (C-C chemokine 2)) attracting immune cells (e.g., monocytes). The damaged hepatocytes necrotize, resulting in the release of intracellular components and consequent increase in serum levels (yellow). Released OPN upregulates collagen-I production in SCs and can lead to fibrosis. Likewise, altered gene expression of damaged hepatocytes initiates further processes, such as increased fatty acid uptake due to upregulated *FABP1* leading in steatosis. [524]

5.4.4 Insufficient contact between PHHs and KCs in the OOC may inhibit the activation of drug-induced immune responses

OMICs profiles are widely used to understand cellular mechanisms including understanding toxicological changes. In addition, this technology is described as a promising tool to identify potential new biomarkers for the early *in vitro* detection of DILI, as it provides a comprehensive insight into the intracellular changes occurring [93]. Several potential DILI biomarkers have already been described in numerous publications (Section 1.4.5). Some of these have been discovered in human serum samples from DILI patients or by increased expression in animal models but have not yet been tested in *in vitro* experiments before. In this study, eleven genes were investigated for their altered expression after long-term treatment in three advanced cell culture models. These included, *KRT18*, *GSTA1*, *HMGB1*, *FABP1*, *ITGB3*, *SDHA*, *FASLG*, *GLDH*, *SPP1*, *CDH5*, and *CSF1*.

A very weak expression was detected for CDH5 and FASLG in all tested models. In the raw data, the *CDH5* value mostly did not extend beyond the background. The calcium-dependent cell adhesion protein maintains the balance between intercellular junction plasticity and integrity of endothelial cells but is also involved in inflammatory pathways [525]. In a proteomics study, elevated CDH5 levels were found in human plasma and serum samples of DILI patients (Figure 60). Therefore, it was described as a potential marker for DILI, specifically reflecting

inflammatory related changes. [194] In addition, elevated CDH5 levels were described in APAP-induced injury and oxaliplatin-induced sinusoidal dilatation [195][218]. CDH5 has not yet been investigated in *in vitro* studies. However, the results do not support the suitability of the *CDH5* gene expression as a biomarker for the early assessment of DILI. Possibly, a higher extracellular level of this protein can be measured in the supernatant and would provide an option as a biomarker. However, this was not investigated in this project.

Compared with *CDH5*, the measured levels of *FASLG*, encoding for the FasL protein, were also weak and additionally fluctuated strongly between the replicates and treatments. In addition to immune cells, hepatocytes produce FasL, which activates the death receptor FasR, leading to activation of the necrosis signaling pathway, also a known mechanism of certain types of DILI (Figure 60) [526][142]. This pathway is driven on the communication between hepatocytes and the surrounding immune cells. Immune cells are absent in the 2.5D and 3D models. This could be a potential reason for the weak *FASLG* level. KCs are part of the OOC model. However, with respect to the measured marker, it seems that the communication between PHHs and KCs is poor. This may be due to the marker or due to the separate channels. A direct contact between hepatocytes and immune cells is necessary to instruct immune responses [527]. In this project, a longitudinal image of the chip was taken with a special microscope at Leica Microsystems CMS in Mannheim, to find out if the cells in the two channels can have direct contact. As depicted in Figure 64, the cells are separated by a 50 µm thick membrane, containing pores with a diameter of 7 µm. Consequently, it would have to be investigated in more detail whether the cells can have contact through this barrier or/and are able to exchange cytokines and other proteins.

5.4.5 NPCs respond to drugs by producing and secreting important factors that trigger the development of liver injury

In the 2.5D, 3D, and OOC models the fold change in gene expression of *CSF1*, *HMGB1*, and *SPP1* was below the threshold for most compounds (Figure 55). The protein CSF1 regulates the development and recruitment of immune cells, which play an important role in liver regeneration after injuries, such as DILI (Figure 60) [528]. For example, increased serum CSF1 levels were found in patients with APAP-induced liver injury [528]. This protein is produced by a variety of cells, including SCs and endothelial cells, thus also LSEC [529]. However, the expression of *CSF1* by LSECs is reported to be very low until activated by KCs. KCs can upregulate strongly the expression of *CSF1* in both, LSECs and SCs. [530] Therefore, the low levels in the OOC could be due to insufficient contact with hepatocytes that could trigger activation of KCs with consequent activation of the CSF1 production in LSECs and SCs. However, as mentioned above, the cell contact through the membrane requires further investigation to confirm this assumption. In the 2.5D and 3D models the weak levels are due to the lack of KCs per se (Figure 55 A).

SPP1 encodes for OPN (Osteopontin) which is highly induced upon liver damage [531]. During injury, the protein upregulates the collagen-I production in SCs and induces the production of TNFα in cholangiocytes which results in periportal scar formation (Figure 60) [532]. Intracellularly OPN increases *HMGB1* expression and extracellularly it induces HMGB1 acetylation in SCs which both also play a significant role in liver fibrosis [212]. SCs were only part of the OOC. In this model, *SPP1* expression levels did not exceed the threshold. One possible reason was published by Eremo et al., who described that the *SPP1* gene expression is not associated with the OPN protein expression [533]. Hence, the investigation of the OPN protein would need further investigation. In 2.5D and 3D, SCs were absent, but a changed expression levels of *SPP1* was detectable in both. This could be as *SPP1* is also reported to be expressed by hepatocytes [534]. In 2.5D, the expression level was increased with seven substances and decreased with five substances. In contrast, the level in 3D was decreased for 11/14 substances. In general, no difference was observed between the DILI and non-DILI groups, so that *SPP1* gene expression seems to be not a suitable biomarker for the detection of DILI in the investigated cell culture models. However, OPN protein was described to be increased in patients with hepatotoxicity and severity criteria [531][93]. This study only deals with the *SPP1* gene expression which was not significantly increased with all DILI compounds. In addition to the reason describes before (Eremo et al.), elevated plasma OPN levels may be a potential marker for liver failure only in the clinic but not relevant for *in vitro* studies. Furthermore, the communication between hepatocytes, SCs, and cholangiocytes is likely to play a role in the pathological development and therefore their integration in an advanced *in vitro* model could be also relevant. In this present study, SCs were not part of the 2.5D and 3D model and cholangiocytes were not included into the tested advanced cell culture models at all. Therefore, the OPN protein and *SPP1* gene would have to be investigated in future *in vitro* studies with modified cell culture models.

In summary, the interplay between the different liver cell types seems to be an important factor that also influences drug sensitivity and the development of hepatotoxicity. The results and attempts of this study are consistent with the observations already described in other publications and summarized in Section 1.5.2.

5.4.6 Level of excreted HMGB1, CK18, L-FABP, and succinate should be investigated as a potential biomarker for liver damage in the medium supernatant

HMGB1 is mainly involved in gene transcription. Extracellular HMGB1 is described as a key mediator of inflammation because it can bind to a variety of receptors that activate cytokine-mediated responses. [535] MET is used to treat type 2 diabetes and has an anti-inflammatory effect by e.g., activation of autophagy. In *in vitro* and *in vivo* studies the compound showed direct binding to the HMGB1 protein leading to decreased inflammation [536] [537]. For example, in APAP-induced liver injury the treatment with MET showed reduced liver damage [537].

In this study, except for MET in the 3D model, no changes in *HMGB1* expression could be detected (Figure 55 B). Probably the *HMGB1* gene is only turned on under certain condition which were not present in the established cell models, including functional toll-like receptors of immune cells [538]. In addition, it is not clear of there is a correlation between the *HMGB1* expression and HMGB1 protein level, however, the results might assume that due to increased extracellular binding of the HMGB1 protein by MET, PHHs slightly upregulated the *HMGB1* gene expression was. This assumption should be tested in a separate study, as it was not part of this work.

The *KRT18* gene encodes for the CK18 protein. CK18 is very abundant in hepatocytes and cholangiocytes and accounts for 5 % of total liver proteins [539]. Since keratins are known to protect hepatocytes from activated stress kinases in a non-mechanistic manner, these proteins also may behave like stress proteins under certain circumstances [542][540]. For example, an imbalance of keratin pairs (e.g., CK8 and CK18) can sensitize hepatocytes to drug-induced damage [542][543]. A recent publication described the application of CK18 as a biomarker for DILI [543]. Cells actively release CK18 into the extracellular space due to the loss of membrane integrity (Figure 60) [544]. In this study, the expression level of *KRT18* was analyzed after treatment with DILI and non-DILI compounds. With all compounds, except of LVX in the 3D model, low KRT18 levels were detected (Figure 55 C). The slight increase after LVX treatment could also be an outlier, seen by the high standard deviation, as the overall results suggest that treatment had no effect on *KRT18* expression. However, it is possible that CK18 protein is more likely to be measured extracellularly in the supernatant and correlated with CK8 levels to detect imbalance. This assumption was not tested in this work and should be investigated in another project.

SDHA in this work showed no significant response to treatment. It encodes for the SDH complex which is part of the TCA cycle. SDH oxidizes succinate into fumarate [545]. In *in vitro* palmitate-treated hepatocytes, an increased secretion of succinate was observed due to the inhibition of the SDH activity by the compound. Consequently, the increased succinate level triggered the activation of SCs (Figure 60) [546]. Elevated concentrations of SDH are reported in acute and mild liver injuries [122]. SDH is generally rarely described as a potential biomarker for liver injury. However, to consider it as a biomarker for DILI, an attempt should be made to measure the level of succinate in the supernatant after treatment with most-DILI-concern compounds, since this study showed that the gene expression was not affected by treatment. In addition, the integration of SCs could be advantageous because they are described to play a role in the development of the inflammatory response [546]. This again supports the theory from Section 5.4.5, that NPCs are important components of the liver and should not be underestimated in the development of DILI.

FABP1 encodes for the *liver fatty acid-binding protein* (L-FABP) involved in uptake, transport and metabolism of fatty acids [194]. Furthermore, it is the main bile acid binding protein [547]. It is described to respond more rapidly to liver injury then ALT and elevated serum levels were detected in patients suffering from acute hepatocellular damage [194]. L-FABP accounts for 3-5 % of total protein content in hepatocytes which is released into the extracellular space upon damage [548]. In this study, *FABP1* expression level increased after treatment with PIO, DIC, and TVX in 2.5D and 3D. A higher expression of *FABP1* is associated with increased fatty acid uptake, which may lead to triglyceride accumulation associated with steatosis (Figure 60) [549]. L-FABP as a biomarker for hepatic steatosis was also already described by Newberry et al. *in vivo* [550]. *FABP1* as potential genetic biomarker cannot be confirmed based on the expression data. Therefore, further examination of the L-FABP level in the supernatant should be performed after treatment, as it is reported to be increased in serum due to damaged hepatocytes [194].

5.4.7 Hepatocyte-like cells and PHHs respond differently with ITGB3 expression after treatment

ITGB3 is an adhesion molecule involved in inflammatory response and liver regeneration [206]. In a small study, serum ITGB3 levels of patients with acute liver injury and iDILI were lower compared with controls, as evidenced by ITGB3-positive cells recruited to the liver from the periphery [206]. Moreover, in hepatocyte-like cells *ITGB3* expression was upregulated after DIC treatment. In this work, a decrease in *ITGB3* level was observed in the 2.5D and 3D model after DIC treatment. This may be due to reason that primary liver cells respond differently from hepatocyte-like cells as differentiated cells may lack certain factors, such as transcription factors and nuclear receptors that are required for the response to xenobiotics comparable to PHHs. The expression of *ITGB3* was strongly increased after BOS treatment, however, only in the 2.5D model. BOS was used as positive control in this study as it is known to induce DILI by inhibition of the BSEP [498]. An increased *ITGB3* expression after BOS treatment was not yet described and due to the high standard deviation, the significant increase in gene expression could be an outlier and should be confirmed in further experiments. In addition, there was no clear distinction between DILI- and non-DILI-treated cells in any of the models tested, suggesting that *ITGB3* expression is not a sensitive marker for DILI.

5.4.8 Secreted GLDH levels as potential biomarker for drug-induced mitochondrial toxicity

The *GLUD1* gene encodes for the protein GLDH which is expressed in the mitochondrial matrix of hepatocytes. It is relatively liver specific and involved in amino acid oxidation and urea production. [551] The protein is described as a better predictor of hepatocyte necrosis than ALT and mir122, as it increases very rapidly and in high concentrations upon injury [552]. Moreover,

it is described as a biomarker of mitochondrial dysfunction due to necrosis induced by mitochondrial toxicity (Figure 60) [122]. In this study, *GLUD1* expression levels were elevated after treatment with AMIO in 2.5D and LVX in 3D. AMIO-induced liver injury is attributed to mitochondrial dysfunction (Section 1.6). However, this is not the case for LVX. In addition, other compounds with reported mitochondrial DILI outcome, such as TOL and TRO, had no effect on *GLUD1* levels. It should be further investigated whether the GLDH level in the supernatant could be a potential biomarker for drug-induced mitochondrial toxicity as this was not part of the present work.

5.4.9 The expression of GSTA1 is statistically significant different between DILI and non-DILI treatment in 2.5D and 3D

GSTA1 encodes for the phase II enzyme αGST which plays an important role in regulating liver-specific gene expression and influences drug metabolism (Section 1.3.2). Elevation of the enzyme in the serum is comparable to the elevation of ALT and AST and therefore a potential marker for liver injury (Figure 60) [174]. For example, αGST was significantly increased in the supernatant of APAP-treated hepatocytes already after 6 h [553]. Furthermore, in mice, *GSTA1* mRNA expression decreased after treatment with various compounds such as APAP, suggesting release into the extracellular space where it acts as an antioxidant and prevents the liver from damage [554]. In this study, changes in *GSTA1* gene expression were detected in all advanced cell culture models after treatment with MET, APAP, DIC, TVX, and LVX (Figure 56). The statistical analysis showed that *GSTA1* is significantly different between the defined groups of most-DILI-concern and less-DILI-concern compounds in the 2.5D and 3D models (Figure 57). Due to the known difference in the configuration between 2D and 3D cultured hepatocytes, a statistical significance was found in 2.5D at the low doses and in 3D at the high doses. In 2.5D, the drug comes into contact with all cells simultaneously. Hence, a lower dose may be sufficient to induce a response.

The decrease in gene expression of *GSTA1* and the increase in αGST in the supernatant could be a potential biomarker for DILI, as exemplary seen in the 3D model after treatment with the positive control BOS (Section 5.4.3, Figure 53 E and Figure 56 D). However, different concentrations must be tested to determine which one triggers a DILI pathomechanism as this could be different in each test model (Appendix 8.9). In addition. more compounds should be tested in a further study to confirm the observation in this work.

5.4.10 Mir122-decrease in all APAP-treated models reinforces its suitability as a marker for hepatocellular damage

As described previously, mir122 and mir192 are enriched in hepatic tissues and are important regulators of gene expression [123][177][555]. In addition, the small non-coding RNAs are de-

scribed as sensitive biomarkers for DILI [501]. Mir122 is the most abundant miRNA in hepatocytes and plays a key role in diseases, maintenance of liver homeostasis, and hepatocyte function (e.g., lipid and cholesterol metabolism) [556]. In hepatitis virus infections, mir122 inhibits viral replication. Therefore, its antagonistic effect is currently being studied in phase II trials [557]. Elevated intracellular levels of mir122 are associated with good liver homeostasis and health, whereas decreased levels indicate poor disease outcome with hepatocellular damage [556].

In this work, the mir122 levels were measured and compared in the advanced cell culture models after long-term treatment with eleven compounds. A reduction with 8/11 compounds was observed in the 2.5D model indicating hepatocellular damage (Figure 59 A). In contrast, 3D cultured liver cells show decreased mir122 levels with five compounds but elevation with six. Especially, with MET an 11.5-fold increase was observed. In a recent study, plasma levels of mir122 were found to decrease during treatment with MET, suggesting improved metabolic health, as MET is known to reduce inflammation during liver injury [555]. A decreased level in plasma may be due to an increased intracellular concentration, as found in this study (Figure 60). However, mir122 elevation was also measurable after DIC, FIA, TVX, and LVX treatment. Therefore, this would need to be investigated in more detail.

When cultured in an OOC, liver cells only showed a weak response to treatment. The expression was slightly reduced by four compounds and even more decreased in 3/11 compounds (TOL, FIA, APAP). In general, the decreased level with APAP was observed in all models. An elevation of mir122 in the plasma in the context of APAP-induced toxicity has been reported [177][172][178]. Decreased intracellular levels can be associated with elevated supernatant levels. Thus, future studies should also investigate the content of mir122 in the supernatant and correlate it with the intracellular level after treatment.

In conclusion, the detection of the intracellular mir122 levels seem not to be able to distinguish between DILI and non-DILI compounds. However, the secretion of miRNA due to destruction of cells may be a promising marker and should be investigated in a further study to get a deeper insight into its role in hepatocellular processes [501]. Another study demonstrated that mir122 plays a critical role in hepatocyte innate immunity by regulating genes that contribute to signal transducer and activator of transcription 3 phosphorylation, thereby abrogating the negative regulation of interferon signaling [558]. The correlation between mir122 and innate immunity could be investigated in advanced cell culture models including KCs [556]

6 Conclusion

The liver is often the initial target for medication-induced damage [85]. Therefore, it is not surprising that new drug candidates have a high failure rate in preclinical and clinical trials due to unacceptable and unexpected drug-induced hepatotoxicity [96]. DILI is the most common cause of acute liver failure, post-marketing drug withdrawal, and restricted-use warnings [86]–[89]. *In vitro*, PHHs remain the gold standard for drug-induced hepatotoxicity and ADME studies as they completely reflect the major functionality of the liver (Section 1.5.1). Nevertheless, primary liver cells rapidly lose their physiological functions when grown in monoculture as a monolayer. Hence, there is an urgent need to develop new methods for the early and reliable prediction of DILI which allow a better identification of drug candidates with high hepatotoxicity potential at an early stage of drug development. The goal of this work was to improve the prediction of DILI in preclinical studies by establishing advanced cell culture models and evaluating new, more reliable and/or sensitive biomarkers.

The results of the thesis demonstrated a successful establishment of a 2.5D, 3D, and OOC coculture model (AIM_1). The *in vitro* adaptation to the *in vivo* physiological conditions, e.g., through integration of more liver cell types and an ECM, improved the *in vitro* stability and performance of primary liver cells especially in the 3D and OOC model (AIM_3). This can be attributed to the defined cell-cell-contact and improved long-term functionalization displayed in robust secretion of hepatic proteins and stable mRNA expression levels of liver specific markers, metabolomic enzymes, and transporters. Moreover, the advanced models showed structural and functional polarization of transporters with successful CMFDA transport via MRP2, indicating the formation of bile canaliculi-like structures. The insufficient formation of bile canaliculi in liver cocultures should be further investigated, as NPCs play an important role in hepatotoxicity and therefore need to be included in the advanced hepatic models [272]. The proteomic analysis has shown that culture configuration has an impact on the induction of multiple signaling pathways. For example, metabolic pathways associated with CYP450 metabolism were more prominent in 3D-grown PHH than in 2D/2.5D cultures, leading to the assumption that experiments involving the CYP450 system (e.g., CYP induction/inhibition assays) should preferably be performed in 3D cultures. Culture configuration dependent differences were also observed in the metabolomics study, in which the same donors were cultured for extended periods in four different models. The detected metabolites differed across the systems in both, cell lysate and supernatant. The differences resulting from the cultural configuration need to be further explored and should be considered when choosing an appropriate study model, as for example, the study of biliary secretion would be beneficial in the OOC model in which bile acids were predominantly found.

A further part of this work was the differentiation of iPSC-derived liver organoids (AIM_2). The initial results suggest a successful differentiation of liver organoids using a three-stage differentiation protocol. Liver organoids showed a typical morphological shape and important hepatic characteristics, including the expression of cell-specific markers and the secretion of albumin, αGST, ALT, and AST. Best results were obtained with method 3 based on the typical morphological shape, robust expression of hepatic markers (e.g., *ALB*, CYP450 enzymes, and transporters) and hepatocyte-like functionality, including formation of canaliculi-like structures, secretion of hepatic enzymes, and response to compounds. The hepatic-like reaction to xenobiotics and the ability for long-term studies, make liver organoids a robust model for the early assessment and mechanistic understanding of DILI. Contrary to advanced cell culture models using primary liver cells, these cells can form an organ-specific architecture, are of unlimited supply, self-renew, and self-organize within the organoid, allowing a *in vivo*-like investigation of hepatotoxic effects and other mechanisms. Recently, another extension was described that combined OOC technology with organoids to recapitulate the complexity of a human organ more closely [558][559]. Achberger et al. integrated a vascular-like perfusion of retina organoids within an OOC which provides more insights into the pathology of retina diseases [558]. To date, no organoid chip for the liver has been described in the literature, but the field is currently growing by increasing interest as it offers a promising platform to analyze an *in-vivo*-like, dynamic, and multicellular system *in vitro*. In conclusion, the organoid field still requires further characterization and optimization regarding e.g., optimized protocols for standardized use in pharmacological and toxicological studies.

The characterized advanced liver models were treated with a set of compounds selected from the most- and less-DILI-concern category of the FDA DILI-rank dataset (AIM_4) [337]. The 2.5D, 3D, and OOC system were treated long-term followed by the detection and comparison of a set of proteins and genes described as potential DILI biomarkers (AIM_5). In general, no model and no examined biomarker was able to reliable detect all DILI causing drugs *in vitro*. However, statistical analysis revealed that expression of *GSTA1* was significantly different between DILI and non-DILI-treated liver cells in 2.5D and 3D. This suggests that *GSTA1* can be a potential DILI biomarker and that the simpler advanced liver models may be better in terms of studying DILI than the complex OOC model. The evidence is strengthened by the fact that the αGST level in the supernatant of the 3D culture was increased for DILI substances. This study has shown that there are potential biomarkers able to detect DILI-risk-compounds, but they need to be further investigated by integrating more compounds to confirm these findings.

The results of this work let assume that advanced cell culture models may be a suitable tool to evaluate potential DILI biomarkers and study unexpected hepatotoxicity in a more physiological related environment. In addition, these hepatic models are a useful tool for long-term toxicology testing as they maintain many important aspects (e.g., metabolic activities, secretion

of hepatic proteins, and formation of bile canaliculi-like structures indicating the reconstruction of cellular polarity). It should be noted that each model has its place in drug development depending on the complexity of the question being asked (Figure 61). The 2.5D model is very simple, allows higher throughput, and can be used to analyze specific targeted questions, e.g., examining a compound's effect on the cellular target. Studies using the 2.5D coculture model, created in this work, have already been requested and performed in the *in vitro* toxicology laboratory of Merck KGaA. The 3D spheroid model can also be used for early screening and the mechanistic understanding of specific issues. Compared to 2.5D, the 3D model showed improved retention of metabolic activity for extended periods, allowing repeated-dose and long-term hepatotoxicity studies in a multicellular and higher throughput manner.

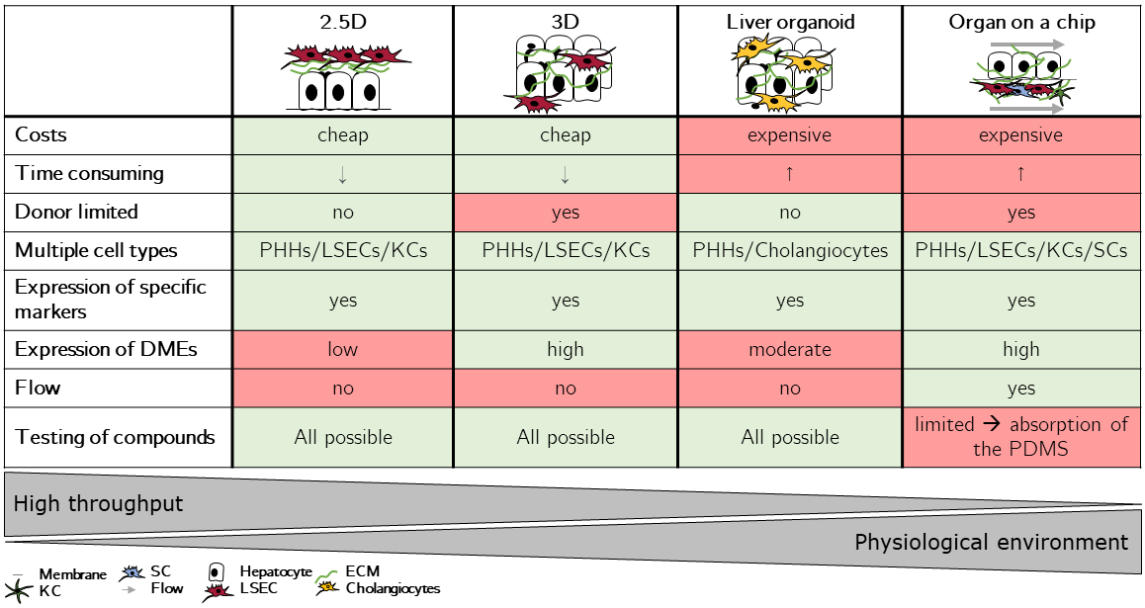

Figure 61. Summary of established and characterized advanced cell culture models with their advantages and disadvantages.

Liver organoids present with an organ-like architecture, have a self-renewal capacity, and are of unlimited supply. These strengths make them a promising tool for studying toxicological effects within a small functional unit of the liver. However, the culture of iPSCs is very expensive and the differentiation into liver organoids is very time-consuming. Moreover, this is a very new field that needs to be optimized and standardized before it can be routinely used in drug development studies. For example, the expression of DMEs in liver organoids was lower than in PHHs which needs further optimization. Similarly, the individual cell types within an organoid must be characterized in more detail and compared to primary cells, such as cholangiocytes in this project. Only fully characterized organoids and standardized protocols can be used in the drug development process. Organoids would allow repeated-dose hepatotoxicity studies and long-term multicellular studies with higher throughput, with the further advantage of additionally analyzing *in vivo*-like organizing and self-renewal mechanisms.

MPS *per se* can be a good tool to understand mechanistic processes. The Emulate OOC used in this work contained four liver cell types recapitulating the physiological architecture of the liver. However, for toxicological screening this system has some limitations (e.g., high cost, number of chips per experiment, used donor, and the compounds that can be tested). Comparable to 3D, it showed improved maintenance of metabolic activity over 14 days, allowing repeated-dose and long-term hepatotoxicity studies in a dynamic model. Another advantage may be the recapitulation of an *in vivo*-like liver zonation that generates metabolic patterns based on gradients (e.g., nutrients, oxygen) described by Kang et al. [559]. However, since the PHHs and NPCs are cultured in different channels in the Emulate OOC model, the communication between the cells needs further investigation.

Today there are already OOC models from other suppliers on the market that are different to the Emulate OOC. For example, a liver chip with high throughput capacity was recently described by Bircsak et al. using the iHeps in the OrganoPlate® from MIMETAS, an OOC-technology-company [560]. In contrast to the Emulate OOC, this technology does not require an external pumping system, does not consist of PDMS, the assembly is less time consuming and not donor dependent [561]. However, the cells are growing in 2D as a tube and so far, there are no publications with primary liver cells. Another example was published by Lohasz et al. using colorectal microtissues in the InSphero AG microfluidic chip [562]. In contrast to the Emulate and MIMETAS OOC models, 3D microtissues from either the same, different, or mixed tissues can be integrated into the InSphero OOC. Like the MIMETAS OOC, perfusion is driven by gravity via a rocker, hence no external pumps are required. However, there are only eight chips per 96-well plate, which, limits the application for higher throughput.

The mechanism of DILI is still poorly understood as it appears in different factettes in man. Therefore, it is necessary, to study the mechanism of DILI in more detail which may help to understand its development and to identify a reliable biomarker. Furthermore, it is also possible that a combination of biomarkers may be required to predict DILI *in vitro*, as it is known that many processes are involved in the development. The generated results also highlighted the importance of integrating multiple cell types, including biliary cells, endothelial cells, and the immune system (e.g., KCs, macrophages, T cells), as the communication between NPCs and hepatocytes plays an important role in the understanding of the development of DILI.

Looking into the future, advanced cell culture systems are increasingly being developed, characterized, and integrated into the early screening tools used across industry and academia. Their utilization can lead to a better understanding of the response of cells to drugs. This will allow a better and faster recognition and interpretation of drug-induced mechanisms, bridging the gap between simple 2D and very complex *in vivo* models. Nevertheless, more in-depth studies and a better understanding of the mechanism of liver damage by drugs are required for the reliable integration into preclinical toxicological studies.

7 Literature

[1] I. Kola and J. Landis, “Can the pharmaceutical industry reduce attrition rates?,” *Nat. Rev. Drug Discov.*, vol. 3, no. 8, pp. 711–715, 2004, doi: 10.1038/NRD1470.

[2] “Toxicology Education Foundation | What is Toxicology?” https://toxedfoundation.org/what-is-toxicology/ (accessed Sep. 13, 2021).

[3] D. Milles, “History of Toxicology,” *Toxicology*, pp. 11–23, 1999, doi: 10.1016/B978-012473270-4/50060-2.

[4] A. M. Tsatsakis *et al.*, “The dose response principle from philosophy to modern toxicology: The impact of ancient philosophy and medicine in modern toxicology science,” *Toxicol. Reports*, vol. 5, pp. 1107–1113, Jan. 2018, doi: 10.1016/J.TOXREP.2018.10.001.

[5] G. Arink, “Toxicology,” *Dent. Regist.*, vol. 16, no. 6, p. 278, Jun. 1862, Accessed: Sep. 13, 2021. [Online]. Available: https://www.ncbi.nlm.nih.gov/pmc/articles/PMC6903545/.

[6] M. J. Alomar, “Factors affecting the development of adverse drug reactions (Review article),” *Saudi Pharm. J. SPJ*, vol. 22, no. 2, p. 83, 2014, doi: 10.1016/J.JSPS.2013.02.003.

[7] L.V. Maximenko, “Preventive toxicology and its role in occupational hygiene - ppt download.” https://slideplayer.com/slide/13229698/ (accessed Sep. 13, 2021).

[8] “The Senate Commission on Animal Protection and Experimentation Animal Experimentation in Research Animal Experimentation in Research.”

[9] O. H *et al.*, “Concordance of the toxicity of pharmaceuticals in humans and in animals,” *Regul. Toxicol. Pharmacol.*, vol. 32, no. 1, pp. 56–67, 2000, doi: 10.1006/RTPH.2000.1399.

[10] S. J. Morgan *et al.*, “Use of Animal Models of Human Disease for Nonclinical Safety Assessment of Novel Pharmaceuticals,” doi: 10.1177/0192623312457273.

[11] E. C. Bryda, “The Mighty Mouse: The Impact of Rodents on Advances in Biomedical Research,” *Mo. Med.*, vol. 110, no. 3, p. 207, 2013, Accessed: Oct. 20, 2021. [Online]. Available: /pmc/articles/PMC3987984/.

[12] L. Lossi, L. D’Angelo, P. De Girolamo, and A. Merighi, “Anatomical features for an adequate choice of experimental animal model in biomedicine: II. Small laboratory rodents, rabbit, and pig,” *Ann. Anat.*, vol. 204, pp. 11–28, Mar. 2016, doi: 10.1016/J.AANAT.2015.10.002.

[13] “FDA (2006) FDA Issues Advice to Make Earliest Stages of Clinical Drug Development More Efficient. - References - Scientific Research Publishing.” https://www.scirp.org/(S(lz5mqp453edsnp55rrgjct55))/reference/ReferencesPapers.aspx?ReferenceID=1265109 (accessed Sep. 14, 2021).

[14] N. Shanks, R. Greek, and J. Greek, “Are animal models predictive for humans?,” *Philos. Ethics. Humanit. Med.*, vol. 4, no. 1, p. 2, Jan. 2009, doi: 10.1186/1747-5341-4-2.

[15] J. Farhat, I. Pandey, and M. AlWahsh, “Transcending toward Advanced 3D-Cell Culture Modalities: A Review about an Emerging Paradigm in Translational Oncology,” *Cells 2021, Vol. 10, Page 1657*, vol. 10, no. 7, p. 1657, Jul. 2021, doi: 10.3390/CELLS10071657.

[16] “3R principle by Russel and Burch: University of Hohenheim.” https://www.uni-hohenheim.de/en/3-r-principle (accessed Sep. 14, 2021).

[17] “EURL-ECVAM - English.” https://en.3rcenter.dk/3r-organizations/eurl-ecvam (accessed Sep. 14, 2021).

[18] “Drug development: the journey of a medicine from lab to shelf - The Pharmaceutical Journal.” https://pharmaceutical-journal.com/article/feature/drug-development-the-journey-of-a-medicine-from-lab-to-shelf (accessed Sep. 14, 2021).

[19] O. J. Wouters, M. McKee, and J. Luyten, “Estimated Research and Development Investment Needed to Bring a New Medicine to Market, 2009-2018,” *JAMA - J. Am. Med. Assoc.*, vol. 323, no. 9, pp. 844–853, Mar. 2020, doi: 10.1001/JAMA.2020.1166.

[20] K. H. Bleicher, H.-J. Böhm, K. Müller, and A. I. Alanine, “Hit and lead generation: beyond high-throughput screening,” *Nat. Rev. Drug Discov. 2003 25*, vol. 2, no. 5, pp. 369–378, May 2003, doi: 10.1038/nrd1086.

[21] A. B. Deore, J. R. Dhumane, R. Wagh, and R. Sonawane, “The Stages of Drug Discovery and Development Process,” *Asian J. Pharm. Res. Dev.*, vol. 7, no. 6, pp. 62–67, Dec. 2019, doi: 10.22270/AJPRD.V7I6.616.

[22] S. Brogi, T. C. Ramalho, K. Kuca, J. L. Medina-Franco, and M. Valko, “Editorial: In silico Methods for Drug Design and Discovery,” *Front. Chem.*, vol. 0, p. 612, Aug. 2020, doi: 10.3389/FCHEM.2020.00612.

[23] D. MA and B. LA, “Toxicology in the drug discovery and development process,” *Curr. Protoc. Pharmacol.*, vol. Chapter

10, 2006, doi: 10.1002/0471141755.PH1003S32.

[24] H. Matthews, J. Hanison, and N. Nirmalan, "'Omics'-informed drug and biomarker discovery: Opportunities, challenges and future perspectives," *Proteomes*, vol. 4, no. 3, Sep. 2016, doi: 10.3390/PROTEOMES4030028.

[25] "Phases of Drug Development Process, Drug Discovery Process | NorthEast BioLab." https://www.nebiolab.com/drug-discovery-and-development-process/ (accessed Sep. 14, 2021).

[26] "DRUG DISCOVERY – Bill Chen Drug Discovery Lab." http://www.drugdiscoverycenter.org/drug-discovery/ (accessed Sep. 14, 2021).

[27] "Machine Learning applied to Drug Discovery." https://doctortarget.com/machine-learning-applied-drug-discovery/ (accessed Sep. 14, 2021).

[28] K. L. Steinmetz and E. G. Spack, "The basics of preclinical drug development for neurodegenerative disease indications," *BMC Neurol. 2009 91*, vol. 9, no. 1, pp. 1–13, Jun. 2009, doi: 10.1186/1471-2377-9-S1-S2.

[29] A. Regev, "Drug-induced liver injury and drug development: Industry perspective," *Semin. Liver Dis.*, vol. 34, no. 2, pp. 227–239, 2014, doi: 10.1055/S-0034-1375962.

[30] E. P. Weledji and E. Ngounou, "The Impact of Segmental Anatomy on Hepatic Oncologic Resections," *Curr. Surg. Reports 2016 41*, vol. 4, no. 1, pp. 1–12, Jan. 2016, doi: 10.1007/S40137-015-0122-1.

[31] C. Olgasi, A. Cucci, and A. Follenzi, "iPSC-Derived Liver Organoids: A Journey from Drug Screening, to Disease Modeling, Arriving to Regenerative Medicine," *Int. J. Mol. Sci. 2020, Vol. 21, Page 6215*, vol. 21, no. 17, p. 6215, Aug. 2020, doi: 10.3390/IJMS21176215.

[32] S. R. Z. Abdel-Misih and M. Bloomston, "Liver Anatomy," *Surg. Clin. North Am.*, vol. 90, no. 4, pp. 643–653, Aug. 2010, doi: 10.1016/J.SUC.2010.04.017.

[33] S. S. Bale *et al.*, "Long-Term Coculture Strategies for Primary Hepatocytes and Liver Sinusoidal Endothelial Cells," *Tissue Eng. Part C Methods*, vol. 21, no. 4, pp. 413–422, 2015, doi: 10.1089/ten.tec.2014.0152.

[34] N. Aizarani *et al.*, "A human liver cell atlas reveals heterogeneity and epithelial progenitors," *Nat. 2019 5727768*, vol. 572, no. 7768, pp. 199–204, Jul. 2019, doi: 10.1038/s41586-019-1373-2.

[35] A. SK, D. H, E. J, and K. PS, "Burden of liver diseases in the world," *J. Hepatol.*, vol. 70, no. 1, pp. 151–171, Jan. 2019, doi: 10.1016/J.JHEP.2018.09.014.

[36] "The global, regional, and national burden of cirrhosis by cause in 195 countries and territories, 1990-2017: a systematic analysis for the Global Burden of Disease Study 2017," *lancet. Gastroenterol. Hepatol.*, vol. 5, no. 3, pp. 245–266, Mar. 2020, doi: 10.1016/S2468-1253(19)30349-8.

[37] K. OZAWA, "Hepatic function and liver resection," *J. Gastroenterol. Hepatol.*, vol. 5, no. 3, pp. 296–309, Jun. 1990, doi: 10.1111/J.1440-1746.1990.TB01632.X.

[38] "Rapid rise in deaths from liver disease in the US over the last decade | BMJ." https://www.bmj.com/company/newsroom/rapid-rise-in-deaths-from-liver-disease-in-the-us-over-the-last-decade/ (accessed Aug. 16, 2021).

[39] J. Xiao *et al.*, "Global liver disease burdens and research trends: Analysis from a Chinese perspective," *J. Hepatol.*, vol. 71, no. 1, pp. 212–221, Jul. 2019, doi: 10.1016/J.JHEP.2019.03.004.

[40] "The Functions of the Liver and Signs You Need to Detox | PatriotDirect Family Medicine | Natick, MA." https://patriotdirectfm.com/2020/05/the-functions-of-the-liver-and-signs-you-need-to-detox/ (accessed Aug. 16, 2021).

[41] "The Radiology Assistant : Segmental Anatomy." https://radiologyassistant.nl/abdomen/liver/segmental-anatomy (accessed Aug. 23, 2021).

[42] Florian Horn, "Biochemie des Menschen," *Georg Thieme Verlag KG*, 2019. thieme.de (accessed Aug. 16, 2021).

[43] "Anatomy of the Liver." https://www.upmc.com/services/liver-cancer/liver/anatomy-liver (accessed Aug. 16, 2021).

[44] "Leberläppchen, aus dem Gesundheitslexikon | Gesundheit, Medizin und Heilkunde auf wissen.de." https://www.wissen.de/medizin/leberlaeppchen (accessed Aug. 16, 2021).

[45] S. H, K. N, and S. M, "Vitamin A-storing cells (stellate cells)," *Vitam. Horm.*, vol. 75, pp. 131–159, 2007, doi: 10.1016/S0083-6729(06)75006-3.

[46] H. J. Seo *et al.*, "Rapid Hepatobiliary Excretion of Micelle-Encapsulated/Radiolabeled Upconverting Nanoparticles as an Integrated Form," *Sci. Rep.*, vol. 5, Oct. 2015, doi: 10.1038/SREP15685.

[47] Z. Zhou, M.-J. Xu, and B. Gao, "Hepatocytes: a key cell type for innate immunity," *Cell. Mol. Immunol. 2016 133*, vol. 13, no. 3, pp. 301–315, Dec. 2015, doi: 10.1038/cmi.2015.97.

[48] A. L. Wilkinson, M. Qurashi, and S. Shetty, "The Role of Sinusoidal Endothelial Cells in the Axis of Inflammation and Cancer Within the Liver," *Front. Physiol.*, vol. 0, p. 990, Aug. 2020, doi: 10.3389/FPHYS.2020.00990.

[49] L. J. Dixon, M. Barnes, H. Tang, M. T. Pritchard, and L. E. Nagy, “Kupffer Cells in the Liver,” *Compr. Physiol.*, vol. 3, no. 2, p. 785, 2013, doi: 10.1002/CPHY.C120026.

[50] J. H. Tabibian, A. I. Masyuk, T. V. Masyuk, S. P. O’Hara, and N. F. LaRusso, “Physiology of Cholangiocytes,” *Compr. Physiol.*, vol. 3, no. 1, pp. 541–565, 2013, doi: 10.1002/CPHY.C120019.

[51] “Architecture of the Liver and Biliary Tract.” http://www.vivo.colostate.edu/hbooks/pathphys/digestion/liver/anatomy.html (accessed Aug. 23, 2021).

[52] X. Gu and J. E. Manautou, “Molecular mechanisms underlying chemical liver injury,” *Expert Rev. Mol. Med.*, vol. 14, p. e4, Jan. 2012, doi: 10.1017/S1462399411002110.

[53] X. C, L. CY, and K. AN, “Induction of phase I, II and III drug metabolism/transport by xenobiotics,” *Arch. Pharm. Res.*, vol. 28, no. 3, pp. 249–268, Mar. 2005, doi: 10.1007/BF02977789.

[54] O. A. Almazroo, M. K. Miah, and R. Venkataramanan, “Drug Metabolism in the Liver,” *Clin. Liver Dis.*, vol. 21, no. 1, pp. 1–20, Feb. 2017, doi: 10.1016/J.CLD.2016.08.001.

[55] X. C, L. CY, and K. AN, “Induction of phase I, II and III drug metabolism/transport by xenobiotics,” *Arch. Pharm. Res.*, vol. 28, no. 3, pp. 249–268, Mar. 2005, doi: 10.1007/BF02977789.

[56] G. L. Truisi, *A multiple endpoint approach to predict the hepatotoxicity of pharmaceuticals in vitro*, PhD Thesis. Weinheim: KIT, 2014.

[57] N. Penner, C. Woodward, and C. Prakash, “Drug Metabolizing Enzymes and Biotransformation Reactions,” *ADME-Enabling Technol. Drug Des. Dev.*, pp. 545–565, May 2012, doi: 10.1002/9781118180778.APP1.

[58] A. Jetter and G. A. Kullak-Ublick, “Drugs and hepatic transporters: A review,” *Pharmacol. Res.*, vol. 154, p. 104234, Apr. 2020, doi: 10.1016/J.PHRS.2019.04.018.

[59] Z. UM and S. M, “Cytochrome P450 enzymes in drug metabolism: regulation of gene expression, enzyme activities, and impact of genetic variation,” *Pharmacol. Ther.*, vol. 138, no. 1, pp. 103–141, Apr. 2013, doi: 10.1016/J.PHARMTHERA.2012.12.007.

[60] T. L. Poulos and E. F. Johnson, “Structures of cytochrome P450 enzymes,” *Cytochrome P450 Struct. Mech. Biochem. Fourth Ed.*, pp. 3–32, Jan. 2015, doi: 10.1007/978-3-319-12108-6_1.

[61] D. R. Nelson, “Cytochrome P450 Nomenclature, 2004,” *Methods Mol. Biol.*, vol. 320, pp. 1–10, 2006, doi: 10.1385/1-59259-998-2:1.

[62] M. 1941- Eichelbaum, “Wirkungen des Organismus auf Pharmaka: allgemeine Pharmakokinetik,” *Allg. und Spez. Pharmakologie und Toxikologie*, 2013.

[63] D. C. Lamb, M. R. Waterman, S. L. Kelly, and F. P. Guengerich, “Cytochromes P450 and drug discovery,” *Curr. Opin. Biotechnol.*, vol. 18, no. 6, pp. 504–512, Dec. 2007, doi: 10.1016/J.COPBIO.2007.09.010.

[64] F. O. and M. Arand, *Toxicology - Xenobiotic Metabolism*. Academic Press, 1999.

[65] T. F. Herman and C. Santos, “First Pass Effect,” *xPharm Compr. Pharmacol. Ref.*, pp. 1–2, Jul. 2021, Accessed: Aug. 23, 2021. [Online]. Available: https://www.ncbi.nlm.nih.gov/books/NBK551679/.

[66] P. Jančová and M. Šiller, “Phase II Drug Metabolism,” *Top. Drug Metab.*, Feb. 2012, doi: 10.5772/29996.

[67] E. F. Barreto, T. R. Larson, and E. J. Koubek, “Drug Excretion,” *Ref. Modul. Biomed. Sci.*, Jan. 2021, doi: 10.1016/B978-0-12-820472-6.99999-7.

[68] R. Seifert, “Pharmacokinetics,” *Basic Knowl. Pharmacol.*, pp. 31–47, 2019, doi: 10.1007/978-3-030-18899-3_2.

[69] “Drug Development and Drug Interactions | Table of Substrates, Inhibitors and Inducers | FDA.” https://www.fda.gov/drugs/drug-interactions-labeling/drug-development-and-drug-interactions-table-substrates-inhibitors-and-inducers (accessed Aug. 26, 2021).

[70] Y. K, Y. N, T. T, and Y. Y, “Constitutive androstane receptor transcriptionally activates human CYP1A1 and CYP1A2 genes through a common regulatory element in the 5’-flanking region,” *Biochem. Pharmacol.*, vol. 79, no. 2, pp. 261–269, Jan. 2010, doi: 10.1016/J.BCP.2009.08.008.

[71] G. B, H. E, D. DJ, R. GR, and L. C, “Transcriptional regulation of the human CYP3A4 gene by the constitutive androstane receptor,” *Mol. Pharmacol.*, vol. 62, no. 2, pp. 359–365, 2002, doi: 10.1124/MOL.62.2.359.

[72] G.-C. S, D. M, P. JM, P.-G. L, V. MJ, and M. P, “Transcriptional regulation of CYP2C9 gene. Role of glucocorticoid receptor and constitutive androstane receptor,” *J. Biol. Chem.*, vol. 277, no. 1, pp. 209–217, Jan. 2002, doi: 10.1074/JBC.M107228200.

[73] S. J *et al.*, “The phenobarbital response enhancer module in the human bilirubin UDP-glucuronosyltransferase UGT1A1 gene and regulation by the nuclear receptor CAR,” *Hepatology*, vol. 33, no. 5, pp. 1232–1238, Jan. 2001, doi: 10.1053/JHEP.2001.24172.

[74] G. A, E. M, and B. O, “Nuclear receptor response elements mediate induction of intestinal MDR1 by rifampin,” *J. Biol. Chem.*, vol. 276, no. 18, pp. 14581–14587, May 2001, doi: 10.1074/JBC.M010173200.

[75] K. HR *et al.*, “Regulation of multidrug resistance-associated protein 2 (ABCC2) by the nuclear receptors pregnane X receptor, farnesoid X-activated receptor, and constitutive androstane receptor,” *J. Biol. Chem.*, vol. 277, no. 4, pp. 2908–2915, Jan. 2002, doi: 10.1074/JBC.M109326200.

[76] A. M *et al.*, “Interactions between hepatic Mrp4 and Sult2a as revealed by the constitutive androstane receptor and Mrp4 knockout mice,” *J. Biol. Chem.*, vol. 279, no. 21, pp. 22250–22257, May 2004, doi: 10.1074/JBC.M314111200.

[77] M. JM, S. CM, G. B, H.-B. D, M. JT, and K. SA, “Nuclear pregnane x receptor and constitutive androstane receptor regulate overlapping but distinct sets of genes involved in xenobiotic detoxification,” *Mol. Pharmacol.*, vol. 62, no. 3, pp. 638–646, Sep. 2002, doi: 10.1124/MOL.62.3.638.

[78] O. CJ, V. H. JP, P. GH, and P. JM, “Xenobiotic metabolism, disposition, and regulation by receptors: from biochemical phenomenon to predictors of major toxicities,” *Toxicol. Sci.*, vol. 120 Suppl 1, no. Suppl 1, 2011, doi: 10.1093/TOXSCI/KFQ338.

[79] P.-F. Hu and W.-F. Xie, “Corticosteroid therapy in drug-induced liver injury: pros and cons,” *J. Dig. Dis.*, pp. 1–16, 2018, doi: 10.1111/1751-2980.12697.

[80] O. Barbier, D. Duran-Sandoval, I. Pineda-Torra, V. Kosykh, J.-C. Fruchart, and B. Staels, “Peroxisome Proliferator-activated Receptor α Induces Hepatic Expression of the Human Bile Acid Glucuronidating UDP-glucuronosyltransferase 2B4 Enzyme *,” *J. Biol. Chem.*, vol. 278, no. 35, pp. 32852–32860, Aug. 2003, doi: 10.1074/JBC.M305361200.

[81] B. O, F. C, F. JC, and S. B, “Genomic and non-genomic interactions of PPARalpha with xenobiotic-metabolizing enzymes,” *Trends Endocrinol. Metab.*, vol. 15, no. 7, pp. 324–330, Sep. 2004, doi: 10.1016/J.TEM.2004.07.007.

[82] S. C. Sahu, “Hepatotoxicity : from genomics to in vitro and in vivo models,” p. 682, 2007.

[83] J. C. Kando, K. A. Yonkers, and J. O. Cole, “Gender as a Risk Factor for Adverse Events to Medications,” *Drugs 1995 501*, vol. 50, no. 1, pp. 1–6, Nov. 2012, doi: 10.2165/00003495-199550010-00001.

[84] A. LM and K. CD, “Coordinated regulation of hepatic phase I and II drug-metabolizing genes and transporters using AhR-, CAR-, PXR-, PPARα-, and Nrf2-null mice,” *Drug Metab. Dispos.*, vol. 40, no. 7, pp. 1366–1379, Jul. 2012, doi: 10.1124/DMD.112.045112.

[85] S. and J. P. H. David, “Drug-induced Liver Injury,” *US Gastroenterol. Hepatol. Rev.*, vol. 6, pp. 73–80, 2010, doi: 10.1016/j.neuroimage.2013.08.045.The.

[86] O. G *et al.*, “Results of a prospective study of acute liver failure at 17 tertiary care centers in the United States,” *Ann. Intern. Med.*, vol. 137, no. 12, pp. 947–954, Dec. 2002, doi: 10.7326/0003-4819-137-12-200212170-00007.

[87] R. A, K. DG, and L. WM, “Drug-induced acute liver failure: results of a U.S. multicenter, prospective study,” *Hepatology*, vol. 52, no. 6, pp. 2065–2076, Dec. 2010, doi: 10.1002/HEP.23937.

[88] L. D and P. GP, “Drug-induced acute liver failure,” *Eur. J. Gastroenterol. Hepatol.*, vol. 17, no. 2, pp. 141–143, Feb. 2005, doi: 10.1097/00042737-200502000-00002.

[89] F. RJ *et al.*, “Idiosyncratic drug-induced liver injury is associated with substantial morbidity and mortality within 6 months from onset,” *Gastroenterology*, vol. 147, no. 1, 2014, doi: 10.1053/J.GASTRO.2014.03.045.

[90] E. S. Björnsson, “Global Epidemiology of Drug-Induced Liver Injury (DILI),” *Curr. Hepatol. Reports 2019 183*, vol. 18, no. 3, pp. 274–279, Jul. 2019, doi: 10.1007/S11901-019-00475-Z.

[91] F. ME *et al.*, “Drug-Induced Liver Injury during Antidepressant Treatment: Results of AMSP, a Drug Surveillance Program,” *Int. J. Neuropsychopharmacol.*, vol. 19, no. 4, Apr. 2016, doi: 10.1093/IJNP/PYV126.

[92] L. S. (Lawrence S. Friedman and E. B. Keeffe, “Handbook of liver disease,” p. 481, 2004.

[93] L. Meunier and D. Larrey, “Drug-Induced Liver Injury: Biomarkers, Requirements, Candidates, and Validation,” *Front. Pharmacol.*, vol. 0, p. 1482, 2019, doi: 10.3389/FPHAR.2019.01482.

[94] A. Pandit, T. Sachdeva, and P. Bafna, “Drug-Induced Hepatotoxicity: A Review,” *J. Appl. Pharm. Sci.*, vol. 2012, no. 05, pp. 13–25, doi: 10.7324/JAPS.2012.2541.

[95] “Hepatotoxizität: Arzneimitteltoxische Hepatopathie | PZ – Pharmazeutische Zeitung.” https://www.pharmazeutische-zeitung.de/arzneimittel-als-wichtige-ausloeser-115626/seite/6/ (accessed Aug. 31, 2021).

[96] I. J. Onakpoya, C. J. Heneghan, and J. K. Aronson, “Post-marketing withdrawal of 462 medicinal products because of adverse drug reactions: a systematic review of the world literature,” *BMC Med. 2016 141*, vol. 14, no. 1, pp. 1–11, Feb. 2016, doi: 10.1186/S12916-016-0553-2.

[97] D. JA, G. HG, and H. RW, “Innovation in the pharmaceutical industry: New estimates of R&D costs,” *J. Health Econ.*, vol. 47, pp. 20–33, May 2016, doi: 10.1016/J.JHEALECO.2016.01.012.

[98] H. PH *et al.*, “Death and liver transplantation within 2 years of onset of drug-induced liver injury,” *Hepatology*, vol. 66, no. 4, pp. 1275–1285, Oct. 2017, doi: 10.1002/HEP.29283.

[99] R. J. Andrade *et al.*, “EASL Clinical Practice Guidelines: Drug-induced liver injury q,” 2019, doi: 10.1016/j.jhep.2019.02.014.

[100] S. Kammerer and J.-H. Küpper, “Human hepatocyte systems for in vitro toxicology analysis,” *J. Cell. Biotechnol.*, vol. 3, pp. 85–93, 2017, doi: 10.3233/JCB-179012.

[101] S. JR, “How can ‘Hy’s law’ help the clinician?,” *Pharmacoepidemiol. Drug Saf.*, vol. 15, no. 4, pp. 235–239, Apr. 2006, doi: 10.1002/PDS.1210.

[102] “Drug-induced liver injury - UpToDate.” https://www.uptodate.com/contents/drug-induced-liver-injury?search=drug-induced-liver- injury&source=search_result&selectedTitle=1~150&usage_type=default&display_rank=1 (accessed Sep. 06, 2021).

[103] B. H. Norman, “Drug Induced Liver Injury (DILI). Mechanisms and Medicinal Chemistry Avoidance/Mitigation Strategies,” *J. Med. Chem.*, vol. 63, no. 20, pp. 11397–11419, Oct. 2020, doi: 10.1021/ACS.JMEDCHEM.0C00524.

[104] B. W, K. S, D. K, and L. ER, “Drug-induced liver injury: review article,” *Dig. Dis. Sci.*, vol. 52, no. 10, pp. 2463–2471, Oct. 2007, doi: 10.1007/S10620-006-9472-Y.

[105] K.-U. GA *et al.*, “Drug-induced liver injury: recent advances in diagnosis and risk assessment,” *Gut*, vol. 66, no. 6, pp. 1154–1164, Jun. 2017, doi: 10.1136/GUTJNL-2016-313369.

[106] S. H. Hussaini and E. A. Farrington, “Idiosyncratic drug-induced liver injury: an overview,” *http://dx.doi.org/10.1517/14740338.6.6.673*, vol. 6, no. 6, pp. 673–684, Nov. 2007, doi: 10.1517/14740338.6.6.673.

[107] G. Aithal *et al.*, “Case Definition and Phenotype Standardization in Drug-Induced Liver Injury,” *Clin. Pharmacol. Ther.*, vol. 89, no. 6, pp. 806–815, Jun. 2011, doi: 10.1038/CLPT.2011.58.

[108] R. J. Fontana *et al.*, “Standardization of Nomenclature and Causality Assessment in Drug-Induced Liver Injury: Summary of a Clinical Research Workshop,” *Hepatology*, vol. 52, no. 2, p. 730, Aug. 2010, doi: 10.1002/HEP.23696.

[109] D. E. Kleiner *et al.*, “Hepatic histological findings in suspected drug-induced liver injury: Systematic evaluation and clinical associations,” *Hepatology*, vol. 59, no. 2, pp. 661–670, Feb. 2014, doi: 10.1002/HEP.26709.

[110] R. J. Lu *et al.*, “Clinical characteristics of drug-induced liver injury and related risk factors,” *Exp. Ther. Med.*, vol. 12, no. 4, pp. 2606–2616, Oct. 2016, doi: 10.3892/ETM.2016.3627.

[111] “A focus on epidemiology of drug-induced liver injury: Analysis of a prospective cohort | Request PDF.” https://www.researchgate.net/publication/318092374_A_focus_on_epidemiology_of_drug-induced_liver_injury_Analysis_of_a_prospective_cohort (accessed Sep. 01, 2021).

[112] G. Danan and R. Teschke, “Drug-Induced Liver Injury: Why is the Roussel Uclaf Causality Assessment Method (RUCAM) Still Used 25 Years After Its Launch?,” *Drug Saf. 2018 418*, vol. 41, no. 8, pp. 735–743, Mar. 2018, doi: 10.1007/S40264-018-0654-2.

[113] N. Chalasani *et al.*, “Causes, Clinical Features, and Outcomes From a Prospective Study of Drug-Induced Liver Injury in the United States,” *Gastroenterology*, vol. 135, no. 6, pp. 1924-1934.e4, Dec. 2008, doi: 10.1053/J.GASTRO.2008.09.011.

[114] R. J. Andrade *et al.*, “Drug-Induced Liver Injury: An Analysis of 461 Incidences Submitted to the Spanish Registry Over a 10-Year Period,” *Gastroenterology*, vol. 129, no. 2, pp. 512–521, Aug. 2005, doi: 10.1053/J.GASTRO.2005.05.006.

[115] D. R. F, C. M, and G. G, “An enzymic test for the diagnosis of viral hepatitis: the transaminase serum activities. 1957,” *Clin. Chim. Acta.*, vol. 369, no. 2, pp. 148–152, Jul. 2006, doi: 10.1016/J.CCA.2006.05.001.

[116] “Characterization of patients diagnosed with drug-induced liver injury,” doi: 10.17352/2455-2283.000095.

[117] B. E and O. R, “Outcome and prognostic markers in severe drug-induced liver disease,” *Hepatology*, vol. 42, no. 2, pp. 481–489, Aug. 2005, doi: 10.1002/HEP.20800.

[118] M. Robles-Diaz *et al.*, “Use of Hy’s Law and a New Composite Algorithm to Predict Acute Liver Failure in Patients With Drug-Induced Liver Injury on Behalf of the Spanish DILI Registry, the SLatinDILI Network, and the Safer and Faster Evidence-based Translation Consortium,” *YGAST*, vol. 147, pp. 109-118.e5, 2014, doi: 10.1053/j.gastro.2014.03.050.

[119] D. E. Kleiner, “Drug-Induced Liver Injury: The Hepatic Pathologist’s Approach,” *Gastroenterol. Clin. North Am.*, vol. 46, no. 2, p. 273, Jun. 2017, doi: 10.1016/J.GTC.2017.01.004.

[120] M. W. Russo, J. A. Galanko, R. Shrestha, M. W. Fried, and P. Watkins, “Liver transplantation for acute liver failure from drug induced liver injury in the United States,” *Liver Transplant.*, vol. 10, no. 8, pp. 1018–1023, Aug. 2004, doi: 10.1002/LT.20204.

[121] “Guidance for Industry Drug-Induced Liver Injury: Premarketing Clinical Evaluation Drug Safety Guidance for Industry

Drug-Induced Liver Injury: Premarketing Clinical Evaluation," 2009, Accessed: Sep. 09, 2021. [Online]. Available: http://www.fda.gov/Drugs/GuidanceComplianceRegulatoryInformation/Guidances/default.htmorTel:800-835-4709or301-827-1800http://www.fda.gov/BiologicsBloodVaccines/GuidanceComplianceRegulatoryInformation/Guidances/default.htm.

[122] S. Fu *et al.*, "Molecular biomarkers in drug-induced liver injury: Challenges and future perspectives," *Front. Pharmacol.*, vol. 10, 2020, doi: 10.3389/FPHAR.2019.01667.

[123] M. Garcia-Cortes, M. Robles-Diaz, C. Stephens, A. Ortega-Alonso, M. I. Lucena, and R. J. Andrade, "Drug induced liver injury: an update," *Arch. Toxicol. 2020 9410*, vol. 94, no. 10, pp. 3381–3407, Aug. 2020, doi: 10.1007/S00204-020-02885-1.

[124] B. ES, B. OM, B. HK, K. RB, and O. S, "Incidence, presentation, and outcomes in patients with drug-induced liver injury in the general population of Iceland," *Gastroenterology*, vol. 144, no. 7, 2013, doi: 10.1053/J.GASTRO.2013.02.006.

[125] M. Vega *et al.*, "The Incidence of Drug- and Herbal and Dietary Supplement-Induced Liver Injury: Preliminary Findings from Gastroenterologist-Based Surveillance in the Population of the State of Delaware," *Drug Saf. 2017 409*, vol. 40, no. 9, pp. 783–787, May 2017, doi: 10.1007/S40264-017-0547-9.

[126] S. C *et al.*, "Incidence of drug-induced hepatic injuries: a French population-based study," *Hepatology*, vol. 36, no. 2, pp. 451–455, 2002, doi: 10.1053/JHEP.2002.34857.

[127] de A. FJ, M. D, M. M, and G. R. LA, "Acute and clinically relevant drug-induced liver injury: a population based case-control study," *Br. J. Clin. Pharmacol.*, vol. 58, no. 1, pp. 71–80, Jul. 2004, doi: 10.1111/J.1365-2125.2004.02133.X.

[128] D. V. MB, A. K. V, A. N, O. R, and B. E, "Drug-induced liver injury in a Swedish University hospital out-patient hepatology clinic," *Aliment. Pharmacol. Ther.*, vol. 24, no. 8, pp. 1187–1195, Oct. 2006, doi: 10.1111/J.1365-2036.2006.03117.X.

[129] F. Bessone *et al.*, "Drug-induced liver injury: A management position paper from the Latin American Association for Study of the liver," *Ann. Hepatol.*, vol. 24, Sep. 2021, doi: 10.1016/J.AOHEP.2021.100321.

[130] M. Chen, A. Suzuki, J. Borlak, R. J. Andrade, and M. I. Lucena, "Drug-induced liver injury: Interactions between drug properties and host factors," *J. Hepatol.*, vol. 63, no. 2, pp. 503–514, Aug. 2015, doi: 10.1016/J.JHEP.2015.04.016.

[131] S. Dragovic *et al.*, "Evidence-based selection of training compounds for use in the mechanism-based integrated prediction of drug-induced liver injury in man," *Arch. Toxicol.*, vol. 90, no. 12, pp. 2979–3003, 2016, doi: 10.1007/s00204-016-1845-1.

[132] B. JG and V. NP, "Paracetamol (acetaminophen)-induced toxicity: molecular and biochemical mechanisms, analogues and protective approaches," *Crit. Rev. Toxicol.*, vol. 31, no. 1, pp. 55–138, 2001, doi: 10.1080/20014091111677.

[133] J. LP, M. PR, and H. JA, "Acetaminophen-induced hepatotoxicity," *Drug Metab. Dispos.*, vol. 31, no. 12, pp. 1499–1506, Dec. 2003, doi: 10.1124/DMD.31.12.1499.

[134] A. Ramachandran, R. G. J. Visschers, L. Duan, J. Y. Akakpo, and H. Jaeschke, "Mitochondrial dysfunction as a mechanism of drug-induced hepatotoxicity: current understanding and future perspectives," *J. Clin. Transl. Res.*, vol. 4, no. 1, p. 75, 2018, doi: 10.18053/JCTRES.04.201801.005.

[135] S. Dragovic *et al.*, "Evidence-based selection of training compounds for use in the mechanism-based integrated prediction of drug-induced liver injury in man," *Arch. Toxicol.*, vol. 90, no. 12, p. 2979, Dec. 2016, doi: 10.1007/S00204-016-1845-1.

[136] R. J. Sokol *et al.*, "Role of Oxidant Stress in the Permeability Transition Induced in Rat Hepatic Mitochondria by Hydrophobic Bile Acids," *Pediatr. Res. 2001 494*, vol. 49, no. 4, pp. 519–531, 2001, doi: 10.1203/00006450-200104000-00014.

[137] P. T, R. LR, J. BA, and G. GJ, "Dysregulation of apoptosis as a mechanism of liver disease: an overview," *Semin. Liver Dis.*, vol. 18, no. 2, pp. 105–114, 1998, doi: 10.1055/S-2007-1007147.

[138] C. M. P. Rodrigues, G. Fan, P. Y. Wong, B. T. Kren, and C. J. Steer, "Ursodeoxycholic Acid May Inhibit Deoxycholic Acid-Induced Apoptosis by Modulating Mitochondrial Transmembrane Potential and Reactive Oxygen Species Production," *Mol. Med. 1998 43*, vol. 4, no. 3, pp. 165–178, Mar. 1998, doi: 10.1007/BF03401914.

[139] L. Ellgaard and A. Helenius, "Quality control in the endoplasmic reticulum," *Nat. Rev. Mol. Cell Biol. 2003 43*, vol. 4, no. 3, pp. 181–191, Mar. 2003, doi: 10.1038/nrm1052.

[140] X. C, B.-M. B, and R. JC, "Endoplasmic reticulum stress: cell life and death decisions," *J. Clin. Invest.*, vol. 115, no. 10, pp. 2656–2664, Oct. 2005, doi: 10.1172/JCI26373.

[141] S. Chen, W. B. Melchior, Jr., and L. Guo, "Endoplasmic Reticulum Stress in Drug- and Environmental Toxicant-Induced Liver Toxicity," *J. Environ. Sci. Health. C. Environ. Carcinog. Ecotoxicol. Rev.*, vol. 32, no. 1, p. 83, Jan. 2014, doi: 10.1080/10590501.2014.881648.

[142] M. Villanueva-Paz *et al.*, “Oxidative Stress in Drug-Induced Liver Injury (DILI): From Mechanisms to Biomarkers for Use in Clinical Practice,” *Antioxidants*, vol. 10, no. 3, pp. 1–35, Mar. 2021, doi: 10.3390/ANTIOX10030390.

[143] N. G *et al.*, “BGP-15 inhibits caspase-independent programmed cell death in acetaminophen-induced liver injury,” *Toxicol. Appl. Pharmacol.*, vol. 243, no. 1, pp. 96–103, Feb. 2010, doi: 10.1016/J.TAAP.2009.11.017.

[144] S. R. Bonam, F. Wang, and S. Muller, “Lysosomes as a therapeutic target,” *Nat. Rev. Drug Discov. 2019 1812*, vol. 18, no. 12, pp. 923–948, Sep. 2019, doi: 10.1038/s41573-019-0036-1.

[145] Z. Zhang, P. Yue, T. Lu, Y. Wang, Y. Wei, and X. Wei, “Role of lysosomes in physiological activities, diseases, and therapy,” *J. Hematol. Oncol. 2021 141*, vol. 14, no. 1, pp. 1–39, May 2021, doi: 10.1186/S13045-021-01087-1.

[146] R. J. Weaver *et al.*, “Managing the challenge of drug-induced liver injury: a roadmap for the development and deployment of preclinical predictive models,” *Nat. Rev. Drug Discov. 2019 192*, vol. 19, no. 2, pp. 131–148, Nov. 2019, doi: 10.1038/s41573-019-0048-x.

[147] A. JM, V. P, and K. PK, “Screening for the drug-phospholipid interaction: correlation to phospholipidosis,” *ChemMedChem*, vol. 4, no. 8, pp. 1224–1251, Aug. 2009, doi: 10.1002/CMDC.200900052.

[148] W. H. Halliwell, “Cationic Amphiphilic Drug-Induced Phospholipidosis:,” *http://dx.doi.org/10.1177/019262339702500111*, vol. 25, no. 1, pp. 53–60, Jul. 2016, doi: 10.1177/019262339702500111.

[149] C. Möbs, C. Slotosch, H. Löffler, W. Pfützner, and M. Hertl, “Cellular and Humoral Mechanisms of Immune Tolerance in Immediate-Type Allergy Induced by Specific Immunotherapy,” *Int. Arch. Allergy Immunol.*, vol. 147, no. 3, pp. 171–178, Oct. 2008, doi: 10.1159/000142039.

[150] J. C. Waddington, X. Meng, D. J. Naisbitt, and B. K. Park, “Immune drug-induced liver disease and drugs,” *Curr. Opin. Toxicol.*, vol. 10, pp. 46–53, Aug. 2018, doi: 10.1016/J.COTOX.2017.12.006.

[151] C. Ju and T. Reilly, “Role of immune reactions in drug-induced liver injury (DILI),” *http://dx.doi.org/10.3109/03602532.2011.645579*, vol. 44, no. 1, pp. 107–115, Feb. 2012, doi: 10.3109/03602532.2011.645579.

[152] P. BK, P. M, and K. NR, “Role of drug disposition in drug hypersensitivity: a chemical, molecular, and clinical perspective,” *Chem. Res. Toxicol.*, vol. 11, no. 9, pp. 969–988, 1998, doi: 10.1021/TX980058F.

[153] P. WJ, “Direct T-cell stimulations by drugs--bypassing the innate immune system.,” *Toxicology*, vol. 209, no. 2, pp. 95–100, Apr. 2005, doi: 10.1016/J.TOX.2004.12.014.

[154] S. B *et al.*, “Recognition of sulfamethoxazole and its reactive metabolites by drug-specific CD4+ T cells from allergic individuals,” *J. Immunol.*, vol. 164, no. 12, pp. 6647–6654, Jun. 2000, doi: 10.4049/JIMMUNOL.164.12.6647.

[155] K. N, “Drug-induced liver injury,” *Clin. Infect. Dis.*, vol. 38 Suppl 2, no. SUPPL. 2, Mar. 2004, doi: 10.1086/381446.

[156] M. Chen, A. Suzuki, J. Borlak, R. J. Andrade, and I. Lucena, “Drug-induced liver injury: Interactions between drug properties and host factors,” 2015, doi: 10.1016/j.jhep.2015.04.016.

[157] D. J. Waxman and M. G. Holloway, “Sex Differences in the Expression of Hepatic Drug Metabolizing Enzymes,” *Mol. Pharmacol.*, vol. 76, no. 2, pp. 215–228, Aug. 2009, doi: 10.1124/MOL.109.056705.

[158] C. M. Hunt, W. R. Westerkam, and G. M. Stave, “Effect of age and gender on the activity of human hepatic CYP3A,” *Biochem. Pharmacol.*, vol. 44, no. 2, pp. 275–283, Jul. 1992, doi: 10.1016/0006-2952(92)90010-G.

[159] R. J. Andrade, M. Robles, E. Ulzurrun, and M. I. Lucena, “Drug-induced liver injury: insights from genetic studies,” *http://dx.doi.org/10.2217/pgs.09.111*, vol. 10, no. 9, pp. 1467–1487, Sep. 2009, doi: 10.2217/PGS.09.111.

[160] G. NASSERI, T. ZAHEDI, F. MOUSAVI-KAZEROONI, and M. SAADAT, “Prevalence of Null Genotypes of Glutathione S-Transferase T1 (GSTT1) and M1 (GSTM1) in Seven Iranian Populations,” *Iran. J. Public Health*, vol. 44, no. 12, p. 1655, Dec. 2015, Accessed: Oct. 21, 2021. [Online]. Available: /pmc/articles/PMC4724738/.

[161] Z. G, T. A, L. C, F. P, and T. M, “Alterations of canalicular ATP-binding cassette transporter expression in drug-induced liver injury,” *Digestion*, vol. 90, no. 2, pp. 81–88, Nov. 2014, doi: 10.1159/000365003.

[162] C. M *et al.*, “Toward predictive models for drug-induced liver injury in humans: are we there yet?,” *Biomark. Med.*, vol. 8, no. 2, pp. 201–213, Feb. 2014, doi: 10.2217/BMM.13.146.

[163] P. T. Giboney, “Mildly Elevated Liver Transaminase Levels in the Asymptomatic Patient,” *Am. Fam. Physician*, vol. 71, no. 6, pp. 1105–1110, Mar. 2005, Accessed: Oct. 22, 2021. [Online]. Available: www.aafp.org/afp.

[164] G. RM and F. S, “AGA technical review on the evaluation of liver chemistry tests,” *Gastroenterology*, vol. 123, no. 4, pp. 1367–1384, 2002, doi: 10.1053/GAST.2002.36061.

[165] G. EG, T. R, and S. V, “Liver enzyme alteration: a guide for clinicians,” *CMAJ*, vol. 172, no. 3, pp. 367–379, Feb. 2005, doi: 10.1503/CMAJ.1040752.

[166] M. Robles-Díaz, I. Medina-Caliz, C. Stephens, R. J. Andrade, and M. I. Lucena, “Biomarkers in DILI: One more step

forward," *Front. Pharmacol.*, vol. 7, no. AUG, pp. 1–7, 2016, doi: 10.3389/fphar.2016.00267.

[167] Y. X *et al.*, "Population-based genome-wide association studies reveal six loci influencing plasma levels of liver enzymes," *Am. J. Hum. Genet.*, vol. 83, no. 4, pp. 520–528, Oct. 2008, doi: 10.1016/J.AJHG.2008.09.012.

[168] A. Vall, Y. Sabnis, J. Shi, R. Class, S. Hochreiter, and G. Klambauer, "The Promise of AI for DILI Prediction," *Front. Artif. Intell.*, vol. 0, p. 15, Apr. 2021, doi: 10.3389/FRAI.2021.638410.

[169] K. R. Przybylak and M. T. Cronin, "In silico models for drug-induced liver injury – current status," *http://dx.doi.org/10.1517/17425255.2012.648613*, vol. 8, no. 2, pp. 201–217, Feb. 2012, doi: 10.1517/17425255.2012.648613.

[170] R. A. Thompson *et al.*, "In Vitro Approach to Assess the Potential for Risk of Idiosyncratic Adverse Reactions Caused by Candidate Drugs," *Chem. Res. Toxicol.*, vol. 25, no. 8, pp. 1616–1632, Aug. 2012, doi: 10.1021/TX300091X.

[171] D. P. Williams, S. E. Lazic, A. J. Foster, E. Semenova, and P. Morgan, "Predicting Drug-Induced Liver Injury with Bayesian Machine Learning," *Chem. Res. Toxicol.*, vol. 33, no. 1, pp. 239–248, Jan. 2019, doi: 10.1021/ACS.CHEMRESTOX.9B00264.

[172] A. DJ *et al.*, "Mechanistic biomarkers provide early and sensitive detection of acetaminophen-induced acute liver injury at first presentation to hospital," *Hepatology*, vol. 58, no. 2, pp. 777–787, Aug. 2013, doi: 10.1002/HEP.26294.

[173] "Alpha-GST Release as a Predictive Marker of Drug Induced Hepatotoxicity in 3D Liver Models Introduction and Background."

[174] G. PS, P. CR, P. MA, W. A, and Y. MJ, "Alpha-glutathione S-transferase in the assessment of hepatotoxicity--its diagnostic utility in comparison with other recognized markers in the Wistar Han rat," *Toxicol. Pathol.*, vol. 30, no. 3, pp. 365–372, 2002, doi: 10.1080/01926230252929945.

[175] R. P. Horgan and L. C. Kenny, "'Omic' technologies: genomics, transcriptomics, proteomics and metabolomics," *Obstet. Gynaecol.*, vol. 13, no. 3, pp. 189–195, Jul. 2011, doi: 10.1576/TOAG.13.3.189.27672.

[176] B. EA, Y. Y, and W. JF, "Use of toxicogenomics to understand mechanisms of drug-induced hepatotoxicity during drug discovery and development," *Toxicol. Lett.*, vol. 186, no. 1, pp. 22–31, Apr. 2009, doi: 10.1016/J.TOXLET.2008.09.017.

[177] T. Kagawa, Y. Shirai, S. Oda, and T. Yokoi, "Identification of Specific MicroRNA Biomarkers in Early Stages of Hepatocellular Injury, Cholestasis, and Steatosis in Rats," *Toxicol. Sci.*, vol. 166, no. 1, pp. 228–239, Nov. 2018, doi: 10.1093/TOXSCI/KFY200.

[178] S. L. PJ *et al.*, "Circulating microRNAs as potential markers of human drug-induced liver injury," *Hepatology*, vol. 54, no. 5, pp. 1767–1776, Nov. 2011, doi: 10.1002/HEP.24538.

[179] T. P *et al.*, "Keratin-18 and microRNA-122 complement alanine aminotransferase as novel safety biomarkers for drug-induced liver injury in two human cohorts," *Liver Int.*, vol. 34, no. 3, pp. 367–378, Mar. 2014, doi: 10.1111/LIV.12322.

[180] R. J. Church *et al.*, "Candidate biomarkers for the diagnosis and prognosis of drug-induced liver injury: An international collaborative effort," *Hepatology*, vol. 00, no. 00, pp. 1–14, 2018, doi: 10.1002/hep.29802.

[181] I. Maina, J. A. Rule, F. H. Wians, M. Poirier, L. Grant, and W. M. Lee, " α-Glutathione S -Transferase: A New Biomarker for Liver Injury? ," *J. Appl. Lab. Med. An AACC Publ.*, vol. 1, no. 2, pp. 119–128, Sep. 2016, doi: 10.1373/JALM.2016.020412.

[182] G. Ozturk, N. Ozturk, H. Aksoy, M. N. Akcay, S. S. Atamanalp, and H. Acemoglu, "Hepatocellular damage following burn injury demonstrated by a more sensitive marker: Alpha-glutathione s-transferase," *J. Burn Care Res.*, vol. 30, no. 4, pp. 711–716, Jul. 2009, doi: 10.1097/BCR.0B013E3181ABFD65.

[183] S. R. Khetani *et al.*, "Use of Micropatterned Cocultures to Detect Compounds That Cause Drug-Induced Liver Injury in Humans," *Toxicol. Sci.*, vol. 132, no. 1, pp. 107–117, Mar. 2013, doi: 10.1093/TOXSCI/KFS326.

[184] W. J. Bailey *et al.*, "A Performance Evaluation of Three Drug-Induced Liver Injury Biomarkers in the Rat: Alpha-Glutathione S-Transferase, Arginase 1, and 4-Hydroxyphenyl-Pyruvate Dioxygenase," *Toxicol. Sci.*, vol. 130, no. 2, pp. 229–244, Dec. 2012, doi: 10.1093/TOXSCI/KFS243.

[185] S. C *et al.*, "JNK Signaling Pathway Mediates Acetaminophen-Induced Hepatotoxicity Accompanied by Changes of Glutathione S-Transferase A1 Content and Expression.," *Front. Pharmacol.*, vol. 10, no. SEP, pp. 1092–1092, Sep. 2019, doi: 10.3389/FPHAR.2019.01092.

[186] A. J. Foster *et al.*, "Integrated in vitro models for hepatic safety and metabolism: evaluation of a human Liver-Chip and liver spheroid," *Arch. Toxicol. 2019 934*, vol. 93, no. 4, pp. 1021–1037, Mar. 2019, doi: 10.1007/S00204-019-02427-4.

[187] M. R. Mcgill and H. Jaeschke, "Biomarkers of drug-induced liver injury: progress and utility in research, medicine, and regulation HHS Public Access," *Expert Rev Mol Diagn*, vol. 18, no. 9, pp. 797–807, 2018, doi: 10.1080/14737159.2018.1508998.

[188] Q. Guo *et al.*, “Biomarkers associated with binaprofen-induced liver injury,” *Mol. Med. Rep.*, vol. 18, no. 6, pp. 5076–5086, Dec. 2018, doi: 10.3892/MMR.2018.9549.

[189] F. Knöspel *et al.*, “In Vitro Model for Hepatotoxicity Studies Based on Primary Human Hepatocyte Cultivation in a Perfused 3D Bioreactor System,” *Int. J. Mol. Sci.*, vol. 17, no. 4, Apr. 2016, doi: 10.3390/IJMS17040584.

[190] D. S, S. S, P. N, B. J, and K. JG, “In vitro inhibition of the bile salt export pump correlates with risk of cholestatic drug-induced liver injury in humans,” *Drug Metab. Dispos.*, vol. 40, no. 1, pp. 130–138, Jan. 2012, doi: 10.1124/DMD.111.040758.

[191] M. RE *et al.*, “Interference with bile salt export pump function is a susceptibility factor for human liver injury in drug development,” *Toxicol. Sci.*, vol. 118, no. 2, pp. 485–500, Dec. 2010, doi: 10.1093/TOXSCI/KFQ269.

[192] A. Buness *et al.*, “Identification of Metabolites, Clinical Chemistry Markers and Transcripts Associated with Hepatotoxicity,” *PLoS One*, vol. 9, no. 5, p. e97249, May 2014, doi: 10.1371/JOURNAL.PONE.0097249.

[193] S. HS, W. A, P. F, C. SD, M. M, and K.-U. GA, “Bile acids in drug induced liver injury: Key players and surrogate markers,” *Clin. Res. Hepatol. Gastroenterol.*, vol. 40, no. 3, pp. 257–266, Jun. 2016, doi: 10.1016/J.CLINRE.2015.12.017.

[194] M. M *et al.*, “Elevated levels of circulating CDH5 and FABP1 in association with human drug-induced liver injury,” *Liver Int.*, vol. 37, no. 1, pp. 132–140, Jan. 2017, doi: 10.1111/LIV.13174.

[195] Fda and Cder, “Letter of Support for Drug-Induced Liver Injuty (DILI) Biomarker(s), July 25, 2016,” 2016, Accessed: Oct. 26, 2021. [Online]. Available: http://www.imi-safe-t.eud.

[196] “Liver Fatty Acid Binding Protein (FABP1) as a Biomarker - Diapharma.” https://diapharma.com/liver-fatty-acid-binding-protein-fabp1-lfabp/ (accessed Oct. 26, 2021).

[197] A. N *et al.*, “Circulating Soluble Fas and Fas Ligand Levels Are Elevated in Children with Nonalcoholic Steatohepatitis,” *Dig. Dis. Sci.*, vol. 60, no. 8, pp. 2353–2359, Aug. 2015, doi: 10.1007/S10620-015-3614-Z.

[198] A. Eguchi, A. Wree, and A. E. Feldstein, “Biomarkers of liver cell death,” *J. Hepatol.*, vol. 60, no. 5, pp. 1063–1074, May 2014, doi: 10.1016/J.JHEP.2013.12.026.

[199] R. Teschke, A. Eickhoff, A. C. Brown, M. G. Neuman, and J. Schulze, “Diagnostic biomarkers in liver injury by drugs, herbs, and alcohol: Tricky dilemma after ema correctly and officially retracted letter of support,” *Int. J. Mol. Sci.*, vol. 21, no. 1, Jan. 2020, doi: 10.3390/IJMS21010212.

[200] S. S *et al.*, “Assessment of emerging biomarkers of liver injury in human subjects,” *Toxicol. Sci.*, vol. 132, no. 2, pp. 276–283, Apr. 2013, doi: 10.1093/TOXSCI/KFT009.

[201] A. H. Harrill *et al.*, “The effects of heparins on the liver: Application of mechanistic serum biomarkers in a randomized study in healthy volunteers,” *Clin. Pharmacol. Ther.*, vol. 92, no. 2, pp. 214–220, Aug. 2012, doi: 10.1038/CLPT.2012.40.

[202] D. S. Umbaugh and H. Jaeschke, “Biomarkers of drug-induced liver injury: a mechanistic perspective through acetaminophen hepatotoxicity,” *https://doi.org/10.1080/17474124.2021.1857238*, vol. 15, no. 4, pp. 363–375, 2020, doi: 10.1080/17474124.2021.1857238.

[203] M. M, R. R, C. Y, and S. MP, “High levels of circulating HMGB1 as a biomarker of acute liver failure in patients with viral hepatitis E,” *Liver Int.*, vol. 33, no. 9, pp. 1341–1348, Oct. 2013, doi: 10.1111/LIV.12197.

[204] A. DJ *et al.*, “RETRACTED: Molecular forms of HMGB1 and keratin-18 as mechanistic biomarkers for mode of cell death and prognosis during clinical acetaminophen hepatotoxicity,” *J. Hepatol.*, vol. 56, no. 5, pp. 1070–1079, 2012, doi: 10.1016/J.JHEP.2011.12.019.

[205] B. LN *et al.*, “Serum proteomic profiling in patients with drug-induced liver injury,” *Aliment. Pharmacol. Ther.*, vol. 35, no. 5, pp. 600–612, Mar. 2012, doi: 10.1111/J.1365-2036.2011.04982.X.

[206] D. Dragoi, A. Benesic, G. Pichler, N. A. Kulak, H. S. Bartsch, and A. L. Gerbes, “Proteomics Analysis of Monocyte-Derived Hepatocyte-Like Cells Identifies Integrin Beta 3 as a Specific Biomarker for Drug-Induced Liver Injury by Diclofenac,” *Front. Pharmacol.*, vol. 9, no. JUL, Jul. 2018, doi: 10.3389/FPHAR.2018.00699.

[207] “Monocyte-Derived Hepatocyte-Like Cells in Combination with Proteomics Identify a Potential Biomarker for Drug-Induced Liver Injury by Diclofenac - European Medical Journal.” https://www.emjreviews.com/hepatology/abstract/drug-induced-liver-injury/ (accessed Sep. 09, 2021).

[208] T. R, “Idiosyncratic DILI: Analysis of 46,266 Cases Assessed for Causality by RUCAM and Published From 2014 to Early 2019,” *Front. Pharmacol.*, vol. 10, Jul. 2019, doi: 10.3389/FPHAR.2019.00730.

[209] “Biomarkers ccK18 and K18 in hepatotoxicity Detection and quantification of liver damage with M30 and M65 Peviva Products M30/M65 are for Research Use in the US and Canada,” Accessed: Oct. 26, 2021. [Online]. Available: www.diapharma.com.

[210] Y. Sato *et al.*, “Serum LECT2 level as a prognostic indicator in acute liver failure,” *Transplant. Proc.*, vol. 36, no. 8, pp.

2359–2361, Oct. 2004, doi: 10.1016/J.TRANSPROCEED.2004.07.007.

[211] K. Wang *et al.*, “Circulating microRNAs, potential biomarkers for drug-induced liver injury,” *Proc. Natl. Acad. Sci. U. S. A.*, vol. 106, no. 11, p. 4402, Mar. 2009, doi: 10.1073/PNAS.0813371106.

[212] E. Arriazu *et al.*, “Signalling via the osteopontin and high mobility group box-1 axis drives the fibrogenic response to liver injury,” *Gut*, vol. 66, no. 6, pp. 1123–1137, Jun. 2017, doi: 10.1136/GUTJNL-2015-310752.

[213] S. K. Ramaiah and S. Rittling, “Pathophysiological Role of Osteopontin in Hepatic Inflammation, Toxicity, and Cancer,” *Toxicol. Sci.*, vol. 103, no. 1, pp. 4–13, May 2008, doi: 10.1093/TOXSCI/KFM246.

[214] J. Marsillach *et al.*, “Paraoxonase-1 is related to inflammation, fibrosis and PPAR delta in experimental liver disease,” *BMC Gastroenterol.*, vol. 9, p. 3, Jan. 2009, doi: 10.1186/1471-230X-9-3.

[215] A. DE, “The discovery and development of proteomic safety biomarkers for the detection of drug-induced liver toxicity,” *Toxicol. Appl. Pharmacol.*, vol. 245, no. 1, pp. 134–142, May 2010, doi: 10.1016/J.TAAP.2010.02.011.

[216] H. Gaskell, X. Ge, and N. Nieto, “High-Mobility Group Box-1 and Liver Disease,” *Hepatol. Commun.*, vol. 2, no. 9, p. 1005, Sep. 2018, doi: 10.1002/HEP4.1223.

[217] J. MA *et al.*, “Interrogation of transcriptomic changes associated with drug-induced hepatic sinusoidal dilatation in colorectal cancer,” *PLoS One*, vol. 13, no. 6, Jun. 2018, doi: 10.1371/JOURNAL.PONE.0198099.

[218] S. Parasuraman, “Toxicological screening,” *J. Pharmacol. Pharmacother.*, vol. 2, no. 2, p. 74, Apr. 2011, doi: 10.4103/0976-500X.81895.

[219] “Drug toxicity testing - Hera BioLabs.” https://www.herabiolabs.com/content/drug-toxicity-testing/ (accessed Sep. 27, 2021).

[220] M. M and W. PB, “Drug-induced liver injury: Advances in mechanistic understanding that will inform risk management,” *Clin. Pharmacol. Ther.*, vol. 101, no. 4, pp. 469–480, Apr. 2017, doi: 10.1002/CPT.564.

[221] B. F, “Preventing Drug-Induced Liver Injury: How Useful Are Animal Models?,” *Dig. Dis.*, vol. 33, no. 4, pp. 477–485, Jul. 2015, doi: 10.1159/000374093.

[222] B. L *et al.*, “Selection and interpretation of clinical pathology indicators of hepatic injury in preclinical studies,” *Vet. Clin. Pathol.*, vol. 34, no. 3, pp. 182–188, 2005, doi: 10.1111/J.1939-165X.2005.TB00041.X.

[223] P. Baldrick, “Safety evaluation to support first-in-man investigations II: Toxicology studies,” *Regul. Toxicol. Pharmacol.*, vol. 51, no. 2, pp. 237–243, Jul. 2008, doi: 10.1016/J.YRTPH.2008.04.006.

[224] M. Martignoni, G. M. M. Groothuis, and R. de Kanter, “Species differences between mouse, rat, dog, monkey and human CYP-mediated drug metabolism, inhibition and induction,” *https://doi.org/10.1517/17425255.2.6.875*, vol. 2, no. 6, pp. 875–894, Dec. 2006, doi: 10.1517/17425255.2.6.875.

[225] “Drug Development | ari.info | ari.info.” https://www.animalresearch.info/en/drug-development/ (accessed Sep. 27, 2021).

[226] P. Godoy *et al.*, *Recent advances in 2D and 3D in vitro systems using primary hepatocytes, alternative hepatocyte sources and non-parenchymal liver cells and their use in investigating mechanisms of hepatotoxicity, cell signaling and ADME*, vol. 87, no. 8. 2013.

[227] L. Kuna *et al.*, “Models of Drug Induced Liver Injury (DILI) – Current Issues and Future Perspectives,” *Curr. Drug Metab.*, vol. 19, no. 10, p. 830, May 2018, doi: 10.2174/1389200219666180523095355.

[228] D. Krewski *et al.*, “TOXICITY TESTING IN THE 21ST CENTURY: A VISION AND A STRATEGY,” *J. Toxicol. Environ. Health. B. Crit. Rev.*, vol. 13, no. 0, p. 51, Feb. 2010, doi: 10.1080/10937404.2010.483176.

[229] V. Y. Soldatow, E. L. Lecluyse, L. G. Griffith, and I. Rusyn, “In vitro models for liver toxicity testing,” doi: 10.1039/C2TX20051A.

[230] M. T. Donato, L. Tolosa, and M. J. Gómez-Lechón, “Culture and Functional Characterization of Human Hepatoma HepG2 Cells,” *Protoc. Vitr. Hepatocyte Res.*, vol. 1250, pp. 77–93, Jan. 2015, doi: 10.1007/978-1-4939-2074-7_5.

[231] M.-D. D, E. S, D. LH, R. M, H. HJ, and S. C, “Ornithine transcarbamylase and arginase I deficiency are responsible for diminished urea cycle function in the human hepatoblastoma cell line HepG2,” *Int. J. Biochem. Cell Biol.*, vol. 39, no. 3, pp. 555–564, 2007, doi: 10.1016/J.BIOCEL.2006.10.007.

[232] G. P *et al.*, “Infection of a human hepatoma cell line by hepatitis B virus,” *Proc. Natl. Acad. Sci. U. S. A.*, vol. 99, no. 24, pp. 15655–15660, Nov. 2002, doi: 10.1073/PNAS.232137699.

[233] A. C *et al.*, “Expression of cytochromes P450, conjugating enzymes and nuclear receptors in human hepatoma HepaRG cells,” *Drug Metab. Dispos.*, vol. 34, no. 1, pp. 75–83, Jan. 2006, doi: 10.1124/DMD.105.006759.

[234] M. Turpeinen, A. Tolonen, C. Chesne, A. Guillouzo, J. Uusitalo, and O. Pelkonen, “Functional expression, inhibition and induction of CYP enzymes in HepaRG cells,” *Toxicol. Vitr.*, vol. 23, no. 4, pp. 748–753, Jun. 2009, doi: 10.1016/J.TIV.2009.03.008.

[235] G. A, C. A, A. C, G. D, M. F, and G.-G. C, “The human hepatoma HepaRG cells: a highly differentiated model for studies of liver metabolism and toxicity of xenobiotics,” *Chem. Biol. Interact.*, vol. 168, no. 1, pp. 66–73, May 2007, doi: 10.1016/J.CBI.2006.12.003.

[236] “HepaRG - Hepatotoxicity screening and mechanistic testing applications.” https://www.heparg.com/rubrique-hepatotoxicity-screening-and-mechanistic-testing-applications (accessed Oct. 28, 2021).

[237] A. A, G. S, C. MG, and B. A, “Morphological and Functional Analysis of Hepatocyte Spheroids Generated on Poly-HEMA-Treated Surfaces under the Influence of Fetal Calf Serum and Nonparenchymal Cells,” *Biomolecules*, vol. 3, no. 1, pp. 242–269, 2013, doi: 10.3390/BIOM3010242.

[238] “HepaRG - The most innovative and useful hepatic cell line.” https://heparg.com/ (accessed Oct. 04, 2021).

[239] “HepG2 liver hepatocellular carcinoma cells transfection.” https://www.hepg2.com/ (accessed Oct. 04, 2021).

[240] B. Berger *et al.*, “Comparison of Liver Cell Models Using the Basel Phenotyping Cocktail,” *Front. Pharmacol.*, vol. 7, no. NOV, p. 443, Nov. 2016, doi: 10.3389/FPHAR.2016.00443.

[241] S. P. Harrison, S. F. Baumgarten, R. Verma, O. Lunov, A. Dejneka, and G. J. Sullivan, “Liver Organoids: Recent Developments, Limitations and Potential,” *Front. Med.*, vol. 0, p. 534, May 2021, doi: 10.3389/FMED.2021.574047.

[242] Nicole J. Hewitt, “HepaRG™ cells and their application to diverse endpoints.,” *HepaRG Cells Appl. Note - Merck* , 2012, Accessed: Oct. 04, 2021. [Online]. Available: milliporehttp://www.merckmillipore.com.

[243] L. Tolosa *et al.*, “Human Upcyte Hepatocytes: Characterization of the Hepatic Phenotype and Evaluation for Acute and Long-Term Hepatotoxicity Routine Testing,” *Toxicol. Sci.*, vol. 152, no. 1, pp. 214–229, Jul. 2016, doi: 10.1093/TOXSCI/KFW078.

[244] S. D. Ramachandran *et al.*, “Applicability of second-generation upcyte® human hepatocytes for use in CYP inhibition and induction studies,” *Pharmacol. Res. Perspect.*, vol. 3, no. 5, Oct. 2015, doi: 10.1002/PRP2.161.

[245] R. L. Sison-Young *et al.*, “A multicenter assessment of single-cell models aligned to standard measures of cell health for prediction of acute hepatotoxicity,” *Arch. Toxicol. 2016 913*, vol. 91, no. 3, pp. 1385–1400, Jun. 2016, doi: 10.1007/S00204-016-1745-4.

[246] N. Nagy, A. M. Guerrero, N. Runge, T. Evenburg, T. Johannssen, and A. Noerenberg, “Generation of proliferating human liver sinusoidal endothelial cells (upcyte® LSECs),” Accessed: Oct. 28, 2021. [Online]. Available: www.upcyte.com.

[247] S. D. Ramachandran *et al.*, “In Vitro Generation of Functional Liver Organoid-Like Structures Using Adult Human Cells,” *PLoS One*, vol. 10, no. 10, Oct. 2015, doi: 10.1371/JOURNAL.PONE.0139345.

[248] R. DA and D. GQ, “The promise of induced pluripotent stem cells in research and therapy,” *Nature*, vol. 481, no. 7381, pp. 295–305, Jan. 2012, doi: 10.1038/NATURE10761.

[249] I. H, N. N, K. H, and Y. S, “iPS cells: a game changer for future medicine,” *EMBO J.*, vol. 33, no. 5, pp. 409–417, Mar. 2014, doi: 10.1002/EMBJ.201387098.

[250] G.-C. S, F. N, C. A, G. C, C. B, and S.-T. K, “Human induced pluripotent stem cells in hepatology: beyond the proof of concept,” *Am. J. Pathol.*, vol. 184, no. 2, pp. 332–347, Feb. 2014, doi: 10.1016/J.AJPATH.2013.09.026.

[251] D. R. Berger, B. R. Ware, M. D. Davidson, S. R. Allsup, and S. R. Khetani, “Enhancing the functional maturity of induced pluripotent stem cell-derived human hepatocytes by controlled presentation of cell-cell interactions in vitro,” *Hepatology*, vol. 61, no. 4, pp. 1370–1381, Apr. 2015, doi: 10.1002/HEP.27621.

[252] S.-T. K *et al.*, “Highly efficient generation of human hepatocyte-like cells from induced pluripotent stem cells,” *Hepatology*, vol. 51, no. 1, pp. 297–305, 2010, doi: 10.1002/HEP.23354.

[253] T. T *et al.*, “Generation of functional hepatocytes from human embryonic stem cells under chemically defined conditions that recapitulate liver development,” *Hepatology*, vol. 51, no. 5, pp. 1754–1765, May 2010, doi: 10.1002/HEP.23506.

[254] V. M. Lauschke, R. Z. Shafagh, D. F. G. Hendriks, and M. Ingelman-Sundberg, “3D Primary Hepatocyte Culture Systems for Analyses of Liver Diseases, Drug Metabolism, and Toxicity: Emerging Culture Paradigms and Applications,” *Biotechnol. J.*, vol. 14, no. 7, p. 1800347, Jul. 2019, doi: 10.1002/BIOT.201800347.

[255] V. M. Lauschke *et al.*, “Massive rearrangements of cellular MicroRNA signatures are key drivers of hepatocyte dedifferentiation,” *Hepatology*, vol. 64, no. 5, pp. 1743–1756, Nov. 2016, doi: 10.1002/HEP.28780.

[256] C. C. Bell *et al.*, “Transcriptional, functional, and mechanistic comparisons of stem cell-derived hepatocytes, HepaRG cells, and three-dimensional human hepatocyte spheroids as predictive in vitro systems for drug-induced liver injury,” *Drug Metab. Dispos.*, vol. 45, no. 4, pp. 419–429, Apr. 2017, doi: 10.1124/DMD.116.074369.

[257] G. H. Underhill and S. R. Khetani, “REVIEW Bioengineered Liver Models for Drug Testing and Cell Differentiation Studies,” 2018, doi: 10.1016/j.jcmgh.2017.11.012.

[258] K. Zeilinger, N. Freyer, G. Damm, D. Seehofer, and F. Knöspel, “Cell sources for in vitro human liver cell culture models,”

Exp. Biol. Med., vol. 241, no. 15, p. 1684, Sep. 2016, doi: 10.1177/1535370216657448.

[259] "Human Plateable Hepatocytes, 5-Donor." https://www.thermofisher.com/order/catalog/product/HMCPP5 (accessed Nov. 12, 2021).

[260] T. E. Ballard *et al.*, "Simplifying the Execution of HepatoPac MetID Experiments: Metabolite Profile and Intrinsic Clearance Comparisons Downloaded from 2 Running Title Page Running Title: Simplified Execution of HepatoPac ® for MetID Corresponding Author," 2020, doi: 10.1124/dmd.120.000013.

[261] M. Chow-shi-yée, M. Grondin, F. Ouellet, and D. A. Averill-Bates, "Control of stress-induced apoptosis by freezing tolerance-associated wheat proteins during cryopreservation of rat hepatocytes," *Cell Stress Chaperones*, vol. 25, no. 6, p. 869, Nov. 2020, doi: 10.1007/S12192-020-01115-Y.

[262] M. E *et al.*, "Expansion, in vivo-ex vivo cycling, and genetic manipulation of primary human hepatocytes," *Proc. Natl. Acad. Sci. U. S. A.*, vol. 117, no. 3, pp. 1678–1688, Jan. 2020, doi: 10.1073/PNAS.1919035117.

[263] G. SJ and H. JB, "Prediction of in vitro intrinsic clearance from hepatocytes: comparison of suspensions and monolayer cultures," *Drug Metab. Dispos.*, vol. 33, no. 1, pp. 200–201, Jan. 2005, doi: 10.1124/DMD.33.1.

[264] J. D *et al.*, "Cryopreserved human hepatocytes in suspension are a convenient high throughput tool for the prediction of metabolic clearance," *Eur. J. Pharm. Biopharm.*, vol. 63, no. 3, pp. 347–355, Jul. 2006, doi: 10.1016/J.EJPB.2006.01.014.

[265] R. L *et al.*, "Cytotoxicity evaluation using cryopreserved primary human hepatocytes in various culture formats," *Toxicol. Lett.*, vol. 258, pp. 207–215, Sep. 2016, doi: 10.1016/J.TOXLET.2016.06.1127.

[266] M. Maurice, E. Rogier, D. Cassio, and G. Feldmann, "Formation of plasma membrane domains in rat hepatocytes and hepatoma cell lines in culture," 1988.

[267] D. C, F. M, and D. P, "Use of Percoll density gradient centrifugation for preparing isolated rat hepatocytes having long-term viability," *Anal. Biochem.*, vol. 122, no. 1, pp. 119–123, May 1982, doi: 10.1016/0003-2697(82)90259-7.

[268] H. Wang, X. Gao, S. Fukumoto, S. Tademoto, K. Sato, and K. Hirai, "Post-Isolation Inducible Nitric Oxide Synthase Gene Expression Due to Collagenase Buffer Perfusion and Characterization of the Gene Regulation in Primary Cultured Murine Hepatocytes," *J. Biochem.*, vol. 124, no. 5, pp. 892–899, Nov. 1998, doi: 10.1093/OXFORDJOURNALS.JBCHEM.A022204.

[269] M. A. Tirmenstein, F. A. Nicholls-Grzemski, T. D. Schmittgen, B. A. Zakrajsek, and M. W. Fariss, "Characterization of Nitric Oxide Production following Isolation of Rat Hepatocytes," *Toxicol. Sci.*, vol. 53, no. 1, pp. 56–62, Jan. 2000, doi: 10.1093/TOXSCI/53.1.56.

[270] C. C. Bell *et al.*, "Characterization of primary human hepatocyte spheroids as a model system for drug-induced liver injury, liver function and disease," *Sci. Reports 2016 61*, vol. 6, no. 1, pp. 1–13, May 2016, doi: 10.1038/srep25187.

[271] M. Cohen, G. Levy, and Y. Nahmias, "Coculture and long-term maintenance of hepatocytes," *Methods Mol. Biol.*, vol. 1250, pp. 161–173, 2014, doi: 10.1007/978-1-4939-2074-7_11.

[272] I. H, N. M, K. A, M. K, and S. S, "Liver architecture, cell function, and disease," *Semin. Immunopathol.*, vol. 31, no. 3, pp. 399–409, Sep. 2009, doi: 10.1007/S00281-009-0155-6.

[273] M. W. Robinson, C. Harmon, and C. O'Farrelly, "Liver immunology and its role in inflammation and homeostasis," *Cell. Mol. Immunol. 2016 133*, vol. 13, no. 3, pp. 267–276, Apr. 2016, doi: 10.1038/cmi.2016.3.

[274] B. SN, B. UJ, Y. ML, and T. M, "Effect of cell-cell interactions in preservation of cellular phenotype: cocultivation of hepatocytes and nonparenchymal cells," *FASEB J.*, vol. 13, no. 14, pp. 1883–1900, Nov. 1999, doi: 10.1096/FASEBJ.13.14.1883.

[275] E. K, S. B, and M. I, "The liver sinusoidal endothelial cell: a cell type of controversial and confusing identity," *Am. J. Physiol. Gastrointest. Liver Physiol.*, vol. 294, no. 2, Feb. 2008, doi: 10.1152/AJPGI.00167.2007.

[276] J. Poisson *et al.*, "Liver sinusoidal endothelial cells: Physiology and role in liver diseases," *J. Hepatol.*, vol. 66, no. 1, pp. 212–227, 2017, doi: 10.1016/j.jhep.2016.07.009.

[277] A. J. Hwa *et al.*, "Rat liver sinusoidal endothelial cells survive without exogenous VEGF in 3D perfused co-cultures with hepatocytes," *FASEB J.*, vol. 21, no. 10, pp. 2564–2579, Aug. 2007, doi: 10.1096/FJ.06-7473COM.

[278] K. P, S. F, K. S, U.-F. K, and P. I, "Maintaining hepatocyte differentiation in vitro through co-culture with hepatic stellate cells," *In Vitro Cell. Dev. Biol. Anim.*, vol. 45, no. 5–6, pp. 205–212, 2009, doi: 10.1007/S11626-008-9166-1.

[279] S. R. Khetani and S. N. Bhatia, "Microscale culture of human liver cells for drug development," *Nat. Biotechnol. 2008 261*, vol. 26, no. 1, pp. 120–126, Nov. 2007, doi: 10.1038/nbt1361.

[280] R. Jindal, Y. Nahmias, A. W. Tilles, F. Berthiaume, and M. L. Yarmush, "Amino acid-mediated heterotypic interaction governs performance of a hepatic tissue model," *FASEB J.*, vol. 23, no. 7, pp. 2288–2298, Jul. 2009, doi: 10.1096/FJ.08-

114934.

[281] J. R, P. SJ, and Y. ML, “Tissue-engineered model for real-time monitoring of liver inflammation,” *Tissue Eng. Part C. Methods*, vol. 17, no. 1, pp. 113–122, Aug. 2011, doi: 10.1089/TEN.TEC.2009.0782.

[282] K. R *et al.*, “A long-term three dimensional liver co-culture system for improved prediction of clinically relevant drug-induced hepatotoxicity,” *Toxicol. Appl. Pharmacol.*, vol. 268, no. 1, pp. 1–16, Apr. 2013, doi: 10.1016/J.TAAP.2013.01.012.

[283] B. Sundhar, MooreLaura, YarmushMartin, and JindalRohit, “Emerging In Vitro Liver Technologies for Drug Metabolism and Inter-Organ Interactions,” *https://home.liebertpub.com/teb*, vol. 22, no. 5, pp. 383–394, Oct. 2016, doi: 10.1089/TEN.TEB.2016.0031.

[284] N. Milosevic, H. Schawalder, and P. Maier, “Kupffer cell-mediated differential down-regulation of cytochrome P450 metabolism in rat hepatocytes,” *Eur. J. Pharmacol.*, vol. 368, no. 1, pp. 75–87, Feb. 1999, doi: 10.1016/S0014-2999(98)00988-1.

[285] L. ZX, G. S, and K. N, “Innate immune system plays a critical role in determining the progression and severity of acetaminophen hepatotoxicity,” *Gastroenterology*, vol. 127, no. 6, pp. 1760–1774, 2004, doi: 10.1053/J.GASTRO.2004.08.053.

[286] Z. Kmiec, “Cooperation of liver cells in health and disease.,” *Adv. Anat. Embryol. Cell Biol.*, vol. 161, 2001, doi: 10.1007/978-3-642-56553-3.

[287] M. Cohen, G. Levy, and Y. Nahmias, “Coculture and Long-Term Maintenance of Hepatocytes,” *Methods Mol. Biol.*, vol. 1250, pp. 161–173, 2015, doi: 10.1007/978-1-4939-2074-7_11.

[288] M. Bajpai and J. D. Esmay, “IN VITRO STUDIES IN DRUG DISCOVERY AND DEVELOPMENT: AN ANALYSIS OF STUDY OBJECTIVES AND APPLICATION OF GOOD LABORATORY PRACTICES (GLP),” *http://dx.doi.org/10.1081/DMR-120015690*, vol. 34, no. 4, pp. 679–689, 2002, doi: 10.1081/DMR-120015690.

[289] A. Sivaraman *et al.*, “A Microscale In Vitro Physiological Model of the Liver: Predictive Screens for Drug Metabolism and Enzyme Induction,” *Curr. Drug Metab.*, vol. 6, no. 6, pp. 569–591, Nov. 2005, doi: 10.2174/138920005774832632.

[290] L. EL, “Human hepatocyte culture systems for the in vitro evaluation of cytochrome P450 expression and regulation,” *Eur. J. Pharm. Sci.*, vol. 13, no. 4, pp. 343–368, 2001, doi: 10.1016/S0928-0987(01)00135-X.

[291] D. JC, T. RG, and Y. ML, “Long-term in vitro function of adult hepatocytes in a collagen sandwich configuration,” *Biotechnol. Prog.*, vol. 7, no. 3, pp. 237–245, 1991, doi: 10.1021/BP00009A007.

[292] B. Sundhar *et al.*, “Long-Term Coculture Strategies for Primary Hepatocytes and Liver Sinusoidal Endothelial Cells,” *https://home.liebertpub.com/tec*, vol. 21, no. 4, pp. 413–422, Oct. 2014, doi: 10.1089/TEN.TEC.2014.0152.

[293] V. Velasco, S. A. Shariati, and R. Esfandyarpour, “Microtechnology-based methods for organoid models,” *Microsystems Nanoeng. 2020 61*, vol. 6, no. 1, pp. 1–13, Oct. 2020, doi: 10.1038/s41378-020-00185-3.

[294] “How are Organoids Different from Spheroids?” https://blog.crownbio.com/organoids-or-spheroids (accessed Oct. 28, 2021).

[295] Y. Wang *et al.*, “In situ differentiation and generation of functional liver organoids from human iPSCs in a 3D perfusable chip system,” *Lab Chip*, vol. 18, no. 23, pp. 3606–3616, Nov. 2018, doi: 10.1039/C8LC00869H.

[296] F. Wu *et al.*, “Generation of hepato-biliary organoids from human induced pluripotent stem cells,” *J. Hepatol.*, no. 2019, 2019, doi: 10.1016/j.jhep.2018.12.028.

[297] R. L. Gieseck *et al.*, “Maturation of induced pluripotent stem cell derived hepatocytes by 3D-culture,” *PLoS One*, vol. 9, no. 1, 2014, doi: 10.1371/journal.pone.0086372.

[298] F. Meier *et al.*, “Hepatic differentiation of human iPSCs in different 3D models: A comparative study,” *Int. J. Mol. Med.*, vol. 40, no. 6, pp. 1759–1771, 2017, doi: 10.3892/ijmm.2017.3190.

[299] R. Foty, “A Simple Hanging Drop Cell Culture Protocol for Generation of 3D Spheroids,” *J. Vis. Exp.*, no. 51, 2011, doi: 10.3791/2720.

[300] M. Zanoni *et al.*, “3D tumor spheroid models for in vitro therapeutic screening: a systematic approach to enhance the biological relevance of data obtained,” *Sci. Reports 2016 61*, vol. 6, no. 1, pp. 1–11, Jan. 2016, doi: 10.1038/srep19103.

[301] A. Kamatar, G. Gunay, and H. Acar, “Natural and Synthetic Biomaterials for Engineering Multicellular Tumor Spheroids,” *Polymers (Basel).*, vol. 12, no. 11, pp. 1–23, Nov. 2020, doi: 10.3390/POLYM12112506.

[302] S. R. Caliari and J. A. Burdick, “A Practical Guide to Hydrogels for Cell Culture,” *Nat. Methods*, vol. 13, no. 5, p. 405, May 2016, doi: 10.1038/NMETH.3839.

[303] L. Huang, A. M. E. Abdalla, L. Xiao, and G. Yang, “Biopolymer-Based Microcarriers for Three-Dimensional Cell Culture and Engineered Tissue Formation,” *Int. J. Mol. Sci.*, vol. 21, no. 5, Mar. 2020, doi: 10.3390/IJMS21051895.

[304] P. B, H. AC, S. PMA, and B. H, “Three-Dimensional Spheroids as In Vitro Preclinical Models for Cancer Research,” *Pharmaceutics*, vol. 12, no. 12, pp. 1–38, Dec. 2020, doi: 10.3390/PHARMACEUTICS12121186.

[305] Marko Tobias Gröger, “INFLAMMATION-ON-A-CHIP: A MICROPHYSIOLOGICAL HUMAN LIVER MODEL,” *2018*. https://www.db-thueringen.de/servlets/MCRFileNodeServlet/dbt_derivate_00043756/dissertationgroeger.pdf (accessed Oct. 29, 2021).

[306] H. Mauriac, C. Pannetier, and G. V. Casquillas, “Organs on chip review,” *Elveflow*, Dec. 2020, Accessed: Oct. 27, 2021. [Online]. Available: https://www.elveflow.com/microfluidic-reviews/organs-on-chip-3d-cell-culture/organs-chip-review/.

[307] B. J. van Meer *et al.*, “Small molecule absorption by PDMS in the context of drug response bioassays,” *Biochem. Biophys. Res. Commun.*, vol. 482, no. 2, pp. 323–328, Jan. 2017, doi: 10.1016/J.BBRC.2016.11.062.

[308] W. JD, D. NJ, T. S, and E. M, “Quantitative analysis of molecular absorption into PDMS microfluidic channels,” *Ann. Biomed. Eng.*, vol. 40, no. 9, pp. 1862–1873, Sep. 2012, doi: 10.1007/S10439-012-0562-Z.

[309] C. J. Henderson, C. R. Wolf, N. Kitteringham, H. Powell, D. Otto, and B. K. Park, “Increased resistance to acetaminophen hepatotoxicity in mice lacking glutathione S-transferase Pi,” *Proc. Natl. Acad. Sci. U. S. A.*, vol. 97, no. 23, p. 12741, Nov. 2000, doi: 10.1073/PNAS.220176997.

[310] B. D. Wilson, A. J. Jaworski, M. E. Donner, and M. L. Lippmann, “Amiodarone-induced pulmonary toxicity in the rat,” *Lung 1989 1671*, vol. 167, no. 1, pp. 301–311, Dec. 1989, doi: 10.1007/BF02714959.

[311] S. M. Markova *et al.*, “Association of CYP2C9*2 with Bosentan-Induced Liver Injury,” *Clin. Pharmacol. Ther.*, vol. 94, no. 6, pp. 678–686, Dec. 2013, doi: 10.1038/CLPT.2013.143.

[312] F. L *et al.*, “Contribution of mrp2 in alterations of canalicular bile formation by the endothelin antagonist bosentan,” *J. Hepatol.*, vol. 37, no. 2, pp. 184–191, 2002, doi: 10.1016/S0168-8278(02)00107-1.

[313] M. Y, U. T, and K. H, “Effects of bosentan, an endothelin receptor antagonist, on bile salt export pump and multidrug resistance-associated protein 2,” *Biopharm. Drug Dispos.*, vol. 28, no. 1, pp. 13–18, Jan. 2007, doi: 10.1002/BDD.527.

[314] U. A. Boelsterli, “Diclofenac-induced liver injury: a paradigm of idiosyncratic drug toxicity,” *Toxicol. Appl. Pharmacol.*, vol. 192, no. 3, pp. 307–322, Nov. 2003, doi: 10.1016/S0041-008X(03)00368-5.

[315] N. DJ, S. LS, M. X, S. AV, C. SE, and P. BK, “Investigation of the immunogenicity of diclofenac and diclofenac metabolites,” *Toxicol. Lett.*, vol. 168, no. 1, pp. 45–50, Jan. 2007, doi: 10.1016/J.TOXLET.2006.10.014.

[316] R. McKenzie *et al.*, “Hepatic Failure and Lactic Acidosis Due to Fialuridine (FIAU), an Investigational Nucleoside Analogue for Chronic Hepatitis B,” *http://dx.doi.org/10.1056/NEJM199510263331702*, vol. 333, no. 17, pp. 1099–1105, Aug. 2009, doi: 10.1056/NEJM199510263331702.

[317] M. FJ and S. M, “Review of the Fialuridine (FIAU) Clinical Trials,” Mar. 1995, doi: 10.17226/4887.

[318] L. W *et al.*, “Fialuridine and its metabolites inhibit DNA polymerase gamma at sites of multiple adjacent analog incorporation, decrease mtDNA abundance, and cause mitochondrial structural defects in cultured hepatoblasts,” *Proc. Natl. Acad. Sci. U. S. A.*, vol. 93, no. 8, pp. 3592–3597, Apr. 1996, doi: 10.1073/PNAS.93.8.3592.

[319] “Levofloxacin,” *LiverTox Clin. Res. Inf. Drug-Induced Liver Inj.*, Mar. 2020, Accessed: Oct. 04, 2021. [Online]. Available: https://www.ncbi.nlm.nih.gov/books/NBK548357/.

[320] L. Panahi, S. S. Surani, G. Udeani, N. P. Patel, and J. Sellers, “Hepatotoxicity Secondary to Levofloxacin Use,” *Cureus*, vol. 13, no. 6, Jun. 2021, doi: 10.7759/CUREUS.15973.

[321] S. PJ, H. MJ, G. PE, and R. RA, “Lipopolysaccharide and trovafloxacin coexposure in mice causes idiosyncrasy-like liver injury dependent on tumor necrosis factor-alpha,” *Toxicol. Sci.*, vol. 100, no. 1, pp. 259–266, Nov. 2007, doi: 10.1093/TOXSCI/KFM218.

[322] G. G *et al.*, “Trovafloxacin-Induced Liver Injury: Lack in Regulation of Inflammation by Inhibition of Nucleotide Release and Neutrophil Movement,” *Toxicol. Sci.*, vol. 167, no. 2, pp. 385–396, Feb. 2019, doi: 10.1093/TOXSCI/KFY244.

[323] M. I. Lucena *et al.*, “Trovafloxacin-induced acute hepatitis,” *Clin. Infect. Dis.*, vol. 30, no. 2, pp. 400–401, 2000, doi: 10.1086/313680.

[324] D. G. Nguyen *et al.*, “Bioprinted 3D Primary Liver Tissues Allow Assessment of Organ-Level Response to Clinical Drug Induced Toxicity In Vitro,” *PLoS One*, vol. 11, no. 7, p. e0158674, Jul. 2016, doi: 10.1371/JOURNAL.PONE.0158674.

[325] L. MJ *et al.*, “Microarray analysis in human hepatocytes suggests a mechanism for hepatotoxicity induced by trovafloxacin,” *Hepatology*, vol. 41, no. 1, pp. 177–186, Jan. 2005, doi: 10.1002/HEP.20514.

[326] F. Stocchi and M. F. De Pandis, “Utility of tolcapone in fluctuating Parkinson’s disease,” *Clin. Interv. Aging*, vol. 1, no. 4, p. 317, 2006, doi: 10.2147/CIIA.2006.1.4.317.

[327] H. Terada, “Uncouplers of oxidative phosphorylation,” *Environ. Health Perspect.*, vol. 87, pp. 213–218, 1990, doi: 10.1289/EHP.9087213.

[328] H. K, K. A, P. KE, and N. E, “Effects of entacapone and tolcapone on mitochondrial membrane potential,” *Eur. J. Pharmacol.*, vol. 453, no. 1, pp. 21–26, Oct. 2002, doi: 10.1016/S0014-2999(02)02383-X.

[329] F. GA and M. RH, “Troglitazone (Rezulin) and hepatic injury,” *Pharmacoepidemiol. Drug Saf.*, vol. 10, no. 6, pp. 537–547, 2001, doi: 10.1002/PDS.652.

[330] S. E. Kostrubsky, S. C. Strom, E. Ellis, S. D. Nelson, and A. E. Mutlib, “Transport, metabolism, and hepatotoxicity of flutamide, drug-drug interaction with acetaminophen involving phase I and phase II metabolites,” *Chem. Res. Toxicol.*, vol. 20, no. 10, pp. 1503–1512, Oct. 2007, doi: 10.1021/TX7001542.

[331] T. MA *et al.*, “Effects of troglitazone on HepG2 viability and mitochondrial function,” *Toxicol. Sci.*, vol. 69, no. 1, pp. 131–138, Sep. 2002, doi: 10.1093/TOXSCI/69.1.131.

[332] B. M, A. E, and B. UA, “Diabetic KKAy mice exhibit increased hepatic PPARgamma1 gene expression and develop hepatic steatosis upon chronic treatment with antidiabetic thiazolidinediones,” *J. Hepatol.*, vol. 35, no. 1, pp. 17–23, 2001, doi: 10.1016/S0168-8278(01)00066-6.

[333] F. C *et al.*, “Troglitazone-induced intrahepatic cholestasis by an interference with the hepatobiliary export of bile acids in male and female rats. Correlation with the gender difference in troglitazone sulfate formation and the inhibition of the canalicular bile salt export pump (Bsep) by troglitazone and troglitazone sulfate,” *Toxicology*, vol. 167, no. 1, pp. 83–98, Oct. 2001, doi: 10.1016/S0300-483X(01)00460-7.

[334] K. Yang, J. L. Woodhead, P. B. Watkins, B. A. Howell, and K. L. Brouwer, “Systems Pharmacology Modeling Predicts Delayed Presentation and Species Differences in Bile Acid-Mediated Troglitazone Hepatotoxicity,” *Clin. Pharmacol. Ther.*, vol. 96, no. 5, p. 589, Jul. 2014, doi: 10.1038/CLPT.2014.158.

[335] W. L *et al.*, “Oral ximelagatran for secondary prophylaxis after myocardial infarction: the ESTEEM randomised controlled trial,” *Lancet (London, England)*, vol. 362, no. 9386, pp. 789–797, Sep. 2003, doi: 10.1016/S0140-6736(03)14287-0.

[336] A. Kindmark *et al.*, “Genome-wide pharmacogenetic investigation of a hepatic adverse event without clinical signs of immunopathology suggests an underlying immune pathogenesis,” *Pharmacogenomics J. 2008 83*, vol. 8, no. 3, pp. 186–195, May 2007, doi: 10.1038/sj.tpj.6500458.

[337] “Drug Induced Liver Injury Rank (DILIrank) Dataset | FDA.” https://www.fda.gov/science-research/liver-toxicity-knowledge-base-ltkb/drug-induced-liver-injury-rank-dilirank-dataset (accessed Oct. 04, 2021).

[338] M. TK, Y. BP, and L. YY, “Dabigatran etexilate versus warfarin as the oral anticoagulant of choice? A review of clinical data,” *Pharmacol. Ther.*, vol. 129, no. 2, pp. 185–194, Feb. 2011, doi: 10.1016/J.PHARMTHERA.2010.09.005.

[339] S. CR *et al.*, “Disposition of metformin (N,N-dimethylbiguanide) in man,” *Clin. Pharmacol. Ther.*, vol. 24, no. 6, pp. 683–693, 1978, doi: 10.1002/CPT1978246683.

[340] B. MM, P. I, and S. ML, “Metformin-induced acute hepatitis,” *Am. J. Med.*, vol. 104, no. 5, pp. 490–492, 1998, doi: 10.1016/S0002-9343(98)00088-6.

[341] E. ME, E.-K. AO, and B. DR, “The metabolism of amiodarone by various CYP isoenzymes of human and rat, and the inhibitory influence of ketoconazole,” *J. Pharm. Pharm. Sci.*, vol. 11, no. 1, pp. 147–159, 2008, doi: 10.18433/J3SG66.

[342] D. M, U. M, E. E, W. L, and A. TB, “In vitro evaluation of major in vivo drug metabolic pathways using primary human hepatocytes and HepaRG cells in suspension and a dynamic three-dimensional bioreactor system,” *J. Pharmacol. Exp. Ther.*, vol. 343, no. 1, pp. 134–144, Oct. 2012, doi: 10.1124/JPET.112.195834.

[343] G. R, L. GP, Z. M, T. CM, W. J, and U. JD, “Facilitated mitochondrial import of antiviral and anticancer nucleoside drugs by human equilibrative nucleoside transporter-3,” *Am. J. Physiol. Gastrointest. Liver Physiol.*, vol. 296, no. 4, Apr. 2009, doi: 10.1152/AJPGI.90672.2008.

[344] D. F. G. Hendriks, T. Hurrell, J. Riede, M. van der Horst, S. Tuovinen, and M. Ingelman-Sundberg, “Mechanisms of Chronic Fialuridine Hepatotoxicity as Revealed in Primary Human Hepatocyte Spheroids,” *Toxicol. Sci.*, vol. 171, no. 2, pp. 385–395, Oct. 2019, doi: 10.1093/TOXSCI/KFZ195.

[345] BazeAudrey *et al.*, “Three-Dimensional Spheroid Primary Human Hepatocytes in Monoculture and Coculture with Nonparenchymal Cells,” *https://home.liebertpub.com/tec*, vol. 24, no. 9, pp. 534–545, Sep. 2018, doi: 10.1089/TEN.TEC.2018.0134.

[346] A. Skardal *et al.*, “Multi-tissue interactions in an integrated three-tissue organ-on-a-chip platform,” *Sci. Rep.*, vol. 7, no. 1, pp. 1–16, 2017, doi: 10.1038/s41598-017-08879-x.

[347] W. BR, D. MJ, M. CP, and K. SR, “A Cell Culture Platform to Maintain Long-term Phenotype of Primary Human Hepatocytes and Endothelial Cells,” *Cell. Mol. Gastroenterol. Hepatol.*, vol. 5, no. 3, pp. 187–207, Mar. 2017, doi: 10.1016/J.JCMGH.2017.11.007.

[348] A. Francavilla, P. Ove, L. Polimeno, C. Sciascia, M. L. Coetzee, and T. E. Starzl, “Epidermal Growth Factor and

Proliferation in Rat Hepatocytes in Primary Culture Isolated at Different Times after Partial Hepatectomy," *Cancer Res.*, vol. 46, no. 3, 1986.

[349] G. MH, M. MA, S. P, M. WT, and B. MD, "Studies on the maintenance of cytochromes P-450 and b5, monooxygenases and cytochrome reductases in primary cultures of rat hepatocytes," *FEBS Lett.*, vol. 190, no. 1, pp. 99–103, Oct. 1985, doi: 10.1016/0014-5793(85)80436-1.

[350] T. G, H. J, W. Y, H. PG, and M. SO, "Serum-free collagen sandwich cultures of adult rat hepatocytes maintain liver-like properties long term: a valuable model for in vitro toxicity and drug-drug interaction studies," *Chem. Biol. Interact.*, vol. 181, no. 1, pp. 124–137, Sep. 2009, doi: 10.1016/J.CBI.2009.05.015.

[351] S. S. Bale, S. Geerts, R. Jindal, and M. L. Yarmush, "Isolation and co-culture of rat parenchymal and non-parenchymal liver cells to evaluate cellular interactions and response," *Sci. Reports 2016 61*, vol. 6, no. 1, pp. 1–10, May 2016, doi: 10.1038/srep25329.

[352] T. B. Andersson, "Evolution of Novel 3D Culture Systems for Studies of Human Liver Function and Assessments of the Hepatotoxicity of Drugs and Drug Candidates," *Basic Clin. Pharmacol. Toxicol.*, vol. 121, no. 4, pp. 234–238, 2017, doi: 10.1111/bcpt.12804.

[353] K. A, K. T, and M. A, "Oncostatin M and hepatocyte growth factor induce hepatic maturation via distinct signaling pathways," *FEBS Lett.*, vol. 492, no. 1–2, pp. 90–94, Mar. 2001, doi: 10.1016/S0014-5793(01)02140-8.

[354] ERS Journal, "Potentially significant drug interactions with pulmonary arterial hypertension(PAH)-targeted therapies." https://erj.ersjournals.com/highwire/markup/95216/expansion?width=1000&height=500&iframe=true&postprocessors=highwire_tables%2Chighwire_reclass%2Chighwire_figures%2Chighwire_math%2Chighwire_inline_linked_media%2Chighwire_embed (accessed Aug. 13, 2021).

[355] F. Yamashita *et al.*, "Modeling of Rifampicin-Induced CYP3A4 Activation Dynamics for the Prediction of Clinical Drug-Drug Interactions from In Vitro Data," *PLoS One*, vol. 8, no. 9, p. 70330, Sep. 2013, doi: 10.1371/JOURNAL.PONE.0070330.

[356] Naina Mohamed Pakkir Maideen, "Drug Interactions of Acetaminophen (Paracetamol) involving CYP and UGT Enzymes," *Eur. J. Med.*, vol. 7, no. 1, Mar. 2019, doi: 10.13187/EJM.2019.1.30.

[357] "EP079 v5.0 Liver-Chip Quad-Culture Protocol," 2019.

[358] "Liver-Chip Culture Protocol // Quad-Culture - Emulate." https://emulatebio.com/support/ep079-v5-0/ (accessed Aug. 09, 2021).

[359] "QuantiGene Plex Gene Expression Assay - DE," Accessed: Oct. 04, 2021. [Online]. Available: //www.thermofisher.com/de/de/home/life-science/gene-expression-analysis-genotyping/quantigene-rna-assays/quantigene-plex-assay.html.

[360] "Luminex Instruments - DE," Accessed: Oct. 04, 2021. [Online]. Available: //www.thermofisher.com/de/de/home/life-science/antibodies/immunoassays/procartaplex-assays-luminex/luminex-instruments.html.

[361] U. Manual, "QuantiGene ® Plex 2.0 Reagent System QuantiGene Plex 2.0 Reagent System User Manual," 2008.

[362] Q. P. Assays, "APPLICATION NOTE."

[363] "QuantiGene miRNA Singleplex Assay: How It Works - DE," Accessed: Nov. 25, 2021. [Online]. Available: //www.thermofisher.com/de/de/home/life-science/epigenetics-noncoding-rna-research/mirna-analysis/quantigene-mirna-singleplex-assay/quantigene-mirna-singleplex-assay-how-it-works.html.

[364] "biocrates - Targeted metabolomics kits and services." https://biocrates.com/ (accessed Nov. 05, 2021).

[365] "Aspartate Aminotransferase (AST) Activity Assay Kit."

[366] Sigma, "Alanine Aminotransferase Activity Assay Kit," 2021. https://www.sigmaaldrich.com/deepweb/assets/sigmaaldrich/product/documents/731/802/mak052bul.pdf (accessed Aug. 10, 2021).

[367] P. Corporation, "LDH-Glo™ Cytotoxicity Assay Instructions for use of Products J2380 AND J2381," Accessed: Aug. 10, 2021. [Online]. Available: www.promega.com.

[368] "Resazurin Cell Viability Assay | Creative Bioarray." https://www.creative-bioarray.com/support/resazurin-cell-viability-assay.htm (accessed Dec. 29, 2021).

[369] J. R. Carvalho and M. V. Machado, "New Insights About Albumin and Liver Disease," *Ann. Hepatol.*, vol. 17, no. 4, pp. 547–560, Jul. 2018, doi: 10.5604/01.3001.0012.0916.

[370] "ab179887-Human Albumin SimpleStep ELISA® Kit," 2020, Accessed: Sep. 17, 2021. [Online]. Available: www.abcam.com/protocols/the-complete-elisa-guide.

[371] H. Clarke *et al.*, "alpha-glutathione s-transferase (alpha-GST) release, an early indicator of carbon tetrachloride

hepatotoxicity in the rat," 1996.

[372] A. Choukér *et al.*, "α-Gluthathione S-Transferase as an Early Marker of Hepatic Ischemia/Reperfusion Injury after Liver Resection," *World J. Surg. 2005 294*, vol. 29, no. 4, pp. 528–534, Mar. 2005, doi: 10.1007/S00268-004-7431-3.

[373] "α-GST, Human Urin, Serum, Plasma."

[374] Harriet Gaskell, Parveen Sharma, H. E. Colley, Craig Murdoch, D. P. Williams, and S. D. Webb, "Characterization of a functional C3A liver spheroid model," *Toxicol. Res. (Camb).*, vol. 5, no. 4, pp. 1053–1065, Jun. 2016, doi: 10.1039/C6TX00101G.

[375] E. Redondo-Castro, C. J. Cunningham, J. Miller, S. A. Cain, S. M. Allan, and E. Pinteaux, "Generation of Human Mesenchymal Stem Cell 3D Spheroids Using Low-binding Plates," *Iss*, vol. 8, 2018, doi: 10.21769/BioProtoc.2968.

[376] K. N. Bergdorf *et al.*, "Immunofluorescent staining of cancer spheroids and fine-needle aspiration-derived organoids," *STAR Protoc.*, vol. 2, no. 2, p. 100578, Jun. 2021, doi: 10.1016/J.XPRO.2021.100578.

[377] T. RM *et al.*, "Human liver cell spheroids in extended perfusion bioreactor culture for repeated-dose drug testing," *Hepatology*, vol. 55, no. 4, pp. 1227–1236, Apr. 2012, doi: 10.1002/HEP.24760.

[378] G. K. Smyth, M. Ritchie, N. Thorne, J. Wettenhall, W. Shi, and Y. Hu, "limma: Linear Models for Microarray and RNA-Seq Data User's Guide."

[379] M. E. Ritchie *et al.*, "limma powers differential expression analyses for RNA-sequencing and microarray studies," *Nucleic Acids Res.*, vol. 43, no. 7, pp. e47–e47, Apr. 2015, doi: 10.1093/NAR/GKV007.

[380] S. Babicki *et al.*, "Heatmapper: web-enabled heat mapping for all," *Nucleic Acids Res.*, vol. 44, no. W1, pp. W147–W153, Jul. 2016, doi: 10.1093/NAR/GKW419.

[381] S. Messner, I. Agarkova, W. Moritz, and J. M. Kelm, "Multi-cell type human liver microtissues for hepatotoxicity testing," *Arch. Toxicol.*, vol. 87, no. 1, p. 209, Jan. 2013, doi: 10.1007/S00204-012-0968-2.

[382] Sujoy Lahiri *et al.*, "Primary Human Hepatocytes 3D in vitro Culture Model for Studying Hepatic Function." https://assets.thermofisher.com/TFS-Assets/BID/posters/human-hepatocytes-3d-in-vitro-culture-model-hepatic-function-poster.pdf (accessed Sep. 21, 2021).

[383] W. R. Proctor *et al.*, "Utility of spherical human liver microtissues for prediction of clinical drug-induced liver injury," *Arch. Toxicol.*, 2002, doi: 10.1007/s00204-017-2002-1.

[384] V. M. Lauschke, D. F. G. Hendriks, C. C. Bell, T. B. Andersson, and M. Ingelman-Sundberg, "Novel 3D Culture Systems for Studies of Human Liver Function and Assessments of the Hepatotoxicity of Drugs and Drug Candidates," *Chem. Res. Toxicol.*, vol. 29, no. 12, pp. 1936–1955, Dec. 2016, doi: 10.1021/ACS.CHEMRESTOX.6B00150.

[385] M. A. M. Vis, K. Ito, and S. Hofmann, "Impact of Culture Medium on Cellular Interactions in in vitro Co-culture Systems," *Front. Bioeng. Biotechnol.*, vol. 0, p. 911, Aug. 2020, doi: 10.3389/FBIOE.2020.00911.

[386] "Liver Function Tests: Normal, High, and Low Ranges, Chart & Results." https://www.medicinenet.com/liver_blood_tests/article.htm (accessed Sep. 21, 2021).

[387] J. K and K. T, "Zonation of parenchymal and nonparenchymal metabolism in liver," *Annu. Rev. Nutr.*, vol. 16, pp. 179–203, 1996, doi: 10.1146/ANNUREV.NU.16.070196.001143.

[388] Abdel-Moneim, "Significance of Serum Alpha-Glutathione S-Transferase Assessment in Hepatitis C Patients with Different Alanine Aminotransferase Patterns," *Gastroenterol. Res.*, 2011, doi: 10.4021/GR269W.

[389] "Measuring Aspartate Transaminase (AST) In Vitro – Closing the Gap to Clinical Data - InSphero." https://insphero.com/blog/aspartate-transaminase-ast-in-vitro/ (accessed Sep. 29, 2021).

[390] S. M. Abdel-Moneim and H. Sliem, "Significance of Serum Alpha-Glutathione S-Transferase Assessment in Hepatitis C Patients with Different Alanine Aminotransferase Patterns," *Gastroenterol. Res.*, vol. 4, no. 1, p. 13, 2011, doi: 10.4021/GR269W.

[391] J. Jiang, C. D. Pieterman, G. Ertaylan, R. L. M. Peeters, and T. M. C. M. de Kok, "The application of omics-based human liver platforms for investigating the mechanism of drug-induced hepatotoxicity in vitro," *Arch. Toxicol. 2019 9311*, vol. 93, no. 11, pp. 3067–3098, Oct. 2019, doi: 10.1007/S00204-019-02585-5.

[392] C. C. Bell *et al.*, "Comparison of Hepatic 2D Sandwich Cultures and 3D Spheroids for Long-term Toxicity Applications: A Multicenter Study," *Toxicol. Sci.*, vol. 162, no. 2, pp. 655–666, Apr. 2018, doi: 10.1093/TOXSCI/KFX289.

[393] B. Swift, N. D. Pfeifer, and K. L. R. Brouwer, "Sandwich-cultured hepatocytes: an in vitro model to evaluate hepatobiliary transporter-based drug interactions and hepatotoxicity.," *Drug Metab. Rev.*, vol. 42, no. 3, pp. 446–471, Aug. 2010, doi: 10.3109/03602530903491881.

[394] F. Mittler, P. Obeïd, A. V. Rulina, V. Haguet, X. Gidrol, and M. Y. Balakirev, "High-content monitoring of drug effects in a 3D spheroid model," *Front. Oncol.*, vol. 7, no. DEC, p. 293, Dec. 2017, doi: 10.3389/FONC.2017.00293/BIBTEX.

[395] “May 07, 2015 - InSphero Launches Enhanced Ultra-low Attachment Spheroid Plate for Scaffold-free 3D Cell Culture - InSphero.” https://insphero.com/media-release/07-05-2015-insphero-launches-enhanced-ultra-low-attachment-spheroid-plate-for-scaffold-free-3d-cell-culture/ (accessed Nov. 16, 2021).

[396] “3D InSight™ Human Liver Microtissues, Human Liver Models | InSphero.” https://insphero.com/products/liver/toxicology-models/human/ (accessed Nov. 16, 2021).

[397] R. Boon *et al.*, “Amino acid levels determine metabolism and CYP450 function of hepatocytes and hepatoma cell lines,” doi: 10.1038/s41467-020-15058-6.

[398] A. Parkinson, D. R. Mudra, C. Johnson, A. Dwyer, and K. M. Carroll, “The effects of gender, age, ethnicity, and liver cirrhosis on cytochrome P450 enzyme activity in human liver microsomes and inducibility in cultured human hepatocytes,” *Toxicol. Appl. Pharmacol.*, vol. 199, no. 3, pp. 193–209, Sep. 2004, doi: 10.1016/J.TAAP.2004.01.010.

[399] W. Ikumi *et al.*, “Cigarette smoke extract induces CYP2B6 through constitutive androstane receptor in hepatocytes,” *Drug Metab. Dispos.*, vol. 39, no. 1, pp. 1–3, Jan. 2011, doi: 10.1124/DMD.110.034504.

[400] B. B. Rasmussen, T. H. Brix, K. O. Kyvik, and K. Brøsen, “The interindividual differences in the 3-demthylation of caffeine alias CYP1A2 is determined by both genetic and environmental factors,” *Pharmacogenetics*, vol. 12, no. 6, pp. 473–478, Aug. 2002, doi: 10.1097/00008571-200208000-00008.

[401] C. Girre, D. Lucas, E. Hispard, C. Menez, S. Dally, and J. F. Menez, “Assessment of cytochrome P4502E1 induction in alcoholic patients by chlorzoxazone pharmacokinetics,” *Biochem. Pharmacol.*, vol. 47, no. 9, pp. 1503–1508, Apr. 1994, doi: 10.1016/0006-2952(94)90524-X.

[402] “Document Connect.” https://www.thermofisher.com/document-connect/document-connect.html?url=https://assets.thermofisher.com/TFS-Assets%2FLSG%2Fmanuals%2FMAN0018280_Cryopreserved-3D-SpheroidQualifiedHumanHepatocytes_UG.pdf (accessed Nov. 08, 2021).

[403] “Gibco Hepatocytes - DE,” Accessed: Nov. 11, 2021. [Online]. Available: //www.thermofisher.com/de/de/home/industrial/pharma-biopharma/drug-discovery-development/adme-tox/gibco-hepatocytes.html.

[404] A. Ullrich, J. Dieckhoff, V. Schwartz, D. Runge, P. Hewitt, and T. Mentzel, “A novel polymer solution to generate ultra-low cell attachment surfaces and highly uniform spheroids in 3D primary cell cultures.”

[405] K. M. O. Goyak, E. M. Laurenzana, and C. J. Omiecinski, “Hepatocyte Differentiation,” doi: 10.1007/978-1-60761-688-7_6.

[406] G. Baffet, B. Clément, D. Glaise, A. Guillouzo, and C. Guguen-Guillouzo, “Hydrocortisone modulates the production of extracellular material and albumin in long-term cocultures of adult rat hepatocytes with other liver epithelial cells,” *Biochem. Biophys. Res. Commun.*, vol. 109, no. 2, pp. 507–512, Nov. 1982, doi: 10.1016/0006-291X(82)91750-8.

[407] D. M. Jefferson, L. M. Reid, M. -A Giambrone, D. A. Shafritz, and M. A. Zern, “Effects of dexamethasone on albumin and collagen gene expression in primary cultures of adult rat hepatocytes,” *Hepatology*, vol. 5, no. 1, pp. 14–20, Jan. 1985, doi: 10.1002/HEP.1840050105.

[408] S. Bhandari *et al.*, “Effect of glucocorticoids on liver sinusoidal endothelial cells in vitro 02 Evaluation of surrogate serum biomarker of Sox9-expressing HCC,” 2020.

[409] A. M. Kemas, S. Youhanna, R. Zandi Shafagh, and V. M. Lauschke, “Insulin-dependent glucose consumption dynamics in 3D primary human liver cultures measured by a sensitive and specific glucose sensor with nanoliter input volume,” *FASEB J.*, vol. 35, no. 3, p. e21305, Mar. 2021, doi: 10.1096/FJ.202001989RR.

[410] G. Damm *et al.*, “EFFECT OF GLUCOSE AND INSULIN SUPPLEMENTATION ON THE ISOLATION OF PRIMARY HUMAN HEPATOCYTES,” *EXCLI J.*, vol. 18, pp. 1071–1091, 2019, doi: 10.17179/excli2019-1782.

[411] J. Fraczek, J. Bolleyn, T. Vanhaecke, V. Rogiers, and M. Vinken, “Primary hepatocyte cultures for pharmaco-toxicological studies: at the busy crossroad of various anti-dedifferentiation strategies,” *Arch. Toxicol.*, vol. 87, no. 4, pp. 577–610, Apr. 2013, doi: 10.1007/S00204-012-0983-3.

[412] L. Sheng, B. Jiang, and L. Rui, “Intracellular lipid content is a key intrinsic determinant for hepatocyte viability and metabolic and inflammatory states in mice,” *Am. J. Physiol. - Endocrinol. Metab.*, vol. 305, no. 9, p. E1115, Nov. 2013, doi: 10.1152/AJPENDO.00401.2013.

[413] C. Géraud *et al.*, “Liver sinusoidal endothelium: A microenvironment-dependent differentiation program in rat including the novel junctional protein liver endothelial differentiation-associated protein-1,” *Hepatology*, vol. 52, no. 1, pp. 313–326, Jul. 2010, doi: 10.1002/HEP.23618.

[414] S. March, E. E. Hui, G. H. Underhill, S. Khetani, and S. N. Bhatia, “Microenvironmental regulation of the sinusoidal

endothelial cell phenotype in vitro," *Hepatology*, vol. 50, no. 3, pp. 920–928, Sep. 2009, doi: 10.1002/HEP.23085.

[415] S. Hoehme *et al.*, "Prediction and validation of cell alignment along microvessels as order principle to restore tissue architecture in liver regeneration," *Proc. Natl. Acad. Sci. U. S. A.*, vol. 107, no. 23, pp. 10371–10376, Jun. 2010, doi: 10.1073/PNAS.0909374107/-/DCSUPPLEMENTAL/PNAS.0909374107_SI.PDF.

[416] M. Ölander, J. R. Wiśniewski, I. Flörkemeier, N. Handin, J. Urdzik, and P. Artursson, "A simple approach for restoration of differentiation and function in cryopreserved human hepatocytes," *Arch. Toxicol.*, vol. 93, no. 3, pp. 819–829, Mar. 2019, doi: 10.1007/S00204-018-2375-9/FIGURES/6.

[417] S. R. Khetani, D. R. Berger, K. R. Ballinger, M. D. Davidson, C. Lin, and B. R. Ware, "Microengineered liver tissues for drug testing," *J. Lab. Autom.*, vol. 20, no. 3, pp. 216–250, Jun. 2015, doi: 10.1177/2211068214566939.

[418] S. Cassim, V. A. Raymond, P. Lapierre, and M. Bilodeau, "From in vivo to in vitro: Major metabolic alterations take place in hepatocytes during and following isolation," *PLoS One*, vol. 12, no. 12, Dec. 2017, doi: 10.1371/JOURNAL.PONE.0190366.

[419] N. Hempel, N. Gamage, J. L. Martin, and M. E. McManus, "Human cytosolic sulfotransferase SULT1A1," *Int. J. Biochem. Cell Biol.*, vol. 39, no. 4, pp. 685–689, 2007, doi: 10.1016/J.BIOCEL.2006.10.002.

[420] P. G. Wells *et al.*, "Glucuronidation and the UDP-glucuronosyltransferases in health and disease," *Drug Metab. Dispos.*, vol. 32, no. 3, pp. 281–290, Mar. 2004, doi: 10.1124/DMD.32.3.281.

[421] E. E. J. Kasteel, K. Darney, N. I. Kramer, J. L. C. M. Dorne, and L. S. Lautz, "Human variability in isoform-specific UDP-glucuronosyltransferases: markers of acute and chronic exposure, polymorphisms and uncertainty factors," *Arch. Toxicol. 2020 948*, vol. 94, no. 8, pp. 2637–2661, May 2020, doi: 10.1007/S00204-020-02765-8.

[422] M. J. Zaya, R. N. Hines, and J. C. Stevens, "Epirubicin glucuronidation and UGT2B7 developmental expression," *Drug Metab. Dispos.*, vol. 34, no. 12, pp. 2097–2101, Dec. 2006, doi: 10.1124/DMD.106.011387.

[423] J. E. Ros *et al.*, "ATP binding cassette transporter gene expression in rat liver progenitor cells," *Gut*, vol. 52, no. 7, pp. 1060–1067, Jul. 2003, doi: 10.1136/GUT.52.7.1060.

[424] C. Hu and L. Li, "In vitro culture of isolated primary hepatocytes and stem cell-derived hepatocyte-like cells for liver regeneration," *Protein Cell*, vol. 6, no. 8, pp. 562–574, Aug. 2015, doi: 10.1007/S13238-015-0180-2/FIGURES/1.

[425] T. Mitaka, F. Sato, T. Mizuguchi, T. Yokono, and Y. Mochizuki, "Reconstruction of hepatic organoid by rat small hepatocytes and hepatic nonparenchymal cells," *Hepatology*, vol. 29, no. 1, pp. 111–125, 1999, doi: 10.1002/HEP.510290103.

[426] M. Shulman and Y. Nahmias, "Long-Term Culture and Coculture of Primary Rat and Human Hepatocytes," *Methods Mol. Biol.*, vol. 945, p. 287, 2013, doi: 10.1007/978-1-62703-125-7_17.

[427] D. G. Levitt and M. D. Levitt, "Human serum albumin homeostasis: a new look at the roles of synthesis, catabolism, renal and gastrointestinal excretion, and the clinical value of serum albumin measurements," *Int. J. Gen. Med.*, vol. 9, pp. 229–255, Jul. 2016, doi: 10.2147/IJGM.S102819.

[428] M. Garcovich, M. A. Zocco, and A. Gasbarrini, "Clinical use of albumin in hepatology," *Blood Transfus.*, vol. 7, no. 4, p. 268, 2009, doi: 10.2450/2008.0080-08.

[429] S. Han, Y. Huang, Z. Li, H. Hou, and A. Wu, "The prognostic role of preoperative serum albumin levels in glioblastoma patients," *BMC Cancer*, vol. 15, no. 1, Mar. 2015, doi: 10.1186/S12885-015-1125-0.

[430] I. Ozaki *et al.*, "Albumin mRNA expression in human liver diseases and its correlation to serum albumin concentration," *Gastroenterol. Jpn.*, vol. 26, no. 4, pp. 472–476, Aug. 1991, doi: 10.1007/BF02782816.

[431] R. Nudischer, K. Renggli, A. Hierlemann, A. B. Roth, and C. Bertinetti-Lapatki, "Characterization of a long-term mouse primary liver 3D tissue model recapitulating innate-immune responses and drug-induced liver toxicity," *PLoS One*, vol. 15, no. 7, Jul. 2020, doi: 10.1371/JOURNAL.PONE.0235745.

[432] "Long-term 3D Culture of Human Primary Hepatocytes in GrowDex® | UPM Biomedicals." https://www.upmbiomedicals.com/resource-center/application-notes/long-term-3d-culture-of-human-primary-hepatocytes-in-growdex/ (accessed Dec. 24, 2021).

[433] C. Terry, A. Dhawan, R. R. Mitry, S. C. Lehec, and R. D. Hughes, "Optimization of the cryopreservation and thawing protocol for human hepatocytes for use in cell transplantation," *Liver Transplant.*, vol. 16, no. 2, pp. 229–237, Feb. 2010, doi: 10.1002/LT.21983.

[434] P. Godoy *et al.*, "Recent advances in 2D and 3D in vitro systems using primary hepatocytes, alternative hepatocyte sources and non-parenchymal liver cells and their use in investigating mechanisms of hepatotoxicity, cell signaling and ADME," *Arch. Toxicol.*, vol. 87, no. 8, p. 1315, Aug. 2013, doi: 10.1007/S00204-013-1078-5.

[435] "A bench guide for drug development applications."

[436] F. Li, S. Parikh, L. Cao, and R. Zuo, “3D Primary Human Hepatocytes (PHH) Spheroids Demonstrate Increased Sensitivity to Drug-induced Liver Injury in Comparison to 2D PHH Monolayer Culture Application Note.”

[437] K. J. Jang *et al.*, “Reproducing human and cross-species drug toxicities using a Liver-Chip,” *Sci. Transl. Med.*, vol. 11, no. 517, p. 5516, Nov. 2019, doi: 10.1126/SCITRANSLMED.AAX5516/SUPPL_FILE/AAX5516_SM.PDF.

[438] “Liver-Chip Predicts Human Toxicity that was Undetected in Animal Studies for Drugs Halted in Clinical Trials | Business Wire.” https://www.businesswire.com/news/home/20191106005813/en/Liver-Chip-Predicts-Human-Toxicity-that-was-Undetected-in-Animal-Studies-for-Drugs-Halted-in-Clinical-Trials (accessed Nov. 16, 2021).

[439] “Protocol for Emulate Organ-Chips: Live Staining of CDFDA Uptake into Bile Canaliculi Live Staining of CDFDA Uptake into Bile Canaliculi EP195 1.0 Protocol Protocol Protocol Protocol,” 2019, Accessed: Nov. 15, 2021. [Online]. Available: https://www.thermofisher.com/order/catalog/product/C369?SID=srch-hj-.

[440] J. A. Kyffin *et al.*, “Characterisation of a functional rat hepatocyte spheroid model,” *Toxicol. Vitr.*, vol. 55, pp. 160–172, Mar. 2019, doi: 10.1016/J.TIV.2018.12.014.

[441] R. J. Thomas *et al.*, “The Effect of Three-Dimensional Co-Culture of Hepatocytes and Hepatic Stellate Cells on Key Hepatocyte Functions in vitro,” *Cells Tissues Organs*, vol. 181, no. 2, pp. 67–79, Mar. 2005, doi: 10.1159/000091096.

[442] A. Damania, E. Jain, and A. Kumar, “Advancements in in vitro hepatic models: Application for drug screening and therapeutics,” *Hepatol. Int.*, vol. 8, no. 1, pp. 23–38, Jan. 2014, doi: 10.1007/S12072-013-9490-8/FIGURES/4.

[443] R. Z. Turncliff, X. Tian, and K. L. R. Brouwer, “Effect of culture conditions on the expression and function of Bsep, Mrp2, and Mdr1a/b in sandwich-cultured rat hepatocytes,” *Biochem. Pharmacol.*, vol. 71, no. 10, pp. 1520–1529, May 2006, doi: 10.1016/J.BCP.2006.02.004.

[444] M. Kiamehr *et al.*, “Dedifferentiation of Primary Hepatocytes is Accompanied with Reorganization of Lipid Metabolism Indicated by Altered Molecular Lipid and miRNA Profiles,” *Int. J. Mol. Sci.*, vol. 20, no. 12, p. 2910, Jun. 2019, doi: 10.3390/IJMS20122910.

[445] S. Rose *et al.*, “Generation of proliferating human adult hepatocytes using optimized 3D culture conditions,” *Sci. Reports 2021 111*, vol. 11, no. 1, pp. 1–16, Jan. 2021, doi: 10.1038/s41598-020-80019-4.

[446] J. Gracia-Sancho, E. Caparrós, A. Fernández-Iglesias, and R. Francés, “Role of liver sinusoidal endothelial cells in liver diseases,” *Nat. Rev. Gastroenterol. Hepatol. 2021 186*, vol. 18, no. 6, pp. 411–431, Feb. 2021, doi: 10.1038/s41575-020-00411-3.

[447] K. Neubauer, A. Ritzel, B. Saile, and G. Ramadori, “Decrease of platelet-endothelial cell adhesion molecule 1-gene-expression in inflammatory cells and in endothelial cells in the rat liver following CCl(4)-administration and in vitro after treatment with TNFalpha,” *Immunol. Lett.*, vol. 74, no. 2, pp. 153–164, Oct. 2000, doi: 10.1016/S0165-2478(00)00203-0.

[448] J. W. Allen and S. N. Bhatia, “Formation of steady-state oxygen gradients in vitro: application to liver zonation,” *Biotechnol. Bioeng.*, vol. 82, no. 3, pp. 253–262, May 2003, doi: 10.1002/BIT.10569.

[449] Y. Xie and W. Xie, “The Role of Sulfotransferases in Liver Diseases,” *Drug Metab. Dispos.*, vol. 48, no. 9, pp. 742–749, Sep. 2020, doi: 10.1124/DMD.120.000074.

[450] C. Rowe *et al.*, “Network analysis of primary hepatocyte dedifferentiation using a shotgun proteomics approach,” *J. Proteome Res.*, vol. 9, no. 5, pp. 2658–2668, May 2010, doi: 10.1021/PR1001687.

[451] S. Chatterjee, L. Richert, P. Augustijns, and P. Annaert, “Hepatocyte-based in vitro model for assessment of drug-induced cholestasis,” *Toxicol. Appl. Pharmacol.*, vol. 274, no. 1, pp. 124–136, Jan. 2014, doi: 10.1016/J.TAAP.2013.10.032.

[452] T. De Bruyn *et al.*, “Sandwich-cultured hepatocytes: utility for in vitro exploration of hepatobiliary drug disposition and drug-induced hepatotoxicity,” *Expert Opin. Drug Metab. Toxicol.*, vol. 9, no. 5, pp. 589–616, May 2013, doi: 10.1517/17425255.2013.773973.

[453] W. R. Proctor *et al.*, “Utility of spherical human liver microtissues for prediction of clinical drug-induced liver injury,” *Arch. Toxicol.*, vol. 91, no. 8, pp. 2849–2863, Aug. 2017, doi: 10.1007/S00204-017-2002-1.

[454] L. Ewart *et al.*, “Application of Microphysiological Systems to Enhance Safety Assessment in Drug Discovery,” *Annu. Rev. Pharmacol. Toxicol.*, vol. 58, pp. 65–82, Jan. 2018, doi: 10.1146/ANNUREV-PHARMTOX-010617-052722.

[455] D. Knobeloch *et al.*, “Human Hepatocytes: Isolation, Culture, and Quality Procedures,” *Methods Mol. Biol.*, vol. 806, pp. 99–120, 2012, doi: 10.1007/978-1-61779-367-7_8.

[456] L. C *et al.*, “Determination of plasma alpha-glutathione S-transferases in patients with HCV-related chronic infection: its significance and possible clinical relevance.,” *Liver*, vol. 18, no. 3, pp. 166–172, Jun. 1998, doi: 10.1111/J.1600-0676.1998.TB00145.X.

[457] K. DJ, Z. M, C. IH, and W. P, “Plasma alpha-glutathione S-transferase: a sensitive indicator of hepatocellular damage during polymicrobial sepsis,” *Arch. Surg.*, vol. 135, no. 2, pp. 198–203, 2000, doi: 10.1001/ARCHSURG.135.2.198.

[458] “Change in alpha glutathione s-transferase levels during liver resection - PubMed.” https://pubmed.ncbi.nlm.nih.gov/15532818/ (accessed Oct. 05, 2021).

[459] “GENE EXPRESSION IN HUMAN HEPATOCYTES IN SUSPENSION AFTER ISOLATION IS SIMILAR TO THE LIVER OF ORIGIN, IS NOT AFFECTED BY HEPATOCYTE COLD STORAGE AND CRYOPRESERVATION, BUT IS STRONGLY CHANGED AFTER HEPATOCYTE PLATING,” vol. 34, no. 5, 3107, doi: 10.1124/dmd.105.007708.

[460] D. Fu, K. Mitra, P. Sengupta, M. Jarnik, J. Lippincott-Schwartz, and I. M. Arias, “Coordinated elevation of mitochondrial oxidative phosphorylation and autophagy help drive hepatocyte polarization,” *Proc. Natl. Acad. Sci. U. S. A.*, vol. 110, no. 18, pp. 7288–7293, Apr. 2013, doi: 10.1073/PNAS.1304285110/-/DCSUPPLEMENTAL.

[461] D. G. Hardie, “AMP-activated protein kinase—an energy sensor that regulates all aspects of cell function,” *Genes Dev.*, vol. 25, no. 18, p. 1895, Sep. 2011, doi: 10.1101/GAD.17420111.

[462] J. Nunnari and A. Suomalainen, “Mitochondria: in sickness and in health,” *Cell*, vol. 148, no. 6, pp. 1145–1159, Mar. 2012, doi: 10.1016/J.CELL.2012.02.035.

[463] “The Citric Acid (Krebs) Cycle | Boundless Microbiology.” https://courses.lumenlearning.com/boundless-microbiology/chapter/the-citric-acid-krebs-cycle/ (accessed Nov. 16, 2021).

[464] E. B. Thorgersen *et al.*, “The Role of Complement in Liver Injury, Regeneration, and Transplantation,” *Hepatology*, vol. 70, no. 2, p. 725, 2019, doi: 10.1002/HEP.30508.

[465] S. Inai, H. Kitamura, and T. Fujita, “Differences between plasma and serum complement in patients with chronic liver disease.,” *Clin. Exp. Immunol.*, vol. 25, no. 3, p. 403, 1976, Accessed: Nov. 16, 2021. [Online]. Available: /pmc/articles/PMC1541414/?report=abstract.

[466] R. Boon *et al.*, “Amino acid levels determine metabolism and CYP450 function of hepatocytes and hepatoma cell lines,” *Nat. Commun. 2020 111*, vol. 11, no. 1, pp. 1–16, Mar. 2020, doi: 10.1038/s41467-020-15058-6.

[467] K. Zeilinger *et al.*, “Scaling down of a clinical three-dimensional perfusion multicompartment hollow fiber liver bioreactor developed for extracorporeal liver support to an analytical scale device useful for hepatic pharmacological in vitro studies,” *Tissue Eng. Part C. Methods*, vol. 17, no. 5, pp. 549–556, May 2011, doi: 10.1089/TEN.TEC.2010.0580.

[468] J. N. van der Veen, J. P. Kennelly, S. Wan, J. E. Vance, D. E. Vance, and R. L. Jacobs, “The critical role of phosphatidylcholine and phosphatidylethanolamine metabolism in health and disease,” *Biochim. Biophys. Acta - Biomembr.*, vol. 1859, no. 9, pp. 1558–1572, Sep. 2017, doi: 10.1016/J.BBAMEM.2017.04.006.

[469] M. Alves-Bezerra and D. E. Cohen, “Triglyceride metabolism in the liver,” *Compr. Physiol.*, vol. 8, no. 1, p. 1, Jan. 2017, doi: 10.1002/CPHY.C170012.

[470] D. W. Russell and K. D. R. Setchell, “Bile acid biosynthesis,” *Biochemistry*, vol. 31, no. 20, pp. 4737–4749, Feb. 1992, doi: 10.1021/BI00135A001.

[471] P. B. Hylemon, H. Zhou, W. M. Pandak, S. Ren, G. Gil, and P. Dent, “Bile acids as regulatory molecules,” *J. Lipid Res.*, vol. 50, no. 8, pp. 1509–1520, Aug. 2009, doi: 10.1194/JLR.R900007-JLR200.

[472] J. P. Jackson, K. M. Freeman, R. L. St Claire, C. B. Black, and K. R. Brouwer, “Cholestatic Drug Induced Liver Injury: A Function of Bile Salt Export Pump Inhibition and Farnesoid X Receptor Antagonism,” *Appl. Vitr. Toxicol.*, vol. 4, no. 3, pp. 265–279, Sep. 2018, doi: 10.1089/AIVT.2018.0011/ASSET/IMAGES/LARGE/FIGURE9.JPEG.

[473] V. Baier *et al.*, “A physiology-based model of human bile acid metabolism for predicting bile acid tissue levels after drug administration in healthy subjects and bric type 2 patients,” *Front. Physiol.*, vol. 10, no. SEP, p. 1192, Sep. 2019, doi: 10.3389/FPHYS.2019.01192/BIBTEX.

[474] S.-Y. Cai and J. L. Boyer, “The role of bile acids in cholestatic liver injury,” *Ann. Transl. Med.*, vol. 9, no. 8, pp. 737–737, Apr. 2021, doi: 10.21037/ATM-20-5110.

[475] T. Roskams, P. Van Eyken, and V. Desmet, “Human liver growth and development,” *Liver Growth and Repair*, pp. 541–557, 1998, doi: 10.1007/978-94-011-4932-7_21.

[476] S. S, S. IS, T. TT, and W. AM, “Activin A-induced differentiation of embryonic stem cells into endoderm and pancreatic progenitors-the influence of differentiation factors and culture conditions,” *Stem cell Rev. reports*, vol. 5, no. 2, pp. 159–173, Jun. 2009, doi: 10.1007/S12015-009-9061-5.

[477] K. A *et al.*, “Development of definitive endoderm from embryonic stem cells in culture,” *Development*, vol. 131, no. 7, pp. 1651–1662, Apr. 2004, doi: 10.1242/DEV.01044.

[478] P. Wang *et al.*, “A Molecular Signature for Purified Definitive Endoderm Guides Differentiation and Isolation of Endoderm from Mouse and Human Embryonic Stem Cells,” *Stem Cells Dev.*, vol. 21, no. 12, p. 2273, Aug. 2012, doi:

10.1089/SCD.2011.0416.

[479] X. Q. Kang *et al.*, “Fibroblast growth factor-4 and hepatocyte growth factor induce differentiation of human umbilical cord blood-derived mesenchymal stem cells into hepatocytes,” *World J. Gastroenterol.*, vol. 11, no. 47, p. 7461, Dec. 2005, doi: 10.3748/WJG.V11.I47.7461.

[480] G. Gómez-Mariano *et al.*, “Liver organoids reproduce alpha-1 antitrypsin deficiency-related liver disease,” *Hepatol. Int. 2019 141*, vol. 14, no. 1, pp. 127–137, Dec. 2019, doi: 10.1007/S12072-019-10007-Y.

[481] S. J. Mun, Y.-H. Hong, H.-S. Ahn, J.-S. Ryu, K.-S. Chung, and M. J. Son, “Long-Term Expansion of Functional Human Pluripotent Stem Cell-Derived Hepatic Organoids,” *Int. J. Stem Cells*, vol. 13, no. 2, pp. 279–286, Jul. 2020, doi: 10.15283/IJSC20060.

[482] H.-Y. Oh *et al.*, “Dexamethasone protects primary cultured hepatocytes from death receptor-mediated apoptosis by upregulation of cFLIP,” *Cell Death Differ. 2006 133*, vol. 13, no. 3, pp. 512–523, Sep. 2005, doi: 10.1038/sj.cdd.4401771.

[483] G. K. Michalopoulos, W. C. Bowen, K. Mulè, and J. Luo, “HGF-, EGF-, and Dexamethasone-Induced Gene Expression Patterns During Formation of Tissue in Hepatic Organoid Cultures,” *Gene Expr.*, vol. 11, no. 2, p. 55, 2003, doi: 10.3727/000000003108748964.

[484] M. R. Alison and W. R. Lin, “Regenerating the liver: not so simple after all?,” *F1000Research*, vol. 5, 2016, doi: 10.12688/F1000RESEARCH.8827.1.

[485] K. E. Moriles and S. A. Azer, “Alanine Amino Transferase,” *StatPearls*, May 2021, Accessed: Dec. 27, 2021. [Online]. Available: https://www.ncbi.nlm.nih.gov/books/NBK559278/.

[486] V. Lala, A. Goyal, P. Bansal, and D. A. Minter, “Liver Function Tests,” *StatPearls*, Aug. 2021, Accessed: Dec. 27, 2021. [Online]. Available: https://www.ncbi.nlm.nih.gov/books/NBK482489/.

[487] J. Zheng *et al.*, “Metformin and metabolic diseases: a focus on hepatic aspects,” doi: 10.1007/s11684-015-0384-0.

[488] L. C. de la Rosa, T. E. Vrenken, M. Buist-Homan, K. N. Faber, and H. Moshage, “Metformin protects primary rat hepatocytes against oxidative stress-induced apoptosis,” *Pharmacol. Res. Perspect.*, vol. 3, no. 2, pp. 1–12, Mar. 2015, doi: 10.1002/PRP2.125.

[489] X. Wang, S. Ge, G. McNamara, Q. L. Hao, G. M. Crooks, and J. A. Nolta, “Albumin-expressing hepatocyte-like cells develop in the livers of immune-deficient mice that received transplants of highly purified human hematopoietic stem cells,” *Blood*, vol. 101, no. 10, pp. 4201–4208, May 2003, doi: 10.1182/BLOOD-2002-05-1338.

[490] K. Sa-ngiamsuntorn *et al.*, “Upregulation of CYP 450s expression of immortalized hepatocyte-like cells derived from mesenchymal stem cells by enzyme inducers,” *BMC Biotechnol. 2011 111*, vol. 11, no. 1, pp. 1–15, Sep. 2011, doi: 10.1186/1472-6750-11-89.

[491] “Overview - Liver Organoids - Organoids - Areas of Interest - Scientific Resources.” https://www.stemcell.com/technical-resources/area-of-interest/organoid-research/hepatic-research/overview.html (accessed Dec. 27, 2021).

[492] K. L *et al.*, “Metformin suppresses pregnane X receptor (PXR)-regulated transactivation of CYP3A4 gene,” *Biochem. Pharmacol.*, vol. 82, no. 11, pp. 1771–1780, Dec. 2011, doi: 10.1016/J.BCP.2011.08.023.

[493] W. Chatuphonprasert, N. Nemoto, T. Sakuma, and K. Jarukamjorn, “Modulations of cytochrome P450 expression in diabetic mice by berberine,” *Chem. Biol. Interact.*, vol. 196, no. 1–2, pp. 23–29, Mar. 2012, doi: 10.1016/J.CBI.2012.01.006.

[494] K. F, W. C, D. M, and O. S, “Drug-Drug Interactions Involving Intestinal and Hepatic CYP1A Enzymes,” *Pharmaceutics*, vol. 12, no. 12, pp. 1–25, Dec. 2020, doi: 10.3390/PHARMACEUTICS12121201.

[495] W. L. Casley, J. A. Menzies, N. Mousseau, M. Girard, T. W. Moon, and L. W. Whitehouse, “Increased basal expression of hepatic Cyp1a1 and Cyp1a2 genes in inbred mice selected for susceptibility to acetaminophen-induced hepatotoxicity,” *Pharmacogenetics*, vol. 7, no. 4, pp. 283–293, 1997, doi: 10.1097/00008571-199708000-00003.

[496] S. Markova *et al.*, “Association of CYP2C9*2 With Bosentan-Induced Liver Injury,” 2013, doi: 10.1038/clpt.2013.143.

[497] N. R. Srinivas, “Clinical drug-drug interactions of bosentan, a potent endothelial receptor antagonist, with various drugs: Physiological role of enzymes and transporters,” *Gen. Physiol. Biophys.*, vol. 35, no. 3, pp. 243–258, Jan. 2016, doi: 10.4149/GPB_2015050.

[498] J. L. Woodhead *et al.*, “Exploring BSEP inhibition-mediated toxicity with a mechanistic model of drug-induced liver injury,” *Front. Pharmacol.*, vol. 5, no. NOV, 2014, doi: 10.3389/FPHAR.2014.00240.

[499] S. Thakral and K. Ghoshal, “miR-122 is a Unique Molecule with Great Potential in Diagnosis, Prognosis of Liver Disease, and Therapy Both as miRNA Mimic and Antimir,” *Curr. Gene Ther.*, vol. 15, no. 2, p. 142, Mar. 2015, doi: 10.2174/1566523214666141224095610.

[500] R. Doddapaneni, Y. K. Chawla, A. Das, J. K. Kalra, S. Ghosh, and A. Chakraborti, “Overexpression of microRNA-122

enhances in vitro hepatic differentiation of fetal liver-derived stem/progenitor cells," *J. Cell. Biochem.*, vol. 114, no. 7, pp. 1575–1583, Jul. 2013, doi: 10.1002/JCB.24499.

[501] L. S. Howell, L. Ireland, B. K. Park, and C. E. Goldring, "MiR-122 and other microRNAs as potential circulating biomarkers of drug-induced liver injury," *https://doi.org/10.1080/14737159.2018.1415145*, vol. 18, no. 1, pp. 47–54, Jan. 2017, doi: 10.1080/14737159.2018.1415145.

[502] X. Gao, R. Li, P. Cahan, Y. Zhao, J. J. Yourick, and R. L. Sprando, "Hepatocyte-like cells derived from human induced pluripotent stem cells using small molecules: Implications of a transcriptomic study," *Stem Cell Res. Ther.*, vol. 11, no. 1, pp. 1–21, Sep. 2020, doi: 10.1186/S13287-020-01914-1/FIGURES/9.

[503] K. Irani, I. Pomerantseva, A. R. Hart, C. A. Sundback, C. M. Neville, and J. P. Vacanti, "Mechanical dissociation of swine liver to produce organoid units for tissue engineering and in vitro disease modeling," *Artif. Organs*, vol. 34, no. 1, pp. 75–78, 2010, doi: 10.1111/J.1525-1594.2009.00784.X.

[504] E. G *et al.*, "Molecular mechanisms underlying the dedifferentiation process of isolated hepatocytes and their cultures," *Curr. Drug Metab.*, vol. 7, no. 6, pp. 629–660, Aug. 2006, doi: 10.2174/138920006778017759.

[505] N. R. F. Hannan, C. P. Segeritz, T. Touboul, and L. Vallier, "Production of hepatocyte like cells from human pluripotent stem cells," *Nat. Protoc.*, vol. 8, no. 2, p. 430, Feb. 2013, doi: 10.1038/NPROT.2012.153.

[506] Y. Guan *et al.*, "Human hepatic organoids for the analysis of human genetic diseases," *JCI insight*, vol. 2, no. 17, Sep. 2017, doi: 10.1172/JCI.INSIGHT.94954.

[507] S. I. Shedlofsky, B. C. Israel, C. J. McClain, D. B. Hill, and R. A. Blouin, "Endotoxin administration to humans inhibits hepatic cytochrome P450-mediated drug metabolism," *J. Clin. Invest.*, vol. 94, no. 6, pp. 2209–2214, 1994, doi: 10.1172/JCI117582.

[508] G. A. Keller, M. A. West, L. A. Wilkes, F. B. Cerra, and R. L. Simmons, "Modulation of hepatocyte protein synthesis by endotoxin-activated Kupffer cells. II. Mediation by soluble transferrable factors," *Ann. Surg.*, vol. 201, no. 4, pp. 429–435, 1985, doi: 10.1097/00000658-198504000-00005.

[509] C. R. Cox, S. Lynch, C. Goldring, and P. Sharma, "Current Perspective: 3D Spheroid Models Utilizing Human-Based Cells for Investigating Metabolism-Dependent Drug-Induced Liver Injury," *Front. Med. Technol.*, vol. 0, p. 14, Nov. 2020, doi: 10.3389/FMEDT.2020.611913.

[510] M. Amouzandeh, G. Nowak, A. Januszkiewicz, J. Wernerman, O. Rooyackers, and A. Norberg, "Albumin mass balance and kinetics in liver transplantation," *Crit. Care*, vol. 22, no. 1, pp. 1–10, Jun. 2018, doi: 10.1186/S13054-018-2053-6/FIGURES/4.

[511] P. Van Brantegem, S. Chatterjee, T. De Bruyn, P. Annaert, and N. Deferm, "Drug-induced cholestasis assay in primary hepatocytes," *MethodsX*, vol. 7, p. 101080, Jan. 2020, doi: 10.1016/J.MEX.2020.101080.

[512] F. Li, L. Cao, S. Parikh, and R. Zuo, "Three-Dimensional Spheroids With Primary Human Liver Cells and Differential Roles of Kupffer Cells in Drug-Induced Liver Injury," *J. Pharm. Sci.*, vol. 109, no. 6, pp. 1912–1923, Jun. 2020, doi: 10.1016/J.XPHS.2020.02.021.

[513] M. Schloss, D. Becak, S. T. Tosto, and A. Velayati, "A Case of Levofloxacin-Induced Hepatotoxicity," *Am. J. Case Rep.*, vol. 19, p. 272, Mar. 2018, doi: 10.12659/AJCR.907440.

[514] I. Grattagliano, L. Bonfrate, C. V. Diogo, H. H. Wang, D. Q. H. Wang, and P. Portincasa, "Biochemical mechanisms in drug-induced liver injury: Certainties and doubts," *World J. Gastroenterol.*, vol. 15, no. 39, p. 4865, 2009, doi: 10.3748/WJG.15.4865.

[515] O. A. Diab, J. Kamel, and A. A. Abd-Elhamid, "Predictors of intravenous amiodarone induced liver injury," *Egypt. Hear. J.*, vol. 69, no. 1, pp. 45–54, Mar. 2017, doi: 10.1016/J.EHJ.2016.05.001.

[516] G. A. Mannes, F. Slellaard, and G. Paumgartner, "Increased Serum Bile Acids in Cirrhosis with Normal Transaminases," *Digestion*, vol. 25, no. 4, pp. 217–221, 1982, doi: 10.1159/000198835.

[517] R. D. Soloway *et al.*, "Clinical, biochemical, and histological remission of severe chronic active liver disease: a controlled study of treatments and early prognosis.," *Gastroenterology*, vol. 63, no. 5, pp. 820–833, 1972, doi: 10.1016/S0016-5085(19)33223-8.

[518] C. Hiley, A. Fryer, J. Bell, R. Hume, and R. C. Strange, "The human glutathione S-transferases. Immunohistochemical studies of the developmental expression of Alpha- and Pi-class isoenzymes in liver.," *Biochem. J.*, vol. 254, no. 1, p. 255, 1988, doi: 10.1042/BJ2540255.

[519] G. Tang *et al.*, "Comparing distress of mouse models for liver damage," *Sci. Reports 2020 101*, vol. 10, no. 1, pp. 1–12, Nov. 2020, doi: 10.1038/s41598-020-76391-w.

[520] S. J. N. B Cuccherini, "Stability of aspartate aminotransferase and alanine aminotransferase activities - PubMed," *J Lab*

Clin Med., 1983, Accessed: Dec. 23, 2021. [Online]. Available: https://pubmed.ncbi.nlm.nih.gov/6886521/.

[521] A. E. Williams, L. M. Kline, and R. Y. Dodd, “Stability of serum alanine aminotransferase activity,” *Transfusion*, vol. 27, no. 5, pp. 431–433, 1987, doi: 10.1046/J.1537-2995.1987.27587320539.X.

[522] T. Riss, A. Niles, R. Moravec, N. Karassina, and J. Vidugiriene, “Cytotoxicity Assays: In Vitro Methods to Measure Dead Cells,” *Assay Guid. Man.*, May 2019, Accessed: Nov. 22, 2021. [Online]. Available: https://www.ncbi.nlm.nih.gov/sites/books/NBK540958/.

[523] E. Yoon, A. Babar, M. Choudhary, M. Kutner, and N. Pyrsopoulos, “Acetaminophen-Induced Hepatotoxicity: a Comprehensive Update,” *J. Clin. Transl. Hepatol.*, vol. 4, no. 2, p. 131, 2016, doi: 10.14218/JCTH.2015.00052.

[524] R. M. W. Hofstra, “Biomarker and Therapeutic Potential of CSF1 in Acute Liver Failure,” 2015, doi: 10.1053/j.gastro.2015.10.023.

[525] E. S. Harris and W. J. Nelson, “VE-cadherin: At the front, center, and sides of endothelial cell organization and function,” *Curr. Opin. Cell Biol.*, vol. 22, no. 5, pp. 651–658, Oct. 2010, doi: 10.1016/J.CEB.2010.07.006.

[526] L. Faletti *et al.*, “TNFα sensitizes hepatocytes to FasL-induced apoptosis by NFκB-mediated Fas upregulation,” *Cell Death Dis. 2018 99*, vol. 9, no. 9, pp. 1–14, Sep. 2018, doi: 10.1038/s41419-018-0935-9.

[527] L. Li and Z. Zeng, “Live Imaging of Innate and Adaptive Immune Responses in the Liver,” *Front. Immunol.*, vol. 11, p. 2210, Sep. 2020, doi: 10.3389/FIMMU.2020.564768/BIBTEX.

[528] C. Weber, “Liver: Macrophage-stimulating CSF1 is important in liver injury,” *Nat. Publ. Gr.*, 2015, doi: 10.1038/nrgastro.2015.167.

[529] J. J. O’Shea, M. Gadina, and R. M. Siegel, “Cytokines and Cytokine Receptors,” *Clin. Immunol.*, pp. 127-155.e1, Jan. 2019, doi: 10.1016/B978-0-7020-6896-6.00009-0.

[530] J. Bonnardel *et al.*, “Stellate Cells, Hepatocytes, and Endothelial Cells Imprint the Kupffer Cell Identity on Monocytes Colonizing the Liver Macrophage Niche,” *Immunity*, vol. 51, no. 4, pp. 638-654.e9, Oct. 2019, doi: 10.1016/J.IMMUNI.2019.08.017.

[531] C. RJ *et al.*, “Candidate biomarkers for the diagnosis and prognosis of drug-induced liver injury: An international collaborative effort,” *Hepatology*, vol. 69, no. 2, pp. 760–773, Feb. 2019, doi: 10.1002/HEP.29802.

[532] X. Wang *et al.*, “Osteopontin induces ductular reaction contributing to liver fibrosis,” *Gut*, vol. 63, no. 11, pp. 1805–1818, Nov. 2014, doi: 10.1136/GUTJNL-2013-306373.

[533] A. Göthlin Eremo, K. Lagergren, L. Othman, S. Montgomery, G. Andersson, and E. Tina, “Evaluation of SPP1/osteopontin expression as predictor of recurrence in tamoxifen treated breast cancer,” *Sci. Reports 2020 101*, vol. 10, no. 1, pp. 1–9, Jan. 2020, doi: 10.1038/s41598-020-58323-w.

[534] S. Patouraux *et al.*, “Osteopontin deficiency aggravates hepatic injury induced by ischemia–reperfusion in mice,” *Cell Death Dis. 2014 55*, vol. 5, no. 5, pp. e1208–e1208, May 2014, doi: 10.1038/cddis.2014.174.

[535] J. Lea, “Mechanistic regulation of HMGB1 function in drug-induced liver injury,” Accessed: Nov. 23, 2021. [Online]. Available: http://livrepository.liverpool.ac.uk/2010080.

[536] B. Sun, S. Ying, Q. Ma, H. Li, J. Li, and J. Song, “Metformin ameliorates HMGB1-mediated oxidative stress through mTOR pathway in experimental periodontitis,” *Genes Dis.*, Jun. 2021, doi: 10.1016/J.GENDIS.2021.06.003.

[537] T. Horiuchi *et al.*, “Metformin directly binds the alarmin HMGB1 and inhibits its proinflammatory activity,” *J. Biol. Chem.*, vol. 292, no. 20, p. 8436, May 2017, doi: 10.1074/JBC.M116.769380.

[538] R. Chen, W. Hou, Q. Zhang, R. Kang, X. G. Fan, and D. Tang, “Emerging Role of High-Mobility Group Box 1 (HMGB1) in Liver Diseases,” *Mol. Med.*, vol. 19, no. 1, p. 357, 2013, doi: 10.2119/MOLMED.2013.00099.

[539] S. Tajima, N. Yamamoto, and S. Masuda, “Clinical prospects of biomarkers for the early detection and/or prediction of organ injury associated with pharmacotherapy,” *Biochem. Pharmacol.*, vol. 170, Dec. 2019, doi: 10.1016/J.BCP.2019.113664.

[540] P. Strnad *et al.*, “Keratin Mutation Predisposes to Mouse Liver Fibrosis and Unmasks Differential Effects of the Carbon Tetrachloride and Thioacetamide Models,” *Gastroenterology*, vol. 134, no. 4, pp. 1169–1179, Apr. 2008, doi: 10.1053/J.GASTRO.2008.01.035/ATTACHMENT/AC545ABD-5DC2-4081-935E-3B2A095B6E88/MMC1.PDF.

[541] K. Bettermann *et al.*, “Keratin 18-deficiency results in steatohepatitis and liver tumors in old mice: A model of steatohepatitis-associated liver carcinogenesis,” *Oncotarget*, vol. 7, no. 45, p. 73309, 2016, doi: 10.18632/ONCOTARGET.12325.

[542] N. O. Ku and M. B. Omary, “A disease- and phosphorylation-related nonmechanical function for keratin 8,” *J. Cell Biol.*, vol. 174, no. 1, p. 115, Jul. 2006, doi: 10.1083/JCB.200602146.

[543] S. Korver *et al.*, “The application of cytokeratin-18 as a biomarker for drug-induced liver injury,” *Arch. Toxicol.*, vol. 95,

no. 11, pp. 3435–3448, Nov. 2021, doi: 10.1007/S00204-021-03121-0/FIGURES/2.

[544] R. J. Church and P. B. Watkins, “The transformation in biomarker detection and management of drug-induced liver injury,” *Liver Int.*, vol. 37, no. 11, pp. 1582–1590, Nov. 2017, doi: 10.1111/LIV.13441.

[545] J. Rutter, D. R. Winge, and J. D. Schiffman, “Succinate Dehydrogenase—Assembly, Regulation and Role in Human Disease,” *Mitochondrion*, vol. 10, no. 4, p. 393, Jun. 2010, doi: 10.1016/J.MITO.2010.03.001.

[546] Y. H. Li, D. H. Choi, E. H. Lee, S. R. Seo, S. Lee, and E. H. Cho, “Sirtuin 3 (SIRT3) Regulates oα-Smooth Muscle Actin (oα-SMA) Production through the Succinate Dehydrogenase-G Protein-coupled Receptor 91 (GPR91) Pathway in Hepatic Stellate Cells,” *J. Biol. Chem.*, vol. 291, no. 19, pp. 10277–10292, May 2016, doi: 10.1074/JBC.M115.692244.

[547] G. G. Martin, B. P. Atshaves, A. L. McIntosh, J. T. Mackie, A. B. Kier, and F. Schroeder, “Liver fatty-acid-binding protein (L-FABP) gene ablation alters liver bile acid metabolism in male mice,” *Biochem. J.*, vol. 391, no. Pt 3, p. 549, Nov. 2005, doi: 10.1042/BJ20050296.

[548] N. H. Haunerland and F. Spener, “Fatty acid-binding proteins--insights from genetic manipulations,” *Prog. Lipid Res.*, vol. 43, no. 4, pp. 328–349, Jul. 2004, doi: 10.1016/J.PLIPRES.2004.05.001.

[549] Y. Kawano and D. E. Cohen, “Mechanisms of hepatic triglyceride accumulation in non-alcoholic fatty liver disease,” *J. Gastroenterol.*, vol. 48, no. 4, pp. 434–441, Apr. 2013, doi: 10.1007/S00535-013-0758-5.

[550] E. P. Newberry, S. M. Kennedy, Y. Xie, B. T. Sternard, J. Luo, and N. O. Davidson, “Diet-induced obesity and hepatic steatosis in L-Fabp / mice is abrogated with SF, but not PUFA, feeding and attenuated after cholesterol supplementation,” *Am. J. Physiol. Gastrointest. Liver Physiol.*, vol. 294, no. 1, 2008, doi: 10.1152/AJPGI.00377.2007.

[551] E. S. Schmidt and F. W. Schmidt, “Glutamate dehydrogenase: biochemical and clinical aspects of an interesting enzyme,” *Clin. Chim. Acta.*, vol. 173, no. 1, pp. 43–55, Mar. 1988, doi: 10.1016/0009-8981(88)90356-7.

[552] P. Thulin *et al.*, “A longitudinal assessment of miR-122 and GLDH as biomarkers of drug-induced liver injury in the rat,” *Biomarkers*, vol. 22, no. 5, pp. 461–469, Jul. 2017, doi: 10.1080/1354750X.2016.1269131.

[553] R. Li *et al.*, “Glutathione S-transferase A1 (GSTA1) as a marker of acetaminophen-induced hepatocyte injury in vitro,” *http://dx.doi.org/10.1080/15376516.2017.1320457*, vol. 27, no. 6, pp. 401–407, Jul. 2017, doi: 10.1080/15376516.2017.1320457.

[554] X. Ma *et al.*, “Expression of glutathione S-transferase A1, a phase II drug-metabolizing enzyme in acute hepatic injury on mice,” *Exp. Ther. Med.*, vol. 14, no. 4, p. 3798, Oct. 2017, doi: 10.3892/ETM.2017.4957.

[555] P. B. Udesen *et al.*, “Metformin decreases miR-122, miR-223 and miR-29a in women with polycystic ovary syndrome,” *Endocr. Connect.*, vol. 9, no. 11, p. 1075, Dec. 2020, doi: 10.1530/EC-20-0195.

[556] S. Bandiera, S. Pfeffer, T. F. Baumert, and M. B. Zeisel, “miR-122 – A key factor and therapeutic target in liver disease,” *J. Hepatol.*, vol. 62, no. 2, pp. 448–457, Feb. 2015, doi: 10.1016/J.JHEP.2014.10.004.

[557] H. L. A. Janssen *et al.*, “Treatment of HCV Infection by Targeting MicroRNA,” *N. Engl. J. Med.*, vol. 368, no. 18, pp. 1685–1694, May 2013, doi: 10.1056/NEJMOA1209026/SUPPL_FILE/NEJMOA1209026_DISCLOSURES.PDF.

[558] H. Xu *et al.*, “MicroRNA-122 supports robust innate immunity in hepatocytes by targeting the RTKs/STAT3 signaling pathway,” *Elife*, vol. 8, Feb. 2019, doi: 10.7554/ELIFE.41159.

[559] Y. B. A. Kang, J. Eo, S. Mert, M. L. Yarmush, and O. B. Usta, “Metabolic Patterning on a Chip: Towards in vitro Liver Zonation of Primary Rat and Human Hepatocytes,” *Sci. Rep.*, vol. 8, no. 1, Dec. 2018, doi: 10.1038/S41598-018-27179-6.

[560] K. M. Bircsak *et al.*, “A 3D microfluidic liver model for high throughput compound toxicity screening in the OrganoPlate®,” *Toxicology*, vol. 450, p. 152667, Feb. 2021, doi: 10.1016/J.TOX.2020.152667.

[561] “Our Technology.” https://www.mimetas.com/en/our-technology/ (accessed Dec. 28, 2021).

[562] C. Lohasz, F. Bonanini, L. Hoelting, K. Renggli, O. Frey, and A. Hierlemann, “Predicting Metabolism-Related Drug–Drug Interactions Using a Microphysiological Multitissue System,” *Adv. Biosyst.*, vol. 4, no. 11, Nov. 2020, doi: 10.1002/ADBI.202000079.

[563] C. Prakash *et al.*, “Nuclear Receptors in Drug Metabolism, Drug Response and Drug Interactions,” *Nucl. Recept. Res.*, vol. 2, p. 20, 2015, doi: 10.11131/2015/101178.

[564] “Abundance of cytochromes P450 in human liver: a meta-analysis – ScienceOpen.” https://www.scienceopen.com/document?vid=cf806feb-3484-4762-9882-3fea1fd910f7 (accessed Nov. 11, 2021).

8 Appendix

8.1 PHH donor differences

Appendix Table 1: Background-corrected expression of liver specific genes in PHH donors.
(Figure 25)

Gene	AKB	HU1951	HU8148	HUM4235
CYP1A2	2.30	7.50	0.30	1.50
CYP2C19	1.10	6.20	1.80	4.50
CYP2C9	28.80	38.40	11.10	44.00
CYP2D6	15.30	15.20	17.30	15.30
CYP3A4	0.30	3.30	0.00	1.40
SULT1A1	2.80	5.50	2.70	3.70
SULT1E1	0.20	0.60	0.10	4.70
UGT1A6	1.40	1.10	1.10	1.40
UGT2B7	9.00	26.20	7.00	15.90
ABCB1	0.20	0.40	0.10	0.40
ABCB11	3.70	3.20	2.80	4.20
ABCC1	0.00	0.00	0.00	0.00
ABCC2	6.60	4.60	6.90	10.40
ALB	238.50	280.70	535.20	176.60

Appendix Table 2: Levels of secreted proteins in PHH donors.
(Figure 26)

Protein	Day	AKB	HU9151	HU8148
LDH [% to control]	D2	52.58	79.36	52.58
	D7	19.55	35.05	20.06
	D14	19.31	6.70	6.59
Albumin [µg/1x10^6 cells/day]	D2	44.25	47.83	47.35
	D7	44.88	47.35	47.01
	D14	36.19	47.75	47.48
AST Activity [nmol/mL]	D2	37.33	49.37	46.48
	D7	34.88	40.69	32.16
	D14	32.10	32.93	35.25
ALT Activity [nmol/mL]	D2	21.04	20.48	22.50
	D7	20.70	16.26	16.15
	D14	16.26	15.82	18.25

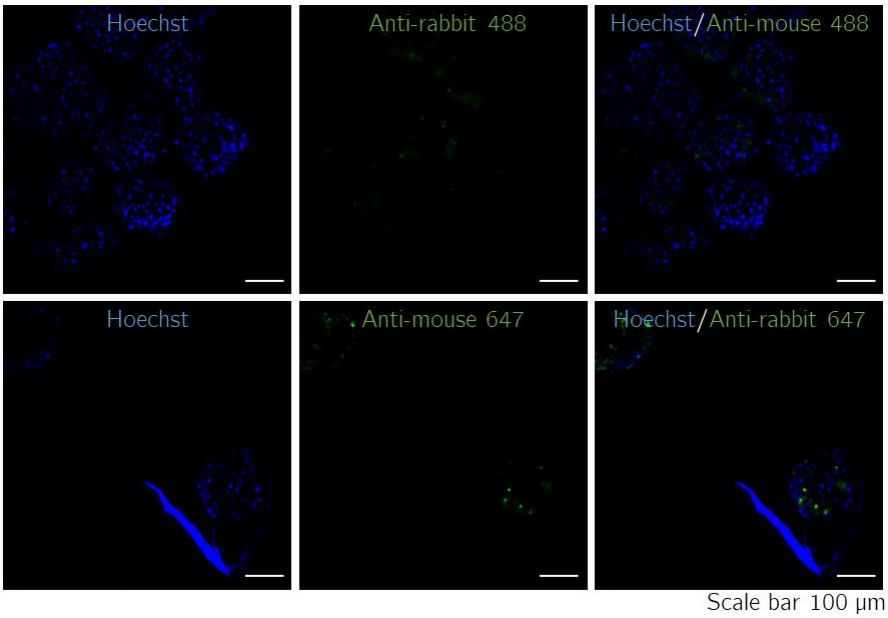

Figure 62: Investigation of non-specific binding in immunofluorescence staining.
3D PHH spheroids (AKB) were fixed, permeabilized, and stained with used secondary antibodies anti-rabbit 488 (ABCAAB, Abcam) and anti-mouse 647 (ab150115, Abcam). Nuclei were stained with Hoechst 33342.

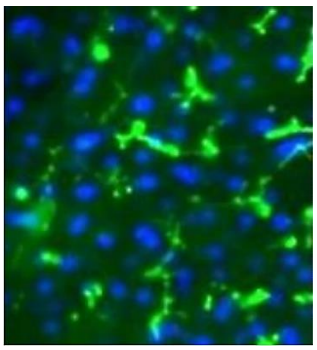

Figure 63: Visualized bile canaliculi structures in the top channel of the Emulate liver-chip.
The fluorescence image was taken by Emulate and can be found in the CDFDA protocol and in the publication of Jang et al. [439][437].

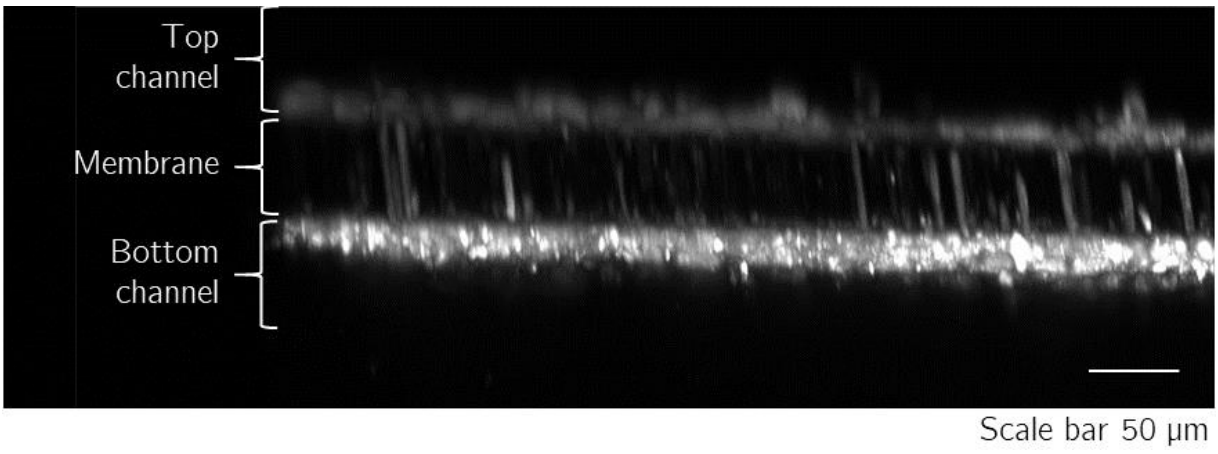

Figure 64: Longitudinal microscopical image across the Emulate OOC.
Imaging was performed with a special confocal microscope at Microsystems CMS in Mannheim.

8.2 Microscopical documentation of EB-formation

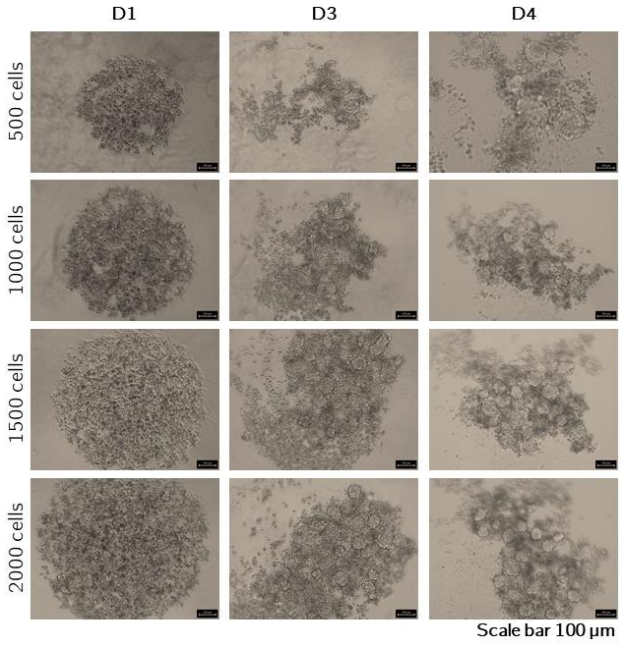

Figure 65: Formation of embryoid bodies in ULA U-bottom plates.
IPSCs were seeded in a defined cell number into a 96 well U-bottom plate. Spheroid formation was observed daily and documented at days 1, 3, and 4.

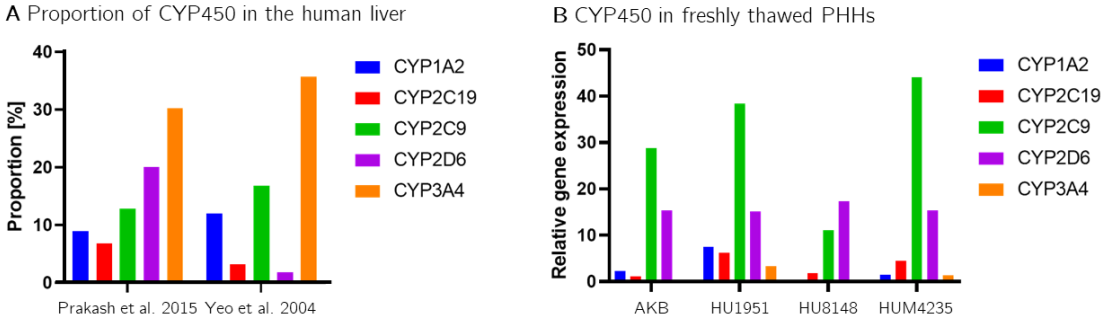

Figure 66: Proportion and relative gene expression of CYP450 enzymes.
(A) Proportion of CYP450 enzymes in human liver described in two publications (Prakash et al. 2015 [563] and Yeo et al. 2004 [564]. **(B)** Relative gene expression of four freshly thawed PHH donors AKB, HU1951, HU8148, and HUM4235 (Figure 25).

8.3 Gene expression and secretion of liver organoids

Appendix Table 3: Response of liver organoids to treatment.
(Figure 33 and Figure 34)

	DMSO	Untreated	MET 750 µM	BOS 30 µM	RIF 25 µM	APAP 100 µM
LDH [mU/mL]	100.0	100.00	126.00	382.00	72.00	261.00
Albumin [FC to control]	1.0	1.00	0.60	0.80	0.60	1.00
CYP3A4 [FC to control]	1.0	1.00	0.40	1.40	0.10	0.00
CYP1A1 [FC to control]	1.0	1.00	8.70	0.60	3.20	7.70
mir122 [FC to control]	1.0	1.00	0.83	1.35	1.48	2.64

Appendix Table 4: Background-corrected gene expression during differentiation of liver organoids.

(Figure 31 and Figure 34)

Gene	Method	iPSC	D0	D5	D10	D15	D20
NANOG	Method 1	1.40	1.00	0.40	0.40	0.20	0.00
	Method 2	1.40	1.00	0.40	0.40	0.20	0.00
	Method 3	1.40	1.50	0.00	0.20	0.00	0.00
FOXA2	Method 1	0.00	ND	0.60	0.40	0.30	0.20
	Method 2	0.00	ND	0.70	1.00	0.00	0.00
	Method 3	0.00	ND	0.00	0.80	0.40	0.10
SOX17	Method 1	0.00	0.70	0.30	ND	0.50	0.00
	Method 2	0.00	3.10	0.30	ND	1.40	1.60
	Method 3	0.00	0.00	0.90	ND	0.20	0.00
AFP	Method 1	0.00	0.00	0.00	8.50	5.20	23.70
	Method 2	0.00	0.00	0.00	6.80	8.70	3.90
	Method 3	0.00	0.00	0.00	15.70	17.50	57.70
ALB	Method 1	0.00	0.00	0.00	0.10	2.10	23.20
	Method 2	0.00	0.00	0.00	0.60	1.60	0.00
	Method 3	0.00	0.00	0.00	0.30	11.90	41.40
CK7	Method 1	0.00	0.10	0.10	1.50	3.50	0.50
	Method 2	0.00	0.00	0.00	0.80	3.60	8.20
	Method 3	0.00	0.10	0.10	1.40	3.60	11.00
CK19	Method 1	0.40	0.80	3.50	7.20	4.30	1.90
	Method 2	0.40	0.00	1.90	6.00	5.40	4.30
	Method 3	0.40	0.00	0.50	3.40	10.30	6.90
ACTA2	Method 1	0.10	0.00	0.00	0.10	0.50	1.80
	Method 2	0.10	0.00	0.10	0.10	1.00	2.10
	Method 3	0.10	0.00	0.00	0.10	0.50	17.50
mir122	Method 3	0.00	0.00	0.00	19469.50	57502.50	2405.50

Appendix Table 5: Levels of secreted proteins measured during liver organoid differentiation.

(Figure 32)

Protein	D5	D10	D15	D20	D25
Albumin [ng/mL/day]	0.00	0.00	0.00	593.30	23.20
αGST [ng/mL/day]	0.00	0.00	103.00	103.00	0.00
ALT [nmol/mL/day]	0.00	0.00	0.00	0.00	2.85
AST [nmol/mL/day]	0.00	3.30	27.92	25.02	24.67

8.4 Expression of liver specific markers in the 2.5D, 3D, and OOC model

Appendix Table 6: Gene expression of liver cell specific markers after thawing and 14 days cultivation.
(Figure 37 and Figure 39)

Gene	OOC			3D			2.5D			from vial
ALB	2.0	1.0	2.8	23.0	22.8	ND	4.6	8.4	ND	4.2
ICAM1	2.6	2.6	ND	0.0	0.0	0.0	0.6	1.4	ND	ND
PECAM1	0.3	0.2	0.3	1.2	ND	ND	1.8	2.0	ND	ND
CD68	2.4	4.6	3.6	0.6	2.2	2.0	1.6	3.0	1.2	ND
ACTA2	2.3	10.4	2.5	0.4	0.5	0.1	0.6	0.4	ND	ND
CYP1A1	0.6	1.0	0.9	3.4	3.8	ND	0.2	ND	0.2	0.0
CYP1A2	2.3	1.6	ND	0.0	ND	0.0	0.0	ND	0.0	0.0
CYP2B6	0.2	0.1	0.2	0.1	0.5	0.0	0.0	0.1	0.0	0.1
CYP2C19	0.1	0.2	0.1	0.0	0.1	0.1	0.3	0.1	0.1	0.1
CYP2C9	0.2	0.1	0.3	0.4	ND	0.5	0.6	1.0	0.5	1.1
CYP2D6	2.6	3.2	2.5	0.1	ND	0.0	0.0	0.4	0.1	0.4
CYP3A4	0.4	0.1	0.3	0.0	0.0	0.0	0.0	0.0	0.0	0.0
AHR	1.5	2.8	1.5	ND	0.9	2.1	2.0	1.0	0.9	0.0
SULT1A1	1.4	1.5	1.0	0.4	1.4	0.3	0.7	1.5	0.6	0.1
SULT1E1	0.8	0.6	0.4	0.0	0.2	0.0	0.1	0.2	0.0	0.1
UGT1A6	2.2	2.2	2.2	2.3	1.7	2.8	1.6	2.8	1.0	0.0
UGT2B7	2.8	ND	2.4	1.1	ND	2.6	0.9	3.6	1.1	0.4
ABCB1	0.6	1.4	0.8	0.5	0.9	0.5	0.9	0.8	0.8	0.0
ABCB11	0.6	0.5	0.4	0.0	0.1	0.0	0.1	0.0	0.0	0.1
ABCC1	0.5	0.5	0.3	0.1	0.3	0.5	0.3	0.4	0.3	0.0
ABCC2	3.1	5.0	3.1	1.2	3.4	0.8	0.8	ND	0.8	0.2

Appendix Table 7: Statistical investigation of liver cell specific markers.

P-values describe statistically different expressed genes across the systems. (Figure 38 and Figure 40)

Gene	2.5D vs. 3D	2.5D vs. OOC	3D vs. OOC	Gene	2.5D vs. 3D	2.5D vs. OOC	3D vs. OOC
CYP3A4	0.245	0.007	0.065	**ABCB11**	0.996	0.001	0.398
CYP2D6	0.072	0.005	0.779	**ABCB1**	0.833	0.994	0.822
CYP2C9	0.179	0.418	0.271	**PPARG**	0.231	0.265	0.435
CYP2C19	0.127	0.247	0.031	**AHR**	0.082	0.418	0.057
CYP2B6	0.018	0.001	0.346	**PECAM1**	0.173	0.401	0.050
CYP1A2	0.238	0.028	0.660	**ICAM1**	0.142	0.878	0.154
CYP1A1	0.005	0.038	0.018	**FCGRT**	0.523	0.262	0.218
UGT2B7	0.264	0.339	0.561	**FCGR2B**	0.485	0.538	0.997
UGT1A6	0.564	0.425	0.912	**ALB**	0.216	0.189	0.037
SULT1E1	0.173	0.050	0.030	**NTRK3**	0.477	0.094	0.337
GSTA1	0.853	0.112	0.779	**NR1I3**	0.946	0.361	0.379
ABCC2	0.095	0.104	0.416	**NIR1I2**	0.387	0.052	0.636
ABCC1	0.991	0.419	0.870	**HMGB1**	0.472	0.285	0.148

8.5 Identified bile acids in the metabolomics study

Appendix Table 8: Bile acids expressed in advanced liver models during long-term culture.
(Figure 50)

	2.5D			3D			OOC Coculture			OOC Quadculture		
	D1	D3	D6	D0	D7	D14	D0	D7	D14	D0	D7	D14
Cholic Acid	0.000	0.000	0.000	0.003	0.000	0.000	-0.003	-0.006	-0.003	-0.006	-0.006	-0.002
Deoxycholic acid	0.000	0.000	0.000	0.000	0.000	0.000	0.001	0.000	0.000	0.000	0.000	0.000
Glycocholic acid	0.140	0.203	0.122	0.030	0.033	0.044	0.726	0.505	0.577	0.533	0.379	0.336
Glycochenodeoxy-cholic acid	-0.019	-0.011	-0.007	-0.004	0.003	0.002	0.068	0.070	0.100	0.055	0.031	0.004
Glycodeoxycholic acid	-0.004	-0.004	-0.004	-0.004	-0.004	-0.004	0.003	0.002	0.003	-0.012	-0.013	-0.012
Glycolithocholic acid	-0.001	-0.001	-0.001	-0.001	0.000	0.000	0.000	0.000	0.001	-0.004	-0.004	-0.004
Glycolithocholic acid sulfate	0.000	0.000	0.000	0.000	0.000	0.000	0.000	0.000	0.000	0.000	0.000	0.000
Glycoursodeoxy-cholic acid	0.000	0.000	0.000	0.000	0.000	0.000	0.000	0.000	0.001	0.000	0.000	0.000
Taurocholic acid	0.011	0.036	0.009	-0.007	-0.007	-0.008	0.003	0.018	0.031	-0.037	-0.037	-0.037
Taurochenodeoxy-cholic acid	-0.046	-0.039	-0.041	-0.029	-0.027	-0.025	-0.007	0.022	0.077	-0.100	-0.100	-0.097
Taurodeoxycholic acid	-0.006	-0.005	-0.006	-0.006	-0.003	-0.004	-0.004	0.001	0.008	-0.017	-0.017	-0.016
Taurolithocholic acid	0.000	0.000	0.000	0.000	0.000	0.000	-0.002	0.002	0.004	-0.013	-0.013	-0.013

8.6 Secretion of hepatic proteins in the 2.5D, 3D, and OOC model

Appendix Table 9: Albumin concentration in 2.5D, 3D, and OOC [ng/mL].
(Figure 41 and Figure 53)

Albumin	3D									2.5D									OOC								
Day	D2			D7			D14			D2			D7			D14			D2			D7			D14		
DMSO	88.0	1673.9	357.3	159.9	74.0	420.8	112.3	684.3	458.1	390.3	2441.1	465.6	451.5	300.3	2652.2	2455.5	442.3	46.8	2637.4	2494.3	432.5	2485.2	2562.3	1483.8	2538.8	2472.0	1437.7	2545.5	2393.5	1417.0
MET 750 µM	29.7	5636.3	250.3	7.1	748.6	378.0	47.8	3298.8	396.1	422.0	131.2	134.7	448.8	453.3	2550.3	2422.7	445.5	647.4	2594.4	2430.9	1326.8	2519.1	2541.3	1452.5	2529.5	204.3	1412.0	2565.1	98.9	1341.5
XIM 200 µM	17.2	361.4	211.3	0.0	6548.5	49.7	0.0	68.7	11.7	13.3	236.2	89.0	452.8	479.7	0.0	8.1	446.4	588.9	0.0	15.6	434.9	ND	ND	ND	ND	ND	ND	ND	ND	ND
XIM 100 µM	30.6	560.7	214.7	0.8	173.2	76.5	0.0	81.1	551.2	13.0	156.1	112.7	437.2	466.3	281.1	239.1	431.4	634.4	316.7	58.1	441.1	2587.0	2477.0	1421.6	2462.8	128.9	1450.6	2576.2		1396.4
XIM 10 µM	188.9	1374.8	386.9	510.4	111.4	395.7	478.0	1121.3	523.5	338.7	2409.9	271.9	440.1	632.7	2654.3	2452.5	437.8	718.9	2545.7	2425.4	433.3	ND	ND	ND	ND	ND	ND	ND	ND	ND
DAB 200 µM	69.1	419.5	196.0	7.1	923.2	50.7	0.0	75.8	14.3	14.7	125.5	198.6	448.4	445.1	0.0	7.2	447.5	658.3	0.0	32.8	4.4	ND	ND	ND	ND	ND	ND	ND	ND	ND
DAB 100 µM	561.3	245.1	170.7	2439.0	100.7	43.3	2425.2	68.7	383.1	6.7	110.8	117.9	1384.7	519.6	0.0	2.7	444.4	827.7	0.0	0.0	341.2	ND	ND	ND	ND	ND	ND	ND	ND	ND
DAB 10 µM	107.5	1084.1	369.7	2.3	88.2	377.0	0.0	214.1	627.9	204.4	2454.2	356.7	436.5	572.9	2642.8	2473.8	1402.4	7907.8	2608.2	2464.4	1373.0	ND	ND	ND	ND	ND	ND	ND	ND	ND
TRO 200 µM	21.6	494.3	167.1	3.1	341.7	218.4	0.0	188.0	491.0	10.4	147.5	265.9	149.8	0.0	0.0	6.4	21.4	0.0	105.4	73.2	4.9	ND	ND	ND	ND	ND	ND	ND	ND	ND
TRO 100 µM	33.0	369.7	172.4	14.6	106.0	173.4	0.0	65.2	422.1	13.0	251.0	291.3	442.0	13.0	2562.9	2454.0	162.3	4246.2	2550.7	155.5	3.6	ND	ND	ND	ND	ND	ND	ND	ND	ND
TRO 10 µM	97.1	1765.2	337.6	219.1	98.9	312.6	95.4	75.8	392.2	376.9	2430.5	318.1	448.1	450.3	2566.1	2477.8	446.8	8324.2	2574.3	2436.3	432.6	ND	ND	ND	ND	ND	ND	ND	ND	ND
PIO 200 µM	56.7	1192.1	271.8	88.7	917.9	376.3	54.4	847.9	368.4	285.8	337.8	242.1	434.2	489.7	2613.2	2456.5	449.5	8481.6	2563.3	2540.4	444.3	ND	ND	ND	ND	ND	ND	ND	ND	ND
PIO 100 µM	46.2	439.3	275.9	79.4	541.7	292.1	52.9	654.0	ND	336.8	2405.8	228.3	442.1	606.3	2639.0	2448.3	436.5	9619.2	2503.8	338.1	1402.0	ND	ND	ND	ND	ND	ND	ND	ND	ND
PIO 10 µM	77.7	385.9	239.0	103.9	487.8	352.6	122.0	445.6	328.0	347.9	439.9	256.0	457.6	438.6	2607.6	2498.9	1433.8	10269.3	2600.7	2430.3	450.3	ND	ND	ND	ND	ND	ND	ND	ND	ND
TOL 200 µM	29.7	136.6	102.7	7.9	552.7	66.9	5.4	539.5	280.4	15.7	261.8	173.2	132.9	424.7	0.0	0.0	16.0	0.0	68.7	0.0	2.6	ND	ND	ND	ND	ND	ND	ND	ND	ND
TOL 100 µM	34.8	184.3	136.6	3.7	100.7	288.6	0.0	60.0	526.5	3.3	2402.5	169.7	448.5	267.4	3.1	5.0	444.8	0.0	58.0	52.4	412.8	2564.1	2395.8	1398.4	2506.9		1250.6	2467.9		5.1
TOL 10 µM	135.5	647.1	357.3	219.1	81.1	392.2	110.8	107.8	ND	410.8	356.7	438.5	450.2	515.3	2653.6	2472.6	443.9	6821.0	2610.8	2483.5	1383.7	ND	ND	ND	ND	ND	ND	ND	ND	ND
ENT 200 µM	34.2	233.0	167.4	5.1	825.1	49.4	0.0	681.9	223.6	10.9	101.8	154.9	294.1	0.0	10.8	10.4	12.3	0.0	27.9	52.1	3.6	ND	ND	ND	ND	ND	ND	ND	ND	ND
ENT 100 µM	58.9	363.6	342.9	14.0	122.2	144.9	0.0	74.0	305.9	66.8	197.7	153.6	449.7	499.2	99.6	169.5	444.0	8999.6	222.6	176.5	437.8	2576.8	2527.3	1443.1	2529.2	2546.5	1430.2	2568.1	2490.5	1385.1
ENT 10 µM	183.4	535.2	171.3	356.7	302.2	353.9	258.9	214.1	268.2	379.5	2414.5	321.8	444.7	631.0	2577.6	2457.7	443.5	11401.8	2614.5	2472.8	446.3	ND	ND	ND	ND	ND	ND	ND	ND	ND
APAP 5000 µM	31.8	331.7	118.2	5.9	968.7	46.3	0.0	1324.0	427.3	10.8	296.6	207.2	175.9	0.0	0.0	3.8	8.3	0.0	33.0	55.6	1.6	ND	ND	ND	ND	ND	ND	ND	ND	ND
APAP 2500 µM	40.3	290.5	117.7	4.5	127.6	67.6	0.0	147.6	ND	64.9	380.4	224.2	427.4	ND	0.0	5.2	412.1	ND	242.7	5.8	29.4	2471.2	2523.9	1444.1	11.4	2455.4	1293.0	0.0	294.0	81.8
APAP 100 µM	81.1	500.6	298.5	215.1	140.3	352.6	137.9	81.1	468.0	275.4	349.9	275.6	438.7	453.7	2655.5	2499.1	435.7	11158.0	2578.6	2413.6	447.4	ND	ND	ND	ND	ND	ND	ND	ND	ND
FIA 200/300 µM	79.8	626.5	249.0	68.4	907.3	285.2	31.8	477.1	ND	163.5	2429.2	313.8	445.6	578.5	2625.8	2439.7	447.7	3961.8	2423.6	477.0	1438.2	2533.5	2439.5	1440.2	241.0	315.9	1420.9	20.4		1387.4
FIA 100 µM	141.9	466.6	316.8	158.2	406.3	391.4	82.8	216.0	ND	282.8	292.0	298.6	446.6	ND	2664.0	2440.7	1426.4	ND	2568.1	2458.5	445.3	ND	ND	ND	ND	ND	ND	ND	ND	ND
FIA 10 µM	151.2	464.5	341.2	305.4	561.5	416.0	119.4	325.8	284.7	411.8	2395.2	527.6	444.8	0.0	2689.7	2425.1	443.8	6917.5	2595.4	2444.5	427.3	ND	ND	ND	ND	ND	ND	ND	ND	ND
DIC 200 µM	103.9	475.0	331.1	117.9	815.0	258.6	102.1	377.8	ND	124.3	2423.9	246.5	453.8	ND	2606.7	2489.5	446.9	ND	2605.2	2458.2	449.7	ND	ND	ND	ND	ND	ND	ND	ND	ND
DIC 100 µM	181.2	535.2	343.2	405.3	539.5	421.4	538.1	325.8	ND	380.8	2407.2	361.1	446.3	ND	2548.6	2459.0	449.3	ND	2423.9	2464.4	432.5	2521.3	2501.1	1468.9	2510.3	38.8	1430.8	2612.8		1407.8
DIC 10 µM	194.9	483.5	348.4	340.9	765.6	405.8	238.9	915.2	ND	387.3	2433.9	220.5	442.6	ND	2620.3	2469.7	441.2	ND	2550.3	2429.3	1361.8	ND	ND	ND	ND	ND	ND	ND	ND	ND
TVX 200 µM	81.1	312.0	242.2	9.4	755.8	144.7	0.0	277.0	ND	21.9	403.1	227.4	426.1	ND	57.0	129.1	166.6	ND	0.0	2.7	0.9	ND	ND	ND	ND	ND	ND	ND	ND	ND
TVX 100 µM	87.0	365.7	200.4	33.6	178.7	234.7	11.1	81.1	ND	41.3	2393.0	231.2	442.2	ND	2469.8	261.5	438.5	ND	2528.8	144.5	155.8	ND	ND	ND	ND	ND	ND	ND	ND	ND
TVX 10 µM	131.6	612.9	296.5	161.6	341.7	404.3	73.0	365.7	ND	240.3	2409.1	231.7	448.0	ND	2629.4	2475.2	444.5	ND	2572.1	2451.0	438.1	2525.2	2426.0	1432.7	2396.9	2441.3	1438.3	2547.0	2421.8	1427.7
LVX 200 µM	188.4	437.2	225.1	321.0	383.8	261.2	184.3	841.5	ND	225.8	372.8	229.1	439.3	ND	2587.9	2480.4	445.1	ND	2590.2	2468.0	433.6	ND	ND	ND	ND	ND	ND	ND	ND	ND
LVX 100 µM	208.2	637.9	197.8	534.4	398.1	402.8	231.4	491.0	ND	329.7	2406.4	228.6	443.9	ND	2656.7	2447.3	440.1	ND	2570.7	2426.9	439.7	2573.5	2517.3	1438.7	2418.3	2451.4	1454.2	0.0	2520.2	1361.2
LVX 10 µM	213.6	441.4	281.2	379.5	597.1	361.2	204.3	836.4	ND	320.8	2432.0	183.2	441.7	ND	2586.0	2447.0	448.4	ND	2571.7	2416.6	422.6	ND	ND	ND	ND	ND	ND	ND	ND	ND
Untreated	197.7	537.3	195.7	222.1	590.4	254.9	286.8	975.5	667.4	255.3	2418.8	216.3	441.7	ND	2634.4	2440.9	437.8	8303.9	503.0	2418.2	428.0	2522.8	2546.5	1448.7	2534.6	2456.4	1409.9	2547.0	2407.5	1434.4
AMIO 100 µM	85.6	341.7	184.5	14.6	743.7	39.5	0.0	1033.6	ND	7.2	334.6	110.3	410.6	ND	0.0	36.8	13.1	ND	0.0	72.5	1.7	2476.0	2492.8	1451.7	2515.3	2495.8	1347.6	2466.9	2553.6	1130.6
BOS 30 µM	238.9	563.7	111.0	241.0	120.4	ND	2393.3	188.9	ND	374.6	2471.7	282.1	455.8	ND	2638.4	2484.9	53.5	ND	2613.2	2409.5	9.0	2502.0	2562.1	1448.2	2480.8	2491.7	1445.0	2544.3	2472.7	1448.4

Appendix Table 10: AGST concentration in 2.5D, 3D, and OOC [µg/L].
(Figure 41 and Figure 53)

αGST	3D										2.5D										OOC								
Day	D2			D7			D14				D2			D7				D14			D2			D7			D14		
DMSO	42.9	84.7	90.1	12.3	542.4	1.2	11.0	1.6	2.4	2.4	385.8	470.1	641.7	43.9	8.5	51.0	70.0	11.3	13.4	2.0	2.7	4.8	8.6	9.0	3.7	2.5	12.7	8.2	1.9	1.4
MET 750 µM	103.7	95.9	81.8	16.0	16.1	5.3	2.1	1.0	4.9	3.8	384.9	480.6	609.1	273.6	28.7	73.6	214.7	21.5	15.7	4.2	6.7	3.1	8.1	9.0	0.8	3.7	8.6	7.7	3.1	4.8
XIM 200 µM	41.3	101.0	82.6	18.7	22.0	0.8	5.0	1.0	1.2	4.6	469.8	458.4	812.1	19.4	11.2	54.4	119.8	17.2	0.0	0.2	1.6	ND	ND	ND	ND	ND	ND	ND	ND	ND
XIM 100 µM	34.3	60.9	86.7	19.1	26.7	4.6	12.6	1.6	2.7	4.6	438.6	459.7	787.1	49.1	8.1	52.6	109.2	11.8	1.1	0.0	1.2	4.2	3.1	9.0	8.1	4.2	11.1	8.6	1.9	3.1
XIM 10 µM	31.7	72.4	99.8	25.5	27.3	9.9	20.1	2.2	1.2	3.8	350.6	446.5	603.1	50.7	12.2	43.6	82.8	12.6	43.9	3.1	ND	ND	ND	ND	ND	ND	ND	ND	ND	ND
DAB 200 µM	38.1	82.1	109.4	23.8	25.3	11.6	6.8	1.6	1.6	3.1	447.0	485.2	812.5	19.4	110.6	36.2	166.5	57.1	0.0	0.2	1.2	ND	ND	ND	ND	ND	ND	ND	ND	ND
DAB 100 µM	34.3	67.5	265.5	91.7	30.7	17.7	15.0	17.7	2.0	3.1	491.1	451.1	828.8	18.0	44.8	16.7	156.3	28.2	2.1	0.0	16.1	ND	ND	ND	ND	ND	ND	ND	ND	ND
DAB 10 µM	38.1	180.0	80.5	4.8	37.2	10.2	7.7	0.0	0.5	3.5	348.9	465.7	663.9	48.6	11.2	56.2	118.0	104.0	32.5	3.1	2.0	ND	ND	ND	ND	ND	ND	ND	ND	ND
TRO 200 µM	38.1	153.7	92.2	19.4	11.6	7.4	7.7	0.0	1.6	1.2	445.8	516.1	803.3	250.9	11.9	46.7	154.6	11.8	0.1	0.0	2.4	ND	ND	ND	ND	ND	ND	ND	ND	ND
TRO 100 µM	52.3	168.6	94.4	20.4	18.3	6.7	22.9	1.0	1.2	3.8	373.7	462.6	600.0	329.5	239.0	53.7	203.2	33.7	44.4	176.2	2.4	ND	ND	ND	ND	ND	ND	ND	ND	ND
TRO 10 µM	43.7	135.4	71.4	21.6	30.7	6.4	8.5	0.4	1.2	2.7	389.3	457.5	619.0	45.5	15.5	35.9	94.0	16.5	5.0	3.7	1.6	ND	ND	ND	ND	ND	ND	ND	ND	ND
PIO 200 µM	38.1	130.8	73.5	18.7	26.7	7.1	6.8	2.7	2.4	2.0	348.9	439.2	590.4	245.8	9.5	47.5	120.9	63.2	72.2	2.0	0.8	ND	ND	ND	ND	ND	ND	ND	ND	ND
PIO 100 µM	38.9	102.8	72.6	21.6	21.4	9.5	5.0	0.0	0.8	4.9	333.0	432.9	590.8	234.5	13.5	68.1	103.6	28.2	53.2	15.9	1.6	ND	ND	ND	ND	ND	ND	ND	ND	ND
PIO 10 µM	31.3	161.3	80.1	19.1	10.9	7.4	8.5	1.6	1.2	3.5	313.4	446.8	610.7	38.9	8.1	35.6	96.0	25.6	2.1	2.6	2.0	ND	ND	ND	ND	ND	ND	ND	ND	ND
TOL 200 µM	46.8	187.8	83.9	25.5	45.3	8.8	4.0	4.3	3.1	3.1	454.5	522.9	840.7	6.8	17.7	4.8	169.2	26.9	1.1	0.8	5.7	ND	ND	ND	ND	ND	ND	ND	ND	ND
TOL 100 µM	47.1	202.9	88.8	23.5	25.0	8.8	5.0	0.0	3.1	3.8	402.5	484.5	761.2	211.5	21.1	56.0	415.3	46.0	3.1	0.8	101.6	6.4	62.5	41.9	11.2	2.5	10.3	7.7	4.8	1.9
TOL 10 µM	92.8	156.6	86.7	19.7	49.0	7.1	5.0	0.4	4.6	1.6	358.4	478.9	641.3	58.1	15.5	17.9	79.0	62.3	15.0	0.2	1.6	ND	ND	ND	ND	ND	ND	ND	ND	ND
ENT 200 µM	79.1	183.3	103.5	28.1	21.1	14.5	3.1	1.6	2.7	3.8	431.4	525.6	818.4	191.9	44.2	96.9	273.6	20.1	3.1	2.0	1.6	ND	ND	ND	ND	ND	ND	ND	ND	ND
ENT 100 µM	85.7	190.5	81.1	28.3	20.5	15.5	6.8	0.4	3.1	3.5	410.3	505.9	766.0	281.3	17.7	94.2	103.6	16.5	0.1	5.3	2.0	2.5	2.5	9.0	2.5	3.7	9.8	9.4	1.9	3.1
ENT 10 µM	75.5	77.2	78.8	25.0	37.2	16.8	3.1	9.0	3.5	2.7	375.1	439.7	593.2	93.2	12.9	18.3	58.5	11.0	24.3	3.7	0.5	ND	ND	ND	ND	ND	ND	ND	ND	ND
APAP 5000 µM	88.6	101.0	72.6	20.7	24.7	19.3	3.1	0.4	2.0	3.1	344.0	470.6	525.3	241.6	25.3	66.7	351.2	21.5	3.1	0.8	2.0	ND	ND	ND	ND	ND	ND	ND	ND	ND
APAP 2500 µM	86.8	132.7	77.8	25.8	13.2	18.6	ND	0.0	4.2	3.1	339.6	479.6	614.3	234.1	78.1	63.0	ND	ND	0.1	2.6	4.9	64.1	3.1	10.3	8.6	2.5	12.7	8.6	1.4	3.1
APAP 100 µM	73.3	104.4	83.9	23.8	12.2	27.9	5.0	3.3	3.1	3.8	339.6	432.2	590.8	31.3	10.9	12.5	86.9	26.2	15.0	0.2	2.7	ND	ND	ND	ND	ND	ND	ND	ND	ND
FIA 200/300 µM	99.3	118.5	97.0	22.9	19.9	22.0	5.0	0.0	1.2	3.8	341.7	445.3	632.9	78.2	15.2	29.2	124.1	19.4	26.2	2.6	7.1	8.6	0.8	7.7	2.5	5.9	8.6	8.6	2.5	4.2
FIA 100 µM	138.2	178.6	109.2	22.0	19.3	13.9	ND	1.6	6.4	3.1	333.3	456.7	669.1	60.9	7.4	24.7	ND	ND	28.2	2.6	4.6	ND	ND	ND	ND	ND	ND	ND	ND	ND
FIA 10 µM	109.8	146.1	93.2	21.6	29.0	15.2	29.4	4.8	3.5	5.7	372.5	466.5	663.9	30.7	11.6	27.1	112.9	19.4	27.5	3.7	0.5	ND	ND	ND	ND	ND	ND	ND	ND	ND
DIC 200 µM	72.8	131.9	83.9	25.2	14.8	14.5	ND	6.7	5.3	4.9	370.5	468.2	646.0	88.9	15.2	56.8	ND	ND	18.0	5.8	3.1	ND	ND	ND	ND	ND	ND	ND	ND	ND
DIC 100 µM	49.2	158.0	83.0	23.2	7.8	16.4	ND	4.3	3.8	4.2	333.0	450.2	634.5	111.1	9.2	24.3	ND	ND	51.7	0.8	0.5	3.1	1.4	8.6	4.2	10.7	9.0	6.4	4.2	2.5
DIC 10 µM	61.8	138.9	85.6	25.8	16.1	20.2	ND	3.8	1.2	4.9	344.3	436.3	625.0	28.8	9.9	17.1	ND	ND	3.3	2.0	0.8	ND	ND	ND	ND	ND	ND	ND	ND	ND
TVX 200 µM	55.5	110.8	89.2	26.4	28.4	14.8	ND	7.7	2.4	4.9	330.4	493.0	688.2	577.7	192.8	162.9	ND	ND	29.2	2.6	3.5	ND	ND	ND	ND	ND	ND	ND	ND	ND
TVX 100 µM	86.1	72.0	90.6	21.3	18.0	15.5	ND	4.8	4.2	4.6	327.8	475.0	690.1	437.5	164.9	141.9	ND	ND	39.9	6.3	25.9	ND	ND	ND	ND	ND	ND	ND	ND	ND
TVX 10 µM	99.3	130.2	103.8	19.7	22.6	20.2	ND	0.4	2.0	3.8	319.1	453.8	650.4	70.9	12.2	39.2	ND	ND	13.8	1.4	2.7	1.9	3.7	9.4	1.4	3.1	9.8	5.1	5.9	0.8
LVX 200 µM	99.1	95.5	108.3	26.7	38.6	16.1	ND	1.6	4.9	2.0	326.4	442.6	674.3	155.3	16.4	51.5	ND	ND	14.2	4.2	2.0	ND	ND	ND	ND	ND	ND	ND	ND	ND
LVX 100 µM	79.4	56.2	97.3	23.8	6.7	15.2	ND	5.3	3.5	3.5	335.0	454.3	660.0	75.6	46.5	38.6	ND	ND	12.7	3.1	0.5	9.1	0.8	8.2	2.5	1.9	9.0	18.5	0.8	5.3
LVX 10 µM	113.7	106.4	84.1	24.4	15.2	12.9	ND	2.7	2.4	3.8	324.3	436.5	658.4	33.7	27.6	26.1	ND	ND	1.0	2.6	1.6	ND	ND	ND	ND	ND	ND	ND	ND	ND
Untreated	158.2	73.5	79.8	20.7	18.6	15.2	5.0	6.3	4.6	2.7	294.3	422.4	603.9	29.4	14.5	17.1	5.9	5.9	136.7	0.8	0.5	1.9	4.8	10.3	1.9	0.8	9.0	8.2	1.9	0.8
AMIO 100 µM	153.9	100.3	98.2	22.6	18.0	18.6	ND	1.6	2.7	3.5	426.5	485.9	831.2	24.3	48.0	12.5	ND	ND	0.0	0.0	1.2	4.2	2.5	12.3	1.4	3.1	9.8	10.3	3.7	3.1
BOS 30 µM	117.1	104.2	86.1	28.3	23.5	18.6	ND	5.8	2.7	ND	285.1	423.2	661.5	41.2		10.2	ND	ND	2.7	6.8	29.3	1.9	9.6	10.7	2.5	3.7	11.1	11.5	3.1	1.9

Appendix Table 11: AST concentration in 2.5D, 3D, and OOC [nmol/min/mL].
(Figure 41 and Figure 68)

AST	3D										2.5D										OOC								
Day	D2			D7			D14				D2			D7				D14			D2			D7			D14		
DMSO	8.48	24.07	11.56	7.42	61.04	5.67	1.99	10.41	7.56	30.71	17.67	55.58	1.89	2.15	16.91	33.54	2.23	1.93	2.12	14.27	60.25	1.34	15.75	19.77	1.78	6.33	18.81	1.94	7.28	15.80
MET 750 µM	10.20	23.49	10.78	7.35	17.01	8.68	1.91	8.96	7.14	33.94	15.55	53.05	1.63	1.76	19.53	31.94	2.42	2.32	1.67	14.00	70.28	1.62	18.76	19.67	1.96	8.18	19.37	1.91	8.53	16.55
XIM 200 µM	7.59	18.30	10.57	5.80	17.30	8.48	1.78	6.79	6.74	25.94	15.88	49.88	1.78	1.91	9.09	34.86	2.58	2.36	1.80	7.56	59.01	ND	ND	ND	ND	ND	ND	ND	ND	ND
XIM 100 µM	8.07	14.34	8.46	6.67	14.61	6.52	1.78	9.92	6.40	23.93	14.95	50.63	1.83	2.19	10.35	32.21	2.65	2.50	2.32	8.11	60.44	2.02	16.01	19.98	1.76	7.08	20.03	1.93	5.87	15.50
XIM 10 µM	7.06	22.91	10.14	6.40	20.60	5.74	1.92	8.55	5.73	29.75	11.63	52.17	1.37	1.59	12.89	32.61	2.65	2.47	1.62	12.12	64.71	ND	ND	ND	ND	ND	ND	ND	ND	ND
DAB 200 µM	7.53	18.58	8.88	7.76	16.02	6.39	1.81	8.55	7.62	21.76	15.22	46.75	1.38	1.68	7.69	24.36	2.35	2.02	1.66	7.35	49.66	ND	ND	ND	ND	ND	ND	ND	ND	ND
DAB 100 µM	8.27	19.74	11.56	7.49	13.64	7.59	1.47	9.92	6.40	23.35	18.10	49.79	1.94	2.22	6.20	25.94	2.42	2.29	2.26	8.60	52.01	ND	ND	ND	ND	ND	ND	ND	ND	ND
DAB 10 µM	9.99	19.59	14.07	7.01	15.74	6.39	1.98	7.80	10.07	24.65	17.92	56.06	1.58	1.62	13.24	33.94	2.69	2.38	0.56	15.28	58.43	ND	ND	ND	ND	ND	ND	ND	ND	ND
TRO 200 µM	11.03	21.04	10.99	8.46	10.52	8.00	1.99	8.61	8.25	10.26	19.58	37.02	1.61	1.94	5.60	12.41	1.92	1.83	5.58	7.42	27.40	ND	ND	ND	ND	ND	ND	ND	ND	ND
TRO 100 µM	8.00	17.01	9.93	6.74	18.44	8.89	1.75	8.27	5.54	12.27	16.72	48.44	1.65	2.22	14.47	28.77	2.10	1.82	0.00	14.41	28.90	ND	ND	ND	ND	ND	ND	ND	ND	ND
TRO 10 µM	9.37	14.20	11.91	7.14	23.20	7.53	1.76	8.55	5.93	23.06	14.61	47.36	1.97	2.47	11.84	34.98	2.62	2.66	8.21	12.68	58.14	ND	ND	ND	ND	ND	ND	ND	ND	ND
PIO 200 µM	8.48	15.74	9.58	7.14	18.58	8.41	1.76	8.20	4.63	23.35	13.45	48.15	1.84	2.42	14.81	29.88	2.63	2.65	10.34	11.27	48.63	ND	ND	ND	ND	ND	ND	ND	ND	ND
PIO 100 µM	8.20	14.48	9.86	7.14	16.16	7.19	1.74	8.14	6.20	21.04	10.14	44.77	1.71	2.25	15.88	25.65	2.63	2.70	4.79	10.85	48.51	ND	ND	ND	ND	ND	ND	ND	ND	ND
PIO 10 µM	8.00	15.31	9.65	6.94	14.89	6.92	1.71	9.09	5.80	26.65	9.58	44.34	1.09	1.64	12.82	30.57	2.71	2.65	5.70	11.27	57.25	ND	ND	ND	ND	ND	ND	ND	ND	ND
TOL 200 µM	8.82	16.16	9.37	5.47	19.88	7.53	1.70	10.06	6.13	10.26	18.88	49.22	1.76	1.70	6.07	10.52	2.03	1.74	3.65	7.01	23.73	ND	ND	ND	ND	ND	ND	ND	ND	ND
TOL 100 µM	10.34	17.30	13.45	6.40	15.17	7.19	1.98	8.07	6.00	19.88	14.27	52.35	2.16	2.41	8.04	24.93	2.12	1.81	3.82	9.02	37.83	2.16	24.02	26.31	1.79	5.14	20.18	1.87	5.60	14.57
TOL 10 µM	14.23	21.90	12.61	8.25	24.36	9.03	1.89	6.72	5.87	28.63	12.05	51.36	1.93	1.53	9.79	33.68	3.01	2.40	5.54	12.82	60.15	ND	ND	ND	ND	ND	ND	ND	ND	ND
ENT 200 µM	10.27	21.47	12.05	8.32	15.88	9.92	1.77	7.19	32.11	12.95	17.48	46.65	2.14	1.73	9.23	21.61	1.89	1.64	3.89	8.25	23.97	ND	ND	ND	ND	ND	ND	ND	ND	ND
ENT 100 µM	10.20	24.36	12.26	7.21	15.46	7.86	1.80	5.67	32.79	26.65	16.79	44.13	2.17	2.32	10.21	33.01	2.69	2.59	4.07	8.18	57.85	2.07	6.13	18.55	1.81	6.20	18.86	2.09	5.34	15.21
ENT 10 µM	9.44	11.32	9.65	7.35	13.64	8.27	1.80	6.33	33.35	25.36	14.13	34.98	1.83	1.48	12.26	37.15	2.60	2.68	6.96	10.85	58.82	ND	ND	ND	ND	ND	ND	ND	ND	ND
APAP 5000 µM	9.23	10.39	8.60	6.67	15.88	7.59	1.76	7.66	31.36	10.79	12.75	28.63	2.13	1.46	7.08	13.09	1.71	1.61	1.79	6.53	25.67	ND	ND	ND	ND	ND	ND	ND	ND	ND
APAP 2500 µM	8.89	13.50	7.62	7.08	10.26	7.12	ND	11.65	33.17	11.86	11.56	43.91	2.21	2.06	7.83	25.36	ND	ND	3.68	6.74	32.84	1.53		19.88	0.86	7.76	19.67	1.73	7.69	15.06
APAP 100 µM	10.61	19.30	9.93	7.28	9.08	7.32	1.76	5.03	32.67	20.31	13.86	51.81	2.15	2.29	7.69	31.26	2.55	2.39	11.01	8.95	49.44	ND	ND	ND	ND	ND	ND	ND	ND	ND
FIA 200/300 µM	12.54	15.60	11.98	12.12	12.54	6.26	1.81	7.26	35.47	17.01	17.61	51.54	2.33	2.40	11.63	28.91	3.23	2.05	11.29	9.72	48.05	1.56	4.63	19.42	0.98	9.37	19.52	1.82	6.27	15.95
FIA 100 µM	12.27	21.76	12.33	10.92	21.61	8.55	ND	7.46	33.66	22.05	15.81	51.09	2.16	2.35	12.96	28.07	ND	ND	2.41	5.80	43.86	ND	ND	ND	ND	ND	ND	ND	ND	ND
FIA 10 µM	10.96	17.58	9.79	9.51	25.51	6.92	2.04	5.22	32.92	18.15	16.20	49.69	2.08	2.29	14.27	31.26	4.94	2.67	2.48	8.18	44.22	ND	ND	ND	ND	ND	ND	ND	ND	ND
DIC 200 µM	10.13	17.58	13.31	9.79	19.74	7.80	ND	12.13	33.42	15.88	15.08	43.37	2.15	1.50	12.19	24.93	ND	ND	2.40	6.60	34.63	ND	ND	ND	ND	ND	ND	ND	ND	ND
DIC 100 µM	7.93	17.58	11.34	10.43	8.56	8.34	ND	3.72	30.73	19.16	15.15	47.05	2.17	2.22	12.19	27.64	ND	ND	0.28	8.11	46.04	2.01		18.96	1.37	7.35	18.65	2.10	6.80	15.55
DIC 10 µM	9.99	16.87	10.21	10.21	18.44	7.86	ND	3.72	33.66	24.36	15.42	46.95	1.92	1.54	11.63	30.85	ND	ND	0.59	5.41	54.38	ND	ND	ND	ND	ND	ND	ND	ND	ND
TVX 200 µM	7.66	15.46	13.45	10.00	15.03	7.80	ND	4.97	32.11	12.00	14.13	32.48	1.98	1.80	8.60	13.64	ND	ND	0.29	5.41	26.90	ND	ND	ND	ND	ND	ND	ND	ND	ND
TVX 100 µM	11.44	14.89	11.98	10.07	16.59	5.80	ND	9.51	31.73	10.79	13.17	34.60	2.24	2.38	8.67	23.64	ND	ND	0.40	6.07	33.35	ND	ND	ND	ND	ND	ND	ND	ND	ND
TVX 10 µM	11.72	18.58	12.19	7.62	16.16	7.73	ND	8.27	33.91	18.73	17.79	44.45	2.20	2.48	11.13	25.65	ND	ND	0.55	7.90	45.56	1.64		14.52	2.31	5.34	18.96	1.99	6.67	15.46
LVX 200 µM	12.95	24.93	11.41	8.11	21.32	11.17	ND	10.61	34.91	25.79	16.85	46.65	2.13	2.38	15.35	26.08	ND	ND	0.64	11.27	58.34	ND	ND	ND	ND	ND	ND	ND	ND	ND
LVX 100 µM	12.40	20.60	9.44	8.32	12.27	10.27	ND	7.53	33.10	29.75	16.07	39.23	2.18	2.21	13.31	25.36	ND	ND	0.57	10.28	59.97	1.75		14.33	2.18	6.40	18.50	1.79	5.67	16.00
LVX 10 µM	8.48	20.75	12.54	6.60	19.16	9.03	ND	3.36	31.73	26.65	16.72	45.30	2.24	2.36	12.47	33.54	ND	ND	0.51	10.43	60.90	ND	ND	ND	ND	ND	ND	ND	ND	ND
Untreated	10.75	19.30	10.71	8.39	17.15	8.89	1.91	7.06	33.04	27.36	16.33	48.54	1.97	1.43	13.38	36.77	ND	2.30	0.40	10.14	60.81	1.89	18.58	18.71	1.85	0.00	19.77	2.10	7.83	16.35
AMIO 100 µM	13.22	21.18	9.16	8.46	20.89	8.00	ND	7.26	32.11	11.32	18.94	51.99	2.29	2.33	6.40	30.71	ND	ND	0.30	6.94	25.91	2.19	ND	22.45	1.16	5.73	18.65	1.60	7.08	15.41
BOS 30 µM	12.13	17.44	6.67	8.67	17.73	7.73	ND	7.73	35.60	20.89	15.01	36.64	2.32	2.41	10.00	28.77	ND	ND	0.66	9.23	50.79	0.94	16.85	19.52	1.99	6.13	16.35	1.85	6.67	15.41

Appendix Table 12: ALT concentration in 2.5D, 3D, and OOC [nmol/min/mL].
(Figure 41 and Figure 68)

ALT	3D										2.5D										OOC								
Day	D2			D7			D14				D2			D7				D14				D2			D7			D14		
DMSO	9.5	4.8	2.2	2.7	0.0	56.6	0.4	1.6	0.0	4.7	0.0	15.1	5.3	6.8	12.1	9.0	1.0	0.8	14.3	17.7	11.5	2.5	28.0	11.0	2.4	14.3	10.0	1.5	11.9	8.5
MET 750 µM	9.0	3.8	3.3	2.0	0.0	3.2	0.5	3.3	4.0	4.6	0.0	14.8	2.7	2.6	6.7	9.3	3.2	3.1	5.6	9.3	8.8	2.6	24.3	7.9	2.2	4.0	5.7	1.3	0.0	4.7
XIM 200 µM	9.0	3.4	1.6	1.5	0.9	3.2	0.3	0.0	0.0	3.2	12.4	14.1	14.2	2.6	6.0	9.5	5.2	4.3	2.0	0.0	15.2	ND	ND	ND	ND	ND	ND	ND	ND	ND
XIM 100 µM	9.0	4.3	1.3	4.0	0.0	0.8	0.5	3.3	0.0	4.4	8.3	13.9	10.7	4.6	7.2	8.4	5.8	5.0	3.5	2.0	13.2	2.5	18.8	12.3	2.5	6.5	11.7	2.2	9.1	8.2
XIM 10 µM	8.5	3.0	0.0	5.4	0.0	2.1	0.1	2.7	12.4	4.4	0.0	13.7	4.0	7.6	10.9	4.6	4.5	4.9	14.2	0.7	12.2	ND	ND	ND	ND	ND	ND	ND	ND	ND
DAB 200 µM	8.5	3.9	2.9	9.5	6.0	0.0	0.4	2.6	0.0	3.8	6.0	16.2	17.0	1.4	3.6	0.0	2.9	1.6	2.1	2.2	5.7	ND	ND	ND	ND	ND	ND	ND	ND	ND
DAB 100 µM	10.5	3.4	2.7	3.5	7.5	1.0	0.1	2.9	6.5	4.6	17.8	12.2	23.0	2.9	4.0	9.3	3.7	4.4	2.0	0.0	10.2	ND	ND	ND	ND	ND	ND	ND	ND	ND
DAB 10 µM	9.5	0.0	2.9	0.9	2.5	3.1	0.3	3.1	3.0	4.9	6.2	15.4	5.2	7.3	11.3	8.6	5.0	5.2	13.8	7.4	10.8	ND	ND	ND	ND	ND	ND	ND	ND	ND
TRO 200 µM	9.5	3.9	2.6	2.9	0.0	3.6	0.2	2.6	0.0	3.9	4.5	10.2	4.3	1.6	3.6	3.5	0.4	0.2	1.3	1.8	2.7	ND	ND	ND	ND	ND	ND	ND	ND	ND
TRO 100 µM	9.0	2.8	3.3	3.3	8.0	3.6	0.2	0.0	5.5	4.3	0.0	20.3	3.2	5.7	15.9	6.1	1.1	1.3	14.2	3.5	3.4	ND	ND	ND	ND	ND	ND	ND	ND	ND
TRO 10 µM	9.5	4.0	3.5	0.5	0.0	2.8	0.2	0.0	4.0	5.1	9.0	13.2	3.8	6.1	9.6	9.5	4.9	4.9	14.2	8.3	14.1	ND	ND	ND	ND	ND	ND	ND	ND	ND
PIO 200 µM	8.0	3.9	3.5	3.8	8.0	3.0	0.0	1.4	0.4	5.2	9.0	12.6	5.0	11.4	11.3	8.9	4.8	4.0	9.0	2.6	12.7	ND	ND	ND	ND	ND	ND	ND	ND	ND
PIO 100 µM	10.0	1.7	3.5	0.1	0.0	4.4	ND	1.1	11.4	0.8	1.1	12.9	4.3	10.2	11.8	9.1	0.4	4.6	9.6	3.8	12.0	ND	ND	ND	ND	ND	ND	ND	ND	ND
PIO 10 µM	9.5	2.5	3.6	5.4	40.1	2.3	ND	0.7	0.0	0.0	3.6	13.0	4.9	9.0	11.3	13.0	3.6	3.3	12.5	4.5	15.9	ND	ND	ND	ND	ND	ND	ND	ND	ND
TOL 200 µM	9.5	3.6	0.7	2.9	5.5	2.3	0.5	0.0	0.0	3.8	7.9	14.8	8.7	0.4	2.4	2.7	0.8	0.2	0.4	1.6	3.1	ND	ND	ND	ND	ND	ND	ND	ND	ND
TOL 100 µM	6.0	3.6	3.1	2.6	4.5	1.4	0.6	0.1	5.5	4.3	0.7	13.0	5.1	1.9	4.2	8.8	0.7	0.3	0.4	2.4	24.6	1.4	16.3	7.8	0.1	1.3	4.9	0.4	5.9	4.1
TOL 10 µM	10.5	4.7	5.0	0.9	16.6	2.7	0.2	0.2	3.2	3.6	0.0	11.2	3.2	8.1	10.2	8.8	3.4	4.7	18.9	0.0	10.7	ND	ND	ND	ND	ND	ND	ND	ND	ND
ENT 200 µM	7.5	4.2	3.3	2.7	4.0	3.9	0.3	0.0	3.0	0.0	0.0	15.3	6.0	1.4	3.5	3.0	0.5	0.2	0.4	1.1	3.2	ND	ND	ND	ND	ND	ND	ND	ND	ND
ENT 100 µM	8.5	2.3	3.1	3.1	0.0	0.8	0.5	0.0	2.1	0.0	7.5	15.2	5.0	2.0	5.2	7.1	4.1	3.9	0.6	1.6	10.2	2.8	11.0	8.6	1.0	17.4	7.1	0.9	12.4	5.5
ENT 10 µM	6.5	2.5	3.3	0.0	11.0	3.1	0.5	0.1	3.4	2.4	8.7	12.5	4.5	7.7	9.9	9.0	4.0	4.5	17.6	7.2	9.8	ND	ND	ND	ND	ND	ND	ND	ND	ND
APAP 5000 µM	3.0	1.8	3.6	1.3	0.0	0.0	0.5	0.0	2.1	0.0	0.0	1.1	0.0	-0.1	2.7	2.0	0.0	0.0	0.0	0.9	2.0	ND	ND	ND	ND	ND	ND	ND	ND	ND
APAP 2500 µM	7.0	2.0	0.9	0.0	0.0	0.0	ND	0.0	1.7	0.0	0.0	2.4	0.0	-0.1	2.6	1.3	ND	ND	0.6	0.0	2.1	0.0	10.1	11.0	0.0	16.3	7.2	0.0	10.5	4.6
APAP 100 µM	7.0	2.7	6.2	2.7	5.5	2.0	0.4	-0.2	2.3	3.0	0.0	8.2	0.9	1.6	7.4	4.7	0.7	0.6	2.7	3.6	4.2	ND	ND	ND	ND	ND	ND	ND	ND	ND
FIA 200/300 µM	11.0	4.6	0.0	0.0	4.5	2.4	0.1	0.7	3.5	4.6	0.0	12.9	3.8	10.7	10.1	8.9	2.6	2.2	9.4	4.0	9.1	0.0	8.8	10.9	0.7	0.0	10.8	1.6	3.5	8.6
FIA 100 µM	4.5	4.4	3.8	3.5	6.0	3.8	ND	1.0	3.4	0.0	9.3	15.0	4.3	8.8	11.3	5.1	ND	ND	12.5	6.9	9.5	ND	ND	ND	ND	ND	ND	ND	ND	ND
FIA 10 µM	9.0	4.8	2.7	4.3	5.0	4.7	0.1	0.1	2.3	4.7	8.7	13.3	4.5	6.7	9.5	5.3	9.6	4.9	14.6	6.9	8.9	ND	ND	ND	ND	ND	ND	ND	ND	ND
DIC 200 µM	4.0	4.4	2.9	2.9	0.0	3.6	ND	0.3	2.4	3.6	8.0	9.2	3.0	7.3	7.2	7.6	ND	ND	17.1	9.5	5.7	ND	ND	ND	ND	ND	ND	ND	ND	ND
DIC 100 µM	8.0	4.6	4.5	5.7	8.0	2.7	ND	0.6	2.8	4.4	8.7	9.1	3.5	7.3	7.2	8.8	ND	ND	7.5	6.5	8.1	4.2	0.0	10.0	2.1	0.7	8.7	2.8	0.0	6.4
DIC 10 µM	9.0	4.9	0.5	2.2	3.5	3.0	ND	0.7	2.0	3.5	9.0	12.8	4.7	3.9	3.8	8.6	ND	ND	8.7	0.0	11.4	ND	ND	ND	ND	ND	ND	ND	ND	ND
TVX 200 µM	8.5	2.7	2.2	3.1	0.0	3.2	ND	0.5	2.5	0.0	8.0	13.2	3.6	1.9	2.2	5.3	ND	ND	4.2	2.2	2.8	ND	ND	ND	ND	ND	ND	ND	ND	ND
TVX 100 µM	9.0	3.8	0.0	3.1	8.5	3.1	ND	0.8	2.5	3.8	7.9	15.8	3.4	5.1	1.5	11.8	ND	ND	6.4	3.3	7.1	ND	ND	ND	ND	ND	ND	ND	ND	ND
TVX 10 µM	9.5	5.1	4.5	0.0	6.0	4.0	ND	0.9	3.2	4.2	7.0	14.0	4.0	5.3	4.2	7.2	ND	ND	5.4	4.9	8.1	2.5	12.1	9.0	1.3	11.2	9.7	1.8	0.0	7.7
LVX 200 µM	0.0	2.7	0.0	0.0	8.0	3.9	ND	0.8	3.6	2.0	8.7	12.7	4.4	8.5	6.9	8.5	ND	ND	4.9	0.9	10.0	ND	ND	ND	ND	ND	ND	ND	ND	ND
LVX 100 µM	3.5	4.4	4.0	3.5	7.0	3.4	ND	0.9	3.1	3.6	8.8	11.4	4.5	7.9	1.3	6.1	ND	ND	7.5	6.5	9.6	2.4	0.0	8.7	1.4	14.6	10.0	0.0	9.6	8.0
LVX 10 µM	25.1	5.1	3.3	2.4	0.0	0.0	ND	0.8	2.1	3.2	8.5	9.1	4.6	7.6	3.1	7.3	ND	ND	9.5	6.7	9.2	ND	ND	ND	ND	ND	ND	ND	ND	ND
Untreated	13.8	0.0	5.5	6.7	36.5	3.2	0.6	2.0	3.1	4.7	7.4	11.1	2.8	5.7	0.0	9.3	ND	3.5	7.2	5.9	12.2	3.2	24.8	10.6	2.5	16.4	8.3	2.2	10.2	5.8
AMIO 100 µM	8.5	4.3	5.5	0.0	0.0	3.0	ND	0.4	3.2	0.0	12.7	14.6	14.0	2.0	0.0	2.3	ND	ND	4.9	3.3	3.1	0.6	10.7	3.2	1.8	2.2	2.8	1.5	5.7	2.9
BOS 30 µM	12.4	0.3	2.9	1.3	28.2	0.0	ND	0.8	3.4	3.4	8.3	10.8	5.0	8.7	2.4	4.0	ND	ND	19.7	1.1	2.8	1.6	24.5	13.2	3.0	12.7	11.3	1.5	12.2	7.0

Appendix Table 13: LDH concentration in 2.5D, 3D, and OOC [mU/mL].
(Figure 42, Figure 69, and Figure 54)

LDH	3D										2.5D										OOC								
Day	D2			D7			D14				D2			D7				D14				D2			D7			D14		
DMSO	4.8	14.4	6.0	1.8	4.7	2.0	0.7	1.1	2.0	2.6	8.9	27.3	5.0	1.0	3.2	4.4	1.7	0.7	0.7	4.5	2.6	0.1	0.5	0.0	0.1	0.1	0.0	0.0	0.1	0.0
MET 750 µM	7.8	22.5	9.6	2.1	4.6	2.0	0.9	1.0	1.8	3.1	13.3	31.3	5.0	1.7	3.3	5.9	2.7	1.7	0.9	9.9	3.1	0.2	0.8	0.0	0.2	0.2	0.0	0.3	0.2	0.0
XIM 200 µM	5.9	12.7	6.2	1.8	4.9	2.3	0.7	0.9	1.7	2.3	16.5	21.1	11.4	1.1	3.6	3.6	1.9	0.9	0.6	8.4	2.1	ND	ND	ND	ND	ND	ND	ND	ND	ND
XIM 100 µM	5.8	12.1	6.1	2.8	5.9	2.5	1.1	0.8	2.1	2.4	12.4	22.3	7.2	1.3	3.1	4.7	2.1	1.0	1.0	5.5	3.1	0.1	0.2	0.0	0.3	0.3	0.0	0.2	0.1	0.0
XIM 10 µM	6.3	11.6	7.7	2.0	6.1	1.9	1.1	1.0	2.1	2.7	7.3	19.7	4.6	0.8	2.7	2.5	1.8	1.0	0.9	4.9	2.6	ND	ND	ND	ND	ND	ND	ND	ND	ND
DAB 200 µM	6.5	15.1	6.7	2.0	5.5	2.2	0.9	1.1	2.1	2.7	13.2	26.3	7.2	0.7	3.0	2.7	2.3	2.2	0.6	15.0	1.8	ND	ND	ND	ND	ND	ND	ND	ND	ND
DAB 100 µM	6.1	12.8	6.7	2.2	5.2	2.7	0.9	1.0	2.0	2.9	16.9	26.9	9.0	1.6	2.9	3.0	2.7	1.6	0.6	12.6	2.0	ND	ND	ND	ND	ND	ND	ND	ND	ND
DAB 10 µM	5.7	13.6	7.9	1.4	2.5	2.5	1.0	1.3	2.0	3.0	8.2	27.2	5.4	0.8	3.0	4.3	2.4	2.8	0.8	8.1	2.6	ND	ND	ND	ND	ND	ND	ND	ND	ND
TRO 200 µM	6.2	14.7	6.2	1.7	5.2	2.7	0.8	0.8	1.3	2.1	19.8	34.6	8.6	1.8	3.2	3.5	2.1	0.7	0.3	1.8	1.7	ND	ND	ND	ND	ND	ND	ND	ND	ND
TRO 100 µM	4.6	14.1	10.3	1.8	4.7	2.5	0.9	0.7	1.5	2.3	11.1	30.5	4.3	1.6	2.8	14.3	2.3	0.9	0.9	2.8	5.2	ND	ND	ND	ND	ND	ND	ND	ND	ND
TRO 10 µM	5.2	12.3	7.3	2.2	5.6	1.9	0.9	0.7	1.7	2.4	16.9	17.6	4.3	1.0	3.1	4.5	1.8	0.9	ND	5.3	2.1	ND	ND	ND	ND	ND	ND	ND	ND	ND
PIO 200 µM	5.3	9.4	7.2	2.6	4.4	2.5	0.6	0.5	1.7	2.2	10.8	13.2	4.3	1.3	2.8	2.2	1.9	1.9	ND	3.1	0.0	ND	ND	ND	ND	ND	ND	ND	ND	ND
PIO 100 µM	4.9	7.8	5.4	2.9	3.0	2.1	0.0	0.7	1.7	2.4	11.7	9.6	4.2	1.6	3.1	2.6	0.6	1.3	0.0	3.1	2.8	ND	ND	ND	ND	ND	ND	ND	ND	ND
PIO 10 µM	5.0	11.1	6.2	2.3	7.6	2.8	0.3	0.7	1.9	2.5	9.1	19.1	4.4	0.7	2.6	3.4	1.9	1.3	0.0	5.6	2.2	ND	ND	ND	ND	ND	ND	ND	ND	ND
TOL 200 µM	4.8	12.0	6.2	2.1	5.6	2.3	0.8	0.8	2.1	2.2	31.0	34.2	21.1	0.7	2.4	2.4	2.5	0.9	0.0	2.2	2.1	ND	ND	ND	ND	ND	ND	ND	ND	ND
TOL 100 µM	5.2	12.9	6.9	2.2	5.9	2.5	1.0	0.9	2.0	2.8	13.9	31.5	8.0	1.7	3.3	3.5	3.5	0.9	0.0	12.5	2.1	0.7	18.7	0.0	0.7	0.1	0.2	0.0	0.4	0.2
TOL 10 µM	9.0	14.5	7.8	2.1	5.8	2.8	0.8	0.6	1.8	2.6	9.5	26.7	4.6	1.0	2.4	4.1	ND	1.7	ND	3.7	2.3	ND	ND	ND	ND	ND	ND	ND	ND	ND
ENT 200 µM	6.9	13.7	11.4	3.0	4.7	3.4	0.8	0.6	1.6	2.5	14.4	34.0	9.9	3.0	4.7	6.0	2.5	0.8	ND	2.5	1.8	ND	ND	ND	ND	ND	ND	ND	ND	ND
ENT 100 µM	7.6	14.9	11.3	2.4	4.9	2.4	1.0	0.6	1.7	2.4	15.1	29.1	6.7	1.1	3.1	4.1	1.3	0.8	ND	5.2	2.5	0.4	0.2	0.0	0.0	0.0	0.0	0.0	0.0	0.1
ENT 10 µM	6.9	6.0	8.4	2.5	5.0	2.8	1.0	0.7	1.7	2.5	11.4	21.5	4.5	0.9	2.6	2.3	1.1	0.8	ND	3.6	2.1	ND	ND	ND	ND	ND	ND	ND	ND	ND
APAP 5000 µM	0.4	0.7	0.1	0.0	0.6	2.9	1.0	0.0	0.3	0.3	0.5	0.6	0.0	0.0	0.3	0.3	0.0	0.0	ND	0.5	0.4	ND	ND	ND	ND	ND	ND	ND	ND	ND
APAP 2500 µM	0.4	0.8	0.1	0.1	0.4	0.2	ND	0.0	0.3	0.4	0.5	0.8	0.0	0.0	0.4	0.4	ND	ND	ND	0.4	0.3	0.0	0.0	0.0	0.0	0.2	0.0	0.1	0.0	0.1
APAP 100 µM	6.5	10.5	3.8	1.9	5.0	0.2	0.8	0.7	1.3	2.7	9.2	28.6	4.5	0.8	2.5	2.2	1.2	0.7	ND	3.4	2.0	ND	ND	ND	ND	ND	ND	ND	ND	ND
FIA 200/300 µM	9.0	12.4	6.2	1.6	6.1	2.9	0.9	0.7	1.8	2.7	8.4	21.5	4.7	1.1	2.9	2.3	0.6	0.9	ND	3.3	2.5	0.0	0.0	0.0	0.1	0.6	0.0	0.1	0.2	0.1
FIA 100 µM	8.6	14.2	6.2	1.5	8.1	3.4	ND	0.7	2.1	3.7	8.0	19.3	4.0	1.0	2.6	2.3	ND	ND	ND	0.8	3.2	2.3	ND	ND	ND	ND	ND	ND	ND	ND
FIA 10 µM	6.6	11.2	7.5	1.8	5.8	3.7	1.4	0.7	2.0	3.3	11.9	23.2	5.8	1.1	2.9	2.7	ND	1.0	0.8	3.2	2.2	ND	ND	ND	ND	ND	ND	ND	ND	ND
DIC 200 µM	7.2	9.6	8.5	1.9	2.7	2.6	ND	0.6	2.0	2.9	5.9	8.6	3.1	0.7	2.4	2.9	ND	ND	0.8	3.4	2.2	ND	ND	ND	ND	ND	ND	ND	ND	ND
DIC 100 µM	5.8	9.4	7.4	2.1	5.6	2.6	ND	0.7	1.6	2.2	5.3	12.9	4.0	1.1	2.5	2.2	ND	ND	1.8	4.1	2.0	0.2	0.0	0.0	0.0	0.0	0.0	0.0	0.1	0.0
DIC 10 µM	6.4	12.1	7.9	1.9	5.9	2.7	ND	0.8	1.2	2.5	7.3	9.5	6.2	0.7	2.2	3.2	ND	ND	0.8	4.0	2.1	ND	ND	ND	ND	ND	ND	ND	ND	ND
TVX 200 µM	6.0	11.1	6.5	2.4	6.5	3.1	ND	0.7	2.1	3.1	8.9	24.4	6.0	2.8	5.6	2.6	ND	ND	1.3	2.3	2.4	ND	ND	ND	ND	ND	ND	ND	ND	ND
TVX 100 µM	6.3	8.9	5.7	2.1	5.8	3.1	ND	0.9	2.1	2.2	7.5	26.8	5.5	2.1	5.4	2.9	ND	ND	1.5	3.2	2.3	ND	ND	ND	ND	ND	ND	ND	ND	ND
TVX 10 µM	8.9	9.5	7.2	1.7	5.5	3.0	ND	0.9	2.1	3.4	6.9	27.9	5.1	1.1	2.6	2.4	ND	ND	1.2	3.2	2.2	0.1	0.1	0.0	0.0	0.0	0.0	0.1	0.2	0.0
LVX 200 µM	5.9	11.0	7.8	2.3	3.8	3.1	ND	0.6	2.7	2.8	8.2	16.4	4.4	1.2	3.2	2.8	ND	ND	1.2	4.4	2.8	ND	ND	ND	ND	ND	ND	ND	ND	ND
LVX 100 µM	6.1	12.7	6.9	1.8	5.7	3.2	ND	0.7	1.8	2.7	9.0	17.8	4.9	1.4	3.4	3.3	ND	ND	1.3	3.7	2.7	0.4	0.5	0.0	0.0	0.0	0.0	0.1	0.0	0.2
LVX 10 µM	6.7	13.8	6.8	2.4	5.6	3.1	ND	0.8	2.0	3.1	9.2	17.4	4.8	0.9	2.8	2.6	ND	ND	1.3	4.0	2.4	ND	ND	ND	ND	ND	ND	ND	ND	ND
Untreated	8.8	10.1	6.6	1.9	6.2	3.3	0.8	0.8	2.2	2.9	8.4	14.4	4.8	0.9	2.5	3.0	ND	1.5	8.0	5.8	2.5	0.4	0.7	0.0	0.1	0.3	0.0	0.1	0.1	0.0
AMIO 100 µM	6.4	11.4	5.8	1.8	5.8	3.5	ND	0.8	2.0	2.8	18.0	30.8	15.8	0.7	2.4	2.1	ND	ND	0.8	2.2	2.4	0.2	0.0	0.0	0.1	0.0	0.0	0.0	0.5	0.1
BOS 30 µM	6.4	10.5	5.7	2.4	6.2	3.2	ND	1.0	2.2	3.3	6.4	13.8	4.4	0.7	2.0	3.3	ND	ND	1.1	8.0	2.9	0.1	0.3	0.0	0.1	0.0	0.0	0.0	0.1	0.1

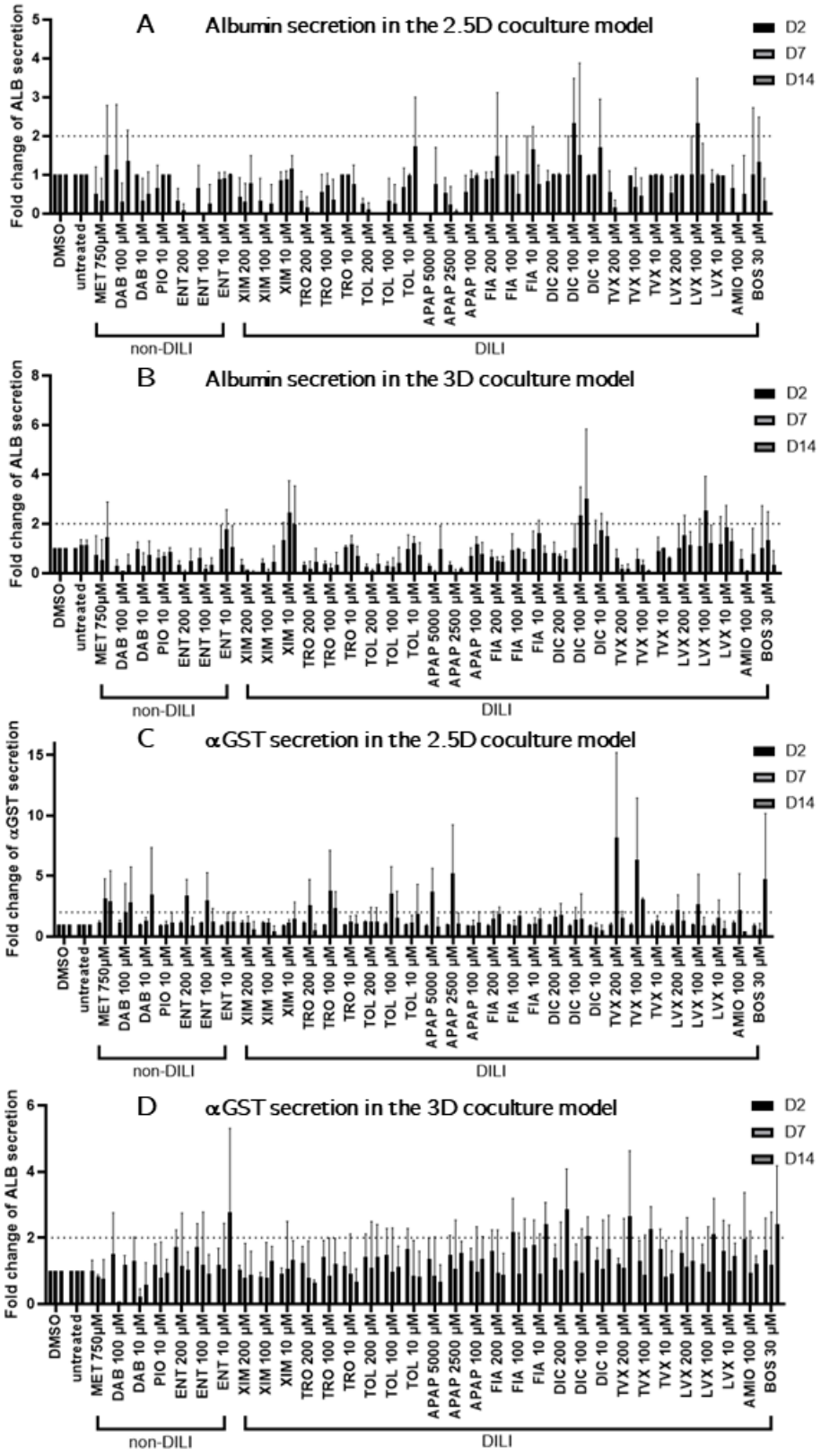

Figure 67: Fold change of albumin and αGST secretion in 2.5D, and 3D normalized to vehicle control.

Supplement to the Figure 53: Graphs, contain all tested concentrations, show fold change in albumin secretion in the **(A)** 2.5D and **(B)** 3D model and fold change in αGST secretion in the **(C)** 2.5D, and **(D)** 3D model. The threshold value was set at 2. N=3/4

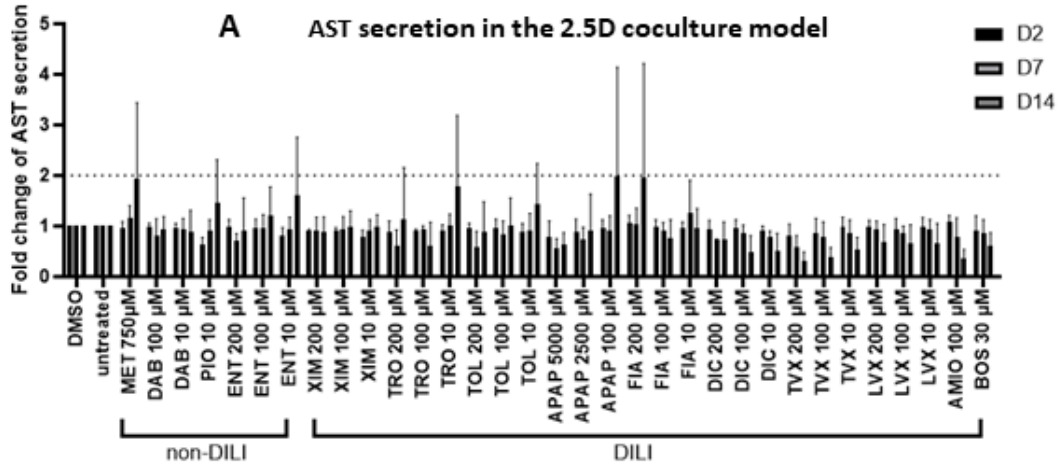
A
AST secretion in the 2.5D coculture model
Fold change of AST secretion
D2
D7
D14
DMSO
untreated
MET 750µM
DAB 100 µM
DAB 10 µM
PIO 10 µM
ENT 200 µM
ENT 100 µM
ENT 10 µM
XIM 200 µM
XIM 100 µM
XIM 10 µM
TRO 200 µM
TRO 100 µM
TRO 10 µM
TOL 200 µM
TOL 100 µM
TOL 10 µM
APAP 5000 µM
APAP 2500 µM
APAP 100 µM
FIA 200 µM
FIA 100 µM
FIA 10 µM
DIC 200 µM
DIC 100 µM
DIC 10 µM
TVX 200 µM
TVX 100 µM
TVX 10 µM
LVX 200 µM
LVX 100 µM
LVX 10 µM
AMIO 100 µM
BOS 30 µM
non-DILI
DILI

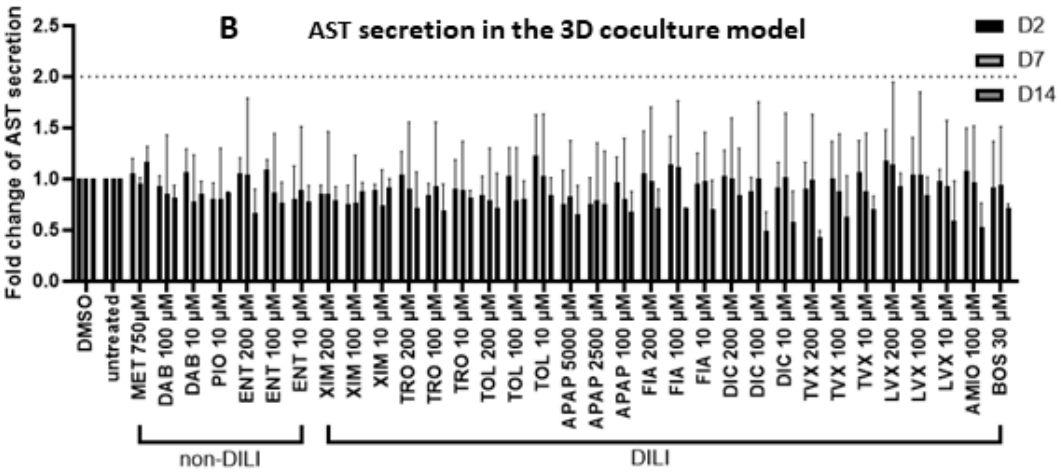
B
AST secretion in the 3D coculture model
Fold change of AST secretion
D2
D7
D14
non-DILI
DILI

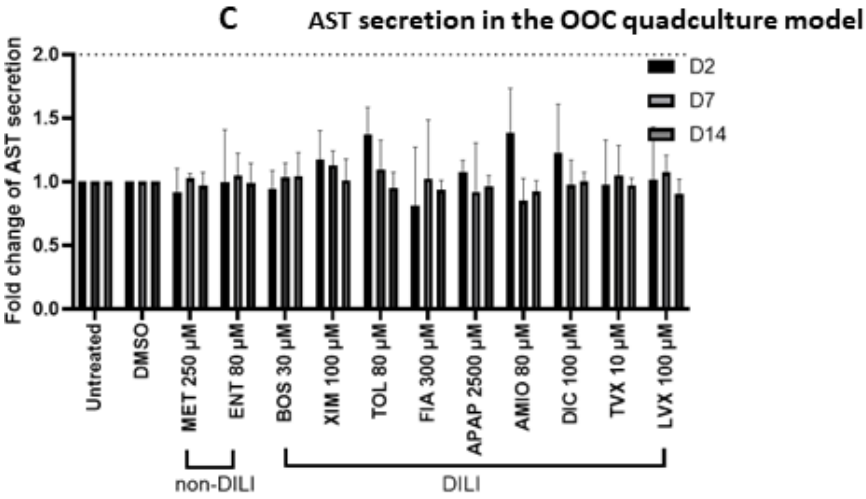
C
AST secretion in the OOC quadculture model
Fold change of AST secretion
D2
D7
D14
Untreated
DMSO
MET 250 µM
ENT 80 µM
BOS 30 µM
XIM 100 µM
TOL 80 µM
FIA 300 µM
APAP 2500 µM
AMIO 80 µM
DIC 100 µM
TVX 10 µM
LVX 100 µM
non-DILI
DILI

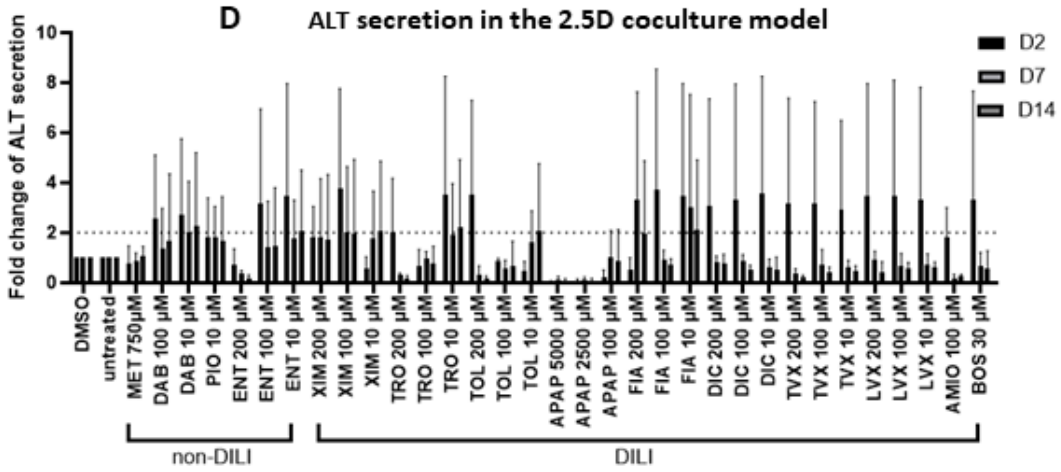
D
ALT secretion in the 2.5D coculture model
Fold change of ALT secretion
D2
D7
D14
non-DILI
DILI

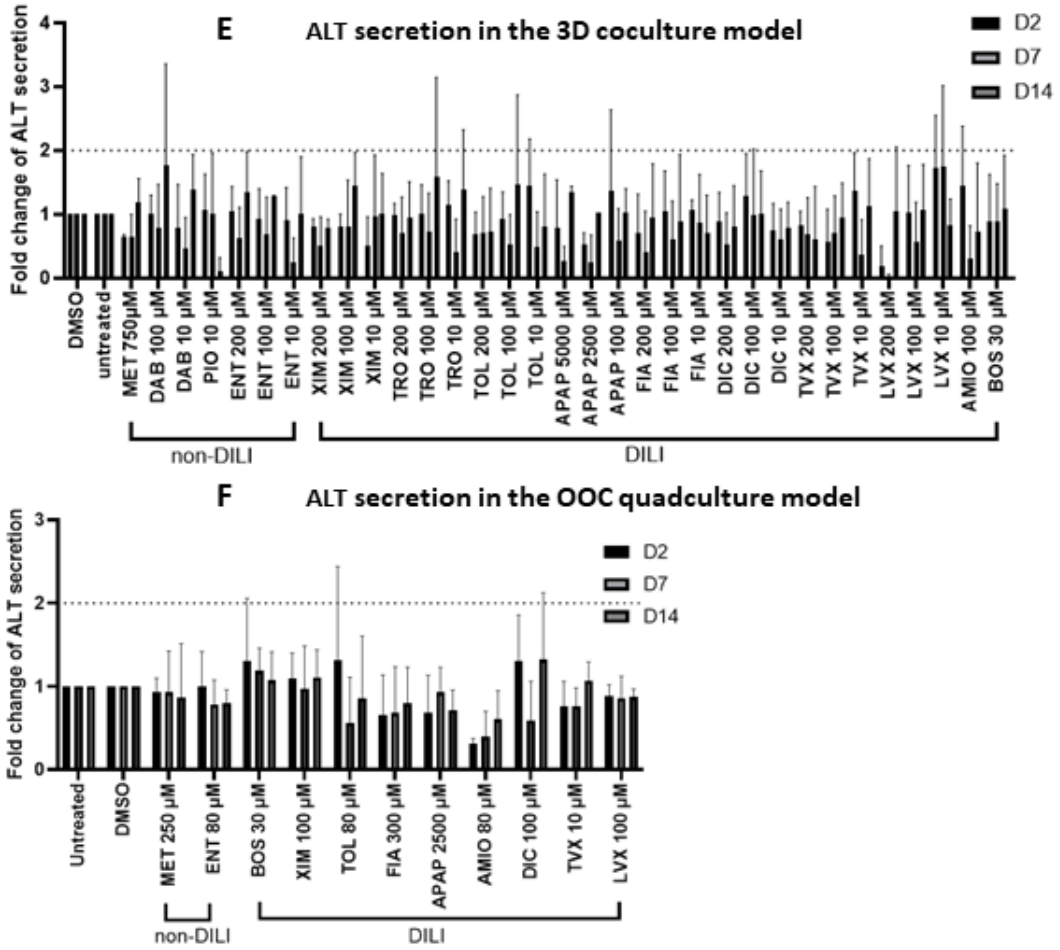

Figure 68: Fold change of AST and ALT secretion in 2.5D, 3D, and OOC.
Graphs, contain all tested concentrations, show fold change in AST secretion in the **(A)** 2.5D **(B)** 3D, and **(C)** OOC model, and fold change in ALT secretion in the **(D)** 2.5D, **(E)** 3D, and **(F)** OOC model. The threshold value was set at 2. N=3/4

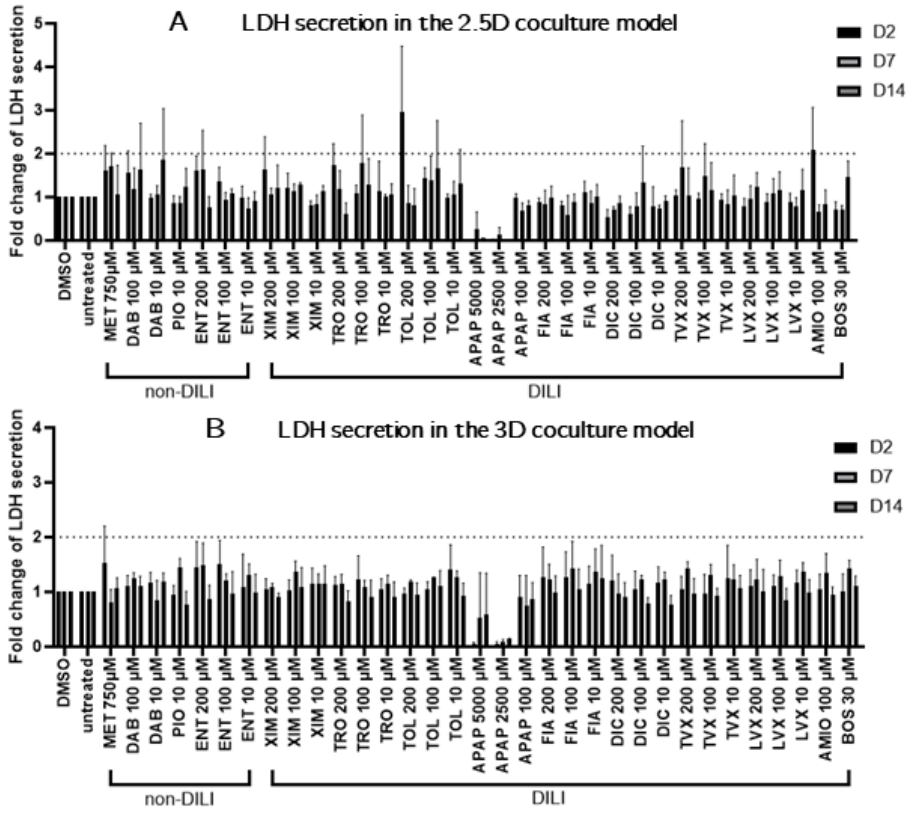

Figure 69: Fold change of LDH secretion in 2.5D and 3D normalized to vehicle control.
Graphs show LDH secretion as fold change of all tested concentrations in he (A) 2.5D and (B) 3D model. The threshold value was set at 2. N=3/4

8.7 Microscopical documentation of liver cells in 2.5D, 3D, and OOC during treatment

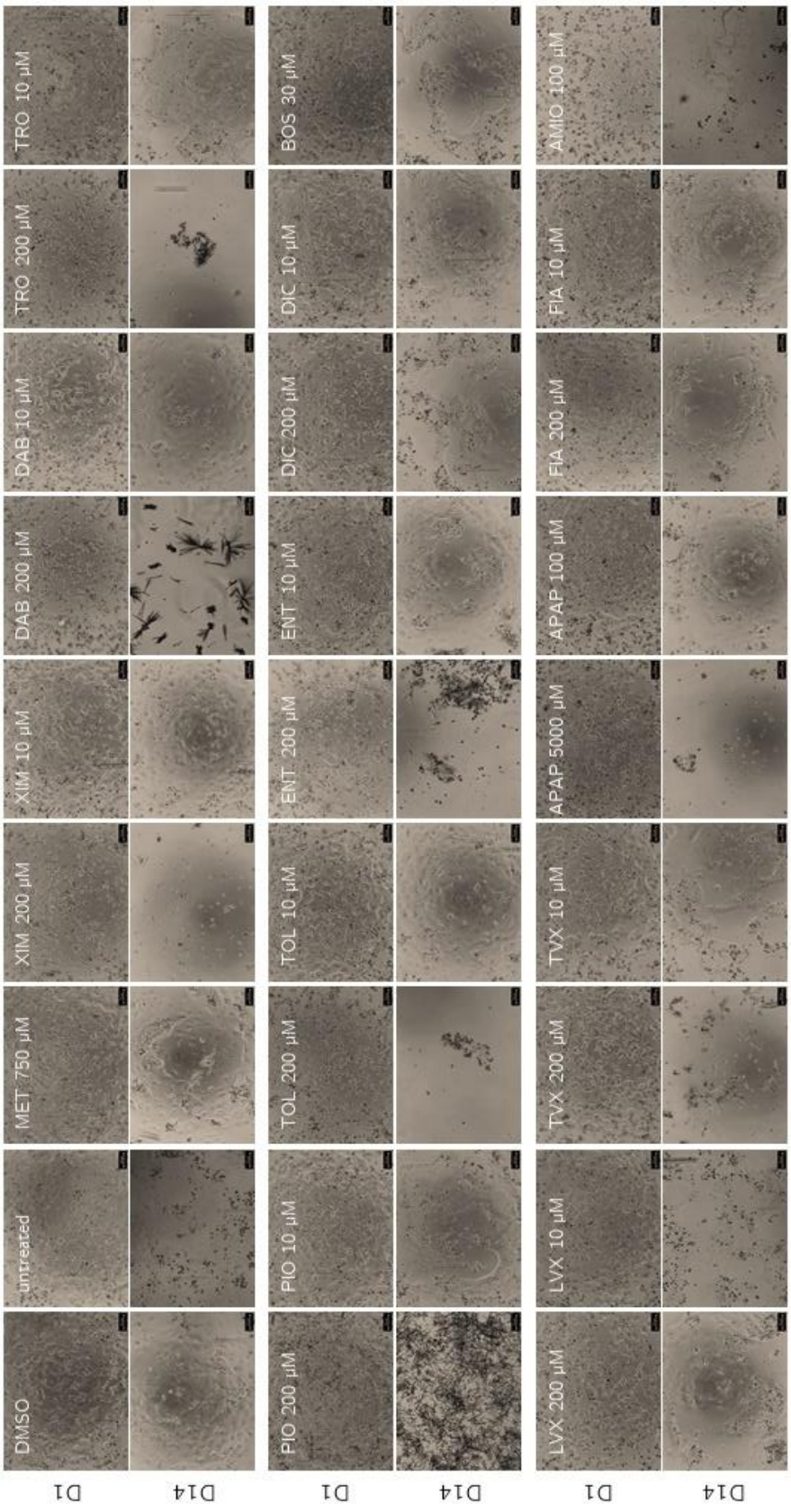

Figure 70: Morphology of cocultured liver cells during treatment in 2.5D.

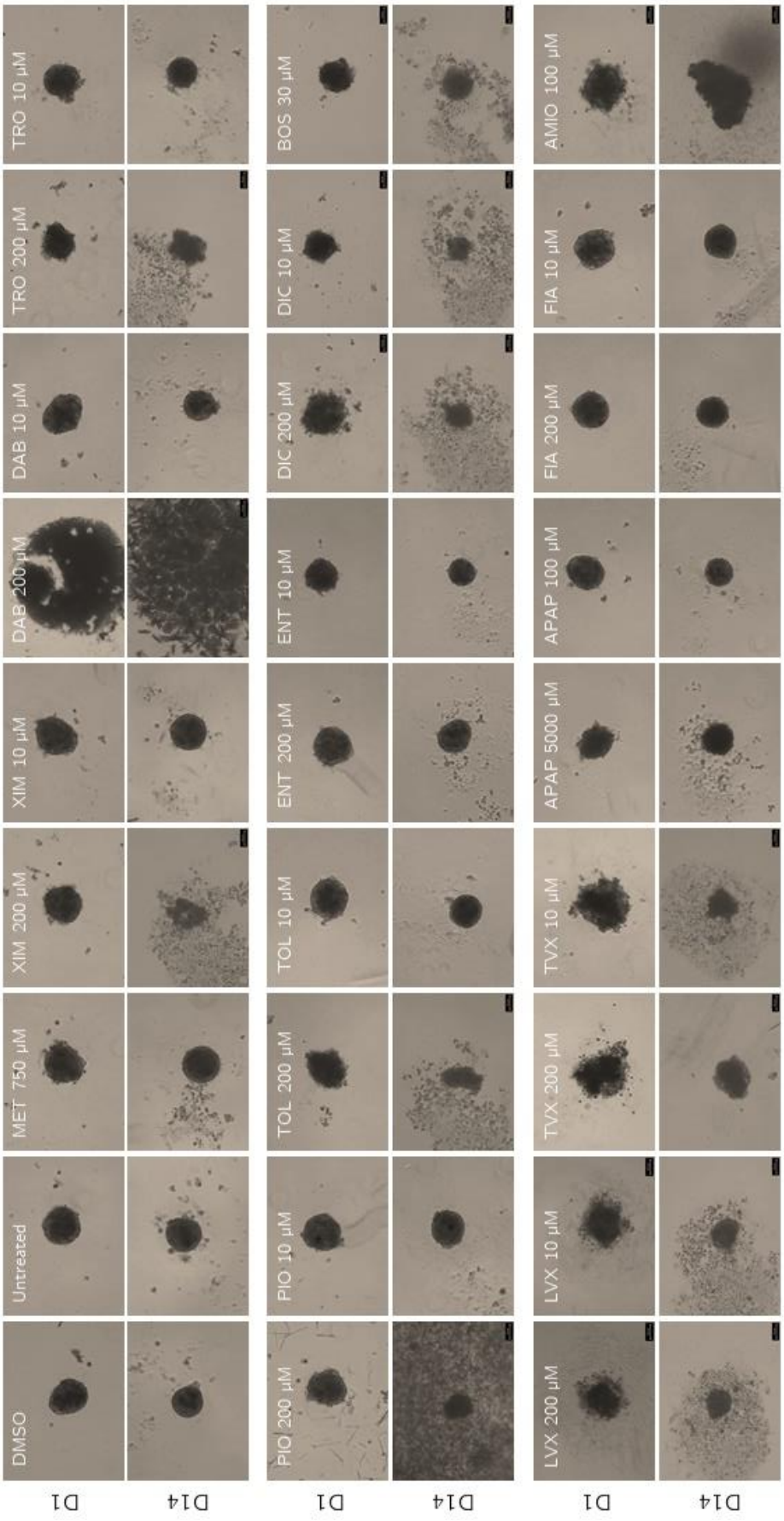

Figure 71: Morphology of cocultured liver cells during treatment in 3D.

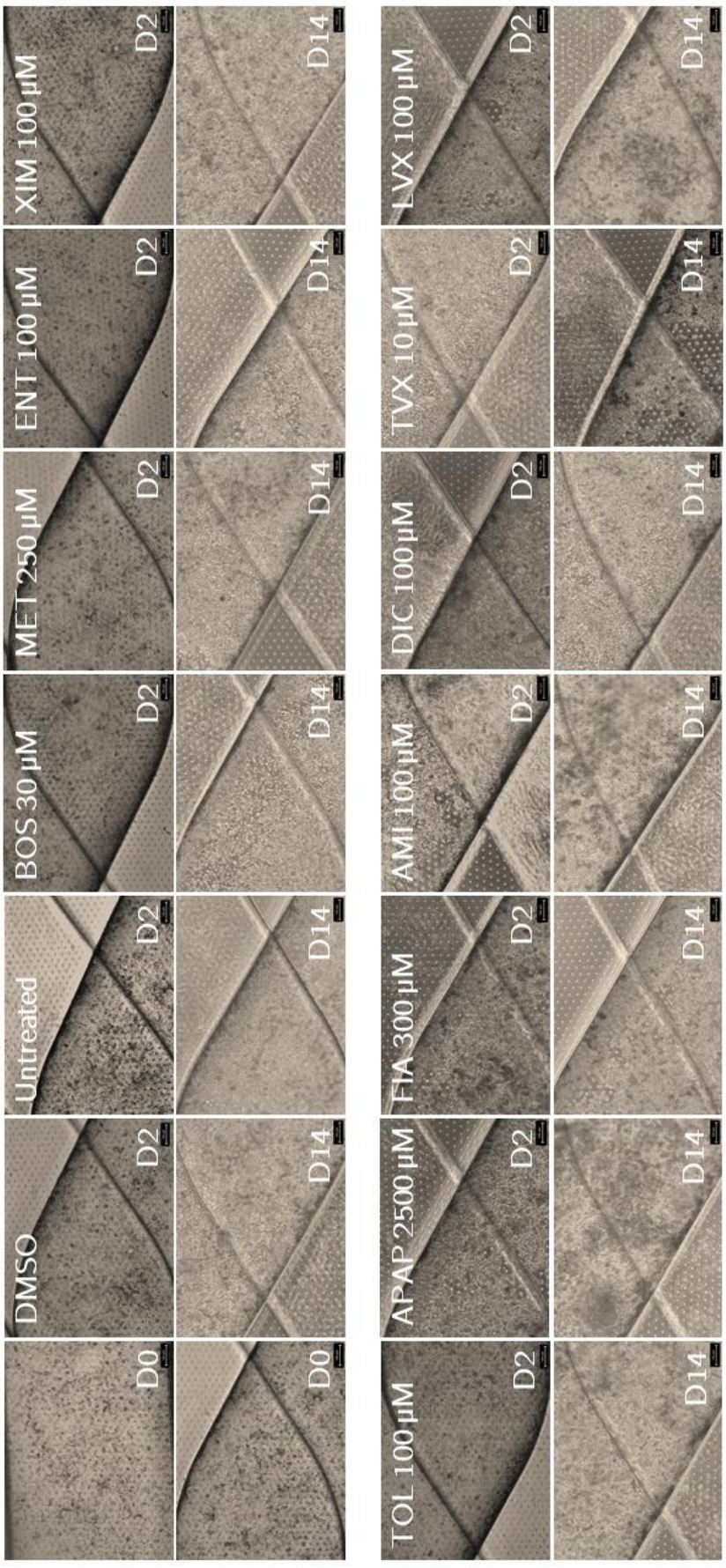

Figure 72: Morphology of cocultured liver cells during treatment in OOC.

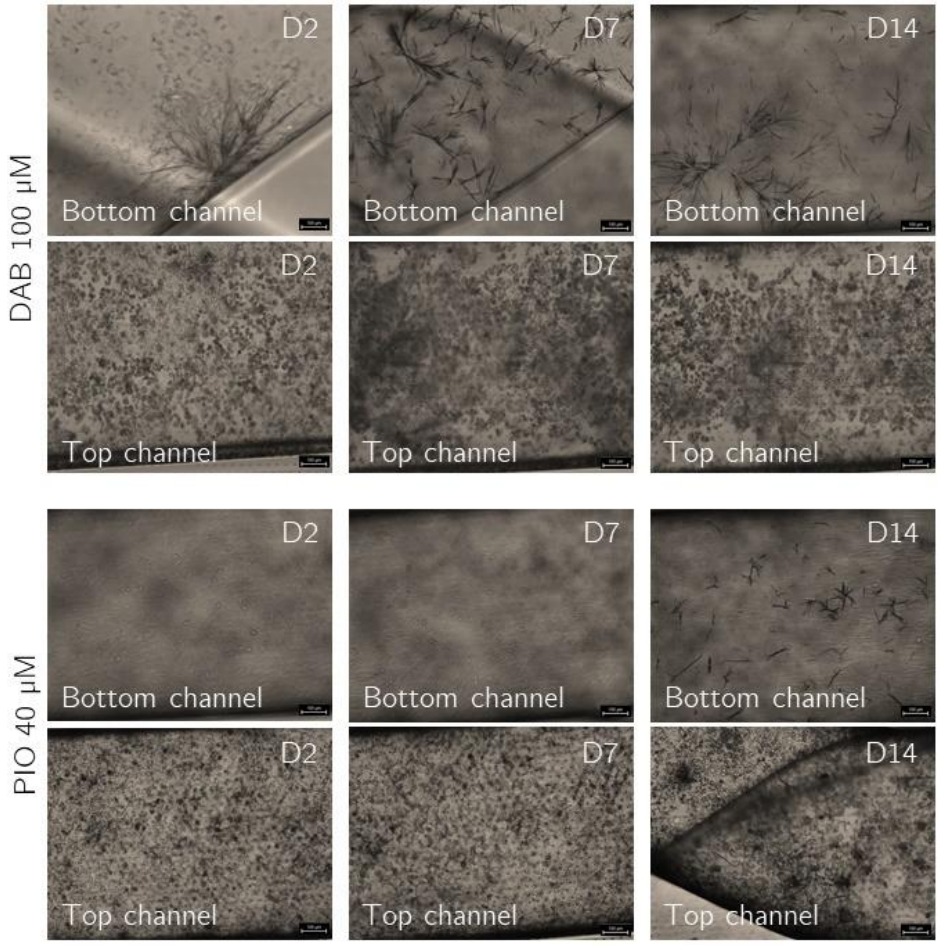

Figure 73: Time series of cultured liver cell treated with DAB and PIO in the OOC.
NPCs were cultured in the bottom channel and PHHs in the top channel. Cells were treated with 100 µM DAB and 40 µM PIO for 14 days. Scale bar 100 µm.

8.8 Protein expression during long-term cultivation of 2.5D and 3D

Appendix Table 14: Protein expression level of DMEs and transporters.
(Figure 46)

	PHH	2D						3D					
		PHH			PHH/LSEC			PHH			PHH/LSEC		
Protein	Thawed	D1	D7	D14	D1	D7	D14	D1	D7	D14	D1	D7	D14
CYP1A2	292590.77	165348.74	116719.65	102038.51	152016.28	47618.92	10797.91	162440.48	224809.93	213337.89	72798.23	145589.70	128275.81
CYP27A1	280578.15	247959.76	223560.96	178830.28	221132.72	176402.36	107169.61	167816.45	461962.73	580279.20	104870.60	207349.52	180376.08
CYP2C18	57245.55	94903.29	62967.07	65566.49	63250.12	55163.69	30552.45	38568.89	63667.25	33553.04	35033.90	32929.54	47591.54
CYP2C8	881963.66	330470.97	227638.49	273047.67	255890.30	120255.10	103185.36	121165.05	340752.50	338305.18	118211.99	196975.94	202311.54
CYP2C9	609708.11	377722.27	120814.33	112393.46	357521.68	73384.69	27898.60	523612.88	429031.38	465114.49	92802.87	306570.35	475470.35
CYP2E1	2864608.88	1895541.76	720408.39	697749.87	2123808.46	409360.18	119730.64	1118086.61	359105.46	259401.89	588999.32	230833.06	187789.80
SULT2A1	1505372.87	1341983.70	692710.05	514529.91	1222687.18	603675.70	429128.90	380263.54	903059.12	2135866.59	359424.31	567858.79	784462.01
UGT1A4	136684.11	178112.38	111824.02	69337.85	208021.99	153479.06	44524.54	174714.84	141596.92	120062.10	168384.42	171967.44	208602.02
UGT1A6	253010.95	486499.55	948721.33	584054.11	453291.11	868733.49	464660.62	554160.26	589140.23	480450.20	425098.81	415007.02	353256.08
UGT2B15	259428.89	374053.55	456616.26	330000.27	392148.06	472487.40	205960.14	310802.91	712780.25	674899.76	257585.54	352220.22	314272.94
UGT2B4	443334.21	968276.80	1008876.85	574279.98	856646.28	897034.04	321265.16	312406.97	1348878.12	1351965.79	435073.50	447753.59	367252.74
UGT2B7	365308.53	708729.08	744841.41	346319.16	642400.92	539547.11	168013.34	701396.70	669141.88	579530.82	330782.25	249339.03	178636.19
ABCB1	102945.99	182597.20	273392.28	274470.80	139964.92	322158.71	232003.04	161162.89	234118.45	139790.94	179491.87	196118.67	135719.01
ABCB8	37196.17	37325.58	53063.10	35249.12	34597.61	36474.27	29846.59	511881.02	69880.89	33757.60	64117.18	58562.84	69221.47
ABCC2	103026.29	192071.02	128901.76	91870.67	119723.64	117568.39	68772.62	117476.89	247381.75	233611.17	212503.18	126508.45	75147.57
ABCD1	21773.58	22090.49	30617.79	29969.79	23610.62	40442.55	32486.71	19330.15	32198.45	36803.36	16385.76	33580.76	56350.01
ABCD3	679659.98	700424.01	476030.25	410089.69	712647.74	699550.87	454913.21	265057.59	531078.21	619749.93	249621.51	321881.18	418861.26
ABCE1	248617.14	426427.19	284683.77	313140.35	384336.95	319884.35	370679.13	255395.04	327393.02	283883.56	292717.90	243036.83	268562.77
ABCF1	193876.76	258255.45	187053.64	197644.22	245517.36	198558.04	175394.10	99351.82	197831.95	160974.64	156104.07	146538.78	132336.52
ABCF3	63879.40	85573.99	91957.08	86146.79	75541.29	68478.77	85185.78	72954.47	92359.36	97020.19	36927.30	20125.99	28922.72

8.9 Gene expression of potential markers after treatment

Appendix Table 15: Background-corrected and housekeeper normalized MFI of DILI genes in the 3D model.
Expression was analyzed with the QuantiGene™ Plex Assay. N=4

Sample	CDH5				CSF1				FABP1				FASLG				GLUD1				GSTA1			
DMSO	0	-0	0	0.01	0.4	1.27	2.5	1.81	14.8	2.78	3.85	14.8	0	0	-0.1	0	2	1.5	1.52	2.7	3.02	0.7	1.29	1.74
Untreated	0	-0	0	-0.1	0.4	0.71	6.8	1.3	14.6	2.77	35.1	24.6	0	-0	-0.4	-0	3	1.2	13.1	4.5	1.14	0.2	0	2.56
MET 750 µM	0	-0	0	0	0.8	0.87	0.8	1.27	6.05	7.9	11.4	12.4	0	0.02	-0	0.03	2.2	3.7	4.02	4.3	2.25	6	3.88	4.76
DAB 10 µM	0	-0.6	-0	0.01	0.4	0	0.5	1.63	9.46	1.26	0.45	4.13	0	1.26	-0.1	0	1.4	1.3	0.34	1.3	1.82	0	0	0.19
DAB 100 µM	0	-0	-2	0.5	0.8	0.54	3	-0.8	13.7	45.5	-0.5	-1.75	0	0	-4	0	1.2	2.8	-1.5	4.5	3.61	9.8	-2	-1.5
PIO 10 µM	0	-0	-0	0.01	0.3	0.35	0.5	0.3	39.8	31.8	44.2	5.57	0.01	0	-0	0	1.9	1.2	1.35	2.2	0.98	0.3	0.84	1.71
ENT 10 µM	0.01	0.03	0	0	3.4	0.79	1.6	1.35	0.19	10.5	17.7	18.3	0	0.01	-0.1	0.02	0.3	2.1	3.2	3.8	0.22	2.7	5.37	4.39
ENT 100 µM	0.01	0.48	-0.4	0.02	0.3	0.48	0.7	0.98	15.3	1.92	-0.55	2.34	0	0	-0.7	0.05	2.5	0	0.55	1.3	6.78	0	-0.44	3.08
ENT 200 µM	0	0.45	-2	-0.1	0.3	0	-3	0.07	15.6	2.71	-0.5	0.83	0	0.9	-4	0	2.5	0	-3.5	0.3	4.88	-0.9	-2	-0.1
XIM 10 µM	0	0	-0.2	-0	0.4	0.3	2.5	2.08	18.8	9.16	23.7	19.4	0	0	-0.3	0.01	2.1	1.3	6.01	4.2	2.76	3.2	4.78	3.71
XIM 100 µM	0.06	0.01	-0.2	0	0.5	0.1	1.1	0.24	8.95	0	-0.31	0	0.06	0	-0.4	0.02	1.4	0	-0.2	0.1	1.96	0	0	0
XIM 200 µM	-0	-0.1	-0.3	-0	3.2	0.9	0.6	1.65	1.2	0.23	-0.06	0.06	-0	-0.2	-0.5	0	1.2	0.2	0.31	0.3	0.04	0	-0.25	0.02
TRO 10 µM	0	0.02	-0	-0	0.2	0.75	0.5	0.25	20.7	8.81	54	38	0	-0	-0.1	0	0.8	1.5	1.92	1.4	0.17	1.5	0.33	0.24
TRO 100 µM	0	-0.2	-0.7	-0.4	0.2	1.22	1	-0.3	33.1	6.65	0.5	0.07	0	-0.1	-1.3	0.13	1.2	1.2	0.83	1.7	0.82	1	-0.33	-0.4
TRO 200 µM	-0.2	-0.5			0.7	0			1.15	0			0	0			0.7	0			-0.5	-1		
TOL 10 µM	0	-0	-0.1	0.03	0.4	1.24	1.6	1.08	12	6.45	8.33	15	0	-0	-0.3	0	1.9	1.6	3.04	2.2	6.05	1.1	4.44	2.79
TOL 100 µM	0.01	0		-0.8	0.5	1.9		-0.1	7.82	1.26		8.38	0	0		0.5	1.1	1		2.5	1.02	0		0.25
TOL 200 µM	-0.1	1		0	0.1	2		-0.1	12.5	2		14.8	-0.1	-2		0.38	1	4		1.4	1.67	0		0.63
APAP 100 µM	0.01	0.02	-0.1	-0	0.7	0.91	2.3	0.78	0.39	8.6	3.68	5.69	0.01	0.04	-0.1	-0	0.5	2.9	1.18	1.7	0.67	7.6	3.01	6.41
APAP 2500 µM		0.69	-0.1	-0.1		2.77	0.7	3.54		1.39	0.05	0.09		0	-0.1	-0.1		4.2	0.02	0.6		1.4	0.07	0.69
APAP 5000 µM	0.01		-0.6	-0.3	0.3	-1.7	0.9	6.69	1.93	2.89	-0.14	3.83	0	1.15	-1.2	0.5	0.7	0	0.72	1.1	4.71	3.5	-0.58	1.35
FIA 10 µM	0.03	0	0		0.5	0.43	1.3		5.75	3.16	4.29		0	0	-0.4		1.2	1.5	2.62		1.81	1.4	3.36	
FIA 100 µM		0.01	-0			0.5	0.4			0.84	10.4			0.02	-0.1			0.9	1.01			1.5	0.27	
FIA 200 µM	0.01	0.03	-0.3		0.8	1.01	1.1		0.4	2.24	1.43		0	0	-0.5		0.5	2.9	2.55		0.59	1.9	1.99	
DIC 10 µM		0.01	0	-0		0.45	0.9	1.13		7.29	21.9	31.7		0	-0.2	0.02		1.4	2.04	4.9		2.7	4.71	8.53
DIC 100 µM		0.01		0		0.14		0.42		14.5		19		-0		0		2.2		2.5		8.4		5.4
DIC 200 µM		-0	0	-0		0.41	0.4	0.31		28	10.1	17.7		0	-0.3	0.01		2.3	3.74	1.9		1.3	5.24	1.19
TXV 10 µM		0.03	0	0.05		1.51	0.7	0.55		4.67	12.8	19.2		0.07	-0.3	0.01		1.9	1.97	2.5		2.2	5.18	5.33
TXV 100 µM		-0.1	0	-0.1		0.77	0	0.09		0.7	20.3	10.5		0.42	-0.8	0.1		1.8	2.19	1.6		2.4	18.2	7.16
TXV 200 µM		0.63	0	-0.2		1.26	-0.5	0.28		5.04	0.75	29.4		0	-2	-0.4		3.8	-0.8	4.2		1.3	-1	7.89
LVX 10 µM		0.02	-0.3	-0		0.61	7.9	0.87		5.83	42.9	19		0.01	-0.6	0.04		1.7	9.62	3.2		1.4	2.68	4.6
LVX 100 µM		0	0	-0		0.38	4.8	1.01		13.6	27.4	22.4		0.02	0	0.01		2.5	8.57	4.2		3.9	5.12	5.63
LVX 200 µM		0.01	0	0		0.42	4	0.66		7.08	16.6	15.2		0.01	-0.3	0.01		1.7	6.49	2.4		3.4	3.33	4.96
AMIO 100 µM		0.12		0		0.73		0.31		1.09		1.69		0.49		0		1.7		1.6		0.5		0.63
BOS 30 µM		0	-0.4	-0.2		0.43	1.5	1.79		2.05	1.16	1.9		0.01	-0.9	0.32		1.1	4.34	2.2		1	-0.42	0.59

Sample	HMGB1				ITGB3				KRT18				SDHA				SPP1			
DMSO	0.24	0.21	0.11	0.25	0.2	0.56	0.6	0.45	1.74	1.68	0.86	2.2	1.7	1.52	1.51	2.55	0.3	0.4	7.94	7.5
Untreated	0.31	0.22	0.07	0.03	0.1	0.31	0.5	0.37	2.56	2.19	1.9	2.3	2.32	1.73	10.7	3.27	0.7	2.4	31.6	4.9
MET 750 µM	0.35	0.31	0.34	0.3	0.3	0.58	0.4	0.75	2.18	2.33	0.91	1.59	2.2	3.32	2.24	3.36	0.7	2.6	1.12	4.4
DAB 10 µM	0.25	-1.3	-0	0.23	0.2	-1.3	0.1	0.66	1.77	0.94	0.02	1.46	1.5	-0.6	0.04	1.75	0.2	-0.6	3.39	6
DAB 100 µM	0.33	0.32	-2	-2.3	0.3	0.41	1	-1.5	1.1	0.94	1	-1	1.75	3.82	-2	-3.5	0.1	0	-0.5	-2.3
PIO 10 µM	0.33	0.15	0.25	0.46	0.1	0.44	0.5	0.11	2.33	1.42	1.08	1.45	2	1.89	2.3	2.57	0.1	0.1	0.19	0
ENT 10 µM	0.2	0.27	0.11	0.37	5	0.46	0.4	0.49	0.6	1.27	1.44	1.48	1.05	1.9	2.71	2.51	0	0.6	6.14	4.5
ENT 100 µM	0.32	-1	0	0.24	0.2	0	0.2	0.68	2.18	0.24	0.22	0.78	1.57	0.48	-0.4	3.51	0.1	0.5	-0.1	0.9
ENT 200 µM	0.32	-0.5	-1	-0.2	0.2	0.9	-1	-0.1	2.44	0.68	-1	-0.1	2.04	-0.5	-2	-0.1	0.1	-0.5	-0.5	0.6
XIM 10 µM	0.27	0.22	0.3	0.36	0.1	0.32	0.8	0.47	1.88	1.67	2.01	1.85	1.83	1.54	4.03	2.78	0.1	0	7.57	2.4
XIM 100 µM	0.32	-0	-0.4	0	0.3	0.06	0.4	0.11	1.39	0	0.12	0	1.29	0.01	-0.2	0	0.2	0	1.16	0.1
XIM 200 µM	0	-0.5	-0.1	-0.1	2.4	0.9	0.3	1.17	0.12	0.17	0.12	0	1.36	0.11	-0.3	0.17	1.4	-0.1	0.18	2.8
TRO 10 µM	0.27	0.18	0.29	0.22	0.1	0.62	0.8	0.28	2.56	2.06	1.19	1.62	1.39	1.84	2.29	2.31	0.2	0.5	0.27	0.2
TRO 100 µM	0.34	0	-0.3	-0.7	0.4	2.31	0.3	-0.1	1.61	1.12	0.33	-0.26	2	1.63	-0.7	-0.1	0.1	0.1	-0.2	-0.6
TRO 200 µM	0	-2			0	-1.5			0	0.75			1.38	-1.5			-0.2	-1.5		
TOL 10 µM	0.32	0.24	0.2	0.47	0.3	0.72	0.7	0.65	2.02	1.44	1.5	1.04	2.26	1.74	3	2.16	0.1	0.8	4.28	7.3
TOL 100 µM	0.24	0		-1.6	0.2	0		-1.3	2.43	0.47		0	1.34	-0.3		-1.3	1.4	0.3		-1.6
TOL 200 µM	0.08	-2		0.19	0.1	0		-0.6	1.52	1.5		0.25	2.05	-3		-0.3	-0	-1		-0.8
APAP 100 µM	0.17	0.13	0.1	0.21	0.3	0.86	1.1	0.43	1.58	1.16	0.24	1.79	1.24	3.33	0.65	1.76	0.4	0.2	1.83	0.8
APAP 2500 µM		-1.4	0	-0		0	2.7	11.9		2.43	0.04	0.52		-0.7	0	0.92		0	0.05	-0.1
APAP 5000 µM	0.17	0	-0.3	0.63	0.3	-1.2	2.6	12.5	2.03	-2.31	0.29	0.84	0.98	-0.9	-0.6	2.44	1.3	-1.7	-0.1	0.6
FIA 10 µM	0.23	0.14	0.1		0.3	0.14	1		2.48	1.5	1.68		1.62	1.92	3.16		2.3	0	0.15	
FIA 100 µM		0.18	0.05			0.31	0.2			1.25	0.58			2.01	1.23			0	-0	
FIA 200 µM	0.19	-0.1	0.12		0.4	0.42	1.1		1.64	1.1	0.87		1.35	7.44	2.24		1	0	0.19	
DIC 10 µM		0.28	0	0.35		0.3	0.2	0.71		1.69	0.83	1.73		1.52	1.32	3.2		0.1	1.74	7.5
DIC 100 µM		0.2		0.27		0.1		0.13		1.36		1.43		2.38		2.54		0.1		0.5
DIC 200 µM		0.07	0.08	0.19		0.64	0.2	0.5		1.5	0.69	1.53		3.27	2.47	2.98		0	-0	0.1
TXV 10 µM		0.46	0.15	0.26		0.33	0.4	0.35		2.39	0.54	1.01		2.6	1.16	1.93		0.1	4.75	2.2
TXV 100 µM		0.07	0.63	0.19		0.14	0.2	0		2.89	1.88	2.62		3.42	5.84	3		0.1	0.31	0
TXV 200 µM		-1.3	0.5	-1		-1.3	0	-0.6		0.94	0.5	1.1		-1.9	-0.5	5.69		0.6	0.25	2.1
LVX 10 µM		0.25	0.45	0.1		0.28	2.5	0.22		1.65	1.94	1.52		1.44	11.3	2.04		0.3	13	3.5
LVX 100 µM		0.29	-0.1	0.22		0.24	2.4	0.57		2.2	4.07	2.45		1.6	5.49	3.02		0.1	1.47	1.5
LVX 200 µM		0.18	-0.1	0.14		0.13	3.3	0.74		2.08	1.32	1.86		1.87	5.14	2.5		0	7.81	2
AMIO 100 µM		0		0.31		0.49		0.63		0.91		0.13		0.12		0.63		0.9		-0.1
BOS 30 µM		0.23	0.21	0.72		0.3	1.5	0.48		1.26	0.63	0.11		1.19	2.12	3.21		0.1	0.32	0.2

Appendix Table 16: Background-corrected and housekeeper normalized MFI of DILI genes in the 2.5D model.

Expression was analyzed with the QuantiGene™ Plex Assay. N=4

Sample	CDH5				CSF1				FABP1				FASLG				GLUD1				GSTA1			
DMSO	0.141	0.016	0.014	0.004	1.470	0.366	0.376	0.942	0.884	5.149	1.337	20.307	0.000	0.001	-0.001	0.000	0.616	1.326	0.718	2.393	0.101	0.478	0.183	0.584
Untreated	0.370	0.066	0.348	0.023	0.746	0.375	0.684	0.860	0.772	2.365	2.368	1.850	0.001	0.004	0.000	0.000	0.559	1.020	0.880	1.126	0.089	0.204	0.045	0.013
MET 750 µM	0.306	0.503	0.595	0.025	0.924	0.533	0.576	0.948	0.408	2.159	2.828	2.182	0.000	0.002	-0.001	0.000	0.523	1.438	1.298	1.401	0.145	1.272	0.872	0.111
DAB 10 µM	0.004	0.026	0.027	0.348	0.556	0.401	0.605	0.017	0.076	3.020	1.403	1.168	-0.001	0.002	-0.003	12.757	0.446	0.866	0.795	0.001	0.239	0.249	0.227	1.666
DAB 100 µM	0.046	1.442	-0.083	2.104	0.605	1.923	-0.041	0.014	0.302	1.442	4.294	1.187	0.000	0.961	-0.166	0.276	0.467	3.846	0.436	0.001	0.165	0.000	-0.083	0.702
Dab 200 µM	0.012	0.572	0.000	0.425	0.541	1.144	0.341	0.001	0.293	2.288	8.931	0.681	-0.001	0.763	-0.455	0.839	0.466	1.907	1.195	0.001	0.161	-0.381	-0.228	0.696
PIO 10 µM	0.007	0.090	0.031	0.023	0.493	0.113	0.334	0.623	0.265	31.432	28.743	32.214	0.000	0.002	-0.003	0.001	0.494	2.827	1.090	1.488	0.221	1.142	0.206	0.123
PIO 100 µM	0.007	0.002	0.004	0.008	0.561	0.196	0.514	0.415	0.112	26.415	8.301	55.528	0.000	0.001	-0.002	0.000	0.516	1.460	0.596	2.154	0.222	0.467	0.269	0.830
PIO 200 µM	0.006	0.003	0.000	0.004	0.635	0.219	0.329	0.563	0.258	29.205	10.606	51.189	0.002	0.001	-0.004	0.000	0.512	1.449	0.578	2.075	0.280	0.462	0.331	0.364
ENT 10 µM	0.008	0.027	0.004	0.009	0.470	0.328	0.433	0.989	0.281	3.485	0.582	10.440	0.000	0.002	-0.002	0.001	0.476	1.060	0.738	1.715	0.299	0.384	0.145	0.288
ENT 100 µM	0.007	0.004	0.045	0.010	0.489	0.616	0.785	0.938	0.200	2.703	1.178	5.492	0.001	0.001	-0.090	-0.001	0.468	0.733	1.065	1.016	0.217	0.477	4.262	0.374
ENT 200 µM	0.000	0.195	0.000	-0.009	0.453	0.715	0.297	1.195	0.923	61.452	3.123	31.352	0.000	0.130	-0.170	0.051	0.432	2.079	0.616	2.671	0.122	0.390	0.000	0.171
XIM 10 µM	0.013	0.017	0.006	0.012	0.546	0.336	0.556	1.082	0.128	1.413	0.304	17.940	0.000	0.001	-0.002	0.000	0.491	0.820	0.750	2.101	0.214	0.291	0.172	0.437
XIM 100 µM	0.004	0.192	1.797	0.016	0.692	0.718	0.887	1.173	0.251	1.335	3.807	10.691	0.000	0.001	-0.030	0.001	0.549	0.803	0.884	1.514	0.171	0.294	0.089	0.139
XIM 200 µM	0.071	4.413	3.252	0.017	0.638	0.572	2.541	1.052	0.228	0.049	57.368	7.072	0.000	0.000	-0.407	0.000	0.476	1.124	4.116	1.304	0.193	0.000	0.000	0.100
TRO 10 µM	0.067	0.047	0.030	0.015	0.593	0.248	0.207	0.809	0.479	14.117	23.892	25.336	-0.001	0.002	-0.001	0.001	0.470	2.185	1.118	1.389	0.161	0.969	0.338	0.041
TRO 100 µM	0.025	0.004	0.000	-0.186	0.516	0.446	0.262	1.614	1.757	3.092	38.381	10.055	0.002	0.000	-0.039	0.124	0.509	0.830	1.419	2.669	0.217	0.102	1.376	-0.248
TRO 200 µM	0.041	0.968	0.000	-0.008	0.587	1.660	0.332	0.922	0.971	1.660	0.623	24.311	-0.012	0.553	-0.332	-0.016	0.509	2.213	1.038	2.132	0.163	0.553	-0.166	0.181
TOL 10 µM	0.011	0.049	0.006	0.004	0.596	0.386	0.382	1.004	0.478	3.905	1.543	15.243	0.001	0.001	-0.001	0.002	0.501	0.925	0.800	1.727	0.322	0.331	0.250	0.356
TOL 100 µM	0.005	0.005	0.000	-0.005	0.511	0.496	-0.045	1.020	0.208	0.303	0.068	7.589	-0.002	0.002	-0.182	0.002	0.436	0.680	-0.068	0.790	0.193	0.351	-0.182	0.116
TOL 200 µM	-0.005	0.408	0.000	0.060	0.532	2.449	0.117	0.723	0.265	6.532	26.159	49.579	0.000	0.816	-0.468	-0.040	0.499	7.348	0.761	0.422	0.211	0.000	-0.234	0.080
APAP 100 µM	0.001	0.024	0.016	0.001	0.480	0.225	0.451	0.762	0.080	8.000	1.050	14.983	0.000	0.002	-0.002	-0.001	0.397	1.641	0.900	1.800	0.458	1.837	1.232	2.192
APAP 2500 µM		0.054	0.000	-0.009		1.738	0.238	1.521		1.611	-0.024	0.279		0.018	-0.190	-0.002		1.339	-0.071	0.526		1.104	-0.095	0.118
APAP 5000 µM	0.007	0.220	0.000	-0.008	0.436	0.504	0.297	0.556	0.260	6.011	0.545	9.706	0.000	0.126	-0.396	0.016	0.459	1.133	0.050	0.977	0.241	0.472	-0.198	-0.032
FIA 10 µM	0.003	0.003	0.006	0.000	0.765	0.429	0.586	0.554	0.031	1.665	0.938	5.949	0.000	0.003	-0.002	0.000	0.399	0.889	0.696	1.462	0.192	0.565	0.390	1.014
FIA 100 µM		0.003	0.001	-0.002		0.945	0.885	0.659		0.058	0.049	0.300		0.002	-0.001	0.001		0.595	0.595	0.844		0.120	0.203	0.722
FIA 200 µM	0.005	0.003	0.000	-0.002	0.592	1.065	1.226	0.813	0.131	0.113	0.029	0.230	0.000	0.003	-0.003	0.002	0.428	0.545	0.684	0.802	0.230	0.199	0.192	0.509
DIC 10 µM		0.053	0.010	0.009		0.302	0.436	1.107		10.951	2.664	8.535		0.002	-0.001	0.000		1.632	0.970	1.447		1.030	0.491	0.251
DIC 100 µM			0.011	0.001			0.436	0.831			12.466	2.915			-0.001	0.001			1.416	0.999			0.990	0.071
DIC 200 µM		0.014	0.017	0.000		0.269	0.293	0.545		2.645	5.467	5.765		0.001	-0.001	0.001		1.037	1.649	1.524		0.211	2.025	0.117
TXV 10 µM		0.049	0.053	0.006		0.417	0.457	0.892		14.929	13.451	41.151		0.001	-0.005	0.000		1.923	1.848	1.639		2.197	2.216	1.714
TXV 100 µM		0.015	0.063	0.035		0.761	2.349	0.904		0.919	0.767	3.101		0.004	-0.125	0.006		0.787	0.767	0.535		2.259	3.257	1.291
TXV 200 µM		0.212	-2.000	-0.006		1.017	-3.000	1.019		1.907	-2.500	10.441		0.254	-4.000	-0.012		1.271	-3.500	1.316		1.398	0.000	0.024
LVX 10 µM		0.011	0.042	0.014		0.233	0.376	1.128		9.958	15.737	13.316		0.004	-0.001	0.001		2.112	1.858	1.888		1.566	1.634	0.317
LVX 100 µM		0.079	0.153	0.011		0.259	0.465	1.186		10.532	28.814	25.625		0.003	-0.003	0.001		1.882	1.982	1.945		1.383	1.639	0.548
LVX 200 µM		0.029	0.027	0.015		0.333	0.427	1.081		8.187	4.014	20.079		0.002	-0.001	0.001		1.520	0.873	1.315		1.379	0.990	0.447
AMIO 100 µM		0.288	0.000	-0.039		0.767	0.737	0.790		3.069	0.368	6.397		0.256	-2.947	0.395		1.151	6.263	1.856		0.384	0.000	-0.158
BOS 30 µM		0.039	0.039	0.013		0.341	1.127	1.524		1.244	0.696	0.073		0.002	-0.002	0.000		0.928	0.765	0.691		0.165	0.998	0.062

Sample	HMGB1				ITGB3				KRT18				SDHA				SPP1			
DMSO	0.101	0.348	0.265	0.302	0.990	0.240	0.291	0.131	3.678	2.344	2.505	1.757	1.475	1.573	1.175	1.142	9.948	0.115	0.448	1.080
Untreated	0.194	0.351	0.367	0.295	0.600	0.150	0.383	0.137	4.153	2.715	2.157	1.444	1.205	1.321	1.451	1.104	####	0.404	4.204	3.929
MET 750 µM	0.176	0.323	0.298	0.237	0.694	0.508	0.545	0.110	4.669	2.074	1.658	0.733	1.216	1.584	1.560	1.253	####	0.259	1.673	0.668
DAB 10 µM	0.218	0.311	0.290	0.247	0.387	0.282	0.750	0.295	3.102	2.547	2.352	0.144	1.072	1.251	1.406	2.078	3.168	0.145	1.329	1.309
DAB 100 µM	0.194	####	-0.041	0.001	0.567	####	0.041	0.277	4.054	0.721	0.705	0.499	1.077	####	0.083	0.412	4.599	1.442	0.145	0.639
Dab 200 µM	0.248	0.763	-0.114	0.011	0.519	0.381	0.341	0.337	3.382	1.049	2.162	1.014	1.018	####	0.228	0.112	2.148	0.954	0.171	0.763
PIO 10 µM	0.230	0.387	0.221	0.222	0.514	0.126	0.447	0.112	3.858	1.656	2.194	1.499	1.170	2.285	1.572	1.383	2.273	0.066	0.199	0.581
PIO 100 µM	0.247	0.267	0.161	0.278	0.615	0.167	0.539	0.103	3.285	1.925	1.417	1.896	1.132	1.703	1.370	1.922	1.632	0.163	0.033	0.158
PIO 200 µM	0.202	0.288	0.171	0.295	0.735	0.190	0.420	0.100	3.236	2.032	1.437	1.740	1.155	1.952	1.331	2.021	1.241	0.178	0.028	0.393
ENT 10 µM	0.217	0.322	0.272	0.255	0.337	0.178	0.469	0.128	3.669	2.242	2.050	2.027	1.025	1.388	1.200	1.110	2.461	0.182	0.657	2.564
ENT 100 µM	0.234	0.245	0.067	0.310	0.375	0.508	1.368	0.093	3.628	3.063	2.086	2.287	1.045	1.115	2.153	1.299	2.379	0.578	0.123	0.344
ENT 200 µM	0.151	0.130	0.042	0.137	0.277	0.130	0.127	0.068	3.615	1.007	1.742	2.475	0.952	0.844	0.340	1.502	2.759	0.195	0.064	3.942
XIM 10 µM	0.226	0.323	0.326	0.275	0.422	0.323	0.716	0.138	3.534	2.576	2.299	1.790	1.205	1.231	1.244	1.285	3.084	0.119	0.523	1.658
XIM 100 µM	0.199	0.278	0.082	0.289	0.573	0.870	1.499	0.113	4.405	2.131	0.716	1.973	1.364	1.122	1.193	1.333	5.927	0.278	1.406	1.845
XIM 200 µM	0.205	0.281	0.102	0.300	0.447	2.317	2.744	0.122	3.755	0.195	0.305	1.411	1.180	1.218	1.829	1.086	5.155	0.261	1.169	1.180
TRO 10 µM	0.196	0.360	0.301	0.222	0.488	0.154	0.394	0.121	3.570	1.641	1.791	1.652	1.103	1.829	1.497	1.095	4.760	0.096	0.194	0.314
TRO 100 µM	0.228	0.316	0.087	-1.365	0.440	0.914	0.048	####	3.442	1.748	0.765	0.621	1.101	1.244	1.976	0.124	3.446	0.081	0.015	0.745
TRO 200 µM	0.110	0.830	-0.083	0.016	0.387	0.830	-0.083	0.099	4.051	1.038	0.415	1.876	1.075	0.138	0.000	1.481	6.620	1.245	0.125	2.880
TOL 10 µM	0.250	0.309	0.355	0.264	0.534	0.245	0.373	0.137	2.987	2.559	2.402	1.920	1.129	1.338	1.167	1.147	2.164	0.146	0.375	2.699
TOL 100 µM	0.210	0.264	0.045	0.183	0.386	0.589	-0.045	0.564	3.431	2.311	0.136	1.625	1.010	1.058	-0.091	1.071	2.380	0.228	0.068	0.137
TOL 200 µM	0.190	0.816	0.117	-0.361	0.496	0.816	0.117	0.602	4.075	1.429	0.351	1.887	1.123	0.408	0.000	0.201	2.534	0.408	-0.059	0.040
APAP 100 µM	0.231	0.324	0.324	0.320	0.480	0.152	0.548	0.189	3.285	1.247	1.657	1.226	0.948	1.566	1.298	1.417	0.767	0.068	0.848	0.666
APAP 2500 µM		0.235	-0.048	0.173		5.520	0.333	2.219		2.199	0.048	0.477		1.520	0.000	1.247		0.072	0.071	0.012
APAP 5000 µM	0.236	0.283	0.099	0.079	0.457	0.189	0.099	0.064	4.087	2.345	0.693	2.367	1.016	1.039	0.000	0.270	2.354	0.283	0.149	1.319
FIA 10 µM	0.176	0.305	0.293	0.305	0.332	0.244	0.414	0.094	1.765	2.551	1.813	1.421	1.299	1.456	1.345	1.582	0.910	0.042	0.012	0.068
FIA 100 µM		0.216	0.240	0.197		0.587	0.742	0.088		1.392	1.245	0.848		1.394	1.329	1.590		0.008	0.005	0.047
FIA 200 µM	0.166	0.193	0.161	0.200	0.433	0.689	1.129	0.194	2.576	0.799	0.864	0.697	1.185	1.326	1.724	1.673	1.177	0.006	0.006	0.049
DIC 10 µM		0.316	0.318	0.293		0.154	0.379	0.128		2.042	1.890	1.753		1.411	1.352	1.078		0.156	0.916	1.957
DIC 100 µM			0.348	0.295			0.142	0.101			1.499	1.921			1.490	1.212			0.916	1.162
DIC 200 µM		0.381	0.340	0.287		0.168	0.147	0.106		2.984	1.308	1.497		1.454	1.723	1.563		0.338	0.708	0.504
TXV 10 µM		0.373	0.341	0.270		0.248	0.320	0.234		1.664	1.555	1.223		1.552	1.702	1.307		0.110	0.962	0.611
TXV 100 µM		0.401	0.282	0.351		0.515	0.658	0.131		2.737	2.787	3.836		1.506	2.913	1.579		0.231	0.110	####
TXV 200 µM		0.297	-1.000	-0.097		0.424	1.000	0.073		2.394	1.000	2.098		1.653	-2.000	0.982		0.127	-0.500	1.928
LVX 10 µM		0.434	0.349	0.300		0.161	0.271	0.167		2.072	1.317	1.870		1.662	1.607	1.096		0.092	1.868	1.594
LVX 100 µM		0.424	0.330	0.290		0.183	0.316	0.200		2.225	1.646	1.949		1.630	1.405	1.327		0.106	0.786	0.519
LVX 200 µM		0.370	0.298	0.264		0.261	0.450	0.121		3.092	2.237	1.478		1.606	1.170	1.116		0.089	0.335	0.471
AMIO 100 µM		0.320	-0.737	-1.027		0.448	-0.737	0.000		1.742	-0.737	0.711		0.480	-1.474	0.553		0.416	1.105	0.000
BOS 30 µM		0.349	0.383	0.380		0.194	0.893	1.519		2.894	0.584	0.419		1.214	1.487	0.988		0.289	1.805	0.348

Appendix Table 17: Background-corrected and housekeeper normalized MFI of DILI genes in the OOC model.
Expression was analyzed with the QuantiGene™ Plex Assay. N=3

Sample	CDH5			CSF1			FABP1			FASLG			GLUD1			GSTA1		
Untreated	2.173	0.9069	0.5847	0.7728	2.0682	0.6865	24.8816	27.5997	35.9496	0.0002	-0.0004	-0.0005	5.5437	3.9985	6.3377	0.2383	0.0541	0.1404
DMSO	1.838	1.1904	0.9789	0.6211	2.5375	1.024	24.2865	32.8472	38.726	0.0008	-0.0005	-0.0015	5.4371	4.1749	5.4634	0.5144	0.0592	0.2372
MET 250 µM	2.6091	2.1942	1.963	0.696	2.9581	0.7871	21.4583	14.892	29.4338	0.0006	-0.0008	-0.0013	5.3581	5.1158	6.3872	0.3935	0.0417	0.3036
ENT 80 µM	2.2608	1.2798	0.64	0.7092	2.4748	1.1499	18.7098	30.4217	24.1223	0.0002	-0.0004	-0.0014	5.473	4.7301	4.0028	0.9846	0.1945	0.6047
BOS 30 µM	1.1227	0.2814	0.4087	0.5359	1.9114	1.1133	26.278	44.2882	23.6786	0.0005	-0.0014	0.0055	4.4638	4.9801	4.3651	3.137	1.2685	1.0859
XIM 100 µM	2.3408	1.6129	1.031	0.6323	2.5028	1.3437	27.8895	1.2489	43.4571	0.0006	-0.0009	-0.0013	5.4204	1.4116	5.3936	0.9279	0	0.3141
TOL 100 µM	3.2512	1.0553	1.8486	0.6351	2.5098	1.121	19.9746	0.0248	0.1323	0.0004	-0.0026	-0.007	3.531	1.4771	1.4745	0.4708	-0.0017	-0.0022
FIA 300 µM	3.3636	2.2044	1.4638	0.6493	2.3337	1.4983	0.7859	0.7172	0.0997	0.0021	-0.0023	0.0017	1.4073	1.6569	1.5074	0.1599	0.0092	0.0393
APAP 2500 µM	0.2652	0.8169	1.1949	1.4503	1.9064	1.0594	0.2995	30.7072	1.6921	0	-0.0004	-0.003	1.3861	4.2617	1.6275	-0.0214	0.1608	0.3585
AMIO 100 µM	2.3121	1.402	0.5866	0.7168	2.0966	0.9755	18.4947	27.421	31.5469	0.0001	-0.0004	-0.0011	3.7938	3.7362	5.1553	1.0748	0.2306	0.1504
DIC 100 µM	1.6306	0.8079	0.6145	0.5254	3.1299	0.9968	21.2895	0.5702	29.4402	0.0007	-0.0028	-0.0004	5.255	1.4157	4.2794	1.4587	-0.0009	0.4998
TXX 10 µM	1.1771	0.4644	2.4933	0.8384	2.9505	0.6336	29.7234	53.7581	44.8121	0.0014	-0.0012	-0.0014	4.658	3.2045	4.7228	1.119	0.1405	0.3471
LVX 100 µM	2.098	0.1944	0.6651	0.8831	2.5042	0.92	22.8904	69.7306	33.2013	0	-0.0014	-0.001	4.9728	5.9371	5.0912	1.061	0.0778	0.1874

Sample	HMGB1			ITGB3			KRT18			SDHA			SPP1		
Untreated	0.7659	0.5542	0.6935	0.6897	0.3327	0.3872	1.7825	1.6277	2.2427	3.9324	2.6867	3.7109	0.1633	0.2035	0.3142
DMSO	0.6977	0.5459	0.6394	0.577	0.4879	0.4646	1.8097	1.1659	1.8994	3.9291	2.7347	3.0564	0.1758	0.1405	0.1824
MET 250 µM	0.6822	0.5541	0.699	0.7119	0.6861	0.6086	1.7598	0.7235	2.0258	3.8793	3.1004	4.0379	0.1905	0.2827	0.2688
ENT 80 µM	0.7033	0.5357	0.5591	0.5856	0.4879	0.403	2.0106	1.8597	3.6404	3.7863	3.2119	2.7294	0.2016	0.1989	0.1405
BOS 30 µM	0.618	0.4582	0.6355	0.4302	0.3885	0.303	2.19	1.9086	2.0824	3.6451	3.9469	2.7217	0.0575	0.1148	0.3195
XIM 100 µM	0.6548	0.4926	0.7023	0.5327	0.4469	0.4054	1.8038	0.5271	1.4661	3.3161	1.2006	2.835	0.0685	0.0717	0.1405
TOL 100 µM	0.6065	0.4406	0.4475	0.4887	0.5729	0.6199	1.2547	0.2342	0.3754	2.9271	1.569	1.2679	0.0698	0.0688	0.058
FIA 300 µM	0.3311	0.3636	0.4422	1.3794	0.8711	0.8055	0.4832	0.5806	0.5781	1.8854	1.9177	1.595	0.0957	0.1297	0.1053
APAP 2500 µM	0.3123	0.5662	0.4393	0.3465	0.4206	0.7063	0.693	1.481	0.9398	1.2749	2.4179	1.6573	0.0257	0.0975	0.3638
AMIO 100 µM	0.5026	0.5587	0.6175	0.7286	0.5517	0.418	1.8458	1.1515	2	2.9846	2.4987	3.0539	0.0412	0.0997	0.1555
DIC 100 µM	0.7617	0.3905	0.5674	0.5818	0.6106	0.3407	1.7839	0.6584	2.5527	3.9239	1.4422	2.9093	0.1584	0.0813	0.2252
TXX 10 µM	0.629	0.4777	0.6036	0.6236	0.4838	0.4728	1.6954	1.0045	1.4775	3.1171	2.2905	2.6516	0.0394	0.053	0.0528
LVX 100 µM	0.5657	0.5058	0.6364	0.5968	0.4142	0.4758	1.9945	1.7786	1.8227	3.2098	3.9301	2.902	0.0553	0.0701	0.135

Appendix Table 18: Fold change in CSF1 expression after 14 days treatment in 2.5D, 3D, and OOC.
(Figure 55 A)

CSF1	2.5D				3D				OOC		
DMSO	1.00	1.00	1.00	1.00	1.00	1.00	1.00	1.00	1.00	1.00	1.00
Untreated	1.00	1.00	1.00	1.00	1.00	1.00	1.00	1.00	1.00	1.00	1.00
MET	1.24	1.42	0.84	1.10	1.77	1.23	0.12	0.98	0.90	1.43	1.15
DAB	0.38	1.10	1.61	1.24	1.05		0.21	0.90	ND	ND	ND
PIO	0.34	0.31	0.89	0.66	0.63	0.28	0.21	0.17	ND	ND	ND
ENT	0.33	1.68	2.09	1.00	0.72	0.38	0.26	0.54	1.14	0.98	1.12
XIM	0.47	1.96	2.36	1.25	1.28	0.08	0.44	0.13	1.02	0.99	1.31
TRO	0.40	0.68	0.55	0.86	0.39	0.59	0.19	0.14	ND	ND	ND
TOL	0.35	1.36	ND	1.08	1.09	1.50	ND	ND	1.02	0.99	1.10
APAP	0.30	1.37	0.79	0.59	0.76	ND	0.35	3.71	2.34	0.75	1.04
FIA	ND	ND	2.35	0.70	ND	0.39	0.15	ND	1.05	0.92	1.46
DIC	ND	ND	1.16	0.88	ND	0.11	ND	0.23	0.85	1.23	0.97
TXV	ND	1.14	1.22	0.95	ND	1.20	0.28	0.30	1.35	1.16	0.62
LVX	ND	0.71	1.24	1.26	ND	0.30	1.95	0.56	1.42	0.99	0.90
AMIO	ND	2.09	1.96	0.84	ND	0.58	ND	0.17	1.15	0.83	0.95
BOS	ND	0.93	3.00	1.62	ND	0.34	0.60	0.99	0.86	0.75	1.09

Appendix Table 19: Fold change in HMGB1 expression after 14 days treatment in 2.5D, 3D, and OOC.
(Figure 55 B)

HMGB1	2.5D				3D				OOC		
DMSO	1.00	1.00	1.00	1.00	1.00	1.00	1.00	1.00	1.00	1.00	1.00
Untreated	1.00	1.00	1.00	1.00	1.00	1.00	1.00	1.00	1.00	1.00	1.00
MET	0.91	0.92	0.81	0.80	1.12	1.39	4.77	ND	0.89	1.00	1.01
DAB	2.16	0.89	1.09	0.98	1.05	ND	ND	0.94	ND	ND	ND
PIO	2.28	1.11	0.83	0.73	1.37	0.70	2.28	1.85	ND	ND	ND
ENT	2.32	0.70	0.25	1.03	1.34	ND	0.00	0.97	1.01	0.98	0.87
XIM	1.97	0.80	0.31	0.96	1.31	ND	ND	ND	0.94	0.90	1.10
TRO	1.94	1.03	1.13	0.74	1.13	0.86	2.67	0.89	ND	ND	ND
TOL	2.08	0.76	0.17	0.61	1.01	ND	ND	ND	0.87	0.81	0.70
APAP	2.34	0.81	0.37	0.26	0.71	ND	ND	2.54	0.45	1.04	0.69
FIA	ND	ND	0.91	0.65	ND	0.86	0.46	ND	0.48	0.67	0.69
DIC	ND	ND	1.31	0.98	ND	0.95	ND	1.09	1.09	0.72	0.89
TXV	ND	1.07	1.29	0.89	ND	2.21	1.44	1.03	0.90	0.88	0.94
LVX	ND	1.22	1.24	0.96	ND	1.40	ND	0.88	0.81	0.93	1.00
AMIO	ND	0.92	ND	ND	ND	ND	ND	1.26	0.72	1.02	0.97
BOS	ND	1.00	1.44	1.26	ND	1.11	1.97	2.91	0.89	0.84	0.99

Appendix Table 20: Fold change in KRT18 expression after 14 days treatment in 2.5D, 3D, and OOC.
(Figure 55 C)

KRT18	2.5D				3D				OOC		
DMSO	1.00	1.00	1.00	1.00	1.00	1.00	1.00	1.00	1.00	1.00	1.00
Untreated	1.00	1.00	1.00	1.00	1.00	1.00	1.00	1.00	1.00	1.00	1.00
MET	1.12	0.76	0.77	0.51	0.85	1.06	0.48	0.69	0.99	0.45	0.90
DAB	0.84	1.09	0.94	1.18	1.02	0.56	0.02	0.66	ND	ND	ND
PIO	1.05	0.71	0.88	0.85	1.34	0.85	1.25	0.66	ND	ND	ND
ENT	0.99	1.31	0.83	1.30	1.26	0.14	0.25	0.35	1.11	1.60	1.92
XIM	1.20	0.91	0.29	1.12	0.80	ND	0.14	0.00	1.00	0.45	0.77
TRO	0.97	0.70	0.72	0.94	1.48	1.23	1.38	0.74	ND	ND	ND
TOL	0.93	0.99	0.05	0.93	1.40	0.28	0.00	0.00	0.69	0.20	0.20
APAP	1.11	1.00	0.28	1.35	1.17	ND	0.34	0.38	0.38	1.27	0.50
FIA	ND	ND	0.50	0.48	ND	0.74	0.68	ND	0.27	0.50	0.30
DIC	ND	ND	0.60	1.09	ND	0.81	ND	0.65	0.99	0.57	1.34
TXV	ND	0.71	0.62	0.70	ND	1.42	0.63	0.46	0.94	0.86	0.78
LVX	ND	0.95	0.66	1.11	ND	1.31	4.74	1.11	1.10	1.53	0.96
AMI	ND	0.74	ND	0.40	ND	0.54	0.00	0.06	1.02	0.99	1.05
BOS	ND	1.23	0.23	0.24	ND	0.75	0.74	0.05	1.21	1.64	1.10

Appendix Table 21: Fold change in SDHA expression after 14 days treatment in 2.5D, 3D, and OOC.
(Figure 55 D)

SDHA	2.5D				3D				OOC		
DMSO	1.0	1.0	1.0	1.0	1.0	1.0	1.0	1.0	1.0	1.0	1.0
Untreated	1.0	1.0	1.0	1.0	1.0	1.0	1.0	1.0	1.0	1.0	1.0
MET	1.0	1.2	1.1	1.1	0.9	1.9	0.2	1.0	1.0	1.2	1.1
DAB	0.7	0.8	1.2	1.1	0.9	ND	0.0	0.7	ND	ND	ND
PIO	0.8	1.5	1.3	1.2	1.2	1.2	1.5	1.0	ND	ND	ND
ENT	0.7	0.7	1.8	1.1	0.9	0.3	ND	1.4	1.0	1.2	0.9
XIM	0.9	0.7	1.0	1.2	0.8	0.0	ND	ND	0.8	0.4	0.9
TRO	0.7	1.2	1.3	1.0	0.8	1.2	1.5	0.9	ND	ND	ND
TOL	0.7	0.7	ND	0.9	0.8	ND	ND	ND	0.7	0.6	0.4
APAP	0.7	0.7	ND	0.2	0.6	ND	ND	1.0	0.3	0.9	0.5
FIA	ND	ND	1.1	1.4	ND	1.3	0.8	ND	0.5	0.7	0.5
DIC	ND	ND	1.3	1.1	ND	1.6	ND	1.0	1.0	0.5	1.0
TXV	ND	1.0	1.4	1.1	ND	1.7	0.8	0.8	0.8	0.8	0.9
LVX	ND	1.0	1.2	1.2	ND	1.1	3.7	1.2	0.8	1.4	0.9
AMIO	ND	0.3	ND	0.5	ND	0.1	ND	0.2	0.8	0.9	1.0
BOS	ND	0.8	1.3	0.9	ND	0.8	1.4	1.3	0.9	1.4	0.9

Appendix Table 22: Fold change in ITGB3 expression after 14 days treatment in 2.5D, 3D, and OOC.
(Figure 56 A)

ITGB3	2.5D				3D				OOC		
DMSO	1.00	1.00	1.00	1.00	1.00	1.00	1.00	1.00	1.00	1.00	1.00
Untreated	1.00	1.00	1.00	1.00	1.00	1.00	1.00	1.00	1.00	1.00	1.00
MET	1.16	3.39	1.42	0.80	2.42	1.88	0.87	2.01	1.03	2.06	1.57
DAB	0.39	1.18	2.57	1.10	1.03	ND	0.17	1.47	ND	ND	ND
PIO	0.52	0.52	1.53	0.86	0.65	0.79	0.79	0.23	ND	ND	ND
ENT	0.38	2.12	4.69	0.71	0.99	0.00	0.36	1.51	1.02	1.00	0.87
XIM	0.58	3.63	5.14	0.87	1.34	0.11	0.60	0.25	0.92	0.92	0.87
TRO	0.49	0.64	1.35	0.93	0.51	1.12	1.23	0.61	ND	ND	ND
TOL	0.39	2.45	ND	4.31	0.93	ND	ND	ND	0.85	1.17	1.33
APAP	0.46	0.79	0.34	0.49	1.26	ND	4.26	ND	0.60	0.86	1.52
FIA	ND	ND	2.55	0.67	ND	0.55	0.25	ND	2.39	1.79	1.73
DIC	ND	ND	0.49	0.77	ND	0.18	ND	0.28	1.01	1.25	0.73
TXV	ND	1.03	1.10	1.78	ND	0.59	0.63	0.78	1.08	0.99	1.02
LVX	ND	0.76	1.08	1.53	ND	0.42	3.89	1.28	1.03	0.85	1.02
AMIO	ND	1.86	ND	ND	ND	0.87	ND	1.40	1.26	1.13	0.90
BOS	ND	ND	3.07	11.59	ND	0.54	2.43	1.07	0.75	0.80	0.65

Appendix Table 23: Fold change in FABP1 expression after 14 days treatment in 2.5D, 3D, and OOC.
(Figure 56 B)

FABP1	2.5D				3D				OOC		
DMSO	1.00	1.00	1.00	1.00	1.00	1.00	1.00	1.00	1.00	1.00	1.00
Untreated	1.00	1.00	1.00	1.00	1.00	1.00	1.00	1.00	1.00	1.00	1.00
MET	0.53	0.91	1.19	1.18	0.53	0.91	1.19	1.18	0.86	0.54	0.82
DAB	0.09	0.59	1.05	0.63	0.09	0.59	1.05	0.63	ND	ND	ND
PIO	0.30	6.10	ND	1.59	0.30	6.10	ND	1.59	ND	ND	ND
ENT	0.23	0.53	0.88	0.27	0.23	0.53	0.88	0.27	0.77	0.93	0.62
XIM	0.28	0.26	2.85	0.53	0.28	0.26	2.85	0.53	1.15	0.04	1.12
TRO	0.54	2.74	ND	1.25	0.54	2.74	ND	1.25	ND	ND	ND
TOL	0.24	0.06	0.05	0.37	0.24	0.06	0.05	0.37	0.82	0.00	0.00
APAP	0.29	1.17	0.41	0.48	0.29	1.17	0.41	0.48	0.01	0.94	0.04
FIA	ND	ND	0.04	0.01	ND	ND	0.04	0.01	0.03	0.02	0.00
DIC	ND	ND	9.32	0.14	ND	ND	9.32	0.14	0.88	0.02	0.76
TXV	ND	2.90	10.06	2.03	ND	2.90	10.06	2.03	1.22	1.64	1.16
LVX	ND	2.05	ND	1.26	ND	2.05	ND	1.26	0.94	2.12	0.86
AMIO	ND	0.60	0.28	0.32	ND	0.60	0.28	0.32	0.76	0.84	0.82
BOS	ND	0.24	0.52	0.00	ND	0.24	0.52	0.00	1.08	1.35	0.61

Appendix Table 24: Fold change in GLUD1 expression after 14 days treatment in 2.5D, 3D, and OOC.
(Figure 56 C)

GLUD1	2.5D				3D				OOC		
DMSO	1.00	1.00	1.00	1.00	1.00	1.00	1.00	1.00	1.00	1.00	1.00
Untreated	1.00	1.00	1.00	1.00	1.00	1.00	1.00	1.00	1.00	1.00	1.00
MET	0.94	1.41	1.48	1.24	0.74	3.21	0.31	0.95	0.97	1.28	1.01
DAB	0.72	0.65	1.11	0.70	0.69	0.85	0.22	0.48	ND	ND	ND
PIO	0.80	2.13	1.52	0.62	0.98	0.79	0.89	0.81	ND	ND	ND
ENT	0.76	0.55	1.48	0.42	1.27	ND	0.36	0.49	1.01	1.13	0.73
XIM	0.89	0.61	1.23	0.63	0.70	0.03	ND	0.02	1.00	0.34	0.99
TRO	0.76	1.65	1.56	0.58	0.41	1.01	1.26	0.52	ND	ND	ND
TOL	0.71	0.51	ND	0.33	0.57	0.64	ND	0.94	0.65	0.35	0.27
APAP	0.74	0.85	0.07	0.41	0.36	ND	0.47	0.41	0.26	1.02	0.30
FIA	ND	ND	0.83	0.35	ND	0.64	0.66	ND	0.26	0.40	0.28
DIC	ND	ND	1.97	0.42	ND	1.49	ND	0.92	0.97	0.34	0.78
TXV	ND	1.45	2.58	0.68	ND	1.29	1.29	0.95	0.86	0.77	0.86
LVX	ND	1.42	2.76	0.81	ND	1.66	5.63	1.60	0.92	1.42	0.93
AMIO	ND	0.87	8.73	0.78	ND	1.15	ND	0.61	0.70	0.90	0.94
BOS	ND	0.70	1.07	0.29	ND	0.73	2.85	0.82	0.82	1.19	0.80

Appendix Table 25: Fold change in GSTA1 expression after 14 days treatment in 2.5D, 3D, and OOC.
(Figure 56 D)

GSTA1	2.5D				3D				OOC		
DMSO	1.00	1.00	1.00	1.00	1.00	1.00	1.00	1.00	1.00	1.00	1.00
Untreated	1.00	1.00	1.00	1.00	1.00	1.00	ND	1.00	1.00	1.00	1.00
MET	ND	6.25	ND	8.39	1.98	ND	ND	1.86	1.65	0.77	2.16
DAB	2.37	0.52	1.24	0.42	0.60	ND	ND	0.11	ND	ND	ND
PIO	2.19	2.39	1.13	0.21	0.32	0.39	0.65	0.98	ND	ND	ND
ENT	2.15	1.00	ND	0.64	2.24	ND	ND	1.77	1.91	3.28	2.55
XIM	1.69	0.61	0.49	0.24	0.65	ND	ND	ND	1.80	ND	1.32
TRO	1.60	2.03	1.85	0.07	0.06	2.08	0.25	0.14	ND	ND	ND
TOL	1.91	0.73	ND	0.20	0.34	ND	ND	0.14	0.92	ND	ND
APAP	2.38	0.99	ND	ND	1.56	4.79	ND	0.77	ND	2.72	1.51
FIA	ND	ND	1.11	1.24	ND	2.09	0.21	ND	0.31	0.16	0.17
DIC	ND	ND	5.42	0.12	ND	11.55	ND	3.10	2.84	ND	2.11
TXV	ND	4.60	12.13	2.93	ND	3.09	4.01	3.06	2.18	2.37	1.46
LVX	ND	2.89	8.97	0.94	ND	5.35	3.97	3.23	2.06	1.31	0.79
AMIO	ND	0.80	ND	ND	ND	0.67	ND	0.36	2.09	3.90	0.63
BOS	ND	0.34	5.46	0.11	ND	1.39	ND	0.34	6.10	ND	4.58

Appendix Table 26: Fold change in SPP1 expression after 14 days treatment in 2.5D, 3D, and OOC.
(Figure 56 E)

SPP1	2.5D				3D				OOC		
DMSO	1.00	1.00	1.00	1.00	1.00	1.00	1.00	1.00	1.00	1.00	1.00
Untreated	1.00	1.00	1.00	1.00	1.00	1.00	1.00	1.00	1.00	1.00	1.00
MET	0.67	0.64	0.40	0.17	1.01	1.07	0.04	0.89	1.17	1.39	0.86
DAB	0.32	1.26	2.97	1.95	0.72	ND	0.43	0.81	ND	ND	ND
PIO	0.23	0.57	0.44	0.54	0.15	0.25	0.02	ND	ND	ND	ND
ENT	0.24	5.02	0.28	0.32	0.31	1.19	ND	0.12	1.15	1.42	0.77
XIM	0.60	2.41	3.14	1.71	0.61	0.05	0.15	0.01	0.39	0.51	0.77
TRO	0.48	0.83	0.43	0.29	0.63	1.13	0.03	0.03	ND	ND	ND
TOL	0.24	1.98	0.15	0.13	4.46	0.78	ND	ND	0.40	0.49	0.32
APAP	0.24	2.46	0.33	1.22	4.29	ND	ND	0.08	0.15	0.69	1.99
FIA	ND	ND	0.01	0.04	ND	0.02	ND	ND	0.54	0.92	0.58
DIC	ND	ND	2.04	1.08	ND	0.12	ND	0.06	0.90	0.58	1.23
TXV	ND	0.95	2.15	0.57	ND	0.24	0.60	0.29	0.22	0.38	0.29
LVX	ND	0.92	1.75	0.48	ND	0.24	0.18	0.20	0.32	0.50	0.74
AMIO	ND	3.61	2.47	ND	ND	2.11	ND	ND	0.24	0.71	0.85
BOS	ND	2.51	4.03	ND	ND	0.30	0.04	0.03	0.33	0.82	1.75

Appendix Table 27: Fold change in mir122 expression after 14 days treatment in 2.5D, 3D, and OOC.
(Figure 59)

Treatment	2.5D			3D			OOC		
DMSO	1.00	1.00	1.00	1.00	1.00	1.00	1.00	1.00	1.00
Untreated	1.00	1.00	1.00	1.00	1.00	1.00	1.00	1.00	1.00
MET 750 µM	0.88	0.73	1.87	0.00	10.10	13.00	1.70	0.80	0.70
ENT 100 µM	0.27	0.05	0.66	0.00	0.80	0.70	0.70	1.50	0.70
BOS 30 µM	0.62	0.57	0.28	2.70	1.20	0.20	0.60	1.10	1.10
XIM 100 µM	0.16	0.06	0.89	0.00	0.00	0.10	0.50	0.10	0.80
TOL 100 µM	0.29	0.01	0.48	0.00	0.40	0.20	0.20	0.10	0.00
DIC 100 µM	0.09	1.57	0.52	4.20	5.90	3.60	1.10	0.10	0.90
AMIO 100 µM	0.01	0.01	0.03	0.00	0.30	0.00	0.30	0.70	0.90
FIA 200 µM	0.09	0.01	0.17	0.40	2.50	1.10	0.00	0.10	0.10
APAP 2500 µM	0.01	0.20	0.05	0.00	0.50	0.30	0.00	0.70	0.00
TVX 10 µM	1.18	1.15	0.74	0.60	3.10	2.80	0.90	1.10	0.80
LVX 100 µM	1.44	2.36	1.00	2.70	5.60	2.00	0.50	1.30	0.90

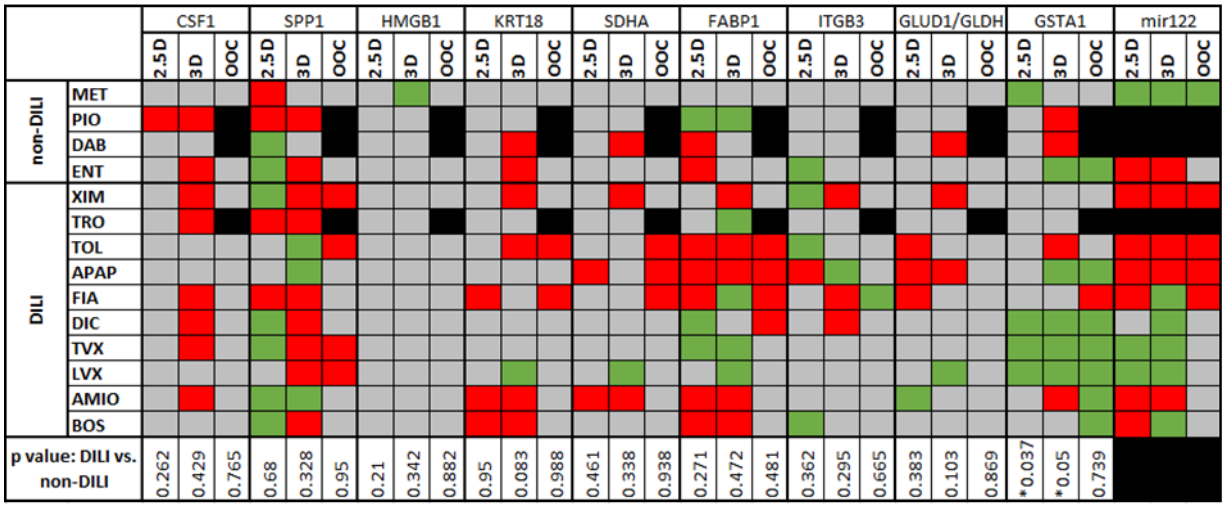

Figure 74: Overview and summary of altered gene expression after 14 days treatment.
Primary liver cells were treated in the 2.5D, 3D, and OOC model with DILI and non-DILI compounds. On day 14, gene expression was analyzed using the QuantiGene™ Plex assay. Table shows increased (≥ 2-fold, green), decreased (≤ 0.5-fold, red), or unchanged (grey) fold change in gene expression, normalized to vehicle control (Summary of Figure 55 and Figure 56). No values were collected for the fields marked in black. Statistical analysis was performed by Julian Kreis using one-sides Wilcoxon test. Statistically significant *p < 0.05. N=3/4.

8.10 Statistical analysis of potential genetic biomarkers

Appendix Table 28: Statistically significant differences in gene expression between DILI and non-DILI.
Primary liver cells were treated for 14 days in the advanced cell culture systems with most-DILI-concern and less-DILI-concern compounds. At days 2, 7, and 14, potential genetic biomarkers were analyzed. Table show calculated p values. Statistical analysis was performed by Julian Kreis using one-sides Wilcoxon test. *p < 0.05 (red). N=3/4

	Gene	2.5D	3D	OOC		Gene	2.5D	3D	OOC		Gene	2.5D	3D	OOC
low dose	GSTA1	0.037	0.053	ND	mid dose	ITGB3	0.070	0.818	0.665	high dose	CDH5	0.076	0.274	ND
	HMGB1	0.210	0.342	ND		CSF1	0.150	0.554	0.765		CSF1	0.138	0.303	ND
	CSF1	0.262	0.429	ND		SDHA	0.186	0.330	0.938		SPP1	0.186	0.175	ND
	FABP1	0.271	0.472	ND		CDH5	0.188	0.171	0.700		ITGB3	0.218	0.216	ND
	ITGB3	0.362	0.295	ND		SPP1	0.380	0.605	0.950		GSTA1	0.327	0.042	ND
	GLUD1	0.383	0.103	ND		HMGB1	0.587	0.512	0.822		SDHA	0.340	0.266	ND
	SDHA	0.461	0.338	ND		GSTA1	0.589	0.187	0.739		FASLG	0.356	0.752	ND
	CDH5	0.674	0.818	ND		KRT18	0.649	0.480	0.988		KRT18	0.527	0.956	ND
	SPP1	0.680	0.328	ND		FASLG	0.686	0.548	0.213		HMGB1	0.571	0.829	ND
	FASLG	0.936	0.024	ND		GLUD1	0.700	0.185	0.869		GLUD1	0.761	0.195	ND
	KRT18	0.950	0.083	ND		FABP1	0.813	0.982	0.481		FABP1	0.968	0.949	ND

A 2.5D low dose

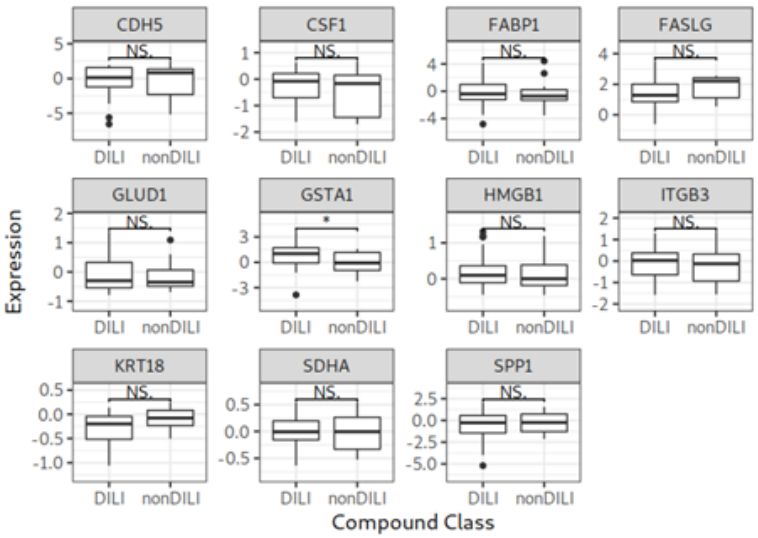

Gene	P value
GSTA1	0.0365
HMGB1	0.21
CSF1	0.262
FABP1	0.271
ITGB3	0.362
GLUD1	0.383
SDHA	0.461
CDH5	0.674
SPP1	0.68
FASLG	0.936
KRT18	0.95

B 2.5D mid dose

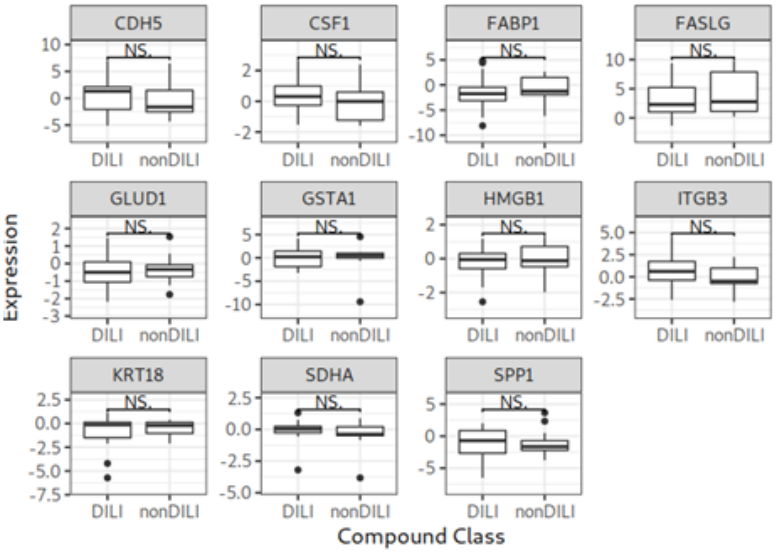

Gene	P value
ITGB3	1
CSF1	0.15
SDHA	0.186
CDH5	0.188
SPP1	0.38
HMGB1	0.587
GSTA1	0.589
KRT18	0.649
FASLG	0.686
GLUD1	0.7
FABP1	0.813

C 2.5D high dose

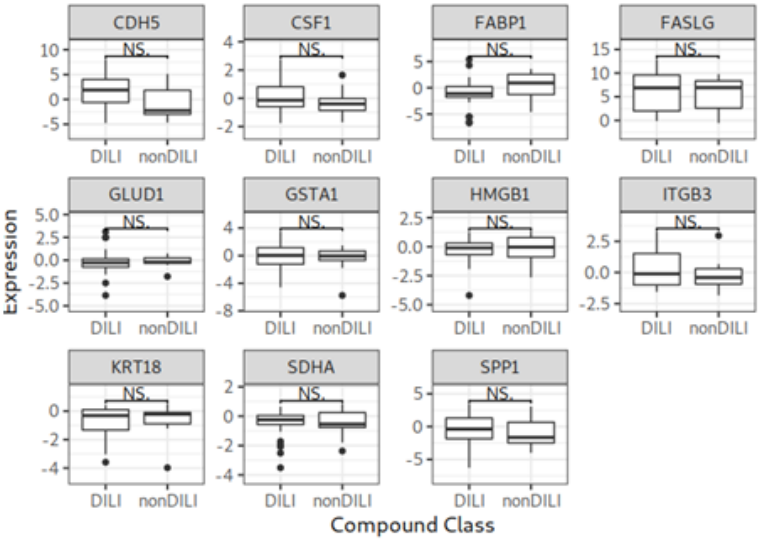

Gene	P value
CDH5	0.0758
CSF1	0.138
SPP1	0.186
ITGB3	0.218
GSTA1	0.327
SDHA	0.34
FASLG	0.356
KRT18	0.527
HMGB1	0.571
GLUD1	0.761
FABP1	0.968

D 3D low dose

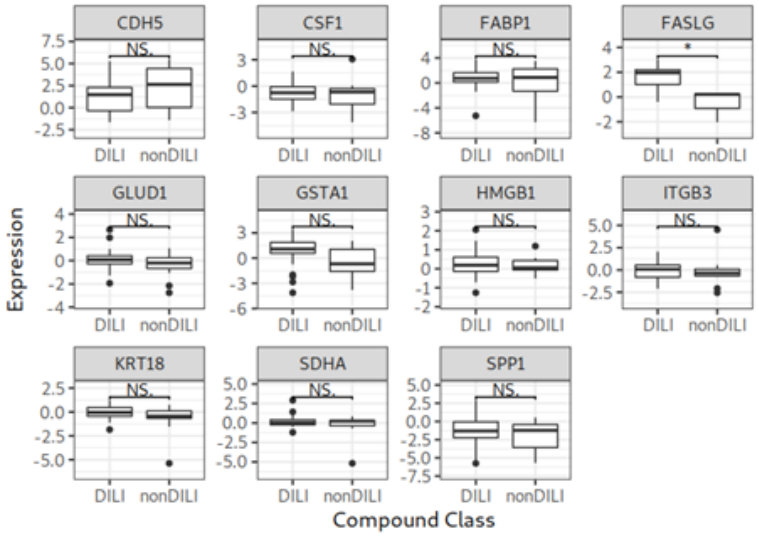

Gene	P value
FASLG	0.0242
GSTA1	0.0525
KRT18	0.0834
GLUD1	0.103
ITGB3	0.295
SPP1	0.328
SDHA	0.338
HMGB1	0.342
CSF1	0.429
FABP1	0.472
CDH5	0.818

E 3D mid dose

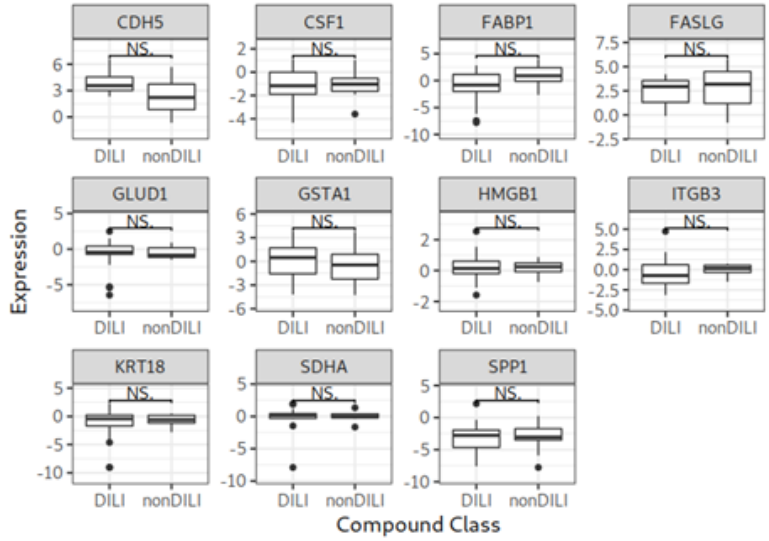

Gene	P value
CDH5	0.171
GLUD1	0.185
GSTA1	0.187
SDHA	0.33
KRT18	0.48
HMGB1	0.512
FASLG	0.548
CSF1	0.554
SPP1	0.605
ITGB3	0.818
FABP1	0.982

F 3D high dose

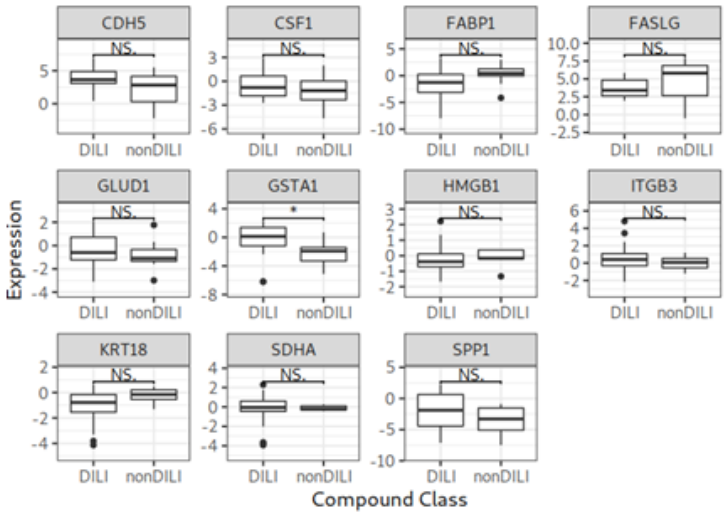

Gene	P value
GSTA1	0.0416
SPP1	0.175
GLUD1	0.195
ITGB3	0.216
SDHA	0.266
CDH5	0.274
CSF1	0.303
FASLG	0.752
HMGB1	0.829
FABP1	0.949
KRT18	0.956

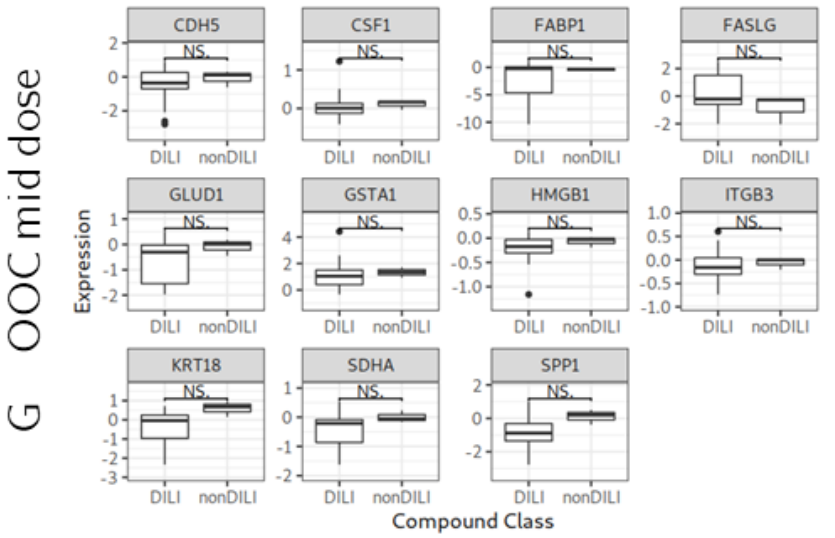

Gene	P value
FASLG	0.213
FABP1	0.481
ITGB3	0.665
CDH5	0.7
GSTA1	0.739
CSF1	0.765
HMGB1	0.822
GLUD1	0.869
SDHA	0.938
SPP1	0.95
KRT18	0.988

Figure 75: Statistically significant differences between DILI and non-DILI.
Primary liver cells were treated for 14 days in the advanced cell culture systems with most-DILI-concern (DILI) and less-DILI-concern (non-DILI) compounds. At day 14, cells were lysed, and gene expression was analyzed by the QuantiGene™ Plex assay. Graphs show statistically significance in (A) 2.5D low dose, (B) 2.5D mid dose, (C) 2.5D high dose, (D) 3D low dose, (E) 3D mid dose, (F) 3D high dose, and (G) OOC mid-dose treated models, normalized to vehicle control. Statistical analysis was performed by Julian Kreis using one-sides wilcoxon test. *p < 0.05. N=3/4.

8.11 Determined and published EC_{50} values

Appendix Table 29: EC_{50} values [µM] determined in 2.5D and 3D.
(Figure 51)

Drug	2.5D					3D			
AMIO	28.46	32.14	ND	ND	ND	3.80	2.93	11.16	17.76
TOL	41.01	32.28	33.04	30.83	27.17	78.68	ND	56.86	95.06
TRO	25.43	37.41	46.86	39.07	ND	14.04	ND	ND	ND
TVX	27.61	34.40	28.42	25.18	ND	54.16	ND	ND	ND
XIM	42.00	ND	ND	75.71	40.75	62.88	78.50	ND	ND
FIA	92.83	90.09	84.00	ND	ND	250.00	ND	ND	ND
DIC	ND	ND	ND	ND	ND	250.00	ND	ND	ND
APAP	ND	ND	ND	ND	ND	250.00	ND	ND	ND
LVX	ND	ND	ND	ND	ND	250.00	ND	ND	ND
PIO	29.04	29.29	101.07	102.90	ND	56.65	17.99	ND	ND
ENT	47.13	ND	52.50	30.88	38.49	119.00	117.60	ND	ND
DAB	74.95	82.63	54.48	21.86	28.75	76.62	73.35	ND	ND

Table 32: Published EC_{50} and EC_{20} values for PHHs mono- and cocultured in 2D, 3D, and OOC.

Com-pound	Cells	Model	Treatment	EC_{50} [µM]	EC_{20} [µM]	Refer-ence
APAP	PHH/NPC (2:1)	3D	14 days	-	300	[265]
	PHH LSECs	OOC	10 days	2400	-	[186]
	PHH	3D	7 days	2703	-	[392]
	PHH	3D	14 days	664.4	-	[392]
	PHH	3D	14 days	~1000	-	[383]
	PHH	2D	14 days	~3800	-	[383]
AMIO	PHH	3D	7 days	6.5	-	[392]
	PHH	3D	28 days	1.6	-	[392]
	PHH	3D	14 days	-	25 µM	[265]
	PHH/NPC (2:1)	2.5D	1 day	-	12 µM	[265]
	PHH	3D	15 days	26.4	-	[436]
	PHH	3D	7 days	16.7	-	[392]
	PHH	3D	14 days	11.9	-	[392]
TRO	PHH	3D	14 days	1.5	0.9	[392]
	PHH/NPC (2:1)	3D	14 days	-	5	[265]
	PHH	3D	7 days	4.2	-	[392]
	PHH	3D	14 days	1.5	-	[392]
	PHH	3D	14 days	<10	-	[383]
XIM	PHH/NPC (2:1)	3D	14 days	-	25	[265]
	PHH	3D	14 days	165.2	-	[392]
	PHH	3D	7 days	379.2	-	[392]
	PHH	3D	14 days	<500	-	[383]
BOS	PHH/NPC (2:1)	3D	14 days	-	100	[265]
	PHH	3D	28 days	41.8	-	[392]
	PHH	3D	7 days	69.5	-	[392]
	PHH	3D	14 days	<90	-	[383]
	PHH/NPC	OOC	10 days	-	30	[186]
DIC	PHH/NPC (2:1)	3D	14 days	-	30	[265]
	PHH	3D	28 days	45.9	-	[392]
	PHH	3D	7 days	56.8	-	[392]
	PHH	3D	14 days	~60	-	[383]
FIA	PHH/NPC (2:1)	3D	14 days	-	<4	[265]
	PHH	3D	28 days	0.1		[392]
	PHH	3D	7 days	0.7		[392]
	PHH/NPC	OOC	10 days	77	-	[186]
	PHH/NPC	3D	10 days	84	-	[186]
TOL	PHH/NPC (2:1)	3D	14 days	-	20	[265]
	PHH	3D	28 days	5.6	-	[392]
	PHH	3D	7 days	9.4	-	[392]
	PHH	3D	14 days	~20	-	[383]
ENT	PHH/NPC (2:1)	3D	14 days	-	100	[265]
	PHH	3D	14 days	150	-	[383]
	PHH	2D	14 days	100	-	[383]

MET	PHH/NPC (2:1)	3D	14 days	-	250	[265]
PIO	PHH/NPC (2:1)	3D	14 days	-	30	[265]
	PHH	3D	14 days	NA	-	[383]
TVX	PHH/NPC (2:1)	3D	14 days	-	100	[265]
	PHH	3D	14 days	NA	-	[383]
	PHH	2D	14 days	NA	-	[383]
LVX	PHH	3D	14 days	NA	-	[383]
	PHH	2D	14 days	NA	-	[383]
DAB	PHH	3D	14 days	NA	-	[383]
	PHH	2D	14 days	NA	-	[383]

Acknowledgment

At the end of my PhD thesis, I would like to thank all colleagues, friends, and relatives who supported me during the dynamic years. First and foremost, I would like to thank Dr. Paul Germann, Dr. Brigitte Simon-Hettich, and Dr. Philip Hewitt for giving me the possibility to conduct this doctoral thesis and made the time at Merck Healthcare KGaA an unforgettable experience for me. I would also like to take this opportunity to thank you for your confidence in me and my abilities, which I will be able to demonstrate in the coming year. My special thanks to Dr. Philip Hewitt for his continuous support, motivation, suggestions, and extensive knowledge. I am very glad that I can benefit at any time from your immense experience, which has also opened new perspectives for me.

Furthermore, I would like to thank Prof. Robert Lukowski and Prof. Dr. Ruth for their support, interest, and advise from my master's degree to the completion of my doctoral thesis. Your broad knowledge always inspired me with new possibilities during our meetings.

Moreover, I would like to thank my great colleagues in the toxicology department who welcomed me so warmly. Particularly, Janike Ehret, Bettina von Eiff, Isabel Koscielski, and Claudia Klement who supported me at all times in the lab and on many other occasions. Also, to Stefanie Hoffmann for the great discussions about our PhD topics, the resulting ideas for further experiments, and coping with the DGPT courses together. Working with you has always been great, and I look forward to the years ahead. I would also like to give special thanks to Anindya Siddharta and Thomas Wild for analysis of my media and protein samples, and to Alex Rolfe, Nicholas Geraci, Julian Kreis, and Dilafruz Juraeva for statistical analysis of my data.

Finally, I would like to thank my family and friends who always believe in me. To my friends - Your moral support always motivates me and kept me going when things were difficult. To my parents and my sister - You have always supported me in all my decisions without scrutinize them. That gave me the space and the opportunity to find my own way and pursue my goals. To my husband - You have always had my back. Your patience, understanding and advice have been with me for over 10 years now, always encouraging me to overcome challenges.

I am so glad to have all of you in my life.